FACULTY OF ENGINEERING AND ARCHITECTURE

Waveguide-Coupled Photodetectors and Light Sources Based on Colloidal Quantum Dots: From Building Blocks to Advanced Demonstrators

Chao Pang

Doctoral dissertation submitted to obtain the academic degree of
Doctor of Photonics Engineering

Supervisors

Prof. Dries Van Thourhout, PhD* - Prof. Pieter Geiregat, PhD** - Prof. Zeger Hens, PhD**

* Department of Information Technology
Faculty of Engineering and Architecture, Ghent University

** Department of Chemistry
Faculty of Sciences, Ghent University

October 2024

GHENT UNIVERSITY

ISBN 978-94-6355-905-8
NUR 950
Wettelijk depot: D/2024/10.500/110

Members of the Examination Board

Chair

Prof. Em. Daniël De Zutter, PhD, Ghent University

Other members entitled to vote

Prof. Jeroen Beeckman, PhD, Ghent University
Prof. Alberto Curto, PhD, Ghent University
Prof. Clément Livache, PhD, Institut Polytechnique de Paris, France
Prof. Delphine Marris-Morini, PhD, Université Paris Sud, France

Supervisors

Prof. Dries Van Thourhout, PhD, Ghent University
Prof. Pieter Geiregat, PhD, Ghent University
Prof. Zeger Hens, PhD, Ghent University

Dankwoord

Over the past 4.5 years, my time at Gent has been filled with unforgettable memories. There are many people I want to thank for their invaluable support throughout this journey.

First and foremost, I express my gratitude to my promoter, Prof. Dries Van Thourhout. Thank you for providing me with the opportunity to work on a project that combines two fascinating fields: silicon photonics and colloidal quantum dots. Your wealth of knowledge and insightful discussions have been impressive, and your expertise in photonics, semiconductor physics, and processing has greatly aided my PhD journey. I am also thankful for the freedom you've granted me, allowing me to work with less stress and explore various avenues.

I extend my appreciation to my other promoters, Prof. Pieter Geiregat and Prof. Zeger Hens. Pieter, your guidance into the world of colloidal quantum dots has been invaluable. Your prompt and kind responses whenever I seek help are greatly appreciated. Zeger, your extensive expertise in QD-based devices has significantly enhanced the quality and depth of my research. The discussions with you are always fruitful.

Within the intersection of silicon photonics and colloidal QDs, my colleagues and collaborators have played a crucial role. Without their contributions, our results would not have been possible. I owe thanks to my colleagues in the colloidal QD team. Lukas, your patient assistance in the cleanroom allowed me to learn the basics of designing and characterizing photonic integrated chips. Ivo, you are a so kind man and are always eager to help. I still remember your clear guidance when I was new to processing. Yuhao, your exploration of QD-based photodetectors has been vital for my project. Your openness to collaboration and rapid responses are impressive. Ezat, I truly appreciate your efforts in synthesizing PbS QDs. Without them, our integrated QD photodetector project wouldn't have taken off. Margarita, your work on bright CdSe/CdS red QDs and bulk CdS green QDs enabled our exploration of integrated light sources. Korneel, I was truly impressed by your expertise and experience in transient absorption spectroscopy. Jan, Papa, Delphine, Servet, Jing, and Dobromil, you all helped me in your own specific way, and for

that I am very grateful. I'd also like to acknowledge colleagues from other groups. Robin, Nithin, and Prof. Christophe Detavernier from CoCooN group, thank you for providing excellent ALD thin layers. Luis Moreno and Prof. David Cheyns from IMEC, your ITO layers were crucial. Frederik from LCP group and Bernhard, Xueshi and Prof. Koen Vandewal from OOE group at UHasselt, thanks for the discussion on QLED fabrication, characterization and analysis.

I am grateful to all my current and former colleagues from the Photonic Research Group for providing me a friendly and warm environment and sharing your knowledge. It's my please to share office with Yuting, Zhongtao, Sarah, Stijn, Laurens, Yanlu, Chenming, Sarah, Xiujun, Shiqi, Ali, Ying and Mohammadamin. It is enjoyable to work with you. Special thanks to Steven, Liesbet, Muneeb, and Elif for their unwavering support in the cleanroom. Clemens and Hasan, thank you for training me the measurement and offering technical solutions during my characterization. Kristien, Ilse Van Royen, Ilse Meersman and Bert, thanks for your support on IT and administration.

I would like to thank all my Chinese colleagues and friends, for the wonderful time we spent at Gent. The list is too long to name completely, please forgive me. Sincere thanks to Yiping, Zhongtao, Chunhui, Chenming, Xin, Yujie, Yang, Yi, Senbiao, Ye, He, Yu, Jing, Hong, Ting, Songyao and Xinyuan, for the happy hours we spent after work.

Most importantly, I want to express my deepest gratitude to my family, especially my parents and my grandma, who always support me with their unconditional love. And to my girlfriend, Shan Wang, who completes my soul. This journey would not have been possible without your understanding and encouragement. Thank you so much.

Gent, 2024
Chao Pang

Contents

Dankwoord **i**

Contents **iii**

List of Figures **vii**

List of Tables **xxiii**

Samenvatting **xxix**

Summary **xxxvii**

1 Introduction **1**

1.1 Research background 1

1.2 Colloidal quantum dots 3

1.2.1 Properties and Characteristics 3

1.2.2 Applications in photodetection and imaging 9

1.2.3 Applications in light sources 13

1.3 Integrated photonics 18

1.3.1 Silicon photonics 19

1.3.2 QDs in integrated photonics 22

1.4 Thesis objectives 22

1.5 Thesis Outline 23

1.6 Publications 25

1.6.1 Publications in international journals 25
1.6.2 Publications in international conferences 25

2 Development of 1.3 µm waveguide-coupled QDPD on SiN 27
2.1 Introduction 28
2.2 Formation and Characterization of PbS QDPD 29
2.2.1 Fabrication 29
2.2.2 Characterization 32
2.3 Design of WG-QDPD 33
2.4 Fabrication of WG-QDPDs 37
2.4.1 Passive waveguides 37
2.4.2 ALD of ZnO and Al_2O_3 39
2.4.3 N-contact patterning 41
2.4.4 ZnO patterning 41
2.4.5 QD patterning 41
2.4.6 P-contact patterning 42
2.5 Characterization of WG-QDPD 45
2.6 Formation of an integrated QD spectrometer 45
2.6.1 Basic knowledge of AWG 46
2.6.2 Design and fabrication of AWG 47
2.6.3 Spectrometer 48
2.7 Discussion 50
2.8 Conclusion 52

3 Development of 2.1 µm waveguide-coupled QDPD on SOI 53
3.1 Introduction 53
3.2 QDPDs with wavelength response up to 2.1 µm 55
3.2.1 Optimization of electron transport layer 56
3.2.2 Optimization of QDPD stack for 2.1 µm 63

3.3 Integration of QDPDs on waveguides 65
3.4 Characterization of WG-QDPDs 70
3.5 Demonstration of a 2.1 μm spectrometer 78
3.5.1 Basic operation of the PCG 78
3.5.2 Integrated spectrometer 79
3.6 Discussion 80
3.7 Conclusion 81

4 Spectrometer based on multi-color cascaded WG-QDPDs 83
4.1 Introduction 83
4.2 Principle 85
4.3 Spectrometer design 89
4.3.1 Choice of dispersive optics 89
4.3.2 Optimization of lengths of cascaded QDPDs 94
4.4 Fabrication 96
4.5 Characterization of QDPDs 100
4.6 Characterization of spectrometer 104
4.7 Discussion 106
4.8 Conclusion 107

5 Fourier transform spectrometer using QDPD array nano-samplers 109
5.1 Introduction 109
5.2 Principle 110
5.3 Design 115
5.3.1 Sampling waveguide 116
5.3.2 Multi-mode interferometer beam splitter 119
5.3.3 Thermal phase shifter 121
5.4 Fabrication 126
5.5 Characterization 131

5.6 Discussion . . . 134
5.7 Conclusion . . . 135

6 Integrated electrically driven QD light sources 137
6.1 Introduction . . . 137
6.2 Challenges related to QD-based lasing . . . 138
6.3 Integration on waveguide . . . 142
6.3.1 Fabrication . . . 142
6.3.2 Characterization . . . 149
6.4 Optimization of the HTL . . . 153
6.4.1 NPB doped with HAT-CN . . . 154
6.4.2 NPB doped with MoO_3 . . . 155
6.4.3 BF-DPB doped with F6-TCNNQ . . . 155
6.5 Discussion . . . 157
6.6 Conclusion . . . 159

7 Conclusion and outlook 161
7.1 Conclusion . . . 161
7.2 Outlook . . . 163

A Material synthesis and deposition 165
A.1 Synthesis of 950 nm PbS CQDs . . . 165
A.2 Synthesis of 1300 nm PbS CQDs . . . 165
A.3 Synthesis of 2100 nm PbS CQDs . . . 166
A.4 Preparation of sol-gel ZnO presursor . . . 166

References R-1

List of Figures

1 Integratie van 1.3 μm QDPD op SiN. (a) Schema van de WG-QDPD. (b) EQE versus optisch vermogen bij een bias spanning van -1 V. Inzet: foto-stroom versus optisch vermogen bij een spanning van -1 V. Het snijpunt van de zwarte stippellijnen geeft het begin van verzadiging aan. xxxi

2 Compacte spectrometer gebaseerd op een WG-QDPD-array en een planair concave rooster. (a) Bovenaanzicht van de spectrometer. Licht wordt geïnjecteerd via de roosterkoppelaar aan de rechterkant. (b) Respons van WG-QDPD's van acht kanalen en een referentiegolfgeleider (grijze lijn). xxxii

3 Breedband spectrometer gebaseerd op cascaderende WG-QDPD's. (a) Bovenaanzicht van de gefabriceerde spectrometer. (b) Spectrumreconstructie. xxxiii

4 QDPD's als nano-samplers voor SWIFT. (a) Basisprincipes van QDPD's als nano-probes. (b) Architectuur van het voorgestelde SWIFTS-systeem. xxxiv

1 Integration of 1.3 μm QDPD on SiN. (a) Device structure of WG-QDPD. (b) EQE vs. optical power at -1 V bias voltage. Inset: photo-current vs. optical power with bias voltage of -1 V. The intersection of the black dashed lines indicates the onset of saturation. xxxviii

2 Compact spectrometer based on a WG-QDPD array and a planar concave grating. (a) Top view of the spectrometer. Light is injected from the grating coupler on the right side. (b) Response of WG-QDPDs from eight channels and a reference waveguide (gray line). xxxix

3 Broadband spectrometer based on cascaded WG-QDPDs. (a) Top view of the fabricated spectrometer. (b) Spectrum reconstruction. . xli

4 QDPDs as nano-samplers for SWIFT. (a) Fundamentals of QDPDs as nano-probes. (b) Architecture of the proposed SWIFTS system. xlii

1.1 QDs synthesis with the hot-injection method 4

1.2 Quantum confinement effect. The conduction band and valence band are quantized into discrete energy levels. Reproduced from [1] 5

1.3 Spectral tunability of QDs with different sizes. (a) UV-excited photoluminescence of CdSe QDs. (b) Absorption spectrum of PbS QDs. Reproduced from [2] (c) Absorption spectrum of HgTe QDs. Reproduced from [3] 6

1.4 The simplified optical-gain model in QDs 7

1.5 Carrier transport mechanism in a QD film. (a) Direct tunneling through the energy barrier. The rate is related to the overlap of the carrier wave functions in adjacent QDs. (b) Hopping over energy barrier with the assistance of thermal energy or phonon. 8

1.6 Ligand exchange process. (a) Solid-phase ligand exchange. (b) Solution-phase ligand exchange. 9

1.7 Structures of QD-based photodetectors. (a) Photoconductors with a planar structure. (b) Photodiodes using a vertical heterojunction structure. 10

1.8 Band alignment of QD-based junctions. (a) Schottky junction formed between QDs and shallow-work-function metal [4]. (b) Heterojunction formed between ZnO and PbS QDs, and junction formed between QDs with different surface ligand treatments [5]. 11

1.9 QD based display technology. (a)QDs are used as the white light color converter to replace the traditional phosphors in Liquid Crystal Display (LCD) (b) QDs are used as electroluminescence emitters pixels, driven by the Thin Film Transistor (TFT)ackplane. (c)QDs are used as color converter pixels on top of a blue OLED emitter array. Reproduced from [6] 14

1.10 State-of-the-art QLED structure for efficiency electroluminescence and key factors that limit emission efficiency. (a) p-i-n multilayer stack with ETL and HTL for better carrier injection and confinement. (b) Non-radiative Auger recombination in QD if the carrier injection is not balanced. 16

1.11 Energy levels of common carrier transport layers used in QLEDs. Reproduced from [6] 16

1.12 Imec's 50G+ silicon photonics platform 19

1.13 Examples of integrating III-V materials into silicon photonics platforms. (a) Flip-chip mounting, reproduced from [7]. (b) Monolithic epitaxial growth, reproduced from [8]. (c) Micro-transfer printing, reproduced from [9]. (d) Wafer bonding, reproduced from [10]. . . 21

2.1 Structure and characterization of BI-QDPD. (a) Device structure of the BI-QDPD, illuminated from the bottom glass side by laser with Gaussian beam shape. (b) Absorption spectra for both types of QDs used in the BI-QPDD, dispersed in n-octane. QDs with exciton peak around 1300 nm were used for absorption, and QDs around 950 nm were used as hole-transport and electron-blocking material. (c) Dark current and photocurrent of BI-QDPD with an area of 1.77 mm^2. The photocurrent was measured for illumination at 1275 nm with a power of 0.16 mW (peak power density of $\sim$100 mW/cm^2). (d) EQE of BI-QDPD vs. optical power density at a bias voltage of -1V. The intersection of the dashed lines indicates the onset of saturation. Inset: photocurrent vs. optical maximum power density. The optical power density is that measured in the center of the Gaussian beam illuminating the BI-QDPD. 30

2.2 Measurement setup for BI-QDPD. The QDPD is illuminated with a 1275 nm laser from a cleaved single-mode fiber. The n-contact of the QDPD is connected using a clamp, while the p-contact is connected via an electrical probe. 32

2.3 Design of WG-QDPD. (a) Device structure of WG-QDPD. (b) Link between saturation of BI-QDPD and WG-QDPD. Red arrows point out the light propagation direction, vertical for the BI-QDPD and horizontal for the WG-QDPD. The electrons and holes are extracted in the vertical direction for both cases. The PbS-PbI_2 absorption layer can be split into small cells. The total carrier generation rate in each cell determines its local saturation. The cell with the maximum total carrier generation rate (indicated by a blue arrow) determines the onset of saturation for the whole PD. (c) Simulated saturation power of WG-QDPD vs. cladding thickness and waveguide width. (d) Slice of (c) for a waveguide width of 30 μm. (e) Slice of (c) for a cladding thickness of 0.35 μm. 34

2.4 Electrical field distribution in the PD stack with an input optical power density of 5.2 W/cm^2 36

2.5 Processing steps to fabricate WG-QDPD. (a) SiN waveguide patterning and top cladding deposition. (b) ALD of ZnO ETL and Al_2O_3 protection layer. (c) N-contact metal patterning with photoresist and liftoff. (d) QD film patterning with PMMA resist and liftoff. The Al_2O_3 protection layer was removed before spin-coating QDs. (e) P-contact metal patterning with PMMA resist and liftoff. (f) Top view of fabricated WG-QDPD. 38

2.6 HSQ as a top cladding. (a) Cross-section of planarized SiN waveguides with a height of 300 nm. (b) The transmission power of 300 nm $\times$ 900 nm single-TE-mode SiN waveguides with different lengths, covered by an HSQ top cladding. 39

2.7 The electrical and optical properties of ALD ZnO (a) TLM structures for resistivity measurement: 20 nm thick ZnO was patterned to a width of 125 μm. A pair of Ti/Au pads was placed on ZnO with different gaps between pad edges (5 μm to 50 μm). (b) Measured resistance with different ZnO lengths. (c) Cross-section of waveguides used for optical loss measurement, with dimensions of 3 μm by 300 nm. ZnO was patterned into different lengths (0.5 mm to 2 mm). (d) Measured propagation loss at 1.3 μm. 40

2.8 Surface contamination. (a) Dirty surface before HCl treatment. (b) Clean surface after HCl treatment. 42

2.9 QD peeling issue and solution. (a) QD peeling observed on HSQ. (b) ZnO patterning limited to the waveguide region for (a). (c) QDs on HSQ without peeling. (d) ZnO patterning extended to the pad region for (c), with a small break to prevent the large dark current from the pad region. 43

2.10 Response of WG-QDPDs. (a) I-V curves of WG-QDPDs under dark condition and illumination at 1275 nm. (b) EQE vs. optical power at -1V bias voltage. Inset: photo-current vs. optical power with bias voltage of -1V. The intersection of the black dashed lines indicates the onset of saturation. (c) Normalized EQE vs. photocurrent at -2V bias voltage for different waveguide widths. The saturation points of WG-QDPDs are indicated by vertical black dashed lines. (d) Saturation photocurrent with different waveguide widths. A linear fit is indicated by the black dashed line. 44

2.11 Principle of the AWG. (a) Schematic.(b) Operational diagram. Reproduced from [11] 46

2.12 AWG designed with IPKISS and fabricated with EBL. (a) Top view of the AWG. (b) Transmission spectrum of eight channels. 49

2.13 Integrated spectrometer with QDPD array and AWG. (a) Top view of the spectrometer. Light is injected from the right grating coupler. (b) Response of eight channels without applying bias voltage. The response of each channel was normalized to its maximum. 50

3.1 1.3 μm BI-QDPD with different ETL. (a) QDPD structure. (b) I-V curves under dark and light conditions (power of 1.6 mW, peak power density of 1.2 W/cm^2). Red: 40 nm ALD ZnO. Blue: 30 nm sol-gel ZnO. 55

3.2 Influence of ALD ZnO treatment on the I-V curves of QDPDs. Red: as-deposited ZnO without extra process. Blue: treated with O_2 plasma for 5 min. Black: annealing at 325 °C in air for 30 min. Light curves were measured under optical power of 1.6 mW (peak power density of 1.2 W/cm^2) 56

3.3 Performance of QDPDs with ALD + sol-gel ZnO as the ETL. Red: 40 nm ALD ZnO with 30 nm sol-gel ZnO on top. Blue: 30 nm sol-gel ZnO. Both samples were annealed in air at 325 °C. Light curves were measured under an optical power of 1.6 mW (peak power density of 1.2 W/cm^2). 58

3.4 Influence of sol-gel ZnO annealing atmosphere on the performance of QDPDs. Red: sol-gel ZnO annealed in air. Blue: sol-gel ZnO annealed in vacuum. Both samples had a sol-gel ZnO layer of 30 nm, annealed at 325 °C for 30 min. Light curves were measured under an optical power of 1.6 mW (peak power density of 1.2 W/cm^2). 59

3.5 ITO induced waveguide loss. (a) Waveguide structure used for absorption measurement at 1.3 μm. 20 nm ITO was sputtered on 300 nm by 3 μm waveguides and patterned into different lengths with wet etching. (b) Waveguide structure used for absorption measurement at 2.1 μm. The waveguides consist of a 30 μm-wide core with 70 nm shallow etch on 220 nm Si and a 45 nm thick HSQ cladding. 20 nm ITO was sputtered on top. (c) Propagation loss measured at 1.3 μm on structure (a). (d) Propagation loss measured at 2.1 μm on structure (b) 60

3.6 The influence of annealing temperature on the performance of QDPDs. (a) and (b) I-V curves under dark and light conditions respectively, annealed in air for 30 min at different temperatures. (c) and (d) microscope images of QDPDs annealing at 325 °C and 370 °C. 62

3.7 Absorption spectra for three types of QD inks (dispersed in n-octane) used in QPDDs. 63

3.8 Structure and Characterization of QDPD. (a) Vertical QDPD structures with surface illumination. (b) Influence of the interface layer on dark current density. (c) Dark current and photocurrent of Structure B QDPD, with an area of 1.77 mm^2. The photocurrent was measured with a 2.1 μm laser Gaussian beam illuminated from the bottom glass side, with a peak power density of 220 mW/cm^2. Inset: responsivity of QDPD vs. bias voltage. 64

3.9 Structure and dark I-V curves of QDPD with 1.3 μm and 2.1 μm PbS active layers. 65

3.10 Dark current and photocurrent of QDPD with an area of 1.77 mm^2. The photocurrent was measured with a 2.1 μm laser with a Gaussian beam illuminating the sample from the bottom glass side, with a peak power density of 220 mW/cm^2. Red: ZnO / 1.3 μm-PbS-TBAI / 2.1 μm-PbS-TBAI / 1.3 μm-PbS-TBAI / 0.94 μm-PbS-EDT. Blue: ZnO / 1.3 μm-PbS-TBAI / 2.1 μm-PbS-TBAI / 1.3 μm-PbS-EDT / 0.94 μm-PbS-EDT. 66

3.11 Spectral response of the QDPD with structure B, measured at a bias of -1 V and a peak power density of 220 mW/cm^2. 66

3.12 Integration steps to fabricate WG-QDPD. (a) Si rib waveguide patterning and planarization. (b) ITO sputtering and patterning with wet etching, followed by ZnO deposition with sol-gel method and patterning with wet etching. (c) N-contact metal patterning with liftoff. (d) QD film patterning with PMMA resist and liftoff. (e) P-contact metal patterning with PMMA resist and liftoff. (f) Cross-section of fabricated WG-QDPD. 67

3.13 HSQ as a low loss cladding layer for planarization. (a) Cross-section. (b) Transmitted power of spiral waveguides with varying lengths, with a waveguide width of 1.6 μm. 67

3.14 Leakage current from ITO/QD contact. (a) Dark current of 1300 nm WG-QDPDs with and without ITO/QD leakage path. (b) Image of WG-QDPD design that will lead to an ITO/QD leakage path. The dashed line indicates the area where QDs and Au will be integrated in the following steps. 69

3.15 Response of WG-QDPDs. (a) I-V curves of WG-QDPDs under dark condition and illumination at 2.1 μm. (b) Responsivity vs. optical power at -3 V bias voltage. Inset: photo-current vs. optical power. (c) Bandwidth of the integrated WG-QDPD. 70

3.16 Intensity profile of the fundamental TE mode in the WG-QDPD. The cross-section at position x=0 is shown in the right figure. Light is absorbed through the evanescent tail of the optical mode extended into the 2.1 μm QD film. 71

3.17 Setup schematics used for bandwidth measurement. PC: polarization controller, EOM: electro-optical modulator, EDFA: Erbium-doped fiber amplifier, RF: radio-frequency source, ESA: electrical spectrum analyzer. 72

3.18 Bandwidth of WG-QDPDs with different areas. WG-QDPDs, with a dimension of 30 μm × 200 μm and 3 μm × 200 μm, were measured under a reverse bias of -5 V. 73

3.19 Performance of WG-QDPDs with different lengths. (a) Top view of WG-QDPDs. (b) Optical absorption resulting from materials integrated onto waveguides. Measurements were obtained through optical transmission, with varying lengths for each material. (c) Darck current of devices with different area. (d) Responsivity of WG-QDPDs with different lengths. The predicted relationship between responsivity and length is presented by a dashed blue line, derived from optical loss measurements shown in (b) 74

3.20 Performance of WG-QDPDs with different shapes. (a) Top view of WG-QDPDs. Light is coupled into waveguides from the left side. (b) Dark current of different WG-QDPDs. (c) Responsivity of different WG-QDPDs. 75

3.21 Simulated light propagation (E^2) in tapered WG-QDPD. (a) Linear taper. (b) Exponential taper. Both tapers have a starting width of 30 μm and a ending width of 0.9 μm. Exponential taper follows a decreasing rate of 0.023 μm^{-1}. 77

3.22 Principle of the PCG. (a) Schematic, reproduced from [12]. (b) Operational diagram, reproduced from [13]. 78

3.23 Compact spectrometer based on a WG-QDPD array and a planar concave grating. (a) Top view of the spectrometer. Light is injected from the grating coupler on the right side. (b) Transmission spectrum of the planar concave grating. (c) Response of WG-QDPDs from eight channels and a reference waveguide (gray line). 80

4.1 Principle of breaking the FSR limit. (a) Planar concave grating and optical transmission at different channels. (b) Traditional photodetection solution for a spectrometer. Signals from different diffraction orders are mixed, so working range is limited to one FSR. (c) Cascaded QDPDs for photodetection. Different QDPDs have different responses to different diffraction orders, extra information is achieved to separate signals beyond one FSR. 85

4.2 Operating principle of the spectrometer based on two-color cascaded QDPDs. 87

4.3 Normalized absorption spectrum of both types of QD. 90

4.4 AWG with different FSR. (a) Waveguide array in Manhattan shape for FSR of 60 nm. (b) Waveguide array with a free-form curved shape for FSR of 90 nm. (c) and (d) Transmission spectra of AWG with FSR of 60 nm (a) and 90 nm (b), respectively. 90

4.5 AWG fabricated using EBL with proximity effect correction. (a) The transmission spectrum of the 90 nm FSR AWG. (b) and (c) indicate the imperfect correction of the proximity effect. Patterning in (c) used a higher base exposure dose compared to (b). 92

4.6 DBR as the grating facet for the PCG. The reflection spectrum is simulated using a 300 nm thick slab of SiN waveguide, featuring a 50/50 duty cycle DBR with a period of 430 nm. 93

4.7 Transmission spectrum of the PCG with etched facet as the grating element. 93

4.8 Fabrication steps for the metal-coated grating facet. (a) The sample is coated with EBL resist. (b) EBL is employed to define the position of the facets. (c) RIE is used to etch the SiN, exposing the facets. (d) Metal is evaporated onto the sample at a 45-degree angle with rotation for better coverage on the vertical facets. (e) Any remaining metal on the chip is removed through lift-off using resist remover. (f) HSQ is spun on top to serve as the top cladding. 94

4.9 The PCG with metal-coated facets. (a) The layout of the PCG. The etched grating (yellow region) will be coated with metal. (b) The SEM image of the tilted metal-coated facet. (c) Transmission spectrum of the PCG. 95

4.10 Measurement of absorption spectra for both types of QDPD. (a) The microscope image of QDPDs with different lengths for absorption loss measurement. (b) Transmission of type 1 QDPD with variable lengths measured at the wavelength of 1275 nm. (c) Transmission of type 2 QDPD with variable lengths measured at the wavelength of 1275 nm. (d) Absorption spectra of both types of QDPD. 97

4.11 Simulated transmission spectrum of the 8-channel PCG. 97

4.12 Optimization of the length of cascaded QDPDs. (a) Condition number mapped for different combinations of the QDPD lengths. (b) and (c) Responsivity of QDPD 1 & 2 for the 8 different channels i, with a length combination of $L_1 = 50\mu$m and $L_2 = 200\mu$m. . . 98

4.13 Integration steps to fabricate cascaded QDPDs. (a) Optical passive structures fabrication and planarization. (b) ITO sputtering and patterning with wet etching. (c) ZnO deposition with solgel method and patterning with wet etching. (d) N-contact evaporation and pattering with liftoff. (e) QDPD 1 deposition and patterning with liftoff. (f) QDPD 2 deposition and patterning with liftoff. (g) P-contact evaporation and patterning with liftoff. (h) Top view of the fabricated spectrometer. 99

4.14 Response of the two types of integrated QDPDs. (a) and (c) I-V curves under dark condition and illumination at 1275 nm for QDPD 1 and QDPD 2 respectively. (b) Photo-current vs. optical power of QDPD 1 at a bias of -1 V. (d) Photo-current vs. optical power of QDPD 2 at a bias of -2 V. 101

4.15 Photoresponse of QDPDs with different widths. (a) Photoresponse of type 1 QDPDs with a length of 50 μm, measured at a bias of -1 V. (b) Photoresponse of type 2 QDPDs with a length of 200 μm, measured at a bias of -2 V. 102

4.16 Responsivity vs. QDPD length at an optical power of 4 μW. (a) Responsivity of type 1 QDPDs, measured at a bias of -1 V. (b) Responsivity of type 2 QDPDs, measured at a bias of -2 V. 102

4.17 Bandwidth of the WG-QDPD. 103

4.18 Time stability of the WG-QDPD. 103

4.19 Measured channel spectral responsivity of QDPDs on eight channels of the PCG. (a) QDPD 1. (b) QDPD 2. 104

4.20 Spectral responsivity of cascaded QDPD j. 104

4.21 Resotred channel spectral responsivity of cascaded QDPDs covering two target diffraction orders. (a) QDPD 1. (b) QDPDs 2. . . . 105

4.22 Spectrum reconstruction. (a) and (b) Measured photocurrent from both types of QDPDs at all 8 channels with different input spectra S1 and S2, respectively. (c) Reconstructed spectrum of spectrum S1 and S2 and their reference spectrum measured from a commercial spectrometer. (d) Condition number of the reconstruction matrix for each channel. 106

5.1 QDPDs as nano-samplers for SWIFTS. (a) Fundamentals of QDPDs as nano-probes. Due to the short diffusion length within the QD layer, only carriers photo-generated in the vicinity of the p-contact contribute to the photocurrent, while carriers outside this region recombine non-radiatively. (b) Schematic of the QDPD array as nano-samplers for SWIFTS. By defining a p-contact array on top of the QDs, the QDPD array effectively serves as an array of nano-samplers for SWIFTS. These nano-samplers efficiently capture the stationary wave pattern within the SiN waveguide via evanescent absorption. 111

5.2 The architecture of our proposed SWIFTS system based on QDPD nano-samplers. On top of the waveguide, the QDPD array is integrated to sample the formed stationary wave. The p-contacts within the array feature a length l and are spaced apart by a pitch d. A thermal phase shifter is positioned on top of one arm to facilitate optical path tuning. 111

5.3 Influence of propagation loss α of the sampling waveguide on SWIFTS performance. (a) Interferogram formed with different propagation loss, using a 1.3 μm monochromatic light as input. The inset shows a zoomed-in view of the interferogram. (b) Normalized Fourier transform of the interferogram under different propagation loss. (c) Intensity of collected signal from QDPD vs. propagation loss. 114

5.4 The impact of the sampling waveguide length and QDPD size on SWIFTS performance. (a) The simulated Fourier spectrum of SWIFTS with varying sampling waveguide lengths. Monochromatic light of 1.3 μm wavelength serves as the input. (b) The simulated Fourier spectrum of SWIFTS with different QDPD lengths. A short (broadband) optical pulse serves as the input signal. 116

5.5 TE and TM modes in the sampling waveguide region. (a) and (b) depict the structure of two types of hybrid waveguides, one without and the other with a p-contact, respectively. The dimensions of each layer are as follows: SiN 350 nm $\times$ 10 μm, HSQ 320 nm, ITO 20 nm, ZnO 40 nm, PbS-TBAI 60 nm, PbS-EDT 75 nm, Au 50 nm. The simulations are conducted at a wavelength of 1.3 μm. (c) and (d) illustrate the mode profiles of the fundamental TE mode in the region without and with p-contact metal, respectively. (e) and (f) display the mode profiles of the fundamental TM mode in the region without and with p-contact metal, respectively. (g) and (h) depict the cross-section in the middle of the waveguides for TE modes and TM modes, respectively. 117

5.6 Effective refractive index and propagation loss of optical modes in the sampling waveguide region. (a) and (b) Fundamental TE modes. (c) and (d) Fundamental TM modes. The simulation is conducted under the same conditions as in Figure 5.5. 118

5.7 Tapering QD layer to reduce the reflection in the sampling waveguide. (a) The taper structure. (b) The reflection of fundamental TM mode from sampling waveguide (with QDs) to passive waveguide (without QDs), with varying taper lengths. 119

5.8 Simulation results of the sampling waveguide with counter-propagated input light. (a) The optical structure utilized for simulation, conducted using the 2D FDTD solver in Lumerical. (b) The simulated electrical field intensity in the PbS-TBAI absorption layer, at the wavelength of 1.3 μm. (c) A zoomed-in view of the stationary wave in (b). (d) The Fourier transform of the stationary wave employing monochromatic light at various wavelengths. Different wavelengths are associated with distinct periods. 120

5.9 Structure of a Multi-Mode Interferometer (MMI). L_w: the length of the multi-mode waveguide section. W_w: The width of the multi-mode section. L_a: aperture length. W_{a1}: the width of the narrow side of the apertures. W_{a2}: the width of the expanded side of the apertures. W_s: the central distance between two output apertures. The optimized parameters for our application are denoted in the brackets. 121

5.10 Simulation results of designed MMI. (a) Wavelength response. (b) Electrical field distribution. 122

5.11 Design and simulation of the thermal phase shifter. (a) The structure of the thermal phase shifter. Triple-path waveguides are employed to obtain a larger achievable phase shift. The top view and cross-section of the structure are presented in the upper and lower parts of the figure, respectively. (b) The simulated optical loss with increased top cladding thickness. (c) The simulated thermal map using a 2D model. The length of the phase shifter is set to 3 mm, and an applied electrical power of 1 W is considered. The top cladding thickness is set to 2 μm. (d) The simulated thermal phase shift with increased electrical power. 122

5.12 Layout of the designed SWIFTS chip. 125

5.13 Integration steps to fabricate the SWIFTS. (a) Preparation of the passive waveguides. (b) ITO and ZnO patterning. (c) n-contact patterning. (d) Ti heater patterning. (e) QDs patterning. (f) p-contact patterning. (g) PECVD SiO_2 deposition and contact opening. (h) Connection metal patterning. 126

5.14 Top cladding deposition. (a) A 2 μm thick HSQ layer was utilized as the top cladding. This was achieved through four rounds of spin-coating and annealing, with each cycle forming a 500 nm thick layer. (b) An 800 nm thick HSQ layer and a 1.2 μm PECVD SiO_2 layer were employed as the top cladding. For improved planarization, two layers of HSQ, each 400 nm thick, were utilized. 127

5.15 Nano p-contact patterning. (a) Liftoff with PMMA baked at different temperatures. (b) Nano p-contact from 20 nm to 1μm. (c) The structure used to test the quality of the nano metal lines with 100 nm width. (d) I-V curves of nano metal lines in (c). 129

5.16 Image of the fabricated P-contact array. 130

5.17 Influence of baking temperature on the performance of QDPDs. (a) Structures used for test. (b) The dark and light responses of the QDPDs. The optical power is 1.13 mW and the optical peak power density is around 1 W/cm^2. 130

5.18 Performance of thermal phase shifters. (a) MZI structure used for thermal phase shift measurement. (b) I-V curves of heaters with different lengths. (c) Transmission spectra of MZI (heater length 1 mm and 4 mm) with varying electrical power. 132

5.19 Photoresponse of nano QDPDs with different p-contact lengths. (a) Mircoscope image of fabricated nano QDPDs. (b) I-V curves of QDPDs with different p-contact lengths under 1.3 μm illumination. (c) The averaged photocurrent (from -3.5 V to - 4.5 V) with different p-contact lengths. 133

5.20 Failed connection metal wire patterning. 134

6.1 Simulation results for waveguide-coupled QLED. (a) Cross-sectional schematic of the hybrid waveguide with the integrated QLED on top. (b) Mode profile showing the fundamental TE mode of this hybrid waveguide. (c) Simulated optical loss with versus thickness of the organics. An ALD ZnO thickness of 10 nm, SiN height of 300 nm and width of 3 μm were used in the simulation. 139

6.2 Transient absorption characterization of QDs. (a) Time-resolved absorption dynamics at a probe wavelength of 630 nm with excitation at 520 nm. (b) Material gain measured 2.5 ps after excitation. [14] 139

6.3 Resistivity of NPB and its influence on QLEDs. (a) TLM structure used to measure the resistivity of NPB. NPB was evaporated to a thickness of 100 nm on pairs of gold electrodes with varying gaps. Interdigitated electrodes, 3 cm in length, were employed to facilitate measurable current. (b) Measured resistance corresponding to different electrode gaps under a bias of 5 V. (c) and (d) Structure and I-V curves of QLEDs with NPB thicknesses of 50 nm and 500 nm, respectively. 141

6.4 Optimization of the QLED structure for integration on SiN waveguide. (a) The QLED structure with 10 nm ALD ZNO, 30 nm QD layer, low-loss HTL consisting of TCTA and NPB, high-mobility HTL consisting of (HAT-CN 20 nm / NPB 20 nm)$_n$ alternating stacks, 10 nm HAT-CN HIL and 200 nm Al top electrode. (b) Simulated optical loss induced by the HTL and p-contact metal at varying thicknesses of the low-loss HTL. The total thickness of the HTL was fixed at 400 nm. Other materials were assumed to be transparent in this simulation. 142

6.5 Processing steps to integrate QLED stack on SiN waveguides. (a) SiN waveguide patterning, defined with EBL and dry etching. (b) ZnO was deposited using ALD as the ETL, while Al_2O_3 was applied as a protective layer. These layers were patterned through photolithography and wet etching techniques to confine the active region, effectively reducing optical loss. (c) N-contact metal patterning with photolithography and liftoff. (d) SiO_2 deposition with PECVD and local planarization using EBL and dry etching. (e) QD film patterning with EBL and liftoff. (f) Organic semiconductor and Al metal electrode patterning using evaporation through a shadow mask. 143

6.6 Optimization of annealing temperature for ALD ZnO. (a) The propagation loss of waveguides (300 nm $\times$ 3 μm) coated with 10 nm ALD ZnO and a 10 nm Al_2O_3 protection layer, rapidly annealed at various temperatures. Optical loss was measured at a wavelength of 640 nm. (b) The resistivity of the ZnO film at different annealing temperatures. Both the optical loss and resistivity were measured using varying length methods. 144

6.7 Process steps of local planarization. (a) Deposition of 300 nm SiO_2 using PECVD. (b) Patterning of e-beam resist using EBL. We took precise control of the overlap alignment and size dimension. The region with additional surface morphology was exposed, while other parts were protected by the resist after development. (c) RIE dry teaching to remove the excess SiO_2. (d) Removal of the resist with O_2 plasma. 145

6.8 SEM images of waveguides after planarization. (a)-(c) SiO_2 etch back using RIE with a self-bias of 380 V. The ZnO and Al_2O_3 layers were susceptible to damage due to the intense ion bombardment. (d) SiO_2 etching with RIE employing a reduced self-bias of 200 V. This resulted in significantly reduced damage to the ZnO and Al_2O_3 layers, and the process exhibited greater stability. 146

6.9 Influence of alignment and dimensional accuracy on local planarization. (a) The width of the etched-back area is smaller than the actual SiO_2 width, resulting in unetched SiO_2 lumps on both sides of the waveguide. This phenomenon affects subsequent QD spin-coating processes and introduces pinholes in the devices. (b) The overlap alignment is shifted compared to the target region. On one side, unetched SiO_2 lumps are present, while on the other side, over-etching of SiO_2 leads to a valley formation. (c) The consequence of the over-etched valley is illustrated. Weak adhesion on the SiO_2 deposited on the sidewall of the waveguide, coupled with strong stress in the deposited SiO_2, causes the SiO_2 to peel off, especially after wet etching of Al_2O_3 to expose the ZnO. (d) SEM image of a planarized waveguide with overetching on the left side and a lump on the right side. Peeling of the SiO_2 on the sidewall is evident. . . 147

6.10 The influence of QD annealing is significant. Without annealing, the QD film on the substrate tends to peel off when immersed in acetone during the liftoff process. However, with annealing, the QD film becomes more physically robust, thereby preventing peeling. 148

6.11 Influce of annealing temperature on the performance of ASE under optical pump. (a) Hybrid waveguide with QDs as gain material embedded in SiN. (b) L-L curves of waveguides with QDs annealed at different temperatures under N_2 atmosphere. 149

6.12 The setup for electrical pulse pumping. The device was connected electrically with probes. The emission was collected from the cleaved facet using a micro-lensed fiber. 150

6.13 Measurement of current driving the QLED under pulsed electrical pumping. (a) The measured current for an active area of 9000 μm^2 at various driving voltages. The measured current exhibits transient behavior at the onset and end of the electrical pulse. The actual current driving the QLED can be determined from the stable region, as indicated by the black frame. (b) and (c) The equivalent circuit of the device and its origin. The emission region, with a narrow area of 9000 μm^2, can be equated to a diode and series resistance R_2. The n-contact, separated from the p-contact by SiO_2 and other layers, constitutes a capacitor C_1 and resistor R_1, in parallel with the diode and R_2. Notably, this area surpasses the emission region in size, exceeding 45000 μm^2, signifying that R_1 is considerably smaller than R_2. A load resistor is positioned in series with these components to convert current into voltage for measurement using the oscilloscope (OSC). 151

6.14 Characterization of the waveguide coupled QLED. (a) Current density at different driving voltage. (b) Output power from the cleaved facet at different current densities. (c) The emission spectra at different current densities. (d) Optical transmission measurement on two types of structures. 640 nm laser was injected into the waveguide from the cleaved facet, and the output power from the grating coupler shows a similar level. 152

6.15 The influence of thick NPB:HAT-CN HTL on the performance of QLEDs. (a) QLED structures, device 2 has an extra layer of 400 nm thick NPB doped with HAT-CN. The emission pixel has a dimension of 2 mm $\times$ 3 mm, defined by the overlap of the bottom ITO electrode and the top p-contact. (b) Characterization of the QLED. Bright emission from the QLED can be distinctly observed. (c) Current density vs. driving voltage. (d) Output optical power density vs. driving voltage. 154

6.16 Structures to measure the conductivity and optical absorption of NPB doped with MoO_3. (a) A pair of Au electrodes with varying gaps from 10 μm to 50 μm was designed, configured into interdigitated shapes with a length of 3 cm, as illustrated in Figure 6.3(a). (b) Spiral SiN waveguides with dimensions of 300 nm $\times$ 1 μm and lengths ranging from 0.9 cm to 1.5 cm were fabricated. To mitigate optical absorption and facilitate measurable transmission power, a 180 nm PECVD SiO_2 layer was deposited on top in the case of NPB with 33wt% MoO_3 doping. 100 nm NPB doped with MoO_3 was coated on these samples. 156

6.17 The performance of BF-DPB doped with F6-TCNNQ. (a) Device 3 and 4 represent QLED samples with or without a 200 nm layer of BF-DPB:F6-TCNNQ, respectively. Device 5 was employed for conductivity measurement, while Device 6 facilitated absorption measurement. (b) Current density vs. driving voltage. (c) Output optical power density vs. driving voltage. 157

6.18 ITO induced optical loss for waveguide-coupled LED with different HTL thickness. 158

List of Tables

2.1 Parameters for designing the AWG. 47

3.1 Annealing influence on the resistivity of ALD ZnO and ITO. The thickness of ALD ZnO and ITO is 40 nm and 20 nm respectively. All annealing processes were conducted at 325°C for 30 minutes. . 58

6.1 Resistivity and complex refractive index of NPB doped with MoO_3. The resistivity was measured using the TLM method. The real refractive index was measured from ellipsometry. The imaginary refractive index was obtained by measuring the waveguide loss and fitting it into a simulation model. Materials with a thickness of 100 nm were deposited on these characterization samples. The missing value for 15% MoO_3 doping is due to the absence of SiO_2 between the SiN core and the deposited organics in this case. The high absorption results in no measurable transmitted optical power. 156

List of Acronyms

ALD	Atomic layer deposition
ASE	Amplified Spontaneous Emission
AWG	Arrayed Waveguide Grating
CMOS	Complementary Metal-Oxide-Semiconductor
CW	Continuous Wave
DBR	Distributed Bragg Reflector
DFB	Distributed Feedback
EDFA	Erbium-doped Fiber Amplifier
EOM	Electro-optical Modulator
EQE	External Quantum Efficiency
ETL	Electron Transport Layer
FBMS	Fixed Beam Moving Stage
FDTD	Finite-difference Time-domain
FSR	Free Spectrum Range
FWHM	Full Width Half Maximum
HIL	Hole Injection Layer
HOMO	Highest Occupied Molecular Orbital
HTL	Hole Transport Layer
IQE	Internal Quantum Efficiency
IR	Infrared
LCD	Liquid Crystal Display
LD	Laser Diode
LDR	Linear Dynamic Range
LED	Light Emitting Diode
LUMO	Lowest Unoccupied Molecular Orbital
LWIR	Long-wave Infrared

MBE	Molecular Beam Epitaxy
MMI	Multi-Mode Interferometer
MOCVD	Metal-Organic Chemical Vapor Deposition
MWIR	Mid-Wave Infrared
MZI	Mach-Zehnder interferometer
NEP	noise equivalent power
OLED	Organic Light Emitting Diode
PC	Polarization Controller
PCB	Printed Circuit Board
PCG	Planar Concave Grating
PD	Photodiode
PEC	Proximity Effect Correction
PIC	Photonic Integrated Circuit
PLQY	Photoluminescence Quantum Yield
QD	Colloidal Quantum Dot
QDPD	Colloidal Quantum Dot based Photodiode
QLED	Quantum-dot Light Emitting Diodes
QLD	Quantum-dot Laser Diode
ROIC	Readout Integrated Circuit
SOI	Silicon on Insulator
SWIR	Short-Wave Infrared
SWIFTS	Stationary-Wave Integrated Fourier Transform Spectrometer
TFT	Thin Film Transistor
TLM	Transfer Length Method
WDM	Wavelength Division Multiplexing

Samenvatting

De Nobelprijs voor Scheikunde van 2023 werd toegekend aan Alexei Ekimov, Luis Brus en Moungi Bawendi voor hun bijzondere bijdragen aan de ontdekking en synthese van colloïdale quantum dots (QDs). Deze nanokristallen vormen een nieuwe klasse van halfgeleiders met talrijke voordelen. Ze vertonen heldere en smalbandige lichtemissie, een hoge absorptie, afstembaarheid over een golflengtebereik van het zichtbaar tot in het infrarood, goedkope chemische synthese, schaalbare oplossing-gebaseerde verwerking en compatibiliteit met verschillende substraten. QDs worden ondertussen gebruikt in commerciële toepassingen zoals televisieschermen en hun gebruik in een breed scala aan andere opto-elektronische applicaties, waaronder lasers, één-foton bronnen en zonnecellen, wordt momenteel onderzocht.

QDs kunnen ook aantrekkelijk zijn voor integratie met fotonische geïntegreerde circuits (PICs). Zo'n PICs, voor het eerst voorgesteld door Stewart E. Miller in 1969, bieden de mogelijkheid om complexe optische bulk systemen te miniaturiseren tot goedkope en robuuste chips. Siliciumfotonica, waarbij voor de fabricage gebruik gemaakt wordt van de bestaande infrastructuur ontwikkeld voor de realisatie van op silicium gebaseerde elektronische ICs, is daarbij bijzonder veelbelovend. De afwezigheid van een geschikte lichtbron belemmert echter de verdere ontwikkeling en exploitatie van dit platform. Ook fotodetectie voorbij de traditionele telecomgolflengtes is niet mogelijk vanwege de bandgap van germanium, het materiaal dat standaard gebruikt wordt voor de realisatie van detectoren op het siliciumfotonica platform. SiN op SiO_2 is een alternatieve substraatoptie en laat propagatie van zichtbaar licht toe. SiN heeft bovendien ook een heel laag propagatieverlies en laat een hoog vermogen toe. Maar het blijft een passief platform, zonder lichtbronnen en fotodetectoren. Heterogene integratie van exotische materialen is vereist om deze beperkingen aan te pakken. QDs zijn dan een veelbelovende kandidaat vanwege hun lage kosten, spectrale afstembaarheid, eenvoudige verwerking en compatibiliteit met een breed scala aan substraten. Deze kenmerken maken QDs een veelbelovende optie in vergelijking met andere integratietechnieken. De heterogene integratie van QDs op PICs bevindt zich echter nog in een vroeg stadium.

In dit proefschrift onderzoeken we de integratie van QDs in PICs als fotodetectoren en elektrisch aangedreven lichtbronnen en verkennen we hun potentiële toepassingen. Beginnend met de integratie van loodsulfide (PbS) QDs op SiN-golfgeleiders, ontwikkelen we een schaalbaar proces om golfgeleider-gekoppelde

op QD-gebaseerde fotodiodes (WG-QDPDs) te integreren als een goedkope fotodetectieoplossing. Verder optimaliseren we het WG-QDPD-proces en gebruiken we grotere PbS QDs om fotodetectie voorbij de absorptiegrens van germanium te demonstreren, waarbij we absorptie tot 2,1 μm aantonen.

Vervolgens demonstreren we twee nieuwe architecturen voor de realisatie van compacte spectrometers, waarbij we gebruik maken van de unieke eigenschappen van QDs. Door de afstembare absorptie van QDs te combineren met dispersieve PICs, demonstreren we een spectrometer met een spectrale bandbreedte die twee keer zo groot is als die van de standaard spectrometer. Daarnaast gebruiken we een rij van QDPDs met sub-golflengte afmetingen als nano-probes voor de realisatie van een zogenaamde stationaire-golf geïntegreerde Fourier-transformspectrometer (SWIFTS). We onderzoeken ook op QD-gebaseerde lichtbronnen, waarbij we streven naar elektrisch aangedreven versterking door QDs met CdSe kern en CdS schil op SiN-golfgeleiders te integreren. Hoewel emissie van een hoog energetische staat wordt waargenomen, is verdere optimalisatie aan de materiaalkant nodig om optische versterking te bereiken.

Ontwikkeling van 1.3 µm WG-QDPD op SiN

In het eerste deel van deze thesis demonstreer ik de integratie van een QDPD op SiN-golfgeleiders, met een fotorespons tot 1.3 μm. De QDPD bestaat uit twee lagen van PbS QDs, die respectievelijk zijn gefunctionaliseerd met loodjodide (PbI_2) en ethanedithiol (EDT), gestapeld op een zinkoxide (ZnO) elektronen injectie laag (ETL) gevormd met een atoomlaagdepositie proces (ALD). De structuur is weergegeven in Figuur 1 (a). Na het analyseren van de vermogenafhankelijke verzadiging van de fotostroom in een een langs onder belichte, vlakke QDPD, concluderen we dat de sterke optische opsluiting en de daaruit volgende hoge optische intensiteiten in golfgeleiders reeds bij heel lage vermogens tot verzadiging van een WG-QDPD kan leiden. Om dit probleem op te lossen, stellen we voor om de overlap met het evanescent veld te verminderen door de claddinglaagdikte en de golfgeleiderbreedte te gebruiken als verstelbare parameters om het verzadigingsvermogen te verhogen.

Vervolgens ontwikkelen we een schema voor de integratie van de relatief eenvoudige 3-laags QDPD-stack op SiN-stripgolfgeleiders, met behulp van standaard schaalbare processen. Met een golfgeleiderbreedte van 30 μm en een claddinglaag van 350 nm, bereiken we een responsiviteit van 0.69 A/W, wat overeenkomt met een externe kwantum efficiëntie (EQE) van ongeveer 67.5% bij 1275 nm. De respons is lineair voor vermogens tot 400 nW bij -1 V spanning, zoals kan worden gezien in Figuur 1 (b).

Om de schaalbaarheid van de voorgestelde integratie-aanpak te demonstreren, ontwerpen en testen we een compacte 8-kanaals spectrometer geïntegreerd met een array van WG-QDPDs. Deze spectrometer toont een duidelijke golflengteafhankelijke respons met kanaaloverspraak van 15 dB. Deze eerste demonstratie,

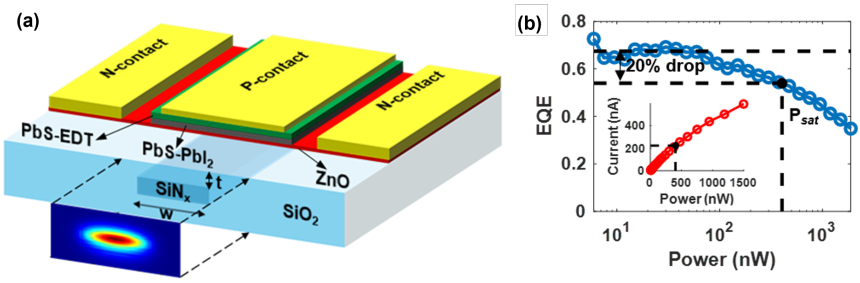

Figuur 1: Integratie van 1.3 μm QDPD op SiN. (a) Schema van de WG-QDPD. (b) EQE versus optisch vermogen bij een bias spanning van -1 V. Inzet: foto-stroom versus optisch vermogen bij een spanning van -1 V. Het snijpunt van de zwarte stippellijnen geeft het begin van verzadiging aan.

waarbij meerdere QDPDs samen werden geintegreerd met een on-chip spectrometer te creëren, toont aan dat we een veelbelovende route voor de schaalbare integratie van QDPDs in complexe PICs hebben ontwikkeld.

Ontwikkeling van 2.1 µm golfgeleider-gekoppelde QDPD op silicium

Het tweede resultaat dat we demonstreren, is de integratie van PbS QDPDs op siliciumgolfgeleiders, waarbij het golflengtebereik wordt uitgebreid voorbij de traditionele telecommunicatie golflengtes.

We optimaliseren het integratieproces door het ALD ZnO te vervangen door meer elektrisch stabiele lagen van indiumtinoxide (ITO) en sol-gel ZnO. We gebruiken een gesputterde ITO laag als de transparante onderste elektrode en een sol-gel ZnO laag als de elektronentransport- en gatenblokkeringslaag. Deze optimalisatie verbetert de reproduceerbaarheid en stabiliteit van het integratieproces aanzienlijk. We optimaliseren ook het QDPD-ontwerp om de lekstroom te verlagen en plaatsen de 2.1 μm QDs tussen 1.3 μm QDs om minder interface-toestanden-gerelateerde lekstroom te verkrijgen.

Met behulp van het geoptimaliseerde QDPD-ontwerp en het tweede generatie proces gebaseerd op een ITO/sol-gel ZnO ETL, demonstreren we WG-QDPDs bij kamertemperatuur, met een responsiviteit van 1.3 A/W bij 2.1 μm, een donkerstroom van slechts 106 nA en een bandbreedte van 1.1 MHz. Bovendien tonen we aan dat onze WG-QDPD een laag ruis-equivalent vermogen (NEP) van 0.15 pW/$\sqrt{\text{Hz}}$ heeft, dankzij de hoge responsiviteit en lage donkerstroom, wat aantrekkelijk is voor de detectie van zwakke signalen. We demonstreren de betrouwbaarheid van de integratieaanpak door een compacte on-chip spectrometer te realiseren die een array van 8 WG-QDPDs bevat en opereert in het spectrale venster tussen 2.063 en 2.135 μm, zoals weergegeven in Figuur 2.

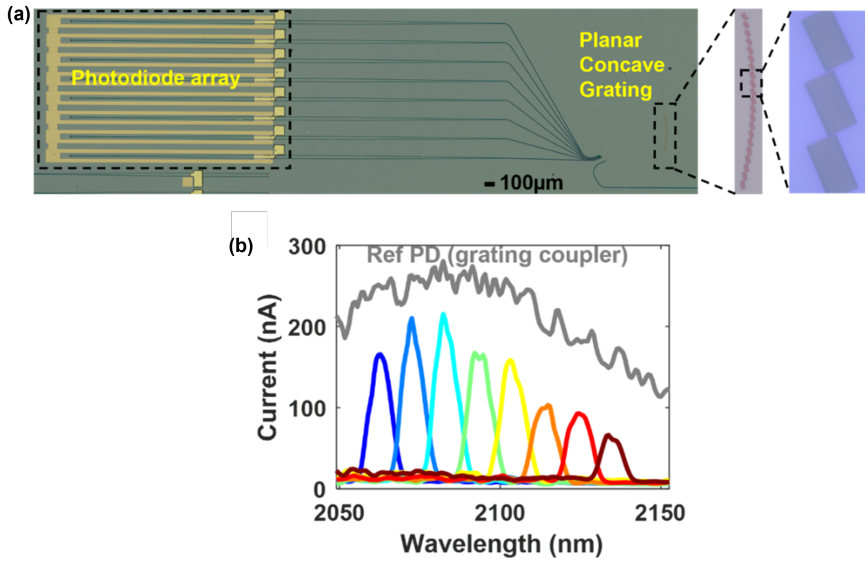

Figuur 2: Compacte spectrometer gebaseerd op een WG-QDPD-array en een planair concave rooster. (a) Bovenaanzicht van de spectrometer. Licht wordt geïnjecteerd via de roosterkoppelaar aan de rechterkant. (b) Respons van WG-QDPD's van acht kanalen en een referentiegolfgeleider (grijze lijn).

Spectrometer gebaseerd op multi-kleur cascaded WG-QDPDs

In het derde deel verkennen we de potentiële toepassingen van onze QDPDs. We ontdekken dat de afstembaarheid van het QD-absorptiespectrum veelbelovend is wanneer de QDPDs geïntegreerd worden in complexere optische systemen. Geïntegreerde dispersieve componenten zoals arrayed waveguide gratings (AWG) of planare concave gratings (PCG) worden vaak gebruikt in siliciumfotonica om on-chip spectrometers te realiseren. Er bestaat echter een fundamentele trade-off tussen het operationele spectrale bereik en de spectrale resolutie. Het bereiken van een betere spectrale resolutie binnen een vergelijkbare oppervlakte vereist een grotere optische dispersie, wat meestal een hogere diffractieorde impliceert en daardoor een kleiner vrij spectrale bereik (FSR) en een smallere spectrale bandbreedte. Deze tradeoff is er omdat in elk kanaal een enkele fotodetector wordt gebruikt, waardoor optische signalen van aangrenzende diffractieordes ononderscheidbaar worden. Door verschillende soorten fotodetectoren in cascade op de individuele kanalen te integreren, elk met een unieke respons voor verschillende diffractieordes, zouden signalen van meer dan één FSR moeten kunnen worden ontkoppeld, waardoor de tradeoff wordt geëlimineerd.

Hier gebruiken we de combinatie van de afstembare eigenschappen van QDs met

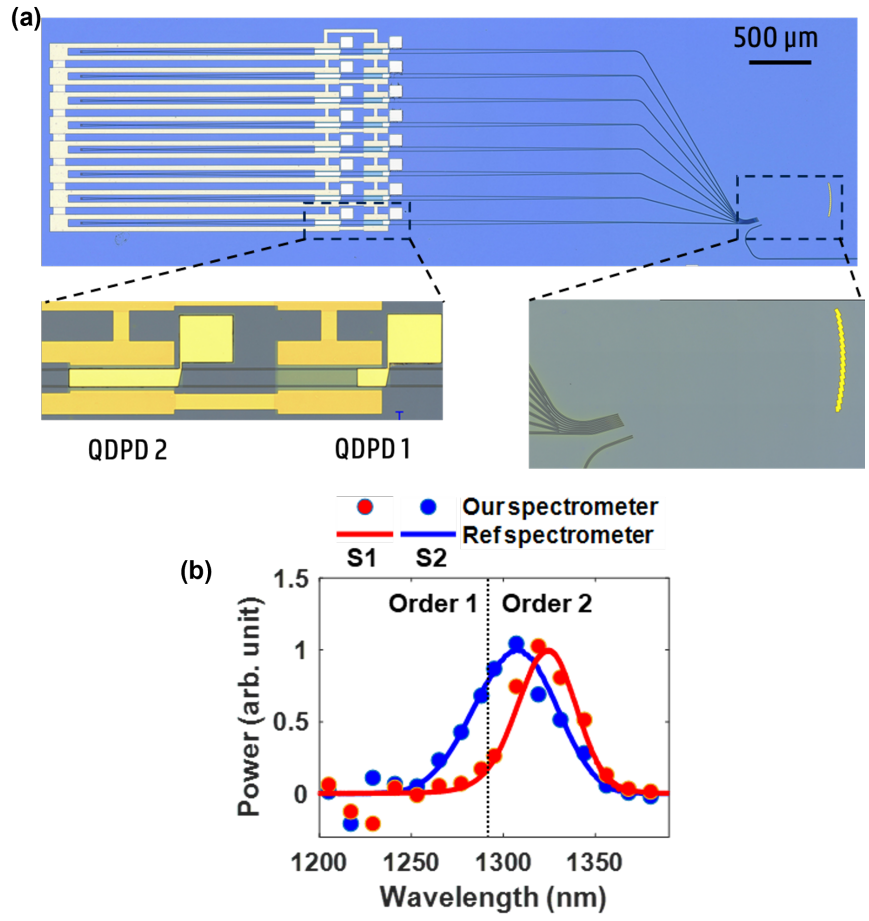

Figuur 3: Breedband spectrometer gebaseerd op cascaderende WG-QDPD's. (a) Bovenaanzicht van de gefabriceerde spectrometer. (b) Spectrumreconstructie.

dispersieve PICs om de spectrale bandbreedte uit te breiden tot meerdere FSRs. In onze demonstratie integreren we twee verschillende soorten QDs, met hun respectieve absorptiepieken overlappend met twee aangrenzende diffractieordes van de PCG. De QDs worden geïntegreerd als golfgeleider-gekoppelde fotodiodes, en in cascade, op de uitgangen van de PCG, zoals weergegeven in Figuur 3 (a), waarbij elk een unieke spectrale respons vertoont. Door de respons van de QDPDs zorgvuldig te ontwerpen, demonstreren we een spectrale bandbreedte van ongeveer 180 nm met een achtkanaals PCG met een intrinsieke FSR van slechts 90 nm, en doorbreken we de FSR-limiet van de spectrometer, zoals weergegeven in Figuur 3 (b). Door gebruik te maken van de veelzijdigheid van QDs op het gebied van afstembare eigenschappen en eenvoudige verwerking, benadrukt dit werk het potentieel van

deze materialen voor geïntegreerde fotonica en creëert het een pad naar on-chip breedband spectrometers.

Fourier-transform spectrometer met QDPD-array nano-samplers

In het vierde deel gebruiken we een andere unieke eigenschap van QDPDs om een Stationary-Wave Integrated Fourier Transform Spectrometer (SWIFTS) te demonstreren. Deze spectrometer bemonstert de stationaire golfpatronen die worden gegenereerd door de interferentie van invallend licht in een golfgeleider. Het bemonsteren van de stationaire golf vormt echter een uitdaging, omdat dit een detectorarray met subgolflengte-elementen vereist, wat moeilijk is met bestaande halfgeleiderdetectoren.

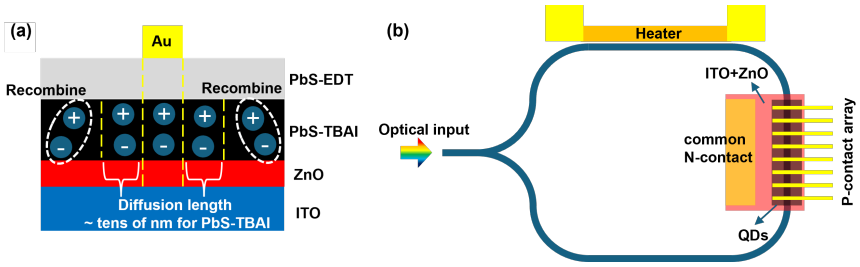

Figuur 4: QDPD's als nano-samplers voor SWIFT. (a) Basisprincipes van QDPD's als nano-probes. (b) Architectuur van het voorgestelde SWIFTS-systeem.

Hier stellen we voor om een rij van QDPDs te gebruiken als nano-samplers voor een SWIFTS spectrometer. We maken daarbij gebruik van de korte diffusielengte van ladingsdragers in de QD-film, zoals weergegeven in Figuur 4 (a). We ontwerpen het spectrometersysteem op basis van een 350 nm SiN-golfgeleider, met een rij van 100 QDPDs als nano-schaal probes, zoals weergegeven in Figuur 4 (b). Deze QDPDs hebben een compacte breedte van 100 nm om lokaal stationaire golfpatronen in de golfgeleider te bemonsteren en een pitch van 1 μm om de elektrische fan-out te vergemakkelijken. Een thermische faseverschuiver met drievoudige golfgeleiders eronder blijkt meer dan voldoende faseverandering te leveren om het interferogram te verplaatsen over 1 μm. Ons eerste onderzoek onthult dat de effectieve lengte van de nano QDPD in goede benadering overeenkomt met de grootte van het bovenste p-contact, wat de haalbaarheid van het gebruik van QDPDs als nano-probes bevestigt. Hoewel de experimentele demonstratie van het SWIFTS-systeem nog in uitvoering is, hebben alle individuele componenten veelbelovende prestaties getoond. Tot dusver zijn er geen significante hindernissen die een volledige demonstratie zouden belemmeren.

Geïntegreerde elektrisch aangedreven QD-lichtbronnen

Naast geïntegreerde fotodetectoren bieden QDs ook een veelbelovende oplossing voor de realisatie van geïntegreerde lichtbronnen. Eerder werden al op CdSe QDs gebaseerde lasers, geïntegreerd met SiN golfgeleiders gedemonstreerd. Tot dusver werd daarbij echter altijd een optische pomp gebruikt. De realisatie van elektrisch aangedreven QD-gebaseerde lasers blijft een uitdaging.

In het laatste deel van de thesis onderzoeken we daarom de integratie van een elektrisch aangedreven QD-gebaseerde lichtbron op SiN-golfgeleiders. We tonen aan dat het minimaliseren van optisch verlies, door een dikke hole-transportlaag (HTL) in te voegen om het optisch verliesgevende p-contact te scheiden van het optische veld, leidt tot een probleem met de injectie van gaten, door de slechte geleidbaarheid van de HTL. Om dit op te lossen gebruiken we een 200 nm dikke $(\text{HAT-CN/NPB})_n$ HTL-laag, bekend om zijn superieure gaten-injectie, als een transparante optische buffer om de absorptie van het p-contact te verminderen. Gecombineerd met gepulst elektrisch pompen om schade door oververhitting te beperken, bereiken we een stroomdichtheid van 61,2 A/cm^2 bij een spanning van 100 V en observeren we emissie van een hogere energietoestand. Dit wijst op het ledigen van de grondtoestand. We proberen de gaten-injectie verder te verbeteren door de zuivere organische HTL te doperen met dopanten zoals MoO_3 en F6-TCNNQ, maar de verminderde weerstand gaat gepaard met significant verhoogde parasitaire optische absorptie. We zijn van mening dat een goed geleidende gaten-transportlaag met lage verliezen essentieel is om golfgeleider-gekoppelde laserdiodes te realiseren.

Summary

The Chemistry Nobel Prize of 2023 was awarded to Alexei Ekimov, Luis Brus, and Moungi Bawendi for their significant contributions to the discovery and synthesis of colloidal quantum dots (QDs). These nanocrystals have emerged as a new class of semiconductors, exhibiting numerous advantages, such as bright and narrowband light emission, high absorption coefficient, spectral tunability from visible to infrared wavelengths, low-cost chemical synthesis, scalable solution-based processing, and compatibility with different substrates. QDs have found extensive applications across a diverse array of optoelectronic domains, encompassing displays, lasers, single photon sources, solar cells, and imaging technologies.

QDs can be equally attractive for integration with photonic integrated circuits (PICs). Integrated photonics, first proposed by Stewart E. Miller in 1969, offers the capability to miniaturize complex bulk optical systems into cost-effective and robust chips. Silicon photonics, leveraging established fabrication infrastructures for Si-based electronic integrated circuits, stands out as a particularly promising platform. However, the absence of a suitable light source due to silicon's indirect bandgap nature has hindered its full adoption. Photodetection beyond telecom wavelengths is also not possible due to the bandgap limit of monolithic Ge-Si detectors. SiN on SiO_2 offers another robust substrate option in silicon photonics, supporting visible light propagation and exhibiting superior performance in terms of low propagation loss and high power handling capability. Nonetheless, it remains a passive platform, lacking both light sources and photodetectors. Heterogeneous integration of exotic materials is required to address these limitations. QDs are a promising candidate due to their low cost, broadband spectral tunability, ease of processing, and compatibility with a wide range of substrates. These features make QDs a compelling option compared to other integration approaches. However, the heterogeneous integration of QDs onto PICs remains in its early stages, particularly concerning optoelectronic applications.

In this thesis, we investigate the integration of QDs into PICs as photodetectors and electrically driven light sources and explore their potential applications. Starting with the integration of lead sulfide (PbS) QDs on SiN waveguides, we develop a scalable process flow to integrate waveguide-coupled QD-based photodiodes (WG-QDPDs) as a low-cost photodetection solution. Expanding upon this, we optimize the WG-QDPD process and use larger PbS QDs to extend photodetection beyond

the absorption limit of germanium in silicon photonics, achieving absorption up to 2.1 μm. Subsequently, we explore two new spectrometer architectures based on the unique features of our developed WG-QDPDs. By combining the tunable absorption features of QDs with dispersive PICs, we demonstrate a spectrometer with a spectral bandwidth extending beyond a single free spectral range (FSR). Additionally, we utilize an array of QDPDs with sub-wavelength lengths as nano-samplers for a stationary-wave integrated Fourier transform spectrometer (SWIFTS). We also investigate integrated QD-based light sources, pursuing electrically driven gain by integrating CdSe/CdS core/shell QDs on SiN waveguides. While emission from a high energy state is observed, further optimization on the material side is needed to achieve optical gain.

Development of 1.3 μm WG-QDPD on SiN

The first work we demonstrate in this thesis is the integration of a QDPD on SiN waveguides, exhibiting a photoresponse up to 1.3 μm. This QDPD configuration consists of two films of PbS QDs, with surfaces functionalized by lead iodide (PbI_2) and ethane-dithiol (EDT), respectively, stacked on a zinc oxide (ZnO) ETL formed by atomic layer deposition (ALD), as shown in Figure 1 (a). After analyzing the power-dependent saturation of the photocurrent in a bottom-illuminated, planar QDPD, we argue that the high optical intensity resulting from the strong optical confinement in waveguides could induce saturation of a WG-QDPD already at low optical powers. To address this issue, we propose a design strategy to reduce the overlap with the evanescent field by using the cladding thickness and the waveguide width as adjustable parameters to raise the saturation power.

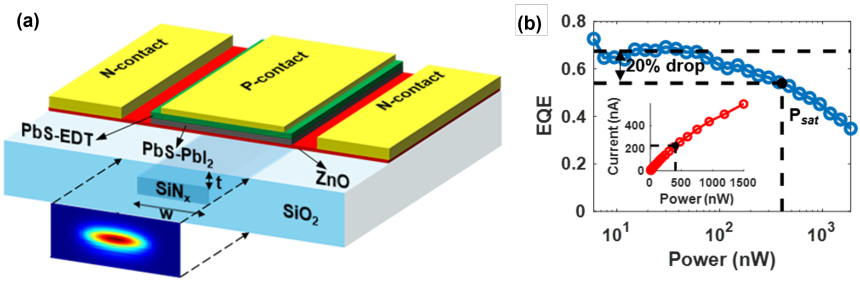

Figure 1: Integration of 1.3 μm QDPD on SiN. (a) Device structure of WG-QDPD. (b) EQE vs. optical power at -1 V bias voltage. Inset: photo-current vs. optical power with bias voltage of -1 V. The intersection of the black dashed lines indicates the onset of saturation.

Subsequently, we develop a first-generation process flow enabling integration of the relatively straightforward 3-layer QDPD stack onto SiN strip waveguides, using standard scalable processing techniques. Employing a waveguide width of 30 μm and a cladding thickness of 350 nm to maintain QDPD operation within the

linear regime, we achieve a responsivity of 0.69 A/W, corresponding to an External Quantum Efficiency (EQE) of approximately 67.5% at 1275 nm, with a linear response observed for illumination powers up to 400 nW at -1 V bias, as shown in Figure 1 (b). To further demonstrate the scalability of the proposed integration approach, we design and test a compact 8-channel spectrometer integrated with an array of WG-QDPDs. This spectrometer shows a clear wavelength-dependent response with channel crosstalk of 15 dB. This first demonstration of integrating multiple QDPDs to create an on-chip spectroscopic system provides a promising route for mass integration of QDPDs in complex PICs.

Development of 2.1 μm waveguide-coupled QDPD on silicon

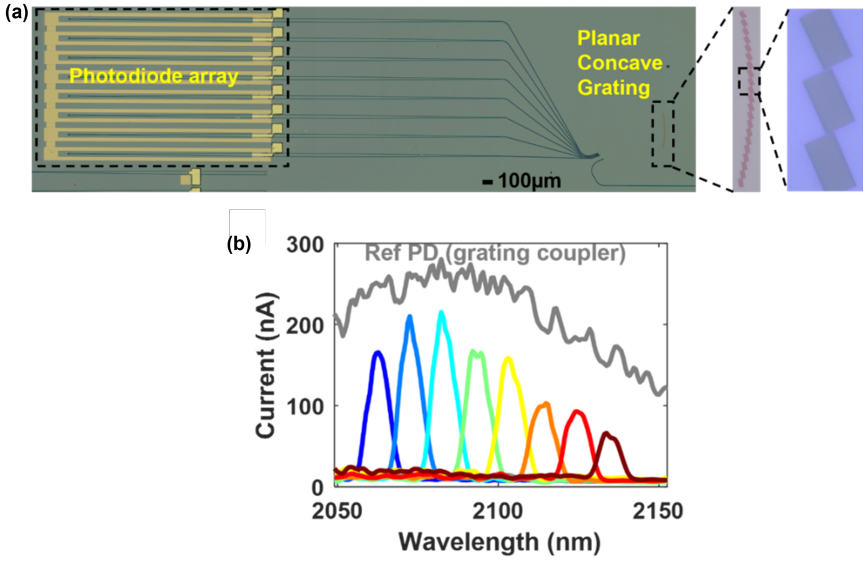

Figure 2: Compact spectrometer based on a WG-QDPD array and a planar concave grating. (a) Top view of the spectrometer. Light is injected from the grating coupler on the right side. (b) Response of WG-QDPDs from eight channels and a reference waveguide (gray line).

The second work we demonstrate is the integration of PbS QDPDs onto silicon waveguides, extending the photodetection capabilities beyond the traditional telecommunication range in silicon photonics. We optimize the integration process by replacing the ALD ZnO with more electrically stable layers of indium tin oxide (ITO) and sol-gel ZnO. Sputtered ITO serves as the transparent bottom electrode and sol-gel ZnO serves as the electron transport and hole block layer. This optimization greatly improves the yield and stability of the integration. We also optimize the QDPD stack design to reduce the leakage current when extending from 1.3

μm to 2.1 μm. We sandwich the 2.1 μm QDs with 1.3 μm ones for less interface states-related leakage current.

Using the optimized QDPD design and the second-generation process flow based on ITO / sol-gel ZnO ETL, we demonstrate WG-QDPDs at room temperature, exhibiting a responsivity of 1.3 A/W at 2.1 μm, a low dark current of 106 nA, and a bandwidth of 1.1 MHz. Moreover, we show that our WG-QDPD exhibits a low noise equivalent power (NEP) of 0.15 pW/$\sqrt{\text{Hz}}$, due to its high responsivity and low dark current, which is attractive for low-noise, weak signal detection. We demonstrate the reliability of the integration approach by realizing a compact on-chip spectrometer that features an array of 8 WG-QDPDs and operates in the spectral window between 2.063 and 2.135 μm, as shown in Figure 2. We believe that QDPD technology holds significant promise for cost-effective photodetection in the near and mid-infrared ranges in silicon photonics, especially for diverse sensing applications.

Spectrometer based on multi-color cascaded WG-QDPDs

In the third part, we explore the potential applications of our developed QDPDs. We find the tunability of the QD absorption spectrum holds promise when integrated into more complex optical systems. Integrated dispersive components such as arrayed waveguide gratings (AWG) or planar concave gratings (PCG) are commonly used in silicon photonics for realizing on-chip spectrometers. However, a fundamental trade-off exists between the operational spectral range and spectral resolution. Achieving better spectral resolution within a similar footprint requires larger optical dispersion, typically implying a larger diffraction order and, consequently, a smaller FSR and a more narrow spectral bandwidth. This traditional trade-off persists since a single photodetector is used in each channel, making optical signals from adjacent diffraction orders indistinguishable. Integrating different types of photodetectors on each channel in cascade, each with a distinct response to different diffraction orders, would decouple signals from more than one FSR, thereby eliminating the aforementioned trade-off.

Here, we propose and demonstrate the integration of the tunable features of QDs with dispersive PICs, pushing the spectral bandwidth beyond a single FSR. In our demonstration, we integrate two distinct types of QDs, with their respective excitonic absorption peaks overlapping with two adjacent diffraction orders of the PCG. The QDs are integrated as waveguide-coupled photodiodes, and in cascade, on the output channels of the PCG, as shown in Figure 3 (a), with each exhibiting a unique spectral response. By carefully designing the response of the QDPDs, we demonstrate a spectral bandwidth of approximately 180 nm using an eight-channel PCG with an intrinsic FSR of 90 nm, breaking the FSR limit of the spectrometer, as shown in Figure 3 (b). By leveraging the versatility of QDs at the level of tunable properties and ease of processing, this work highlights the potential of these

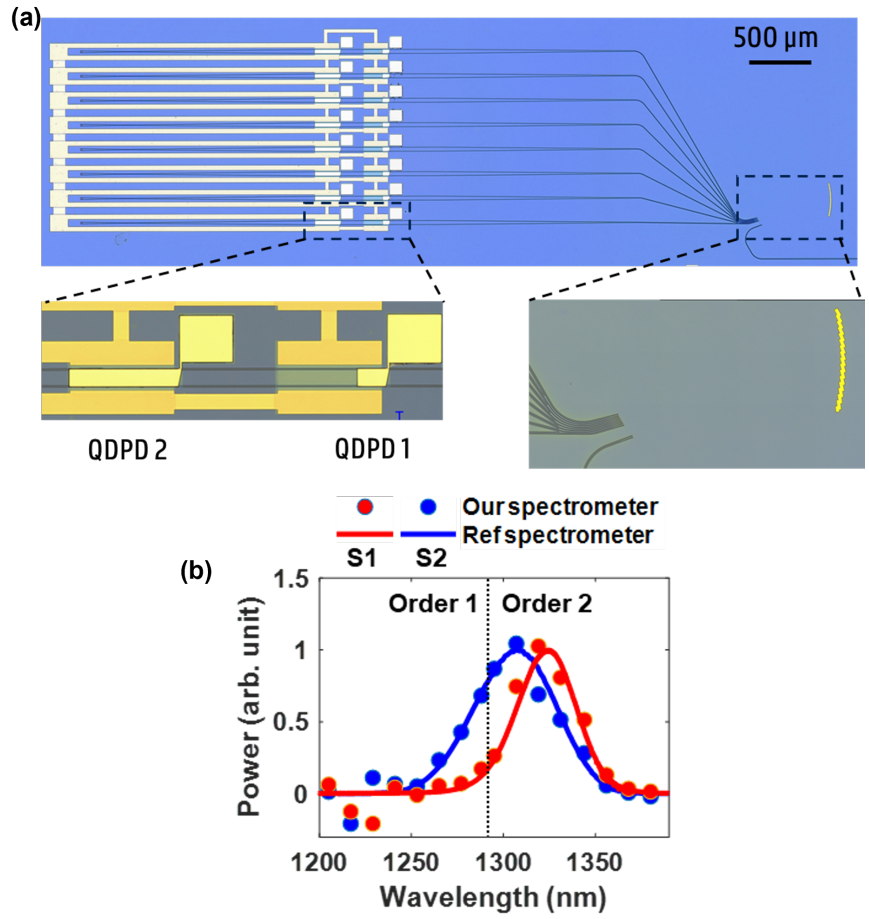

Figure 3: Broadband spectrometer based on cascaded WG-QDPDs. (a) Top view of the fabricated spectrometer. (b) Spectrum reconstruction.

materials for integrated photonics, and creates a path toward on-chip broadband spectrometers.

Fourier transform spectrometer using QDPD array nano-samplers

In the fourth part, we explore another application by utilizing the unique features of QDPDs. The stationary-wave integrated Fourier transform spectrometer (SWIFT), operating by directly sampling the stationary wave patterns generated by the interference of input light in a waveguide, is a promising candidate for miniaturized spectroscopy with high resolution, broad bandwidth, and ultra-compact footprint.

However, sampling the stationary wave presents a challenge, which requires a nano-detector array with subwavelength-sized elements, a task difficult with existing semiconductor detectors.

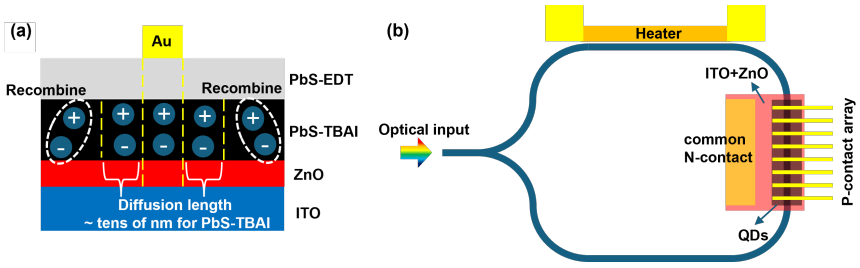

Figure 4: QDPDs as nano-samplers for SWIFT. (a) Fundamentals of QDPDs as nano-probes. (b) Architecture of the proposed SWIFTS system.

Here, we propose the utilization of a QDPD array as nano-samplers for SWIFTS by employing the short diffusion length feature of the QD film, as shown in Figure 4 (a). We design the spectrometer system based on a 350 nm SiN waveguide, incorporating a 100-channel QDPD array as the nano-scale samplers, as shown in Figure 4 (b). These QDPDs feature a compact length of 100 nm to locally probe stationary wave patterns in the waveguide and a pitch of 1 μm to facilitate the electrical fan-out. A thermal phase shifter with triple-path waveguides underneath, proves to supply sufficient phase change to move the interferogram for stitching. Our initial investigation reveals that the effective length of the nano QDPD closely aligns with the top p-contact size, thereby validating the feasibility of employing QDPDs as nano-probers. Although the experimental demonstration of the SWIFTS system is still pending, all individual components have exhibited promising performance. Thus far, no significant hurdles are found that impede our demonstration efforts.

Integrated electrically driven QD light sources

In addition to integrated photodetectors, QDs also offer a promising solution for integrated light sources. QDs can be deposited onto the substrate using simple and cost-effective solution-based techniques, facilitating seamless integration with existing silicon photonics fabrication processes. CdSe QD-based lasers have been successfully demonstrated on SiN platforms as visible light sources under optical pumping. However, the realization of electrically driven QD-based lasers remains challenging.

As the final part of the thesis, we investigate the integration of an electrically driven QD-based light source on SiN waveguides. We find that minimizing optical loss, achieved by introducing a thick hole transport layer (HTL) to separate the optically lossy p-contact metal from the guided optical mode, leads to a hole-injection problem due to the poor conductivity of the HTL. To solve this, we utilize a 200 nm

thick (HAT-CN/NPB)$_n$ HTL layer, known for its superior hole injection capabilities, as a transparent optical buffer to mitigate p-contact metal absorption. Combined with pulsed electrical pumping to mitigate heating effects and damage, we attain a current density of 61.2 A/cm^2 at a driving voltage of 100 V and observe emission from a higher energy state, indicating the bleaching of the ground state. We attempt to further enhance hole injection by doping the pristine organic HTL with other dopants (MoO_3 or F6-TCNNQ), but the reduced resistivity is accompanied by significantly increased parasitic optical absorption. We believe a conductive and low-loss hole transport layer is essential to achieve waveguide-coupled laser diodes.

1

Introduction

1.1 Research background 1
1.2 Colloidal quantum dots 3
1.2.1 Properties and Characteristics 3
1.2.2 Applications in photodetection and imaging 9
1.2.3 Applications in light sources 13
1.3 Integrated photonics 18
1.3.1 Silicon photonics 19
1.3.2 QDs in integrated photonics 22
1.4 Thesis objectives 22
1.5 Thesis Outline 23
1.6 Publications 25
1.6.1 Publications in international journals 25
1.6.2 Publications in international conferences 25

1.1 Research background

The Chemistry Nobel Prize of 2023 was awarded to Alexei Ekimov, Luis Brus, and Moungi Bawendi for their significant contributions to the discovery and synthesis

of Colloidal Quantum Dots (QDs) [15]. QDs, as semiconductor nanocrystals synthesized in chemical colloidal solution, were first developed in aqueous solution in the 1980s [16–18]. QDs underwent rapid development from 1993 onwards when a chemical method, known as the hot-injection method, was developed for QDs growth, greatly improving the size control and monodispersity of colloidal particles [19]. Following this, QDs emerged as a new class of semiconductors and have been applied to a wide range of optoelectronic applications, including Light Emitting Diode (LED)s [20], lasers [21], single photon sources [22], solar cells [23], and photodetectors [24]. This wide adaption was enabled by their numerous advantages such as bright and narrowband light emission, high absorption coefficient, spectral tunability from visible to infrared wavelengths, low-cost chemical synthesis, scalable solution-based processing, and compatibility with different substrates.

Following the rapid material development and the improved understanding of QD-based devices, interest has now shifted towards the integration of QDs in established optoelectronic technology platforms. For example, QDs have been included as color converters in liquid crystal [25] and micro-LED displays [26], and combined with a driver backplane for electroluminescent displays [27] or a readout backplane for infrared imagers [28].

QDs can be equally attractive for integration with photonic integrated circuits (PICs). Integrated photonics, first proposed by Stewart E. Miller in 1969, offers the capability to miniaturize complex bulk optical systems into cost-effective and robust chips. Various platforms have emerged for integration, with silicon photonics being particularly appealing due to its high-throughput and cost-effective manufacturing, leveraging the well-established fabrication infrastructure of the electronics industry. In silicon photonics, Silicon on Insulator (SOI) serves as the standard substrate capable of supporting the propagation, modulation, and detection of light. However, the light source is a missing part due to the indirect bandgap nature of silicon. Photodetection beyond telecom wavelengths is also not possible due to the bandgap limit of monolithic Ge-Si detectors. SiN on SiO_2 offers another robust substrate option in silicon photonics, facilitating visible light propagation and showcasing superior performance in terms of low propagation loss and high power handling capability [29]. Nonetheless, it remains a passive platform, lacking both light sources and photodetectors. Heterogeneously integrated semiconductors are required to address these limitations. Here, QDs emerge as a promising candidate due to their low cost, broadband spectral tunability, ease of processing, and compatibility with a wide range of substrates, making them a compelling option compared to other integration approaches.

1.2 Colloidal quantum dots

QDs are small semiconductor nanocrystals with sizes typically between 1 nm and 20 nm. Their great potential in optoelectronics as a new class of semiconductor is closely linked to their unique properties and characteristics.

1.2.1 Properties and Characteristics

Semiconductors in solution phase

QDs are typically synthesized using a hot-injection-based wet chemical method [19], where molecular precursors are rapidly injected into a solvent at elevated temperatures (100 °C to 350 °C). This kind of synthesis yields QDs in a low-cost way, for example, 10 to 60 $ per g for PbS QDs [30]. Covering an 8-inch wafer with a 500 nm thick semiconductor film costs less than 5 $ in material [30]. The low-cost material synthesis makes it competitive compared to commonly used III-V active materials grown with Molecular Beam Epitaxy (MBE) or Metal-Organic Chemical Vapor Deposition (MOCVD). To have a feeling, it costs more than 5000 $ to make an 8-inch gallium arsenide wafer [31].

Synthesized QDs are surrounded by long organic ligands, such as oleic acid and oleylamine on the surface, which stabilize them in the solvent and prevent aggregation, as depicted in Figure 1.1. This ink-like feature of QDs makes them suitable for integration with various substrates using low-cost and scalable solution-based deposition techniques [32], including spin-coating, spray coating [33, 34], inkjet printing [35–37], and blade coating [38, 39].

Quantized electronic states

A QD can be conceptualized as a spherical quantum box that confines electrons and holes. When the QD is sufficiently small, with a size comparable to the Bohr radius of the electron-hole pair (also known as an exciton), carriers sense the boundary, leading to the emergence of quantum confinement. The quasi-continuous conduction band and valence band in bulk semiconductors are quantized into atomic-like density of states, as depicted in Figure 1.2. The quantum confinement effect results in an increase of the effective bandgap of the QD, which is related to the radius as:

$$E_g = E_{g,0} + \frac{\hbar^2 \pi^2}{2 m_{eh} R^2} - \frac{1.765 e^2}{\epsilon R} \tag{1.1}$$

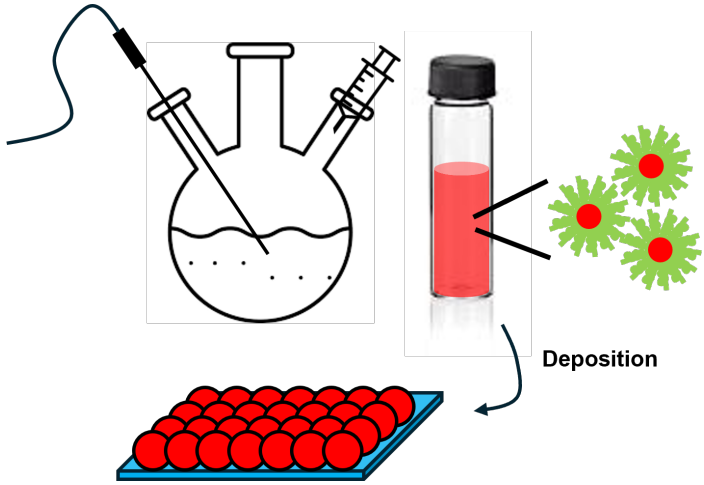

Figure 1.1: QDs synthesis with the hot-injection method

where E_g is the effective bandgap, $E_{g,0}$ is the bandgap of the parent bulk semiconductor, $\hbar$ is the reduced Planck constant, $m_{eh} = m_e m_h/(m_e + m_h)$ is the reduced electron - hole mass (e-h), e is the elementary charge, ϵ is the dielectric constant of the semiconductor material, R is the radius of the semiconductor nanocrystal. The third item on the right side is from the Coulomb interaction between the electron and hole.

The strong relationship between the effective bandgap of QDs and their size facilitates easy tuning of the emission and absorption spectrum. For instance, by adjusting the size of CdSe QDs, it is possible to cover the entire visible wavelength range, as depicted in Figure 1.3 (a). The absorption spectrum exhibits similar tunability. For example, synthesized PbS QDs have demonstrated absorption spanning almost the entire Short-Wave Infrared (SWIR) range (Figure 1.3 (b) [2]), while HgTe QDs absorb at even longer wavelengths (Figure 1.3 (c) [3]).

The strong quantization of electronic states in QDs also results in narrow linewidth emission, typically ranging from 20 meV to 60 meV of Full Width Half Maximum (FWHM) [40]. The narrow spectral emission of a QD film is further enhanced by the well-developed synthesis process, ensuring tight size distributions and pushing the ensemble emission linewidth close to that of a single QD. Additionally, advanced shell engineering techniques contribute to the high Photoluminescence Quantum Yield (PLQY), approaching 100%. These characteristics make QDs highly tunable, bright, and narrowband emitters, positioning them as the leading-edge emitters in the display market.

Furthermore, the discrete electronic states inherent in QDs also enhance their po-

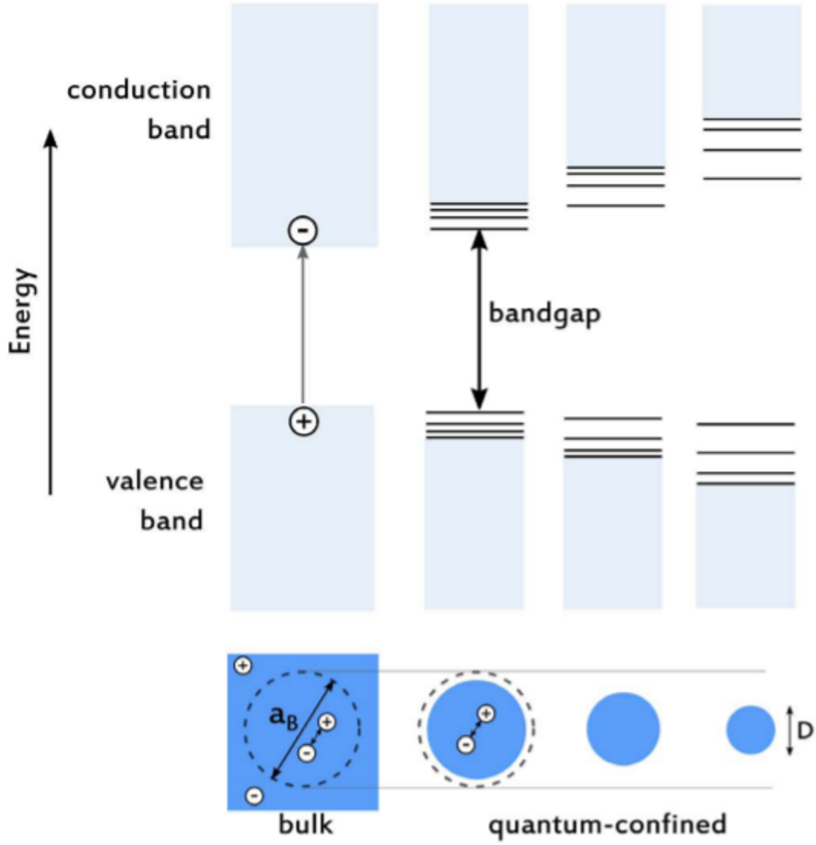

.

Figure 1.2: Quantum confinement effect. The conduction band and valence band are quantized into discrete energy levels. Reproduced from [1]

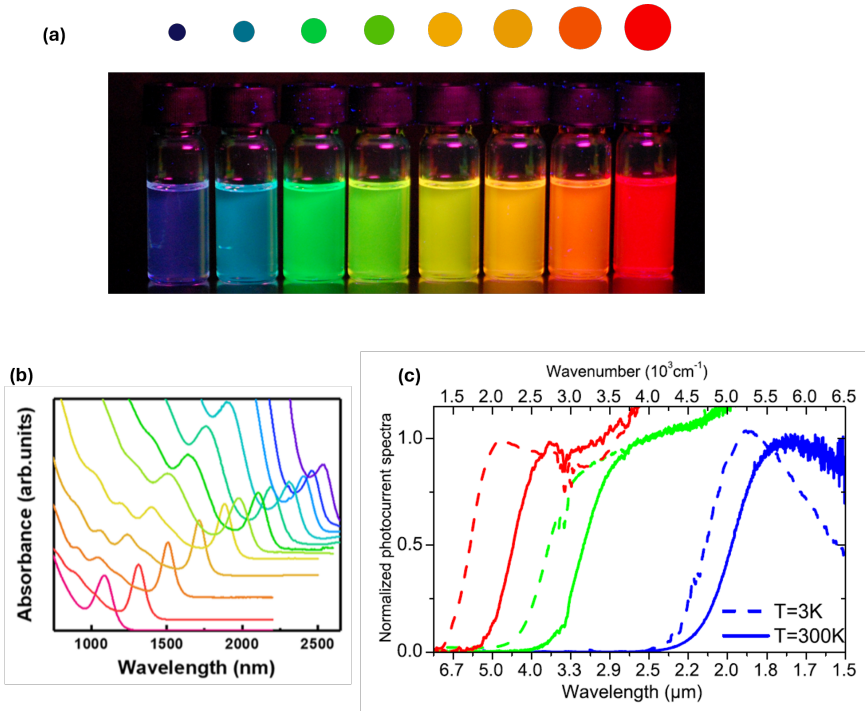

Figure 1.3: Spectral tunability of QDs with different sizes. (a) UV-excited photoluminescence of CdSe QDs. (b) Absorption spectrum of PbS QDs. Reproduced from [2] (c) Absorption spectrum of HgTe QDs. Reproduced from [3]

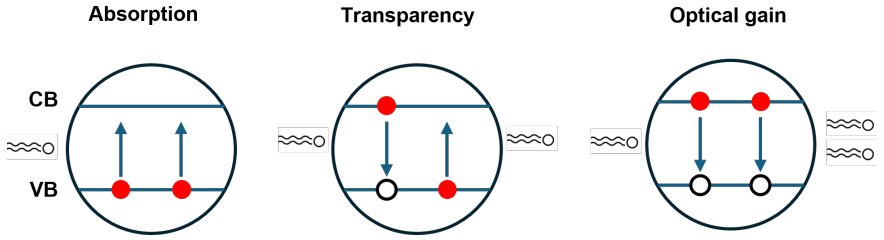

Figure 1.4: The simplified optical-gain model in QDs

tential in lasing applications. As depicted in Figure 1.4, the strong quantization characteristic transforms QDs into a two-level system near the band edge, comprising spin-degenerate valence band and conduction band levels. When an electron transits from the valence band to the conduction band, generating an electron-hole pair (single-exciton state), QDs achieve a transparent state where photons can traverse without net absorption. In the case where both valence band electrons are excited, forming a biexciton state, an incident photon induces stimulated emission from a conduction band electron, resulting in optical gain. In the context of an ensemble QD film, achieving an average exciton number exceeding 1 initiates the gain regime, facilitating low-threshold lasing. Moreover, the strongly quantized electronic states inhibit the thermal depopulation of the emitting band-edge states, thereby reducing the sensitivity of laser performance to temperature.

Carrier transport

The ability to transport carriers within a QD film is crucial for optoelectronic applications. Ideally, if the QDs are assembled with high order, forming a so-called superlattice, carriers can exhibit band-like transport behavior similar to bulk crystals, as per Bloch's theorem. However, achieving such highly ordered assembled QDs is challenging. Carrier transport in disordered QD films is predominantly facilitated by mechanisms such as hopping assisted by thermal energy or phonons, as well as direct tunneling. These mechanisms depend strongly on inter-dot distance [41, 42], as illustrated in Figure 1.5.

As-synthesized QDs are typically capped with long-chain organic molecules, such as oleic acid and oleyamine, to ensure good colloidal stability. However, these long ligands result in a large inter-dot distance exceeding 1.5 nm [43], which poses challenges for carrier transport. Consequently, replacing the original long-chain ligands with shorter ones is essential for optoelectronic applications using QDs.

Two common methods have been developed for ligand exchange: solid-phase ligand

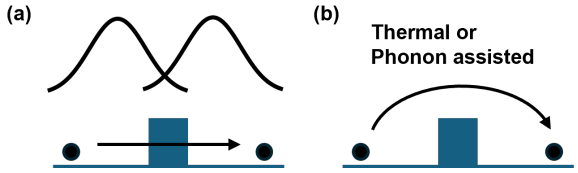

Figure 1.5: Carrier transport mechanism in a QD film. (a) Direct tunneling through the energy barrier. The rate is related to the overlap of the carrier wave functions in adjacent QDs. (b) Hopping over energy barrier with the assistance of thermal energy or phonon.

exchange and solution-phase ligand exchange. In solid-phase ligand exchange, QD ink containing long-chain ligands is intially deposited on the substrate. Subsequently, the film is immersed in a solution containing short ligand chemicals to replace the original long ligands. This process is repeated layer by layer to achieve the desired thickness, as depicted in Figure 1.6 (a). To ensure complete ligand exchange throughout the QD film and to prevent cracking and peeling caused by film shrinkage during the ligand exchange process, the thickness of each exchange cycle is typically controlled to be around 30 nm. While this method is straightforward to operate and easily extendable to different ligand species, it requires tedious layer-by-layer processes for thick layers and poses a risk of film peeling due to accumulated stress during deposition.

Solution-phase ligand exchange involves intially exchanging the long-chain ligands in solution to obtain a new ink with shorter ligands on the surface of QDs. This ink is then used for deposition on the substrate, as illustrated in Figure 1.6 (b). This method allows for the fabrication of thick QD films with short ligands in high quality. Currently, the best-performing solar cells and photodetectors using PbS QDs predominantly rely on solution-phase ligand exchange. However, an ink with short ligands typically exhibits less colloidal stability and needs to be freshly prepared for each fabrication cycle.

Moreover, QDs possess a notably large surface-to-volume ratio, rendering them highly sensitive to surface chemistry modifications. Consequently, the ligands can impact their Fermi level (doping) and energy levels by introducing shallow trap states and surface dipoles [5, 44].

These unique features of QDs hold great promise for optoelectronic applications, particularly as light sources and for photodetectors. Currently, they are being commercialized for high-quality displays and low-cost infrared cameras.

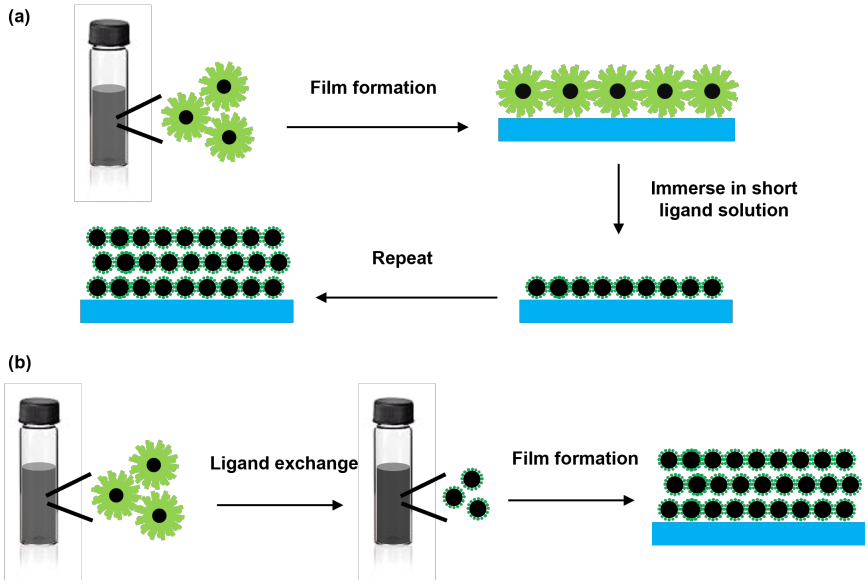

Figure 1.6: Ligand exchange process. (a) Solid-phase ligand exchange. (b) Solution-phase ligand exchange.

1.2.2 Applications in photodetection and imaging

QD-based photodetectros

QDs as photodetectors were first studied in the 1990s when cadmium chalcogenide (CdS, CdSe. CdTe) QDs were mixed with a conductive polymer matrix to separate photo-generated carriers [45]. This research experienced rapid development in the 2000s with the assistance of ligand exchange techniques to significantly enhance carrier transport in QD solid films [46–48]. A photodetector with Internal Quantum Efficiency (IQE) of 70% was demonstrated with CdSe QDs. While CdX QDs for photodetection remains primarily of academic interest, insights from these studies were rapidly applied to PbS QDs for photodetection in the infrared range [49–51], offering significant industrial potential.

QD photodetectors based on PbS nanocrystals operating in the SWIR are among the most mature developments to date. Two primary types of photodetectors, namely photoconductors with planar structures and photodiodes with vertical structures, have been extensively studied, as shown in Figure 1.7.

In QD-based photoconductors, a pair of electrodes is fabricated on an insulator substrate with a narrow gap (usually several micrometers), and QDs are deposited

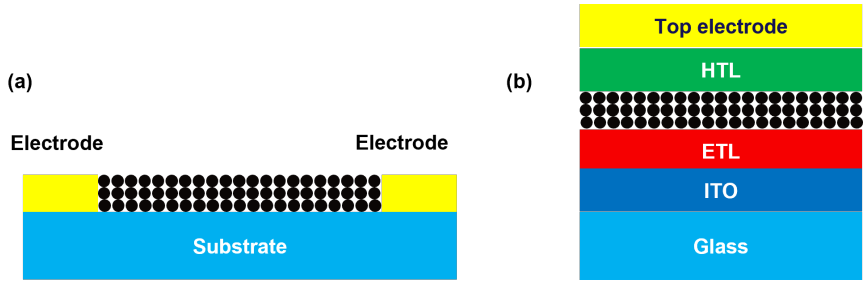

Figure 1.7: Structures of QD-based photodetectors. (a) Photoconductors with a planar structure. (b) Photodiodes using a vertical heterojunction structure.

between the electrodes as a low-conductivity semiconductor layer. Upon illumination, additional carriers are generated, increasing the conductivity of the QD film. Typically, these photoconductors exhibit gain, resulting from one type of photogenerated carrier (electron or hole) circulating in the circuits more than once until they recombine with the opposite carriers which are trapped in the gap states. This photoconductive gain can lead to a larger responsivity, which is advantageous for achieving a high detectivity (low detection limit). The Sargent group has demonstrated PbS QD-based photoconductors with a responsivity exceeding 1000 A/W and a high detectivity of 1.8×10^{13} Jones (cm $\text{Hz}^{0.5}\text{W}^{-1}$) at 1.3 μm by removing the ligands and introducing oxidation for improved carrier transport and surface traps [49]. Combining QDs with 2D materials such as graphene can further enhance the detectivity, with demonstrated responsivity reaching 10^7 A/W and detectivity of 7×10^{13} Jones [52]. Photocarriers generated in QDs are separated at the interface between the QDs and graphene (electrons are trapped in the QD film while holes are transferred to the graphene). The holes in the graphene can circulate more times under an external voltage bias due to the high carrier mobility of graphene (> 1000 $\text{cm}^2\text{V}^{-1}\text{s}^{-1}$) compared to the QD film (typically < 1 $\text{cm}^2\text{V}^{-1}\text{s}^{-1}$) [53]. Despite their high sensitivity, these photoconductors exhibit slow speeds due to the prolonged circulation of carriers. The demonstrated ultrasensitive photoconductors with a detectivity exceeding 10^{13} Jones [49, 52] exhibit a bandwidth of less than 20 Hz. Another prevalent issue for photodetectors is their nonlinear response to optical power due to the filling of trap states (reduced gain) at increased optical power levels.

QD-based photodiodes rely on establishing a built-in electrical field to separate photo-generated electrons and holes and reduce dark current. Over the last two decades, both Schottky and heterojunctions have been developed for QDs. Schottky Photodiodes (PDs) form a junction between the QD film and the metal electrode interface. Shallow work function metals can bend the energy band of QDs downwards, forming a Schottky junction, as shown in Figure 1.8 (a). This junction assists

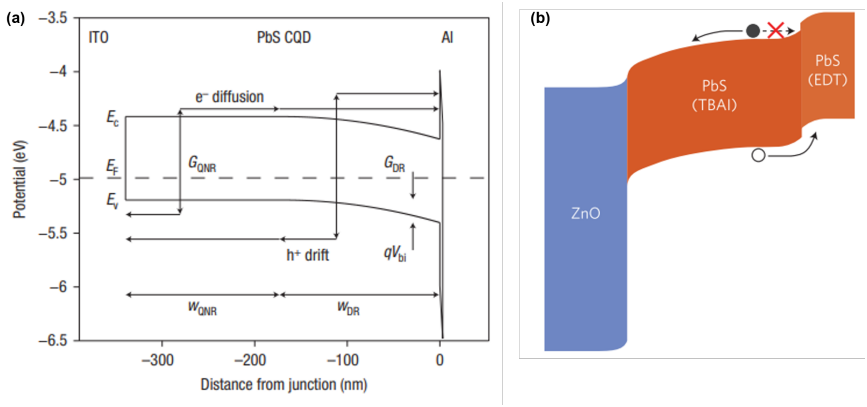

Figure 1.8: Band alignment of QD-based junctions. (a) Schottky junction formed between QDs and shallow-work-function metal [4]. (b) Heterojunction formed between ZnO and PbS QDs, and junction formed between QDs with different surface ligand treatments [5].

in extracting photo-generated carriers and reduces the dark current by blocking hole injection from the metal contact into the QDs [4, 54]. The Sargent group demonstrated a Schottky PD using a Schottky junction between PbS QDs and an aluminum contact, with ITO forming the opposite ohmic contact. This structure exhibited a detectivity of $> 10^{11}$ Jones and a bandwidth of > 1 MHz without bias [4]. However, Schottky junctions still exhibit relatively large dark currents under external bias due to majority carrier injection from the limited Schottky barrier height. Recent developments in Colloidal Quantum Dot based Photodiodes (QDPDs) have focused on using heterojunction junctions instead.

The state-of-the-art QDPDs feature a structure as shown in Figure 1.7 (b). Here, QDs are sandwiched between organic or inorganic semiconductors on both sides, forming two hetero-junctions at the interfaces with QDs, as shown in Figure 1.8 (b). Typically, n-doped ZnO or TiO_2 serves as as an Electron Transport Layer (ETL), bending the energy band of the QDs downward to facilitate the extraction of photo-generated electrons and blocking hole injection from the electrode. A p-doped semiconductor (such as NiO_2,QDs or an organic semiconductor) acts as an Hole Transport Layers (HTLs), bending the energy band of QDs upward to assist in extracting photo-generated holes and blocking electron injection from the electrode. QDs sandwiched in between form the absorption layer.

This device stack has been widely optimized for high-performance QDPDs. ZnO, formed by sputtering [55] or Atomic layer deposition (ALD) [56], are promising candidates for the ETL, effectively reducing interface defects and leading to suppressed dark current density, improved responsivity, and faster response. Demonstrations have showcased a responsivity of 2.15×10^{12} Jones and a 3 dB

bandwidth of 95 KHz [55].

For the absorption layer, Sargent's group recently developed a high-concentration bromine treatment and an additional passivation step for enhanced passivation of the (100) surface of the 1550 nm PbS QDs. This advancement resulted in a QDPD with a high External Quantum Efficiency (EQE) of over 80%, a detectivity of 8×10^{11} Jones, and a short response time of 10 ns (equivalent to a 3 dB bandwidth of around 35 MHz) [57].

For the HTL, PbS QD treated with Ethanedithiol (EDT) have shown promise as the p-type layer with favorable band alignment and are commonly used in current QD-PDs [5, 56, 57]. Sol-gel NiO has been reported as a promising alternative, achieving a detectivity of 1.1×10^{12} Jones at 1130 nm and a bandwidth exceeding 35 kHz [58]. Sputtered NiO combined with sputtered ZnO and an evaporated C_{60} protection layer, has shown improved stability, a detectivity of 2.1×10^{12} Jones and 3 dB bandwidth of 140 kHz [59]. Additionally, organic semiconductors, such as lithium-doped 2,2′,7,7′-tetrakis-(N,N-di-4-methoxyphenylamino)-9,9′-spirobifluorene (Spiro) also demonstrated high detectivity of 1.4×10^{12} Jones and a bandwidth of 41 kHz at 1050 nm [60].

In addition to PbS, other materials are also under development for photodetection. HgTe QDs have demonstrated photodetection capability up to 5 μm [61] and 12 μm [62], covering the Mid-Wave Infrared (MWIR) and even Long-wave Infrared (LWIR) range. QDs using less toxic materials, such as InAs [63–65] and Ag_2Te [66, 67], have also been demonstrated with good SWIR photodetection capability. The advancements in QD-based photodetectors form the foundation for low-cost infrared imagers. Further information on the progress of QD-based photodetection can be found in recent review papers [24, 68–70].

QD-based imagers

In the visible and near-infrared range, silicon PDs can be monolithically integrated with Readout Integrated Circuits (ROICs). These integrated circuits store the signal charge at each pixel and then route the signal onto output taps for readout [71]. This solution currently dominates the market for visible imaging due to its ultralow cost and excellent performance. However, for imaging with wavelengths beyond 1 μm, other semiconductors such as indium gallium arsenide (InGaAs) for SWIR, indium antimonide (InSb) for MWIR, and mercury cadmium telluride (HgCdTe) for both MWIR and LWIR are required to be integrated with silicon ROICs. Nevertheless, the integration of these materials is a complex and expensive process. Crystalline semiconductors typically need to be grown on specific single-crystalline substrates using high-temperature vacuum methods such as metalorganic chemical vapor

deposition (MOCVD) and molecular beam epitaxy (MBE). Subsequently, these infrared photodetectors are electrically connected to Si ROICs using indium bumps — a technique called flip-chip hybrid integration. Therefore, infrared imagers are much more expensive (a typical infrared camera costs 30 k€ – 100 k€ [69]) and their use remains limited to defense and scientific applications.

QDs, due to their tunable and strong absorption in the infrared, low cost and solution-processable nature, are emerging as promising candidates to address the price problem and bring infrared imagers to a mass-market level. In the SWIR range, which finds applications in see-through vision, identification, sorting, surveillance, and process quality control [28], the first QD-based infrared image sensor was demonstrated by Siemens, based on a polymer-PbS blend thin film PD [72]. Since then, significant advancements have been made. PbS QDs are the material of choice for most research groups. [59, 73–77]. Apart from their low cost, QD-based imagers also show dense integration potential. Traditional flip-chip bonding relies on solder bumps for electrical connections, which limits pixel resolution to tens of micrometers. With advanced copper-to-copper (Cu-Cu) bonding techniques, the pixel pitch can be reduced to single-digit micrometers. For QD-based imagers, the flexible material deposition on ROICs and compatibility with photolithography-based pixelation patterning make them competitive for achieving high resolution. Currently, pixel pitches of less than 2 μm have been demonstrated by Imec [78] and InVisage [75, 79], outperforming the best InGaAs-based imagers (with a 5 μm pitch) using advanced Cu-Cu bonding techniques [80]. PbS QD-based cameras with a sensing range up to 2000 nm are now commercially available [81].

HgTe QDs are appealing for low-cost imaging in the MWIR and LWIR ranges, suitable for thermal imaging applications. HgTe QD based imagers operating in the wavelength range up to 5 μm have been demonstrated [82, 83]. Apart from PbS and HgTe QD-based imagers, a toxic-heavy-metal-free silver telluride (Ag_2Te) QD based imager was demonstrated at SWIR recently, paving the way to the consumer electronics market [67].

1.2.3 Applications in light sources

Display

The features of tunable emission wavelength, narrow emission linewidth, and near-unity PLQY make QDs highly competitive semiconductors for next-generation high-quality displays. There are two primary strategies: utilizing QDs as color conversion materials or employing QDs directly as electroluminescence emitters akin to Organic Light Emitting Diode (OLED) structures, as illustrated in Figure

1.9.

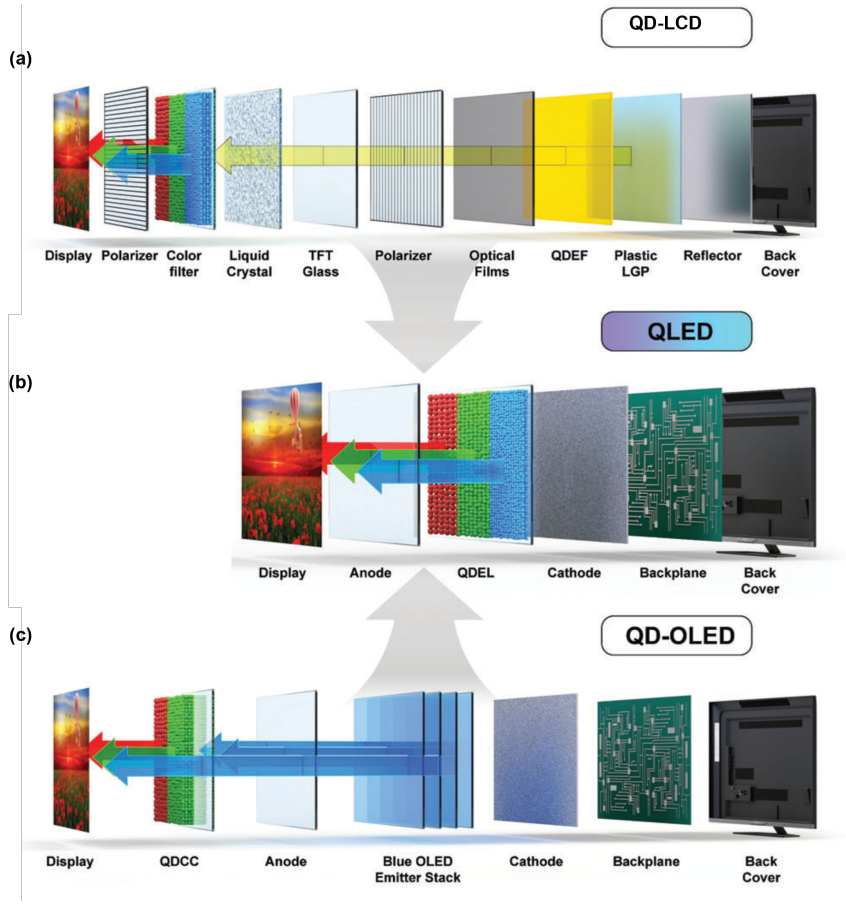

Figure 1.9: QD based display technology. (a)QDs are used as the white light color converter to replace the traditional phosphors in LCD. (b) QDs are used as electroluminescence emitters pixels, driven by the TFT backplane. (c)QDs are used as color converter pixels on top of a blue OLED emitter array. Reproduced from [6]

In a traditional LCD architecture, phosphors are employed to convert InGaN blue LED to white light as a backlight. By replacing the phosphors with a polymer containing red and green QDs, RGB backlighting can be generated (Figure 1.9 (a)), thereby enhancing the color gamut and reducing optical losses during color filtering [25]. Another approach utilizing QDs photoluminescence involves combining a blue emitter matrix (e.g., OLED [84] or InGaN micro-LED [26]) with a pixelated QD color converter (Figure 1.9 (c)), leading to improved performance in contrast, power consumption, and viewing angle. QD-based display products available in the current consumer market utilize these technologies.

Emerging as a leading candidate for next-generation displays, the electroluminescence route involves directly driving RGB QDs by the backplane, as depicted in Figure 1.9 (b). This technology holds the potential to surpass OLED displays, offering superior color gamut and longer lifetimes. An efficient, bright, and long-lasting Quantum-dot Light Emitting Diodes (QLED) stack is essential for realizing the full potential of next-generation displays.

LED

The first QLED was demonstrated by V. L. Covin et al. in 1994 using CdSe QDs. Over the past two decades, significant advancements in QLED performance have been achieved, driven by a deeper understanding of the mechanisms behind the electroluminescence of QLEDs. The record-high EQE (the ratio of emitted photons to injected electrons) reported for CdSe QLEDs is 33.1% for red [85], 28.7% for green, and 21.9% for blue [86]. Progress in Cd-free QLEDs has also been notable, with reported record EQEs of 21.8% for red [87] using InP QDs, 17.6% for green [88], and 20.2% for blue [89] using ZnSeTe QDs. Regarding lifetime, the T_{50} (the time for the EQE to drop to 50% of its initial value) at 100 cd/m^2 has been reported as 10^8 hours for CdSe-based red QLEDs, 10^6 hours for green, and 10^4 hours for blue. However, Cd-free QLEDs still lag in this respect and require further investigation.

In QLEDs, a thin QD emission layer is sandwiched between an ETL and a HTL, facilitating the injection of electrons and holes from the cathode and anode while confining the carriers in the QD emission layer, as shown in Figure 1.10 (a). The state-of-the-art QLEDs employ inorganic ETL / QDs / organic HTL hybrid structure. ZnO stands out as the preferred ETL due to its favorable energy band alignment and high electron mobility. Conversely, organic semiconductors such as Poly(9,9-dioctylfluorene-alt-N-(4-sec-butylphenyl)-diphenylamine) (TFB), Poly(N-vinylcarbazole) (PVK), 4,4'-Bis(N-carbazolyl)-1,1'-biphenyl (CBP), Tris(4-carbazoyl-9-ylphenyl)amine (TCTA) are commonly utilized as HTL due to their favorable band alignment, superior electron blocking capabilities and less exciton quenching at the interface compared to inorganic HTL materials [90, 91].

To achieve high EQE, especially at high luminescence levels, maintaining a delicate balance between electron and hole injection in QDs is essential. Otherwise, the QDs can become charged, typically negatively charged, leading to non-radiative Auger recombination competing with radiative recombination, as illustrated in Figure 1.10 (b). Achieving this balance is not trivial. ZnO ETL exhibits better band alignment compared to commonly used organic HTL, as depicted in Figure 1.11, and also possesses better mobility ($> 10^{-3}$ cm^{2}V^{-1}s^{-1} for ZnO nanocrystals compared to

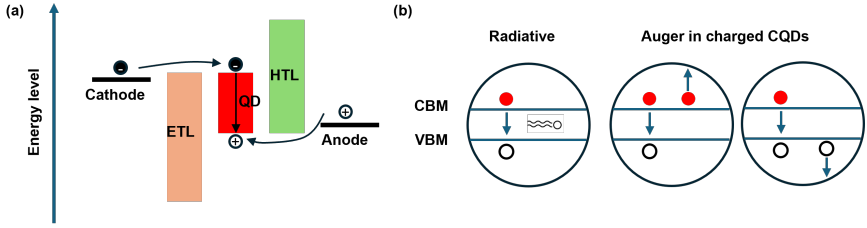

Figure 1.10: State-of-the-art QLED structure for efficiency electroluminescence and key factors that limit emission efficiency. (a) p-i-n multilayer stack with ETL and HTL for better carrier injection and confinement. (b) Non-radiative Auger recombination in QD if the carrier injection is not balanced.

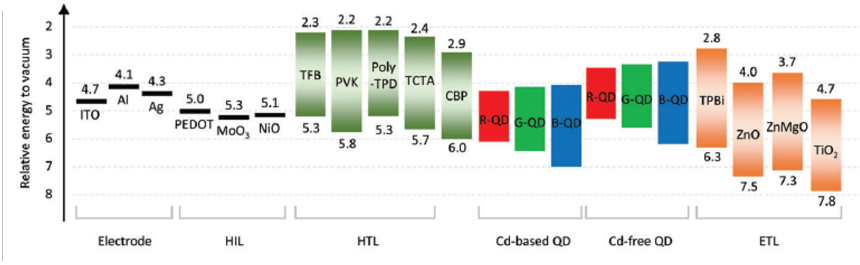

Figure 1.11: Energy levels of common carrier transport layers used in QLEDs. Reproduced from [6]

10^{-6} $cm^2V^{-1}s^{-1}$ to 10^{-3} $cm^2V^{-1}s^{-1}$ for typical HTL). Significant efforts have been made to enhance hole injection by optimizing the HTL. Using a step-wise multilayer HTL [92] or blended organics [93–95] has shown promise in improving hole injection into QDs. Another approach to balancing carrier injection involves reducing the injection of excess electrons. Dai et al. inserted a 6 nm thick PMMA layer between the QD layer and ETL, resulting in an EQE of 20.5% [96]. Using compositionally graded QDs can suppress Auger recombination, particularly when combined with an additional barrier shell to balance carrier injection, resulting in drop-free QLEDs even at high luminance levels exceeding 100,000 cd/m^2 (500 mA/cm^2) [97]. Surface modifications have also been explored for improved and more balanced carrier injection, enabling a slow EQE drop in the high-injection-current region (approximately 1000 mA/cm^2) and achieving bright green emission of 460,000 cd/m^2 [98].

Ensuring the confinement of exciton recombination within QDs is another critical factor for achieving high EQE. Recent studies on CdSe-based green and blue QLEDs have identified electron leakage into the HTL caused by energetic disorder, leading to carrier loss within the HTL. To address this issue, poly((9,9-

dioctylfluorenyl-2,7-diyl)-alt-(9-(2-ethylhexyl)-carbazole-3,6-diyl)) (PF8Cz), with reduced energetic disorder and a shallower Lowest Unoccupied Molecular Orbital (LUMO), was used as the HTL. This choice effectively blocked electron migration across the QD-HTL interface, resulting in record-high EQE values of 28.7% for green and 21.9% for blue QLEDs [86]. More progress on the development of QLED can be found in recent review papers [6, 20, 99].

Lasing

QDs are also interesting solution-processable gain materials due to their excellent compatibility with various platforms. Among the QD family, CdSe QDs stand out as the most promising gain candidates, featuring twofold-degenerate electron and hole band-edge states. Optical gain necessitates population inversion, wherein the average number of electron-hole pairs per dot exceeds one. However, the multi-exciton requirement for optical amplification presents challenges for lasing, as fast non-radiative Auger recombination competes with radiative radiation in QDs [100, 101]. For typical CdSe QDs with a size of 2.5 nm, the biexciton Auger lifetime is less than 100 ps, whereas the radiative lifetime is typically on the order of ten nanoseconds. This characteristic makes it difficult for QDs to achieve lasing under Continuous Wave (CW) optical pumping, with a threshold around 10^5 - 10^6 W cm^{-2} [102]. The observation of optical gain and stimulated emission from QDs was initially reported by Klimov in 2000, utilizing a femtosecond (fs) optical pump [101], which, with a duration shorter than the Auger lifetime, facilitates easier population inversion. Single-exciton gain in core/shell type II QDs [103, 104] and sub-single-exciton gain in charged QDs [105, 106] have been explored to mitigate fast Auger recombination, showing reduced thresholds for Amplified Spontaneous Emission (ASE) or lasing.

Thermal management is also crucial for achieving CW lasing. Utilizing ultra-compact QD films (with halide ligand exchange) on thermally conductive MgF_2 substrates has enabled microsecond-sustained lasing with an average peak power of around 50kW cm^{-2}. Furthermore, biaxially strained QDs on MgF_2 substrates, with decreased band-edge degeneracy and an extended Auger lifetime of 600 ps, have demonstrated lasing under CW optical pumping with a threshold of 6.4 - 8.4 kW cm^{-2} [107].

Considerable efforts have been directed towards suppressing fast Auger recombination. Alloyed QDs with a smooth confinement potential, as opposed to an abrupt one, have shown strong capabilities in suppressing Auger recombination [102, 108–110]. For instance, alloyed QDs consisting of a 2 nm radius CdSe core, a 7 nm thick graded $Cd_xZn_{1-x}Se$ shell, and a final 0.4 nm thick $ZnSe_{0.5}S_{0.5}$ layer exhibit a long

biexciton Auger lifetime of 2.4 ns [111], comparable to the biexciton radiative lifetime. These alloyed QDs are being employed in the pursuit of electrically pumped QD lasers by Klimov's group.

While electrically driven QD-based Laser Diodes (LDs) are the ultimate objective, they remain highly challenging to achieve. The idea of attaining a LD might seem straightforward, essentially combining an optical cavity with QLEDs which are well-developed. However, the current density used in a QLED is much lower than that required for a LD (< 1 A cm^{-2} vs. kA cm^2). In 2018, optical gain in QDs was achieved with electrical pumping for the first time [111]. By embedding alloyed QDs in a typical QLED structure with a reduced pixel size for current focusing and improved heat dissipation, population inversion was achieved with a current density of 3-4 A cm^{-2}. Subsequently, the possibility of achieving optically pumped lasing in LED-like devices with an integrated optical cavity was demonstrated, suggesting that the QD film has sufficient gain to compensate for cavity losses, particularly from the ITO electrode absorption [112]. Short electrical pulses (duration 1 μs, repetition rate 100 Hz) were then employed to further reduce overheating of the QLED, resulting in a record high current density of 1000 A cm^{-2} and strong electroluminescence from both the band-edge (1S) and higher-energy (1P) transitions, indicating population inversion of both energy states [113]. In 2023, ASE from electrically pumped QDs was successfully demonstrated [114]. This achievement relied on the optimization of both optical gain and loss. Alloyed QDs with smaller sizes were utilized for enhanced optical gain, while a dielectric Bragg reflector substrate was employed to improve optical confinement in the QD layer for better modal gain and to suppress optical intensity in the lossy ITO layer. Furthermore, the commonly used MoO_3 Hole Injection Layer (HIL), with strong optical absorption, was replaced with less lossy dipyrazino[2,3-f:2',3'-h]quinoxaline-2,3,6,7,10,11-hexacarbonitrile (HAT-CN) [115]. With these advancements, QD-based LDs seem to be around the corner now. More progress on QD based lasing development can be found in recent review papers [21, 116, 117].

1.3 Integrated photonics

Integrated photonics is a technology integrating multiple optical components and devices onto a single chip, analogous to how electronic components are integrated on semiconductor chips. This integration enables the creation of compact and highly functional photonic circuits capable of various optical functions. Integrated photonics has found applications in various fields including telecommunications [118], data communications [119], sensing [120] and photonic computing [121]. As integrated photonics technology has advanced, silicon photonics has emerged as a

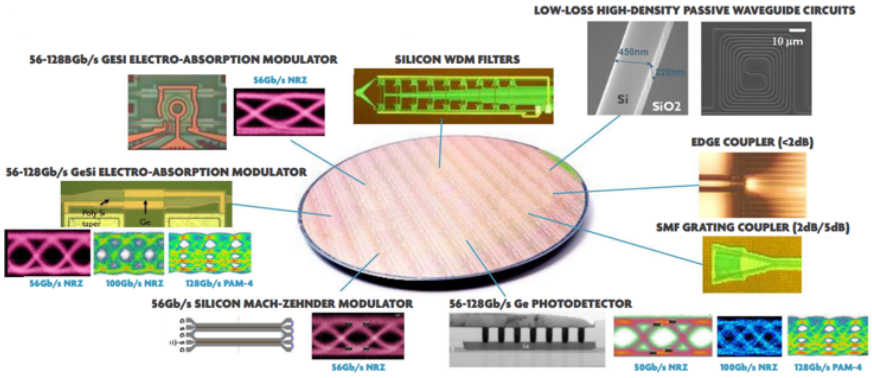

Figure 1.12: Imec's 50G+ silicon photonics platform

dominant platform due to its compatibility with existing semiconductor fabrication processes and its potential for large-scale integration [122].

1.3.1 Silicon photonics

Silicon photonics typically leverages the SOI platform, which is transparent from 1.1 μm (limited by silicon absorption) to 3.7 μm (limited by SiO_2 absorption). Silicon possesses a high refractive index (3.5 @ 1550 nm) compared to SiO_2, enabling efficient light guidance and manipulation within silicon. This platform has facilitated the development of high-performance passive components with compact footprints. In addition, electro-optical modulators leveraging free-carrier plasma dispersion are naturally achievable in silicon photonics and have demonstrated bandwidths of 60 GHz and higher [123, 124]. Furthermore, the successful growth of germanium on silicon has enabled photodetection below 1.6 μm (band-edge absorption of germanium), monolithically within the platform. Some studies have reported photodetectors with a 3 dB-bandwidth of up to 265 GHz [125]. These advancements have propelled silicon photonics to great success, particularly for realizing transceivers operating at O-band and C-band frequencies. Figure 1.12 shows the silicon photonics platform established at Imec.

Silicon photonics has also been extended to the SiN on SiO_2 and Ge-on-Si platforms, broadening its application domain. SiN extends the wavelength range of silicon photonics into the visible due to its wide bandgap. Additionally, SiN is renowned for its extremely low propagation loss and high power handling capability [29]. On the other hand, Ge-on-Si extends the capabilities of silicon photonics towards the infrared region, reaching wavelengths of up to about 8 μm [126]. This extension is

particularly advantageous for gas and chemical sensing applications, leveraging the well-known absorption fingerprints of various molecules in this spectral range.

However, the silicon platform still lacks certain optical functionalities that cannot be natively integrated, such as lasers and optical amplifiers, photodetectors beyond 1.6 μm, high-performance modulators, optical isolators, and circulators. Therefore, new materials are necessary to augment silicon photonics platforms. Several methods exist for integrating new materials, including flip-chip mounting [127,128], micro-transfer printing [129], die-to-wafer or wafer-to-wafer bonding [130, 131], and monolithic epitaxial growth [132, 133].

Flip-chip mounting is a straightforward assembly technique involving the pickup of a fully processed and tested die, which is then placed in a predefined trench on the Photonic Integrated Circuit (PIC), as shown in Figure 1.13(a). The optical connection is established through butt-coupling, while the electrical connection is achieved using metallic solder bumps. The main advantage of this technique lies in its simplicity and flexibility regarding the types of chips that can be mated. However, the sequential nature of the process, which requires each die to be individually picked up and placed due to the high alignment accuracy required for butt-coupling, significantly restricts manufacturing throughput.

Micro-transfer printing is another assembly process with significant improvements in assembly throughput compared to flip-chip mounting, as shown in Figure 1.13(c). In this process, the target components are processed on the source wafer and suspended with weak holding tethers. Subsequently, they are picked and placed on the silicon photonic waveguides with evanescent coupling for the optical connection, which demands less precise alignment compared to butt-coupling. The greater alignment tolerance makes it possible to transfer thousands of devices simultaneously in principle. For devices such as lasers and modulators, this high throughput remains to be demonstrated.

Wafer bonding is a technique whereby unprocessed blank dies or wafers, normally III-V material, are bonded onto a processed silicon photonic wafer, as shown in Figure 1.13(d). The III-V material is then fabricated and patterned, leaving it only on the target waveguide regions using standard lithographic and waferscale processing. Intel launched its first commercial product using this heterogeneous integration route in 2016. One drawback of this technique is the substantial investment needed to establish a fabrication line for the III-V material process on a large 200 mm or 300 mm hybrid wafer. The approach also requires large-area planarized surfaces which makes it challenging to heterogeneously integrate several different materials.

Monolithic epitaxial growth in principle could be the ideal approach to integrate III-V semiconductors on silicon photonic wafers, offering efficient material utiliza-

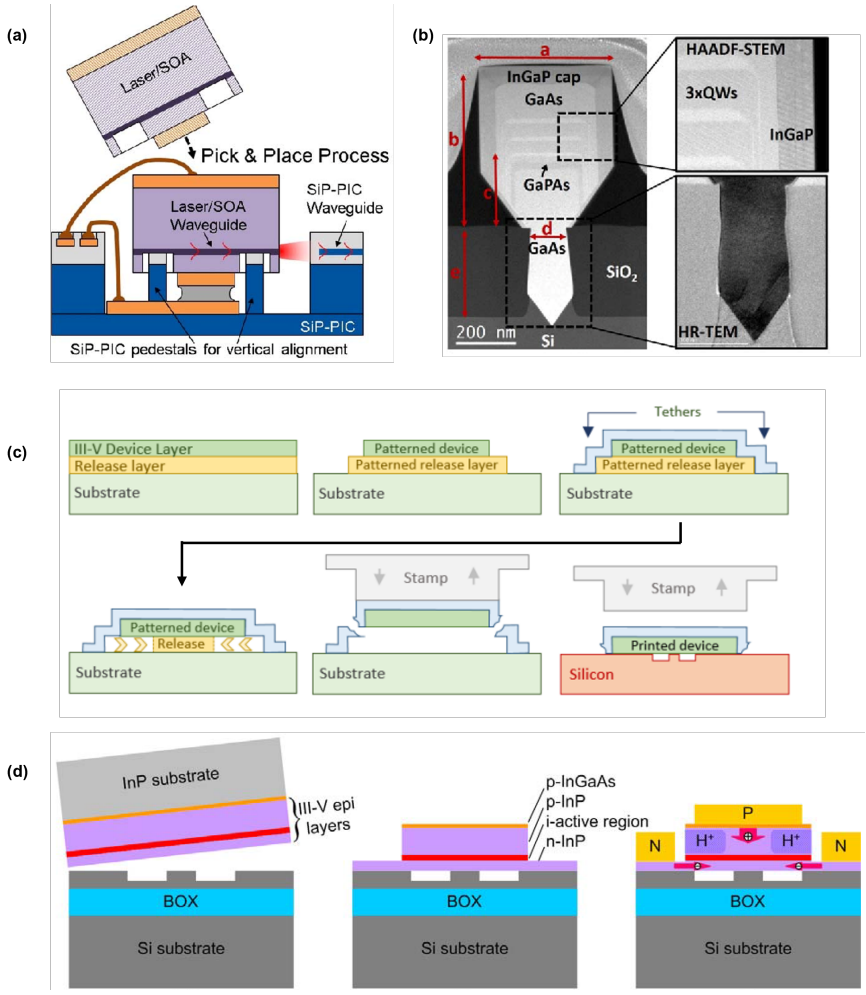

Figure 1.13: Examples of integrating III-V materials into silicon photonics platforms. (a) Flip-chip mounting, reproduced from [7]. (b) Monolithic epitaxial growth, reproduced from [8]. (c) Micro-transfer printing, reproduced from [9]. (d) Wafer bonding, reproduced from [10].

tion and high manufacturing throughput. However, the lattice mismatch between different materials poses a significant challenge to epitaxial growth. Researchers at the University of California, Santa Barbara have addressed this challenge by employing a thick buffer layer to grow high-quality quantum dots on silicon, leading to the demonstration of lasers with promising reliability lifetimes [134]. Imec has developed a nano ridge-engineering approach aimed at trapping defects in a narrow trench, thereby achieving defect-free III-V material on top (Figure 1.13(b)) [135]. Despite these advancements, further efforts are necessary to enhance the epitaxial quality and fully unlock its potential.

1.3.2 QDs in integrated photonics

Compared to other integration techniques discussed earlier, QDs promise a cost-effective and scalable solution for light generation and detection in integrated photonics. This potential stems from their low material cost, solution-based processing, and compatibility with various substrates. Several preliminary studies have already explored this direction of heterogeneous integration.

QDs as on-chip light sources have been investigated under optical excitation. Xie et al. successfully integrated CdSe-based QDs into the SiN platform, demonstrating multi-mode lasing from micro-disks with femtosecond optical pumping [136]. Subsequently, Zhu et al. demonstrated single-mode lasing using a distributed feedback (DFB) cavity with nanosecond optical pumping [137]. Eich et al. achieved single-photon emission using CdSe-based QDs in an integrated tantalum pentoxide waveguide [138].

Efforts to integrate QDs on chip for optoelectronic functions have also been reported. Elsinger et al. integrated a CdSe-based QLED stack on SiN waveguides, demonstrating electroluminescence at forward bias and photodetection at reverse bias in the visible range [139]. Zhu et al. integrated plasmonic HgTe-based photoconductors operating at 2.3 μm on silicon waveguides [140], showcasing QDs as potential candidates to extend the photodetection capability of the silicon photonic platform beyond the Ge limit. Additionally, Grotevent et al. demonstrated HgTe-based photoconductors with subwavelength width as integrated photodetectors in compact Fourier-transform waveguide spectrometers [141].

1.4 Thesis objectives

This thesis aims to integrate QDs for optoelectronic functions in silicon photonics, specifically as photodetectors and light sources, and to explore their applications.

There are two main objectives in this thesis.

Firstly, we aim to develop scalable process flows to integrate QDs as photodetection or light generation units on waveguides. For the photodetectors, we will focus on PbS QDs with infrared absorption capability. We will start the process development using a widely studied p-i-n PbS photodiode stack with bandgap absorption around 1.3 μm on SiN waveguides. This integration will provide a cost-effective photodetection solution for the passive SiN platform. Moreover, we aim to extend to longer wavelengths by demonstrating QD-based photodiodes on silicon waveguides with spectral response beyond 1.6 μm, surpassing the limit of monolithic germanium detectors and extending photodetection capabilities beyond the traditional telecommunication range in silicon photonics. For the light sources, we plan to integrate CdSe/CdS core-shell QDs on SiN waveguides, exploring the possibility and challenges of achieving electrically driven optical gain or lasing.

Secondly, we aim to demonstrate two applications based on integrated QD units. One application involves combining the tunable absorption features of QDs with dispersive PICs to extend the spectral bandwidth of on-chip spectrometers beyond a single Free Spectrum Range (FSR). By using different sizes of QDs, we could integrate waveguide-coupled photodetectors with distinct absorption spectra. Integrating these detectors in cascade, each showing a different response to different diffraction orders of the dispersive PIC, will allow us to decouple mixed information from different FSRs. Another application focuses on integrating an array of nano QD detectors as nano-samplers for stationary-wave integrated Fourier transform spectrometers. The short diffusion length of the QD film makes QD-based photodetectors potential candidates for nano-probes with a sub-wavelength footprint, addressing a critical pain point in such spectroscopy systems.

By achieving these objectives, this thesis aims to advance the integration of QDs in silicon photonics, enhancing the functionality and application scope of PICs.

1.5 Thesis Outline

In Chapter 1, we introduced the background of QDs and integrated photonics. We emphasized the unique characteristics of QDs and their wide-ranging applications in optoelectronics. Additionally, we discussed the significance of integrated photonics, particularly focusing on silicon photonics, and outlined current strategies for extending the platform's capabilities through heterogeneous integration. Finally, we discussed the emerging of using QDs for heterogeneous integration, thanks to their cost-effectiveness and excellent substrate compatibility.

In Chapter 2, we develop the first-generation process flow to integrate a QDPD design on SiN waveguides, targeting the 1.3 μm range. We will show the high power saturation problems in waveguide-coupled QDPDs (WG-QDPDs) and propose a strategy to mitigate this issue by carefully designing the cladding thickness and waveguide width. Our efforts yield WG-QDPDs with a responsivity of 0.69 A/W and a linear response for illumination powers up to 400 nW at -1 V bias. As a final step, we will demonstrate the integration of a QDPD array with an eight-channel arrayed waveguide grating, effectively functioning as a compact infrared spectrometer.

In Chapter 3, we will demonstrate WG-QDPDs featuring a spectral response extending beyond 1.6 μm on silicon photonics, by optimizing the QDPD design and the integration process flow. The WG-QDPDs exhibit a responsivity of 1.3 A/W at 2.1 μm, a low dark current of 106 nA, and a bandwidth of 1.1 MHz. Moreover, we will demonstrate the reliability of the integration approach by realizing a compact on-chip spectrometer that features an array of 8 WG-QDPDs and operates in the spectral window between 2.063 and 2.135 μm.

In Chapter 4, we will explore the combination of the tunable spectral response features of QDPDs with dispersive PICs, demonstrating a spectrometer with a working spectral bandwidth beyond a single FSR. We will discuss the principle and carefully design the system to ensure robust spectrum reconstruction. Experimentally, two types of PbS QDPDs, with different absorption features, are integrated in cascade on the output channels of a Planar Concave Grating (PCG) with a 90 nm FSR. The differential responses of these QDPDs to two adjacent diffraction orders of the PCG enable the creation of a spectrometer with a spectral range of approximately 180 nm, effectively decoupling two FSRs of the PCG.

In Chapter 5, we will investigate the potential of utilizing a QDPD array as nano-samplers for stationary-wave integrated Fourier transform spectrometers (SWIFTS). The spectrometer, designed on a SiN platform, aims to sample the stationary wave patterns generated by the interference of input light in a waveguide. We will experimentally verify the performance of the designed discrete components, including 1×2 Multi-Mode Interferometer (MMI), thermal phase shifter, and QDPDs with nano p-contacts of subwavelength lengths, all showing sufficient capability for the system. While the experimental demonstration of the SWIFTS system is pending, we anticipate its demonstration soon.

In Chapter 6, we will pursue electrically driven lasing from QDs integrated on SiN waveguides. We will show that minimizing optical loss, achieved by introducing a thick HTL to separate the optically lossy p-contact metal from the guided mode, leads to a hole-injection problem due to the poor conductivity of the HTL. By optimizing the HTL and using electrical pulse pumping to mitigate heating damage,

we achieve a current density of 61.2 A/cm^2 at a driving voltage of 100 V and observe emission from a higher state. Further efforts to enhance hole injection by doping the pristine organic HTL result in reduced resistivity but are accompanied by significantly increased parasitic optical absorption. Further optimization is needed to reach the goal of electrically driven gain.

Finally, Chapter 7 summarizes the work presented in this thesis and outlines future perspectives.

1.6 Publications

This dissertation has led to the following list of publications in conferences and international peer-reviewed journals.

1.6.1 Publications in international journals

C. Pang, R. Lopez March, E. Kheradmand, Y. Deng, L. Moreno Hagelsieb, L. Elsinger, Y. Guo, D. Cheyns, P. Geiregat, Z. Hens, and D. Van Thourhout. *On-chip spectrometer with multi-color cascaded colloidal quantum-dot photodetectors*. (submitted)

C. Pang, Y. Deng, E. Kheradmand, L. Moreno Hagelsieb, Y. Guo, D. Cheyns, P. Geiregat, Z. Hens, and D. Van Thourhout. *A silicon photonics waveguide-coupled colloidal quantum dot photodiode sensitive beyond 1.6 μm*. APL Photonics, 2024.

Y. Deng, **C. Pang**, E. Kheradmand, J. Leemans, J. Bai, M. Minjauw, J. Liu, K. Molkens, J. Beeckman, C. Detavernier, P. Geiregat, D. Van Thourhout, and Z. Hens. *Short-Wave Infrared Colloidal QD Photodetector with Nanosecond Response Times Enabled by Ultrathin Absorber Layers*. Advanced Materials, 202402002, 2024.

C. Pang, Y. Deng, E. Kheradmand, N. Poonkottil, R. Petit, L. Elsinger, C. Detavernier, P. Geiregat, Z. Hens, and D. Van Thourhout. *Integrated PbS Colloidal Quantum Dot Photodiodes on Silicon Nitride Waveguides*. ACS Photonics, 10(12): 4215-4224, 2023.

1.6.2 Publications in international conferences

C. Pang, R. March, E. Kheradmand, Y. Deng, L. Hagelsieb, L. Elsinger, D. Cheyns, P. Geiregat, Z. Hens, and D. Van Thourhout. *Beyond the free spectral range: on-chip spectrometer with multi-color cascaded colloidal quantum-dot photodiodes*.

In European Conference on Integrated Optics (ECIO), Germany, 2024.

C. Pang, Y. Deng, E. Kheradmand, L. Moreno Hagelsieb, D. Cheyns, P. Geiregat, Z. Hens, and D. Van Thourhout. *A colloidal-quantum-dot solution for photodetection beyond 1.6 μm*. In Annual Symposium of the IEEE Photonics Society Benelux Chapter, Belgium, 2023.

C. Pang, Y. Deng, E. Kheradmand, N. Poonkottil, R. Petit, L. Elsinger, C. Detavernier, P. Geiregat, Z. Hens, and D. Van Thourhout. *Integrated Spectrometer Based on Arrayed Waveguide Grating and PbS Colloidal Quantum Dot Photodiode Array*. In Conference on Lasers and Electro-Optics (CLEO), United States, 2023.

C. Pang, Y. Deng, E. Kheradmand, R. Petit, L. Elsinger, C. Detavernier, P. Geiregat, Z. Hens, and D. Van Thourhout. *Monolithic heterogeneous integration of PbS colloidal quantum dot photodiode on silicon nitride*. In Frontiers in Optics, United States, 2022.

2

Development of 1.3 μm waveguide-coupled QDPD on SiN

2.1 Introduction 28
2.2 Formation and Characterization of PbS QDPD 29
2.2.1 Fabrication 29
2.2.2 Characterization 32
2.3 Design of WG-QDPD 33
2.4 Fabrication of WG-QDPDs 37
2.4.1 Passive waveguides 37
2.4.2 ALD of ZnO and Al_2O_3 39
2.4.3 N-contact patterning 41
2.4.4 ZnO patterning 41
2.4.5 QD patterning 41
2.4.6 P-contact patterning 42
2.5 Characterization of WG-QDPD 45
2.6 Formation of an integrated QD spectrometer 45
2.6.1 Basic knowledge of AWG 46
2.6.2 Design and fabrication of AWG 47
2.6.3 Spectrometer 48
2.7 Discussion 50
2.8 Conclusion 52

2.1 Introduction

Silicon nitride is a promising integrated photonics platform characterized by a low propagation loss, high power handling capability, a broad transparency window and compatibility with processing in CMOS fabs [29]. Applications of SiN-based integrated photonics range from lidar [142–144] to biosensing [120, 145, 146] and quantum photonics [147–149]. However, the integration of active components on SiN remains a challenge. Leveraging their excellent substrate compatibility and patterning flexibility, solution-processed materials have been introduced into the SiN photonics platform for different purposes, for example, as gain material for lasers [136,137,150] and as single photon emitter [138,151,152]. However, most of these devices are driven optically. Integration on SiN of electrically driven devices, such as Infrared (IR) photodetectors, has only been achieved by heterogeneous or hybrid methods involving bonding [153] or transfer printing [154]. Given the limitations of these approaches mentioned in Chapter 1, QDPDs offer an appealing alternative for IR detection on SiN due to the low cost, ease of processing and good substrate compatibility.

Building on extensive research into QD solar cells, current IR-sensitive QDPDs based on PbS QDs can attain an external quantum efficiency (EQE) of 80% [57], a response time of 10 ns [57], a dark current density of 2.9×10^{-5} mA·cm^{-2}, and a detectivity of 6.7×10^{12} Jones at 980 nm [155]. Moreover, infrared detection capability up to 1.55 μm [57] has been demonstrated, and even up to 3 μm [156] has been achieved. These levels of efficiency and detectivity have led to the first commercial introduction of IR imagers based on a PbS QDPDs pixel array [76]. A similar integration of QDPDs on PICs could enable complex functionality, such as pocket spectrometers for sensing or compact Wavelength Division Multiplexing (WDM) receivers for datacom applications. However, integration of QDPDs on waveguides and PICs is still in its infancy. A first prototype involving a CdSe QDPD on a SiN waveguide was demonstrated by Elsinger et al., but this QDPD was only sensitive to visible light, had a modest external quantum efficiency of 6% at best, and featured a strongly sub-linear response [139]. Clearly, such issues need to be addressed for QDPDs to become widely deployed as IR detectors on SiN integrated photonics.

In this work, we demonstrate the integration on SiN waveguides of a QDPD consisting of two films of PbS QDs, with surfaces functionalized by lead iodide (PbI_2) and ethane-dithiol (EDT), respectively, stacked on a ZnO ETL. After analyzing the power-dependent saturation of the photocurrent by means of a bottom-illuminated, planar QDPD, we first map the design parameters of an integrated QDPD that would ensure a linear power response at relevant power levels. Next, we show that the relatively simple 3-layer QDPD stack can be integrated on SiN strip waveguides.

Using a waveguide width and cladding thickness that keeps the QDPD operating within the linear regime, we show a responsivity of 0.69 A/W, corresponding to an EQE of ∼67.5% at 1275 nm, and a linear response for illumination powers up to 400 nW at -1 V bias. Interestingly, this EQE is significantly better than that of the planar stack, probably due to the better absorbance of light incident parallel to the surface of the integrated QDPD. As a final step, we demonstrate a QDPD array integrated with an eight-channel Arrayed Waveguide Grating (AWG) demultiplexer, which works as a compact infrared spectrometer. This first demonstration of integrating multiple QDPDs to create an on-chip spectroscopic system provides a promising route for mass integration of QDPDs in complex photonic ICs applicable in a wide range of applications. [1]

2.2 Formation and Characterization of PbS QDPD

On-chip waveguides can be very compact, with a typical cross-sectional area below 1 μm^2. The ensuing strong optical confinement increases the power density and the carrier generation rate within a photo-active layer positioned on top of the waveguide, possibly leading to photodetector saturation. In literature, analysis of QDPDs is mostly carried out at relatively low power levels, i.e., smaller than 100 mW/cm^2 [56, 157]. Few studies, if any, have addressed the power-dependent saturation of QDPDs. To assess the limits of a linear photoresponse, we therefore first analyzed planar, bottom-illuminated QDPDs (BI-QDPDs).

2.2.1 Fabrication

The BI-QDPDs consisted of a stack of 100 nm ITO-on-glass, 50 nm ZnO, 60 nm PbS-PbI_2, 60 nm PbS-EDT, and 100 nm Au [2], as shown in Figure 2.1 (a). The n-doped ZnO film, formed using a sol-gel process, acts as an electron transport and hole-blocking layer, while the specifications PbI_2 and EDT refer to layers of as-synthesized QDs that had a surface treatment with lead iodide and ethanedithiol, respectively. According to literature [57], these treatments enhance charge-carrier mobility and result in PbS QD films with n-type and p-type characters, respectively.

The ITO glass (Ossila) was ultrasonically cleaned with acetone, ethanol, and deionized water, followed by exposure to O_2 plasma for 10 min. A ∼25 nm thick

[1] The content of this chapter has been adapted from the following journal paper: Pang, Chao, et al. "Integrated PbS Colloidal Quantum Dot Photodiodes on Silicon Nitride Waveguides." ACS Photonics 10.12 (2023): 4215-4224.

[2] PbS QDs were synthesized by Ezat Kheradmand from PCN group. The fabrication of BI-QDPDs was conducted by Dr. Yuhao Deng from PCN group

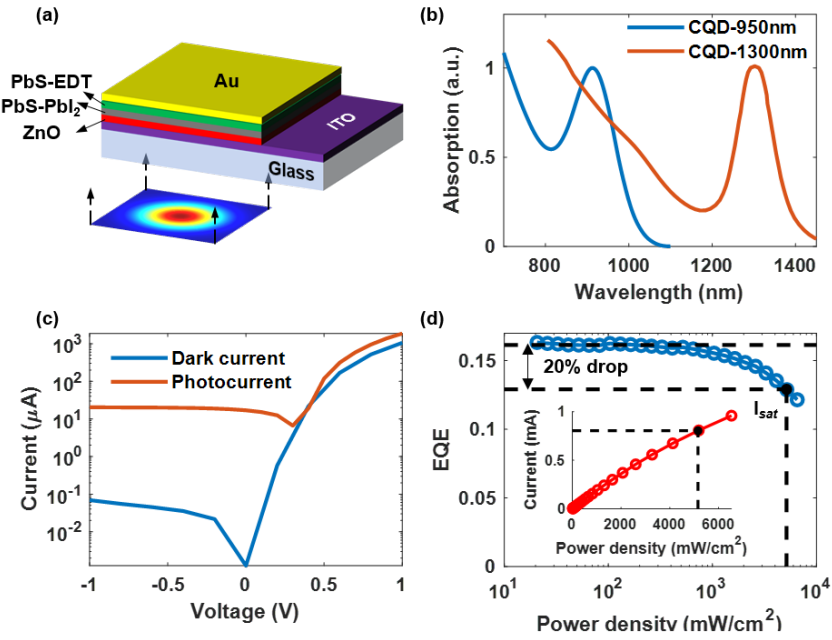

Figure 2.1: Structure and characterization of BI-QDPD. (a) Device structure of the BI-QDPD, illuminated from the bottom glass side by laser with Gaussian beam shape. (b) Absorption spectra for both types of QDs used in the BI-QPDD, dispersed in n-octane. QDs with exciton peak around 1300 nm were used for absorption, and QDs around 950 nm were used as hole-transport and electron-blocking material. (c) Dark current and photocurrent of BI-QDPD with an area of 1.77 mm^2. The photocurrent was measured for illumination at 1275 nm with a power of 0.16 mW (peak power density of ∼100 mW/cm^2). (d) EQE of BI-QDPD vs. optical power density at a bias voltage of -1V. The intersection of the dashed lines indicates the onset of saturation. Inset: photocurrent vs. optical maximum power density. The optical power density is that measured in the center of the Gaussian beam illuminating the BI-QDPD.

ZnO layer was deposited on the cleaned ITO substrate via spin-coating of the precursor solution. The samples were then annealed at 250°C for 20 min in air. The above step was repeated twice to get 50 nm of ZnO.

Oleate-capped QDs are electrically insulating, and the ligands have to be replaced by shorter ligands. The exchange of the long lead oleate ligands by PbI_2 was accomplished through solution-phase ligand exchange [57]. 345 mg of PbI_2 (99.999%, Alfa Aesar), 110 mg of $PbBr_2$ (98%, Sigma-Aldrich), and 27 mg of NaOAc (99.999%, Sigma-Aldrich) were dissolved in 7.5 mL of N,N-dimethylformamide (DMF, anhydrous, 98%, Sigma-Aldrich) in a 50-mL centrifuge tube. A 5-mL solution of PbS-OA in n-octane (98%, Alfa Aesar) at a concentration of 5 mg/mL was then added to the exchange solution. The tube was vigorously shaken for 30 s to facilitate dot transfer to the DMF phase. Subsequently, the n-octane phase was discarded. After the main exchange step, the remaining solution was washed three times with n-octane. Subsequently, a 10-µL volume of butan-1-amine (BTA) (99%, Sigma-Aldrich) was added to the tubes to restabilize the colloid. Next, 6 mL (v/v 50%) of toluene was added to precipitate the QDs, and the tubes were centrifuged at 2000 rpm again for 2 min. The QDs were then dried in a vacuum for 3 min. The exchanged QDs solid was dispersed in a solution of BTA, amylamine, and hexylamine (volume ratio 10:3:2) at desired concentrations. Here, DMF was not used for dispersing the iodine-capped PbS QDs since it dissolved the photoresist (ARP672.08, Allresist) used for patterning the QD film during the integration. Iodine-capped QDs were spin-coated on the ZnO layer at 2000 rpm for 30 s and annealed in N_2 for 10 min at 70 °C, forming the absorption layer with a thickness around 60 nm.

The EDT surface treatment involved a solid-phase ligand exchange. PbS-OA QDs in n-octane solution were first spin-coated on the substrate coated with the above-mentioned layers. The EDT solution (0.01 vol% in methanol) was applied to the surface for 30 s and spun at 2000 rpm for 10 s, followed by two methanol rinses. The deposition process was repeated twice to get a thickness of 60 nm. Methanol was chosen over the more gentle solvent acetonitrile [158] due to the latter's tendency to swell the resist polymer utilized for patterning the QD film in the subsequent integration process.

Importantly, as shown in Figure 2.1 (b), the PbS-PbI_2 and PbS-EDT layers consisted of QDs with a band-gap of 1300 nm and 950 nm, respectively. In this way, the first layer serves as the absorber layer for light with wavelengths up to 1300 nm, while the second layer acts as the hole transport layer. Finally, the PbS-EDT layer was contacted by a gold film, thermally evaporated using a shadow mask. According to literature, such a heterogeneous stack of PbS-EDT/PbS-PbI_2/ZnO forms a p-i-n junction, where the 60 nm absorption region of PbS-PbI_2 is fully depleted [57].

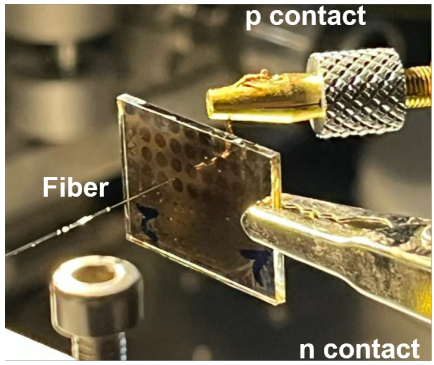

Figure 2.2: Measurement setup for BI-QDPD. The QDPD is illuminated with a 1275 nm laser from a cleaved single-mode fiber. The n-contact of the QDPD is connected using a clamp, while the p-contact is connected via an electrical probe.

2.2.2 Characterization

To analyze the photoresponse of the BI-QDPD, we illuminated the device using a 1275 nm laser beam with a Gaussian beam profile and variable incident power, see Figure 2.1 (a). In detail, the light was illuminated from a cleaved single-mode optical fiber with a fixed distance, as shown in Figure 2.2. The mode profile was Gaussian shaped and had a mode profile diameter of 9.2 μm on the cleaved fiber facet according to the product sheet. The optical power density at the PD can be calculated from the Gaussian beam propagation equation:

$$I(r,l) = \frac{2P}{\pi w(l)^2} \exp\left(-\frac{2r^2}{w(l)^2}\right) \tag{2.1a}$$

$$w(l) = w_0\sqrt{1+\left(\frac{\lambda l}{\pi w_0^2}\right)^2} \tag{2.1b}$$

where P is the optical power, w_0 is the mode profile radius at the fiber facet, $w(l)$ is the radius of the Gaussian beam at a propagation distance l from the fiber facet, and r is the radial distance away from the central axis. With $w_0 = 4.6$ μm and $l = 3.1$ mm in the measurement, the calculated mode profile diameter on the PD is 547 μm. The peak power density of the Gaussian beam can be calculated at $r = 0$ position, which will be used for evaluation of power saturation of QDPD in the following section.

Because of this inhomogeneous illumination profile, we quantified the photore-

sponse by means of the photocurrent, rather than the photocurrent density. Accordingly, Figure 2.1 (c) represents the current-voltage characteristics of a typical BI-QDPD. In the dark, we observed a pronounced diode behavior with a dark current of 70 nA – corresponding to a dark current density of $\sim$4 μA/cm^2 – at a bias voltage of -1 V (Figure 2.1 (c)). In addition, we measured a nearly constant photocurrent under reverse bias upon illumination, which we believe to reflect the efficient extraction of photo-generated carriers from the PbS-PbI_2 layer. Quantitatively, we obtained a photocurrent of 0.02 mA for a total illumination power of 0.12 mW, corresponding to an external quantum efficiency (EQE) of 16%, where EQE is defined as the ratio of the number of collected photo-generated carriers and the number of incident photons. Figure 2.1 (d) displays the EQE of the BI-QDPD measured at a bias voltage of -1 V as a function of the peak power density of the laser, where a total power of 0.12 mW corresponds to a peak power density of 100 ± 10 mW/cm^2. As can be seen, a transition occurs from a constant EQE of 16% to a regime where the EQE drops with increasing power density, which implies that at such power densities, the photocurrent no longer increases linearly with the incident power. To quantify this saturation effect, we define the saturation power density I_{sat} as the power density at which the EQE drops by 20% from its initial value (averaged EQE for power density < 400 mW/cm^2). Figure 2.1 (d) shows that I_{sat} defined in this way amounts to 5.2 W/cm^2, which we will take as a reference for the design of a WG-QDPD that operates in the linear regime at relevant power levels.

2.3 Design of WG-QDPD

Our aim was to realize an evanescently coupled QDPD (WG-QDPD) by fabricating the device stack on top of a 300 nm thick SiN waveguide layer, see Figure 2.3. Such a configuration offers multiple design parameters to adjust the power density in the absorbing layer, and thus maximize the optical power of the guided light at which detector saturation occurs. In this study, we limited the parameter space to the waveguide width w and the cladding thickness t. Wider waveguides limit the power density of the guided light, while increasing the separation between the top of the SiN waveguide and the QDPD stack reduces the overlap of the evanescent optical field with the QDPD.

Different from the BI-QDPD, illumination occurs parallel to the PbS QD films in the WG-QDPD design proposed in Figure 2.3 (a). To use the saturation power density of 5.2 W/cm^2 measured on a BI-QDPD as a design constraint in this different geometry, we started from the notion that carrier extraction occurs in the same vertical (z) direction for both QDPDs. Hence, when splitting the PbS-PbI_2

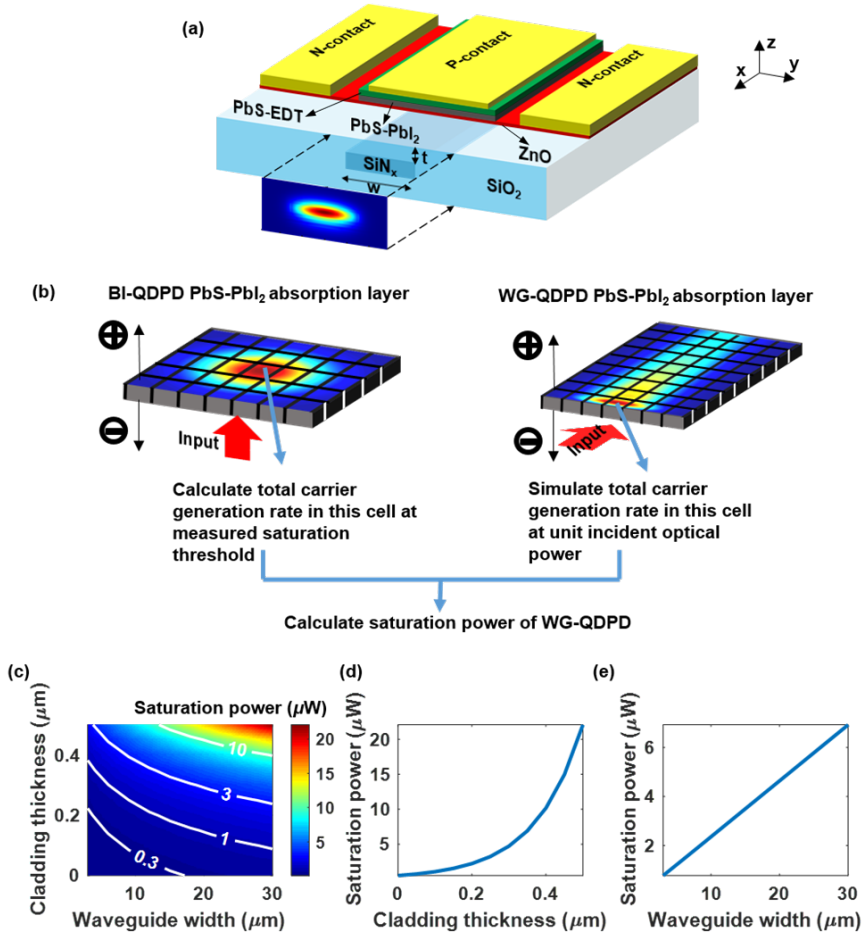

Figure 2.3: Design of WG-QDPD. (a) Device structure of WG-QDPD. (b) Link between saturation of BI-QDPD and WG-QDPD. Red arrows point out the light propagation direction, vertical for the BI-QDPD and horizontal for the WG-QDPD. The electrons and holes are extracted in the vertical direction for both cases. The PbS-PbI$_2$ absorption layer can be split into small cells. The total carrier generation rate in each cell determines its local saturation. The cell with the maximum total carrier generation rate (indicated by a blue arrow) determines the onset of saturation for the whole PD. (c) Simulated saturation power of WG-QDPD vs. cladding thickness and waveguide width. (d) Slice of (c) for a waveguide width of 30 µm. (e) Slice of (c) for a cladding thickness of 0.35 µm.

absorber layer into small cells parallel to the z direction, see Figure 2b, the total carrier generation in each cell will determine a concomitant local saturation. For both QDPDs, it is the cell with the highest total generation rate that determines the onset of saturation of the entire QDPD. As depicted in Figure 2b, this is the cell in the center of the film for the BI-QDPD, while it is the central cell at the edge of the film for the WG-QDPD as depicted in Figure 2b.

In general, the maximum carrier generation rate Γ_{max} across the different cells in a given film can be calculated as:

$$\Gamma_{\text{max}} = \max[\Gamma(x,y)] = \max\left[\int_{-\infty}^{\infty} G(x,y,z)\,dz\right] \tag{2.2a}$$

$$G(x,y,z) = \frac{P_{\text{abs}}(x,y,z)}{h\nu} = \frac{2\pi n\kappa\varepsilon_0}{h}|E(x,y,z)|^2 \tag{2.2b}$$

Here, $G(x,y,z)$ is the carrier-generation rate (units $\text{m}^{-3}\text{s}^{-1}$) at a specific point in the film, while $\Gamma(x,y)$ is the integrated carrier-generation rate along the z direction. In addition, $P_{\text{abs}}(x,y,z)$ is the optical power absorbed per unit volume, $h\nu$ is the photon energy, ε_0 is the vacuum permittivity, $n = 2.55$ and $\kappa = 0.15$ are the real and imaginary parts of the complex refractive index of the PbS-PbI_2 film respectively, and $E(x,y,z)$ is the electrical field. Note that we considered the z-integrated generation rate, rather than the (x,y,z) point generation rate. This approach assumes that the actual distribution of the carrier generation rate in the z-direction has minimal influence on the carrier extraction, a reasonable consideration since the QD absorber layer utilized here is thin enough to consider a uniform built-in electrical field for carrier extraction throughout the absorber layer.

For the BI-QDPD, the saturation happens when the laser output power exceeds 6.1 mW, corresponding to a power density of ~ 5.2 W/cm^2 at the peak of the Gaussian beam. Γ_{max} for the BI-QDPD is determined by the equation:

$$\begin{aligned}\Gamma_{\text{max, BI-QDPD}} &= \max\left(\int \frac{2\pi n\kappa\varepsilon_0}{h}|E(x,y,z)|^2 dz\right) \\ &= \int \frac{2\pi n\kappa\varepsilon_0}{h}|E(0,0,z)|^2 dz \\ |E(0,0,z)|^2 &= \frac{2}{\varepsilon_0 nc} I(r=0, l=3.1\text{ mm})\end{aligned} \tag{2.3}$$

where c is the speed of light, $I(r,l)$ represents the optical power density of the Gaussian beam as described in Equation 2.2.2. The integration covers the absorption layer (PbS-PbI_2). The maximum value is located at the center of the Gaussian beam ($x = 0$, $y = 0$). The electric field distribution along the z-direction can be obtained

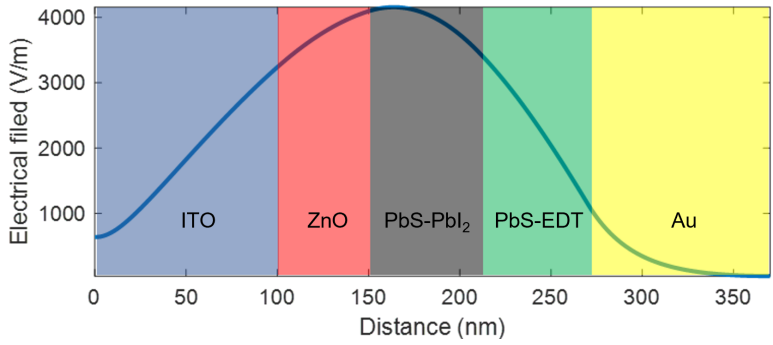

Figure 2.4: Electrical field distribution in the PD stack with an input optical power density of 5.2 W/cm^2

from optical simulations using the transfer matrix method (Lumerical Stack solver), as shown in Figure 2.4. Given the measured saturation power density of 5.2 W/cm^2 of the BI-QDPD, we estimated the threshold Γ_{max} at 3×10^{22} m^{-2}s^{-1}.

For WG-QDPDs, the light is injected from a single-mode waveguide through an adiabatic taper to the PD region. The target mode is the fundamental TE mode, and its electric field distribution was simulated with the Lumerical finite difference eigenmode solver. Γ_{max} of the WG-PD was calculated by numerically integrating the electric field distribution in the z-direction for a unit of incident optical power. By keeping Γ_{max} at the threshold value of $3 \times 10^{22}\,\mathrm{m}^{-2}\mathrm{s}^{-1}$, we then mapped the optical power of the guided light at which the WG-QDPD will saturate as a function of the waveguide width and the cladding thickness. As shown in Figure 2.3 (c)-(e), we found that the saturation power increases exponentially with cladding thickness, an outcome that reflects the exponential decay of the evanescent tail of the waveguide mode, and increases linearly with waveguide width in agreement with the linear extension of the optical mode. Note, however, that to keep the fraction of absorbed light constant, a lowering of the power density in the absorbing layer will come at the expense of a longer QDPD, which will increase the dark current without yielding more photocurrent.

For a single-mode waveguide with a width of 1 μm and no top cladding, the calculated saturation power is as low as 28 nW. On the other hand, a combination of a top cladding thickness of 350 nm and a waveguide width of 30 μm should yield a saturation power up to 6.9 µW. For these design parameters, we estimated the loss of the waveguide functionalized with the WG-QDPD stack at 623 dB/cm, of which 87% involves absorption of light within the PbS-PbI$_2$ QDs and the remainder mostly related to absorption within the ZnO layer and the metal top contact. As a result, a 200 μm long WG-QDPD is needed to absorb 95% of the input light, with

a maximally attainable EQE of 82%. The above design targets the fundamental TE mode. However, given the large waveguide width utilized and potential perturbations, guided light could couple into higher-order TE modes or even TM modes. Nonetheless, our simulations indicate that there is no obvious change ($< 0.3\%$) in terms of optical loss and attainable EQE for the ten lowest order TE-like modes. TM modes exhibit a higher optical loss of 1432 dB/cm, yet a similar attainable EQE of 77%. We thus conclude that the proposed integrated QDPD design can achieve efficient light absorption and stable performance. According to the dark current density recorded on the BI-QDPD, such a WG-QDPD would have a dark current of 0.3 nA, which is considerably smaller than the expected photocurrent. Since further increasing the cladding thickness or waveguide width will deteriorate the trade-off between power saturation and dark current, we settled for a waveguide width of 30 μm and a top cladding thickness of 350 nm to demonstrate a first generation of WG-QDPDs.

Increasing the thickness of the absorption layer enhances light absorption, allowing for shorter devices and reduced dark current. However, stronger absorption means more carriers need to be locally extracted within each cell, as shown in Figure 2.3 (b), which will lower the saturation optical power. Moreover, increasing the thickness will reduce the electrical field inside the absorption layer, impairing carrier extraction and further decreasing the saturation optical power. From an optical perspective, the QD film has a refractive index of 2.55, significantly higher than that of SiN. As the QD thickness increases, the optical mode shifts further into the QD layer, increasing coupling loss between the passive SiN waveguides and the photodetectors due to mode mismatch. These considerations drive the choice of a thin QD film as the absorption layer.

2.4 Fabrication of WG-QDPDs

We developed a process flow in our cleanroom, starting with a Si substrate with 3000 nm thermal oxide on top, as shown in Figure 2.5.

2.4.1 Passive waveguides

A SiN layer was deposited onto a silicon substrate with a 3 μm thermal oxide using a plasma-enhanced chemical vapor deposition (PECVD) system (Advanced Vacuum Vision 310 PECVD) at 270 °C, employing N_2, NH_3, and SiH_4 chemistry. Prior to patterning the waveguides, metal markers were placed on the blank chip for improved overlay alignment in subsequent patterning steps. These markers were

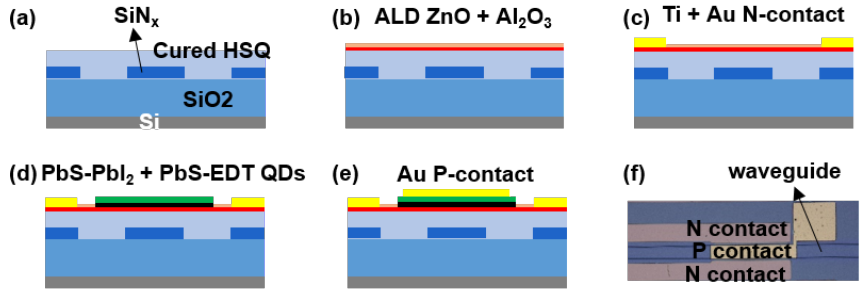

Figure 2.5: Processing steps to fabricate WG-QDPD. (a) SiN waveguide patterning and top cladding deposition. (b) ALD of ZnO ETL and Al_2O_3 protection layer. (c) N-contact metal patterning with photoresist and liftoff. (d) QD film patterning with PMMA resist and liftoff. The Al_2O_3 protection layer was removed before spin-coating QDs. (e) P-contact metal patterning with PMMA resist and liftoff. (f) Top view of fabricated WG-QDPD.

patterned using a 50 kV Ebeam lithography (EBL) system (Voyager Raith) with a positive resist ARP6200.13 (∼400 nm, Allresist) and a dose of 200 μC/cm^2. The pattern was developed in n-amyl acetate for 60 seconds. Subsequently, the sample was transferred to an E-gun evaporator (Leybold 560) for deposition of 5 nm Ti / 100 nm Au / 5 nm Ti. The use of two thin layers of Ti aimed to enhance adhesion between SiN and Au, as well as between Au and the subsequently deposited top cladding. Following metal evaporation, the metal outside the detector region and the sacrificial e-beam resist underneath were lifted off in resist remover AR600-71 (Allresist), assisted by sonication.

To pattern the waveguide, a 400 nm layer of ARP6200.13 ebeam resist was spun onto the sample, followed by EBL with a dose of 160 µC/cm^2 and development in n-amyl acetate for 60 s. The resist pattern was then transferred to SiN using reactive ion etching (RIE, Advanced Vacuum Vision 320) with CF_4 and H_2 chemistry. After etching, the resist was removed by immersing the sample in resist remover AR600-71 for 10 min and in O_2 plasma (PVA TePla 600) for 5 min.

To planarize the sample, flowable oxide hydrogen silsesquioxane (HSQ, Dow FOX-15) was spin-coated on top. Diluted HSQ (HSQ : MIBK = 2:1) was spin-coated at a speed of 1300 rpm (acceleration 500 rpm/s), then baked on a hotplate at 150 °C for 2 min. To enhance the stability of the top cladding layer both physically and chemically, the sample was cured at 400 °C for 2 h in a N_2 atmosphere. After complete curing, the thickness of the HSQ film decreased to approximately 350 nm. HSQ effectively smooths the surface of SiN, as depicted in Figure 2.6 (a). Additionally, the HSQ cladding exhibits transparency in the O-band. Measurements were conducted on 900 nm-wide (single-TE-mode) SiN spiral waveguides with varying lengths, revealing a propagation loss of approximately 1.25 dB/cm around

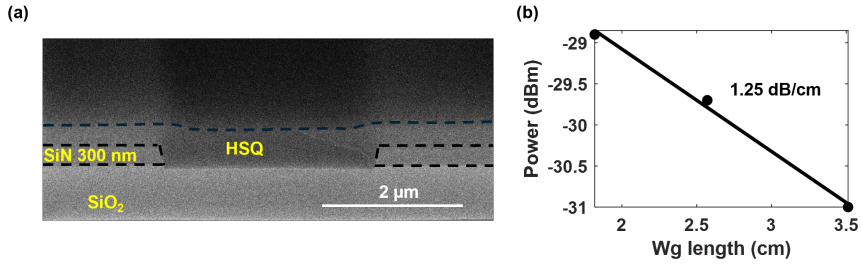

Figure 2.6: HSQ as a top cladding. (a) Cross-section of planarized SiN waveguides with a height of 300 nm. (b) The transmission power of 300 nm × 900 nm single-TE-mode SiN waveguides with different lengths, covered by an HSQ top cladding.

1275 nm, as illustrated in Figure 2.6 (b).

Note that while we made use of lab-processed waveguides in this study, a similar integration approach could be used for integrating QDPDs on waveguides fabricated in a classical foundry process using DUV lithography and wafer scale processes.

2.4.2 ALD of ZnO and Al_2O_3

Sol-gel ZnO exhibits low electrical conductivity, making it unsuitable for supporting carrier transport horizontally over lengths of several micrometers in the WG-QDPD. Conversely, ALD ZnO demonstrates significantly lower resistivity and therefore holds promise as an ETL for integration applications [139].

The depositions were performed in a custom-built ALD reactor [3] with a base pressure of ca. 10^{-6} mbar. Prior to the ALD growth, the samples were exposed to a remote O_2 plasma (10 s, 3×10^{-3} mbar, at 200 W) to remove potential contamination from air exposure. ZnO ALD was then performed using diethylzinc ($> 95\%$, Strem Chemicals, Inc.) as a precursor and deionized water as a co-reactant at a deposition temperature of 150 °C. After depositing 20 nm ZnO, 10 nm Al_2O_3 was deposited on top with trimethylaluminum ($> 98\%$, Strem Chemicals, Inc.) as a precursor and deionized water as a co-reactant at 150 °C. Al_2O_3 was used here as a protection layer, protecting ZnO from losing conductivity due to exposure to the O_2 plasma in the following fabrication. After ALD, the sample was annealed in an N_2 and H_2 atmosphere at 400 °C for 1 min to increase the conductivity of the ZnO layer.

The resistivity of the 20 nm thick ALD ZnO layer, measured using the Transfer Length Method (TLM), was determined to be $2.1 \times 10^{-5} \Omega \cdot$ m, as illustrated in

[3] The ALD was conducted by Robin Petit and Nithin Poonkottil from CoCooN group

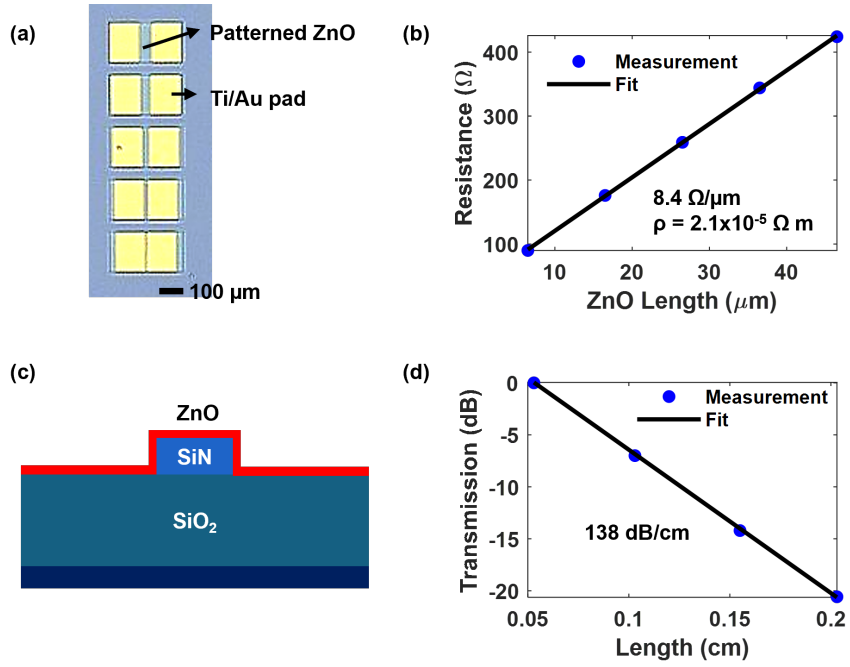

Figure 2.7: The electrical and optical properties of ALD ZnO (a) TLM structures for resistivity measurement: 20 nm thick ZnO was patterned to a width of 125 µm. A pair of Ti/Au pads was placed on ZnO with different gaps between pad edges (5 µm to 50 µm). (b) Measured resistance with different ZnO lengths. (c) Cross-section of waveguides used for optical loss measurement, with dimensions of 3 µm by 300 nm. ZnO was patterned into different lengths (0.5 mm to 2 mm). (d) Measured propagation loss at 1.3 µm.

Figure 2.7(a) and (b). In our WG-QDPD configuration, electrons must traverse a distance of 25 μm horizontally from the center of the waveguide to the n-contact metal, resulting in a series resistance of 131 Ω for a cross-section of 20 nm (ALD ZnO thickness) by 200 μm (WG-QDPD length). This indicates that the ALD ZnO layer provides sufficient electrical conductivity for our application.

In addition, ALD ZnO exhibits limited absorption in the O-band. A SiN waveguide (3 μm by 300 nm) covered by 20 nm ALD ZnO demonstrates a propagation loss of around 138 dB/cm at 1.3 μm. Based on the measured waveguide loss, we can estimate the complex refractive index to be $1.74 + 0.014i$ using the measured refractive index (real part) from ellipsometry and simulation (Lumerical FDE solver). The imaginary part of ALD ZnO is one order of magnitude smaller than that of the QD absorption layer (0.15), indicating its excellent optical transparency and its suitability as the ETL in our WG-QDPD.

2.4.3 N-contact patterning

Contact photolithography and lift-off were used to pattern the n-contact. Ti 35E (Microchemicals) photoresist was used in image reversal mode to ease the metal liftoff. Ti prime (Microchemicals) adhesion promoter was spun before the photoresist to improve its adhesion with Al_2O_3. After exposure, the sample was immersed in diluted AZ400K (buffered KOH, Microchemicals) solution (AZ400K:H_2O=1:3) for 5 min 20 s. The resist was developed in 90 s, with the additional time of 3 min 50s used to remove the Al_2O_3 layer on top of ZnO. The etching time was critical since the KOH solution can also etch ZnO. Then the n-contact metal was evaporated, with a composition of 20 nm Ti / 100 nm Au. Ti was used for lowering the contact resistance with ZnO. After evaporation, the sample was immersed in an acetone puddle for 30 min and then rinsed with acetone to lift off the metal on the photoresist. After lift-off, the sample was cleaned by exposing it to an O_2 plasma for 5 min (PVA TePla 600).

The adhesion promoter played a crucial role in this process. Its absence would result in the attack of Al_2O_3 near the edge of the patterned resist. Over-etching of Al_2O_3 is particularly harmful since a single pattern is employed for both Al_2O_3 removal and metal patterning. Removing the Al_2O_3 protection layer exposes the sensitive ZnO, which would lose conductivity during subsequent O_2 plasma cleaning. This severe conductivity degradation would lead to a loss of electrical connection between the n-contact and the QDPD. An alternative approach is to utilize a two-step patterning, employing a smaller pattern to remove the Al_2O_3 and a larger pattern to deposit the metal, ensuring complete coverage of the exposed ZnO by the metal.

2.4.4 ZnO patterning

The ZnO layer was patterned using contact photolithography and chemical wet etching. Ti prime and Ti 35E were used again. After exposure, the sample was developed for 2 minutes in a diluted AZ400K solution (AZ400K:H2O = 1:3). Subsequently, the Al_2O_3 layer was locally removed using a solution of AZ400K:H_2O = 1:10, heated to 50°C to accelerate Al_2O_3 removal and mitigate photoresist attack. ZnO was then removed by immersing the sample in a dilute HCl solution (37% HCl:H2O = 1:50) for 30 seconds.

2.4.5 QD patterning

The QD film was patterned using electron beam lithography (EBL) and lift-off . PMMA (ARP672.08:anisole=2:1, Allresist) was spin-coated at 3000 rpm (accel-

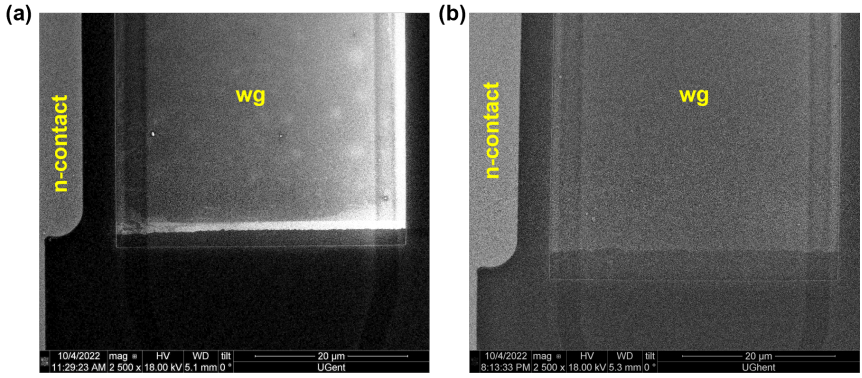

Figure 2.8: Surface contamination. (a) Dirty surface before HCl treatment. (b) Clean surface after HCl treatment.

eration 1000 rpm/s) and baked at 150 °C for 3 minutes (thickness approximately 400 nm). PMMA patterning employed an exposure dose of 400 µC/cm^2, followed by development in AR600-55 (Allresist) for 90 seconds. Short sonication was utilized at the end of the development process to remove undeveloped resist residue. PMMA was selected for its compatibility with the solvent methanol used during QDs deposition.

Before depositing the QDs, the Al_2O_3 layer atop ZnO was removed by immersion in a dilute HCl solution (37% HCl:H_2O=1:50) for 20 seconds and a buffered KOH solution (AZ400K:H_2O=1:40) at 50 °C for 1 minute. The dilute HCl solution was employed to remove the residual Ti prime layer from the previous photolithography process, which otherwise acted as an etching barrier and resulted in a dirty ZnO surface, as shown in Figure 2.8. Following the exposure of the ZnO surface, PbS QDs (60 nm PbS-PbI_2 and 60 nm PbS-EDT) were deposited using the same process as mentioned in the fabrication of the BI-QDPD [4]. After the QDs film deposition, the sample underwent liftoff in acetone for 10 minutes to complete the QD patterning.

2.4.6 P-contact patterning

The p-contact was patterned by EBL and lift-off. PMMA (ARP672.08, Allresist) was spin-coated with a speed of 3000 rpm (acceleration 1000 rpm/s), and baked on a hotplate at 60 °C for 5 min. Then the patterning area was exposed with a dose of 400 µC/cm^2, and developed in AR600-55 for 90 s with sonication. A low baking temperature was used to avoid increasing the dark current of the QDPDs [155]. After

[4]The spin-coating of QDs was conducted by Dr. Yuhao Deng from PCN group

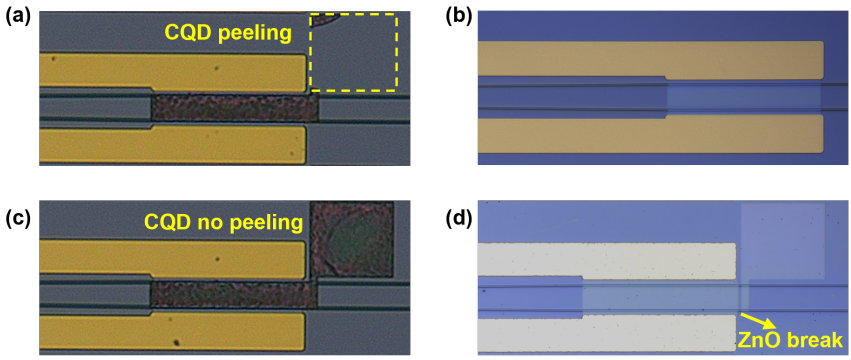

Figure 2.9: QD peeling issue and solution. (a) QD peeling observed on HSQ. (b) ZnO patterning limited to the waveguide region for (a). (c) QDs on HSQ without peeling. (d) ZnO patterning extended to the pad region for (c), with a small break to prevent the large dark current from the pad region.

development, the sample was coated with 100 nm Au using an E-gun evaporator (Leybold), followed by a lift-off process in acetone for 30 min.

Figure 2.5 (f) shows a top-view microscopy image of a fabricated WG-QDPD, in which all relevant parts have been highlighted. To facilitate characterization, the p-contact pad was extended outside the waveguide. However, Au exhibited poor adhesion with HSQ and posed the risk of peeling off. To address this, we extended the QD layer to the pad region as a supporting layer for the Au pad. However, this resulted in a secondary issue: weak adhesion between QDs and the HSQ top cladding. During the ligand exchange step to obtain PbS-EDT, the stress caused by volume shrinkage led to QD peeling. This peeling problem was resolved (Figure 2.9 (c)) by extending the ZnO pattern to the pad region (Figure 2.9 (b), (d)), thanks to the better adhesion between QDs and ZnO. A short interruption in the ZnO layer was introduced between the QDPD and the pad to avoid the dark current from the large pad.

Using this integration approach, WG-QDPDs with different waveguide widths were fabricated on a single chip to confirm the predicted width-dependent saturation of the WG-QDPD. We also defined a WG-QDPD array on an eight-channel AWG to realize a more complicated functionality using WG-QDPDs. Reference waveguides without integrated QDPD were also included on the chip to calibrate the power coupled into the waveguides.

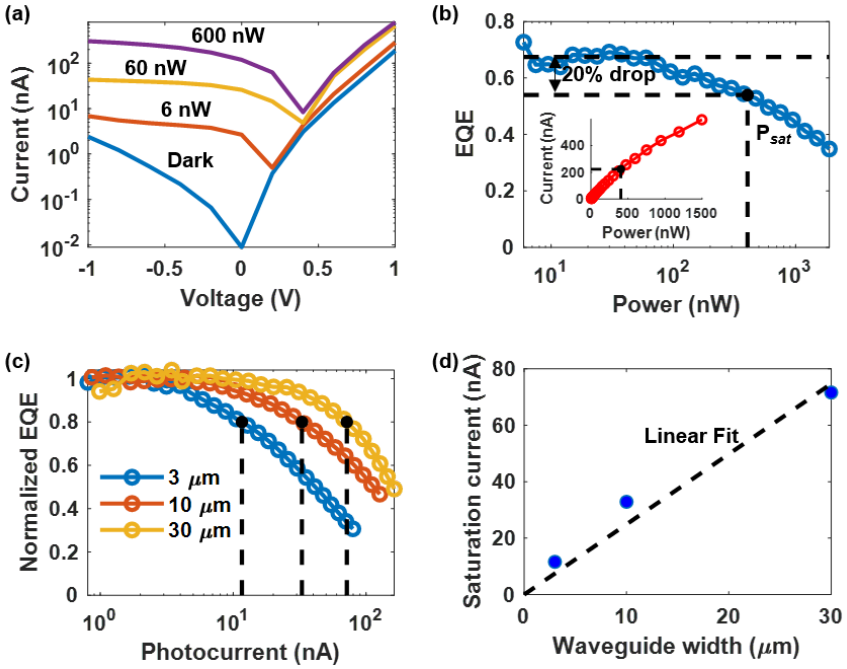

Figure 2.10: Response of WG-QDPDs. (a) I-V curves of WG-QDPDs under dark condition and illumination at 1275 nm. (b) EQE vs. optical power at -1V bias voltage. Inset: photo-current vs. optical power with bias voltage of -1V. The intersection of the black dashed lines indicates the onset of saturation. (c) Normalized EQE vs. photocurrent at -2V bias voltage for different waveguide widths. The saturation points of WG-QDPDs are indicated by vertical black dashed lines. (d) Saturation photocurrent with different waveguide widths. A linear fit is indicated by the black dashed line.

2.5 Characterization of WG-QDPD

We characterized the WG-QDPDs using a source measurement unit (Keithley 2450), DC probes and an O-band tunable laser. The light was coupled into the SiN waveguides through grating couplers. The optical power of the guided light was calibrated by measuring the coupling efficiency of the grating coupler for the reference waveguide without QDPDs. Figure 2.10 (a) represents the current-voltage curves of a WG-QDPD in the dark and upon illumination with 1275 nm light of various intensities. One sees that the dark current increases from the expected $<$ 1 nA at low reverse bias to 2.4 nA at a -1V bias. Possibly, this difference with the BI-QDPD is related to the different way of forming the n-ZnO layer in both cases, i.e., through ALD for the WG-QDPD and through a sol-gel process for the BI-QDPD.

On the other hand, a nearly constant photocurrent is obtained upon illumination. As shown in Figure 2.10 (b)-(c), the best devices showed a linear responsivity and a constant EQE at low illumination power. More precisely, an average EQE of 67.5% is obtained in the range 6-60 nW, which drops to 54% at the saturation optical power (P_{sat}) of 400 nW, a 20% reduction that we took as marking the end of the linear regime. Note that this experimental result is about one order of magnitude smaller than the predicted saturation power of 6.9 μW, which was based on the characteristics of the BI-QDPD. Probably, this outcome reflects the differences between the idealized structure used for the simulations, and the actually formed WG-QDPD, which can accumulate contamination and defects during the different fabrication steps. Even so, we do retrieve the expected variation of the saturation behavior of the WG-QDPDs with varying waveguide widths, for which we characterized saturation by the measured photocurrent rather than the optical power so as to circumvent possible measurement errors induced by variations of the optical coupling efficiency, see Figure 2.10 (c). Notably, WG-QDPDs with different waveguide widths, increasing from 3 to 10 and 30 μm, exhibited the predicted proportional increase in saturation power as the optical power intensity in the absorbing layer decreased, see Figure 2.10 (d). We therefore conclude that a PbS-based QDPD stack can be successfully integrated on SiN waveguides, and that the issue of detector saturation can be mitigated by the design parameters of the WG-QDPD, such as the waveguide width.

2.6 Formation of an integrated QD spectrometer

To illustrate what our approach of integrating QDPDs can accomplish, we fabricated a set of WQ-QDPDs on the output channels of an AWG, which can work as a

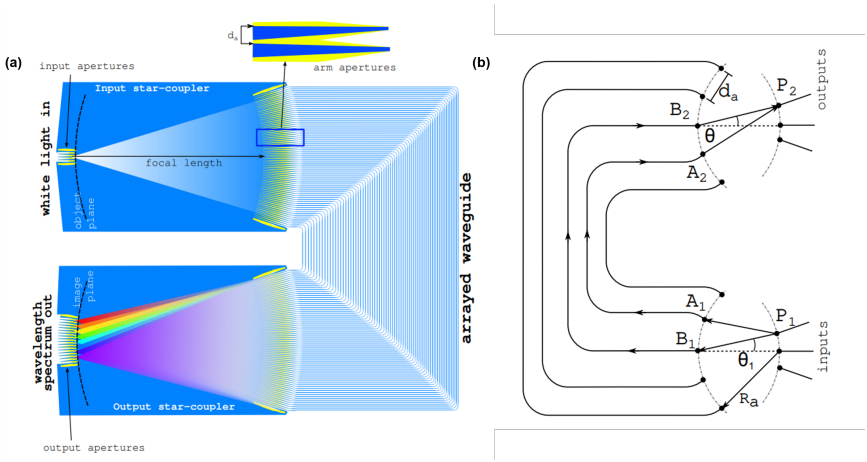

Figure 2.11: Principle of the AWG. (a) Schematic.(b) Operational diagram. Reproduced from [11]

compact spectrometer.

2.6.1 Basic knowledge of AWG

The AWG is a well-established dispersive component in integrated photonics, consisting of two star couplers and a waveguide array, as shown in Figure 2.11(a). Light entering the initial star coupler is diffracted and coupled into the waveguide array with a specific phase difference between adjacent arms. This phase difference causes different wavelengths to focus at different positions, achieving wavelength dispersion. The grating equation determines the in-phase condition of input light:

$$n_{slab} d_a \sin\theta_1 + n_{wg}\Delta L - n_{slab} d_a \sin\theta = m\lambda \tag{2.4}$$

where n_{slab} is the effective index of the slab waveguide in the free propagation region of the star coupler, θ_1 and θ are the angles of input and output with respect to the center of the star coupler respectively, as shown in Figure 2.11(b). n_{wg} is the effective index of the waveguide in the array. ΔL is the length difference between adjacent waveguides in the array. d_a is the array aperture pitch. m is the diffraction order, and λ is the wavelength.

The waveguide array is the core part of the AWG. The length difference ΔL between adjacent waveguides is related to the central wavelength λ_c and FSR λ_{FSR} of the AWG:

$$\Delta L = \frac{\lambda_c^2}{n_{g,wg}\lambda_{FSR}} \tag{2.5}$$

where $n_{g,wg}$ is the group index of the waveguide in the array:

$$n_{g,wg} = n_{wg}(\lambda_c) - \lambda_c \frac{\mathrm{d}n_{wg}}{\mathrm{d}\lambda} \tag{2.6}$$

The array aperture pitch d_a is a critical parameter in determining the dispersion characteristics of the AWG. It can be approximately expressed as:

$$\frac{\mathrm{d}\theta}{\mathrm{d}\lambda} = -\frac{\lambda_c}{n_{slab} d_a \lambda_{FSR}} \tag{2.7}$$

The star coupler serves for imaging, usually employing a Rowland-type mounting to decrease aberration. To minimize insertion loss, most of the divergent light from the input aperture should be collected by the apertures in the array. This relationship links the focal length of the star coupler R_a, the array aperture pitch d_a, and the number of waveguides in the array N_{arms}:

$$R_a = \frac{d_a N_{arms}}{\theta_d} \tag{2.8}$$

here θ_d is the diffraction angle of the input aperture where the intensity drops to $1/e^2$.

2.6.2 Design and fabrication of AWG

The AWG was designed with IPKISS [159], with the following design parameters:

Parameter	Value
central wavelength	1290 nm
FSR	60 nm
n_{slab}	1.661
n_{wg}	1.622
$n_{g,wg}$	1.925
N_{arm}	28
d_a	2.1 μm
Array aperture width	2 μm
Number of output channel	8
I/O aperture width	4 μm
I/O aperture width	4 μm

Table 2.1: Parameters for designing the AWG.

The size of the waveguide array is 400 μm $\times$ 300 μm, as shown in Figure 2.12(a), allowing it to fit within a single write field of the EBL (500 μm $\times$ 500 μm for our

system) to avoid stitching errors in the waveguides. The straight sections of the waveguides in the array are extended to 1.5 μm to reduce the crosstalk resulting from fabrication-induced phase errors. The other sections in the waveguide array are kept at a width of 0.9 μm to maintain the single TE mode condition.

The AWG was fabricated on a single chip together with the passive waveguides discussed above. The AWG was characterized by sweeping a tunable laser (Santec TSL-510) and measuring the transmission power on a vertical coupling setup with grating couplers as optical I/O. The measured transmission spectra of all eight channels are shown in Figure 2.12(b). The shape of the grating couplers was removed by subtracting the transmission spectrum of a reference waveguide.

The AWG was designed to have a FSR of 60 nm, splitting the light into eight wavelength channels with a spacing of 7.5 nm. Consistent with the design specifications, the 8-band AWG covers a wavelength range of 51 nm, corresponding to a channel spacing of 7.3 nm. The AWG exhibits an insertion loss of -2 dB and a crosstalk of 15 dB. This crosstalk is limited by phase errors in the dispersive waveguide array introduced during fabrication. We observed that the performance of the AWG was not stable, with crosstalk varying between -23 dB and -10 dB from batch to batch. It has been shown that by optimizing the design and processing, e.g., by using DUV lithography instead of electron beam lithography, these phase errors can be minimized, and crosstalk values up to 30 dB can be readily achieved [160, 161].

2.6.3 Spectrometer

The QDPDs were integrated on the output channels of the AWG to form the spectrometer, as shown in Figure 2.13 (a).

We characterized the spectral response of this compact spectrometer by injecting monochromatic light, tuned in wavelength from 1260 nm to 1320 nm, from the input grating coupler and measuring the photocurrent in each channel without applying a bias voltage. Figure 2.13 (b) represents the normalized photocurrent in each channel. One sees that sweeping the wavelength indeed leads to a photoresponse in the different WQ-QDPDs. The 8-band spectrometer exhibits a similar spectral response to the transmission spectrum measured on the passive AWG. The small shifts observed in the spectral response can be attributed to the fabrication variation. The measured channel crosstalk was around 15 dB, which is already sufficient for many applications. The AWG design can be adapted to meet the requirements of given applications. To reach higher resolution, the channel spacing can be reduced or more channels can be added. Alternatively, e.g. in data applications, the AWG can be designed with a flat channel response instead of a Gaussian shape, by using multimode interference couplers as input apertures [162]. This demonstrates

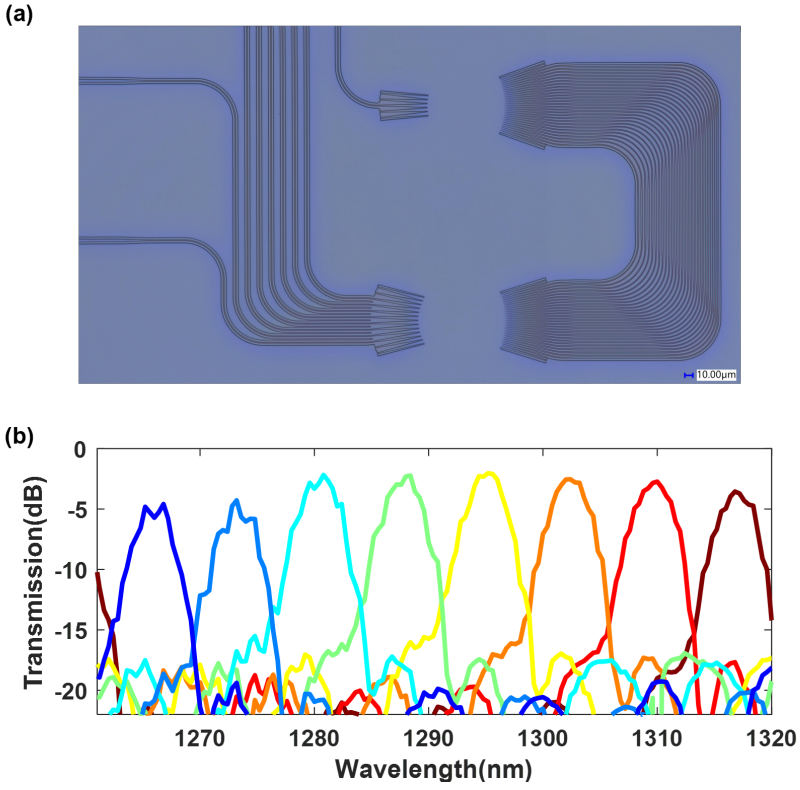

Figure 2.12: AWG designed with IPKISS and fabricated with EBL. (a) Top view of the AWG. (b) Transmission spectrum of eight channels.

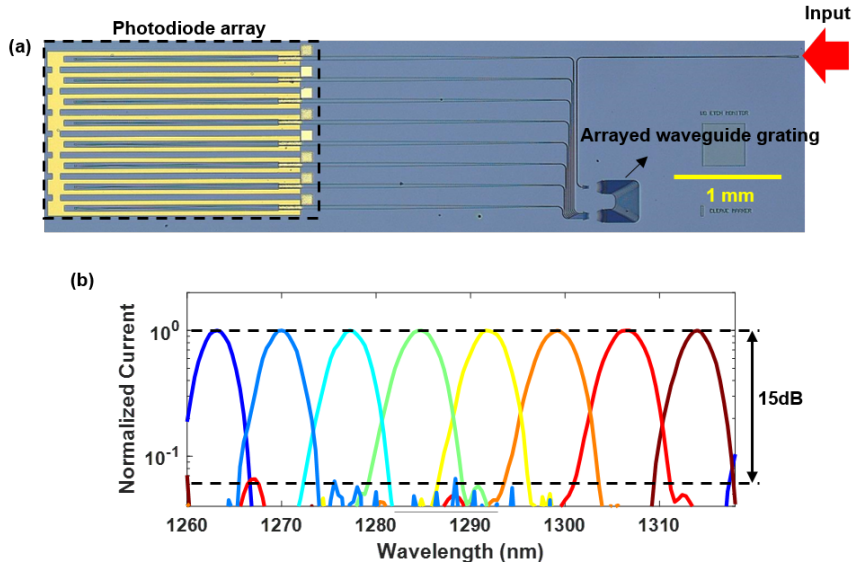

Figure 2.13: Integrated spectrometer with QDPD array and AWG. (a) Top view of the spectrometer. Light is injected from the right grating coupler. (b) Response of eight channels without applying bias voltage. The response of each channel was normalized to its maximum.

the flexibility of this on-chip approach and opens up its use in many different applications such as in-vivo glucose monitoring [163, 164] and fiber Bragg grating readout [165].

2.7 Discussion

Most of the photodetectors integrated on SiN waveguides reported in literature were based on bonded or transfer-printed III-V semiconductors [153, 166], Ge monolithically grown on Si [167, 168], and two-dimensional materials [169, 170]; approaches that result in increased integration complexity. Integration of evaporated amorphous [171] and poly-crystalline [172] photoconductors have also been demonstrated, offering promising pathways for less complex heterogeneous integration. However, such photoconductors have been associated with the observation of a notable dark current and low detectivity [171, 172], attributed to the inherent photoconductor mechanism. Here, we have demonstrated the formation of QD-based photodiodes on SiN waveguides by means of standard film deposition and patterning techniques. These WG-QDPDs exhibit a lower dark current (2.4 nA at -1V) than most of the previously demonstrated photodetectors. In addition, our WG-

QDPDs demonstrate a high responsivity of 0.69 A/W at around 1.3 μm, which is comparable to, or even better than, reported waveguide-coupled PDs [153, 166, 168]. Moreover, the use of QDs as active material offers the benefits of a low-cost material, compatibility with standard fabrication techniques, ease of processing and scalability towards higher volume production. These features make WG-QDPDs attractive for low cost, low-power and noise-sensitive applications. Finally, planar QDPDs have been demonstrated to exhibit a response time as short as 10 ns [57]. However, this fast response time has been observed only in small pixel devices, indicating the response time is primarily limited by the resistance-capacitance (RC) product. In this respect, WG-QDPDs, with their smaller active area and consequently reduced capacitance, hold great potential for achieving even faster response times. In more detail, the capacitance of our WG-QDPD is expected to approximate 15 pF, considering a dielectric constant of 34 [57], a device area of 6000 μm^2, and a QD layer thickness of 120 nm. With a load resistance of 50 Ω, the RC limited response time (10% to 90% rise time, calculated as $2.2 \times$ RC) is estimated to be 1.7 ns.

Although in this work E-beam lithography was used for patterning the QD layer and the p-contact metal, nothing prevents the use of photolithography as an alternative [173, 174], enabling the fabrication of WG-QDPDs on wafer scale with high throughput. Furthermore, the process used to integrate PbS QDPDs on the SiN waveguide platform can be extended to other QDs materials and photonics integrated platforms. For the silicon-on-insulator (SOI) platform, monolithically integrated Ge detectors are the preferred solution for wavelengths below 1.6 μm. However, for longer wavelengths, there is still no straightforward integrated solution. In the next chapter, we will demostrate the possibility of integrating larger PbS QDs with absorption onsets beyond 2 μm on silicon waveguides, thereby extending the photodetection capabilities beyond the traditional telecommunication range in silicon photonics. For other platforms like flexible photonics which meet with similar challenges of integrating active components, QDPDs are also a promising candidate.

While the saturation power of WG-QDPDs is better than that of two-dimensional materials photodetectors [170], it is still not on par with III-V or Ge photodetectors, which have saturation powers exceeding 1 mW [166, 175]. Hence, a significant enhancement of the saturation power is needed to make WG-QDPDs competitive in this way, a step that is contingent upon better fabrication techniques and the design and operation of the QDPD stack. For the fabrication, we believe minimizing damage to the QD and transport material films, as well as ensuring cleaner interfaces, could significantly enhance the performance of WG-QDPDs, bringing them closer to that of planar QDPDs. For the QDPD stack, however, limited literature is available on the origin of detector saturation. Possibly, the low saturation power

of PbS QDPDs compared with epitaxial PDs is related to a high series resistance induced by the low mobility of the QDs film. As a result, higher carrier densities are needed to sustain a given photocurrent. More in general, however, the results presented here call for a better understanding of detector saturation in QDPDs.

Benefiting from the wide tunability of the QD absorption spectrum, the concept of computational spectrometers based on the wavelength multiplexing principle [176] has emerged as a compelling option. In this scheme, hundreds of QDs, each characterized by a distinct absorption spectrum, function as specialized filters that randomly sample the desired spectrum. Subsequent computational techniques enable the reconstruction of the sampled data. A key departure from traditional spectrometers, including the one exemplified in our current study, is that the inherent trade-off between resolution and bandwidth becomes obsolete in the realm of computational spectrometry. The integration of QD-based computational spectrometers into integrated photonics also holds substantial promise. However, a series of potential challenges needs to be overcome, such as the efficiency and yield concerns of multi-step QD deposition, effectively controlling QDs absorption behavior, and realizing low-loss and broadband power splitters.

2.8 Conclusion

In this work, we have demonstrated for the first time PbS QDPDs integrated on SiN waveguides using standard process techniques. Based on the characterization of planar QDPDs, we argue that the high optical intensity resulting from the strong optical confinement in waveguides could induce saturation of a WG-QDPD at low optical power. We overcome this issue through a design in which the WG-QDPD overlaps is coupled to the evanescent field, while using the cladding thickness and the waveguide width as adjustable parameters to raise the saturation power by reducing the overlap with the evanescent field. In particular, we demonstrate that a 30 μm wide device with a 350 nm cladding layer can exhibit a responsivity of 0.69 A/W and a linear response up to 400 nW for 1275 nm light at -1 V reverse bias. Such a combination, however, involves a trade-off between an increased saturation threshold and an enhanced dark current since longer detectors are needed to absorb a given fraction of the guided light. To further demonstrate the scalability of the integration approach proposed here, we also designed and tested a compact 8-channel spectrometer integrated with an array of WG-QDPDs. This spectrometer showed a clear wavelength dependent response with channel crosstalk of 15 dB. We believe that these results will inspire further research into the integration of colloidal active materials on PICs.

3

Development of 2.1 µm waveguide-coupled QDPD on SOI

3.1 Introduction 53
3.2 QDPDs with wavelength response up to 2.1 µm 55
3.2.1 Optimization of electron transport layer 56
3.2.2 Optimization of QDPD stack for 2.1 µm 63
3.3 Integration of QDPDs on waveguides 65
3.4 Characterization of WG-QDPDs 70
3.5 Demonstration of a 2.1 µm spectrometer 78
3.5.1 Basic operation of the PCG 78
3.5.2 Integrated spectrometer 79
3.6 Discussion 80
3.7 Conclusion 81

3.1 Introduction

Despite the widespread use of silicon photonics, current applications predominantly use light with wavelengths shorter than 1.6 μm. This limitation is not a choice. Numerous applications, including environmental monitoring, medical diagnostics,

and industrial sensing, would profit from photonic chips operating at longer wavelengths [177, 178]. Such applications are, however, hampered by the lack of a scalable and cost-effective integrated technology for photodetection beyond 1.6 μm.

Different strategies are being explored to extend the photodetection wavelength range of silicon photonics. A commonly used technique involves wafer or die bonding of III-V materials, typically GaSb-based compounds, onto silicon [179–182]. However, this method requires large-area planarized surfaces and relies on costly III-V epitaxy and bonding technology. Also, two-dimensional (2D) materials like graphene and black phosphorus are extensively investigated for on-chip photodetection beyond 1.6 μm [183]. The promise of these materials lies in favorable substrate compatibility and a broad absorption range, yet scalability poses a substantial hurdle for the practical integration of 2D photodetectors. Moreover, the performance of these photodetectors needs further improvement, for example, to enhance dark current performance and responsivity [184, 185]. Alternatively, the direct deposition on Si of GeSn alloys [186–189], III-V quantum dots epitaxially grown on silicon [190], or polycrystalline tellurium thin films [172] can result in cost-effective photodetectors with straightforward fabrication processes. However, the current implementations of these methods result in photodetectors with high dark current and low responsivity, necessitating further development.

To address the challenge of cost-effective photodetection beyond the telecom range in silicon photonics, QDs offer a promising solution. QDs present an economic advantage in both material synthesis and deposition processes, in stark contrast with more traditional III-V epitaxial semiconductors. Moreover, the absorption spectrum of QDs can be readily tuned across the infrared spectrum by adjusting the QD size and utilizing different materials. Photodetectors made from PbS [55–57, 77], HgTe [61, 191], Ag2Se [192, 193], or InAs [65] QDs have all exhibited sensitivity to short-wave and mid-wave infrared light.

In Chapter 2, we have demonstrated the integration of waveguide-coupled QD-based photodiodes operating at around 1.3 μm on the SiN platform, which underscores the potential of QDs as scalable photodetectors within photonic integrated circuits (PICs) [194]. For wavelengths beyond 1.6 μm, recent developments include the demonstration of plasmonic HgTe-based photoconductors on silicon waveguides operating at 2.3 μm with a responsivity of 23 mA/W [140]. On the other hand, PbS QDPDs sensitive up to 2.1 μm with a responsivity of 0.385 A/W were achieved by sandwiching the QD film between a NiO p-type and a ZnO n-type contact [2]. Such reports point towards the promise of using integrated QDPDs for photodetection beyond 1.6 μm, provided that low dark currents and high responsivity can be realized in integration-ready QDPD stacks.

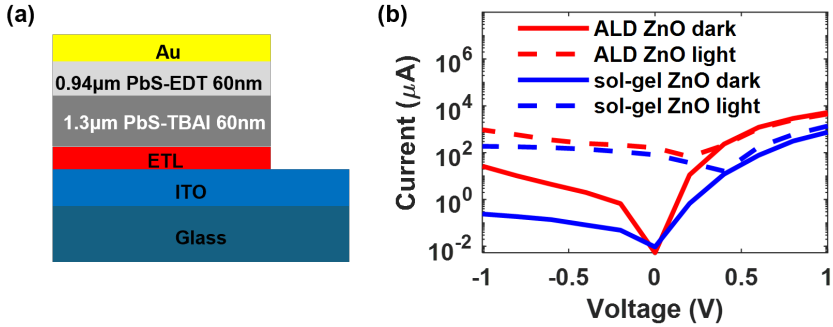

Figure 3.1: 1.3 µm BI-QDPD with different ETL. (a) QDPD structure. (b) I-V curves under dark and light conditions (power of 1.6 mW, peak power density of 1.2 W/cm^2). Red: 40 nm ALD ZnO. Blue: 30 nm sol-gel ZnO.

In this chapter, we report on a silicon photonics, waveguide-coupled QD photodiode (WG-QDPD) that features a spectral response extending beyond 1.6 μm. Leveraging an optimized QDPD design and a proven process flow [194], we demonstrate WG-QDPDs exhibiting a responsivity of 1.3 A/W at 2.1 μm, a low dark current of 106 nA, and a bandwidth of 1.1 MHz. Moreover, we show that our WG-QDPD exhibits a low noise equivalent power (NEP) of 0.15 pW/$\sqrt{\text{Hz}}$, due to its high responsivity and low dark current, which is attractive for low-noise, weak signal detection. We demonstrate the reliability of the integration approach by realizing a compact on-chip spectrometer that features an array of 8 WG-QDPDs and operates in the spectral window between 2.063 and 2.135 μm. [1]

3.2 QDPDs with wavelength response up to 2.1 µm

Before integrating QDPDs on waveguides, we again optimized the material stack using dummy BI-QDPDs fabricated on glass-ITO substrates [2]. Our approach involved adapting the p-i-n structure developed for 1.3 μm WG-QDPDs to accommodate PbS QDs with a band gap transition at 2.1 μm [194].

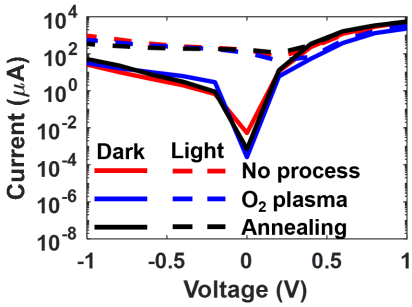

Figure 3.2: Influence of ALD ZnO treatment on the I-V curves of QDPDs. Red: as-deposited ZnO without extra process. Blue: treated with O_2 plasma for 5 min. Black: annealing at 325 °C in air for 30 min. Light curves were measured under optical power of 1.6 mW (peak power density of 1.2 W/cm^2)

3.2.1 Optimization of electron transport layer

ALD ZnO was chosen as the ETL in our initial demonstration of 1.3 μm WG-QDPDs due to its low sheet resistance (approximately 1000 $\Omega/\square$) and minimal optical loss. Its low sheet resistance facilitates horizontal electron transport. However, its performance proved to be unstable. Most QDPDs exhibited poor rectification characteristics and a high dark current. For BI-QDPDs (with a pixel area of 1.77 mm^2) utilizing 1.3 μm QDs as the absorption layer (see Figure 3.1(a)), those employing ALD ZnO as an ETL demonstrated a dark current of 26.5 μA, which is 110 times higher than the dark current observed in QDPDs utilizing sol-gel ZnO (0.24 μA), as depicted in Figure 3.1(b). This increased dark current in QDPDs with ALD ZnO ETL can be attributed to its inferior hole-blocking performance, likely stemming from trap-assisted tunneling [55]. We attempted various strategies to enhance the performance of the ETL. For this optimization, we utilized a BI-QDPD structure, chosen for its straightforward fabrication process, as depicted in Figure 3.1(a). In this optimization process, we selected 1.3 μm QDs as the absorption layer instead of directly using 2.1 μm QDs, leveraging their established performance as a benchmark.

ALD ZnO post-processing

Since earlier published work [56] demonstrated that QDPDs based on ALD ZnO exhibited low dark current density of 0.03 μA/cm^2, high EQE, and improved stability, our initial approach was to enhance the quality of ALD ZnO by post-processing.

ZnO is a semiconductor with a large bandgap of 3.37 eV [195], theoretically resulting in very low conductivity for pure ZnO. However, as-grown ALD ZnO often exhibits strong intrinsic n-type conductivity attributed to defects and impurities within the ZnO crystal lattice. The oxygen vacancy is believed to be one of these defects [196], a hypothesis consistent with our observations: exposure to O_2 plasma or annealing in air reduced the conductivity of ALD ZnO.

We treated ZnO with an O_2 plasma in RIE chamber or annealed it in air at 325 °C, aiming to passivate the defects and reduce the leakage current. However, we did not observe any significant improvement, as depicted in Figure 3.2. Optimizing the ALD ZnO growth conditions could potentially enhance its quality and reduce the leakage current in QDPDs [56], but would demand considerable effort and time from our collaborators and was not further pursued.

Sol-gel ZnO on top of ALD ZnO

Due to the significantly better hole-blocking performance of sol-gel ZnO compared to our ALD ZnO, another potential strategy is to apply a layer of sol-gel ZnO on top of the ALD ZnO. In this configuration, the ALD ZnO serves as a transparent and conductive ETL, while the sol-gel ZnO layer helps reduce the leakage current. Indeed, the QDPD with this combined ETL exhibits similar dark current and optical response compared to the QDPD with sol-gel ZnO alone, as illustrated in Figure 3.3. However, the annealing process required to obtain high-quality sol-gel ZnO compromised the conductivity of the underlying ALD ZnO. As depicted in Table 3.1, after annealing in air, the resistivity of the ALD ZnO layer increased by more than three orders of magnitude (from $1.18 \times 10^{-5}\Omega$·m to $4.47 \times 10^{-2}\Omega$·m). This increase in resistivity suggests that oxygen penetrated the sol-gel ZnO layer and reacted with the ALD ZnO underneath.

Annealing in vacuum can somewhat mitigate the degradation of the conductivity of ALD ZnO, with a resistivity of 3×10^{-3} Ω·m) after annealing, as shown in Table

[1]The content of this chapter has been adapted from the paper: Pang, Chao, et al. "A silicon photonics waveguide-coupled colloidal quantum dot photodiode sensitive beyond 1.6 μm." APL Photonics (2024).

[2]The fabrication of BI-QDPDs was moved to the cleanroom of PRG for faster and more stable iterations.

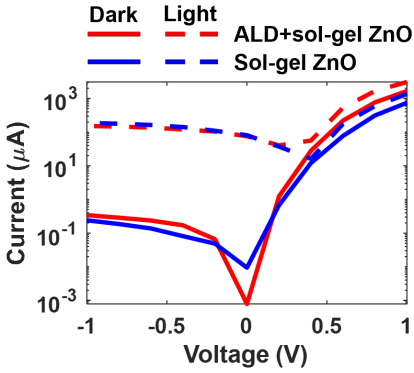

Figure 3.3: Performance of QDPDs with ALD + sol-gel ZnO as the ETL. Red: 40 nm ALD ZnO with 30 nm sol-gel ZnO on top. Blue: 30 nm sol-gel ZnO. Both samples were annealed in air at 325 °C. Light curves were measured under an optical power of 1.6 mW (peak power density of 1.2 W/cm^2).

Condition	Resistivity (Ω·m)
ALD ZnO without annealing	1.18×10^{-5}
ALD ZnO annealing in air	4.15×10^{-2}
ALD + sol-gel ZnO annealing in air	4.47×10^{-2}
ALD + sol-gel ZnO annealing in vacuum	3×10^{-3}
ITO without annealing	2.89×10^{-6}
ITO + sol-gel ZnO annealing in air	3.45×10^{-6}

Table 3.1: Annealing influence on the resistivity of ALD ZnO and ITO. The thickness of ALD ZnO and ITO is 40 nm and 20 nm respectively. All annealing processes were conducted at 325° C for 30 minutes.

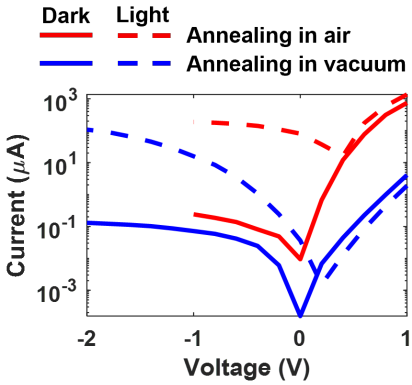

Figure 3.4: Influence of sol-gel ZnO annealing atmosphere on the performance of QDPDs. Red: sol-gel ZnO annealed in air. Blue: sol-gel ZnO annealed in vacuum. Both samples had a sol-gel ZnO layer of 30 nm, annealed at 325 °C for 30 min. Light curves were measured under an optical power of 1.6 mW (peak power density of 1.2 W/cm^2).

3.1. This resistivity will introduce a series resistance in the order of ten kilohms for WG-QDPDs, which is acceptable for the μA-level saturation photocurrent (A 10 kΩ series resistance results in a voltage drop of only 0.01 V for a photocurrent of 1 μA). However, the electrical properties of sol-gel ZnO deteriorate under such annealing conditions. As shown in Figure 3.4, the dark current in the forward bias decreases by two orders of magnitude compared to the QDPD with sol-gel ZnO annealed in air, indicating an increase in the device's series resistance. These inferior electrical properties make it challenging to extract the light-generated carriers effectively.

Sol-gel ZnO on top of sputtered ITO

Despite our extensive efforts to enhance the performance of QDPDs based on an ALD ZnO ETL, the results remained unsatisfactory. Consequently, we shifted our focus to using sputtered ITO as a transparent bottom electrode and sol-gel ZnO as both an ETL and HBL for WG-QDPD.

Before transitioning to sputtered ITO, we conducted a thorough assessment of its absorption, conductivity and stability.

For characterization of the absorption, we deposited 20 nm of ITO onto waveguides, then patterned it into various lengths and measured the propagation loss. Around 1.3 μm, the absorption of ITO is not strong. When directly deposited onto SiN waveguides with dimensions of 3 μm width and 300 nm height (Figure 3.5(a)), the propagation loss was approximately 55 dB/cm, as depicted in Figure 3.5(c). For the

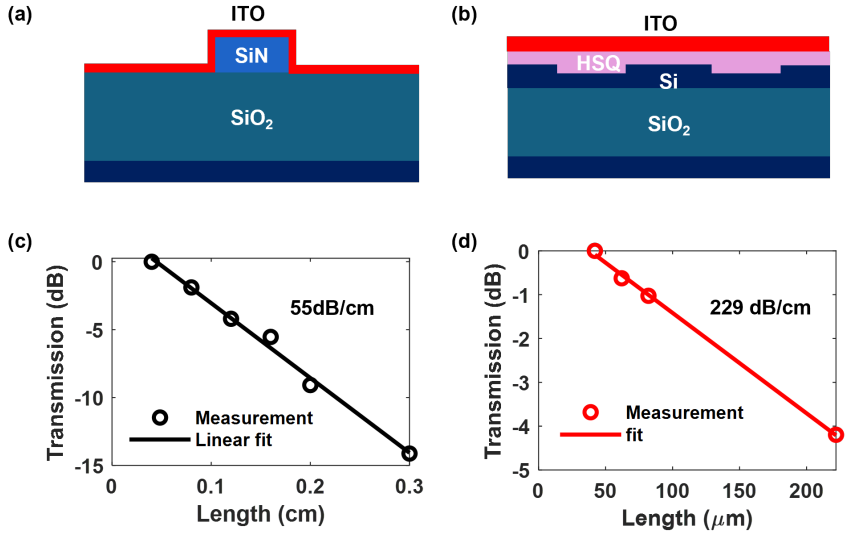

Figure 3.5: ITO induced waveguide loss. (a) Waveguide structure used for absorption measurement at 1.3 μm. 20 nm ITO was sputtered on 300 nm by 3 μm waveguides and patterned into different lengths with wet etching. (b) Waveguide structure used for absorption measurement at 2.1 μm. The waveguides consist of a 30 μm-wide core with 70 nm shallow etch on 220 nm Si and a 45 nm thick HSQ cladding. 20 nm ITO was sputtered on top. (c) Propagation loss measured at 1.3 μm on structure (a). (d) Propagation loss measured at 2.1 μm on structure (b)

WG-QDPD with a 350 nm HSQ cladding, as utilized in our first-generation 1.3 μm WG-QDPDs, its loss is estimated to be only 3.2 dB/cm (simulated with Lumerical FDE solver based on the measured 55 dB/cm propagation loss).

At 2.1 μm, the absorption of ITO is more pronounced. For 70 nm shallow-etched waveguides with a top cladding of 45 nm (Figure 3.5(b)), the propagation loss introduced by 20 nm ITO is approximately 229 dB/cm (see Figure 3.5(d)). However, considering that the absorption of QDs is several times stronger than that of ITO, the presence of ITO will only marginally decrease the EQE of our WG-QDPDs.

In terms of electrical performance, ITO demonstrates higher conductivity, with a measured resistivity of 2.89×10^{-6} Ω·m, which is four times better than ALD ZnO. A 20 nm thick layer of ITO will introduce less than 50 Ω of extra resistance to the WG-QDPD, which meets our requirements. Additionally, ITO exhibits much more stable electrical conductivity. After annealing in air, the resistivity shows only a small increase, as shown in Table 3.1.

Given the significantly improved electrical stability, we decided to transition from ALD ZnO to a combination of ITO and sol-gel ZnO as the ETL in WG-QDPDs.

Sol-gel ZnO annealing temperature

The annealing temperature of sol-gel ZnO significantly influences the performance of QDPDs. Annealing at a low temperature of 250°C results in reduced optical response, as illustrated in Figure 3.6(a) and (b). Upon examining the I-V curve under dark conditions, we observed a lower current at forward bias, likely due to the high series resistance induced by an inferior carrier transport capability. Increasing the annealing temperature to 325°C markedly improves both the dark I-V rectification and the optical response.

Further increasing the annealing temperature marginally enhances the optical response; however, the dark current increases significantly, as depicted in Figure 3.6(a). This notable increase in dark current is attributed to the formation of leakage paths not present when annealing at 325°C, as shown in Figure 3.6(c) and (d). These leakage paths result from the random peeling of QDs, leading to short paths after Au p-contact evaporation.

Although we did not observe any surface morphology changes under the microscope after ZnO annealing at 370°C, we speculate that annealing at high temperatures begins to alter the adhesion between ZnO and QDs, causing local peeling of the QDs. In summary, for sol-gel ZnO formation, we identified 325°C as the optimized temperature for our fabrication process.

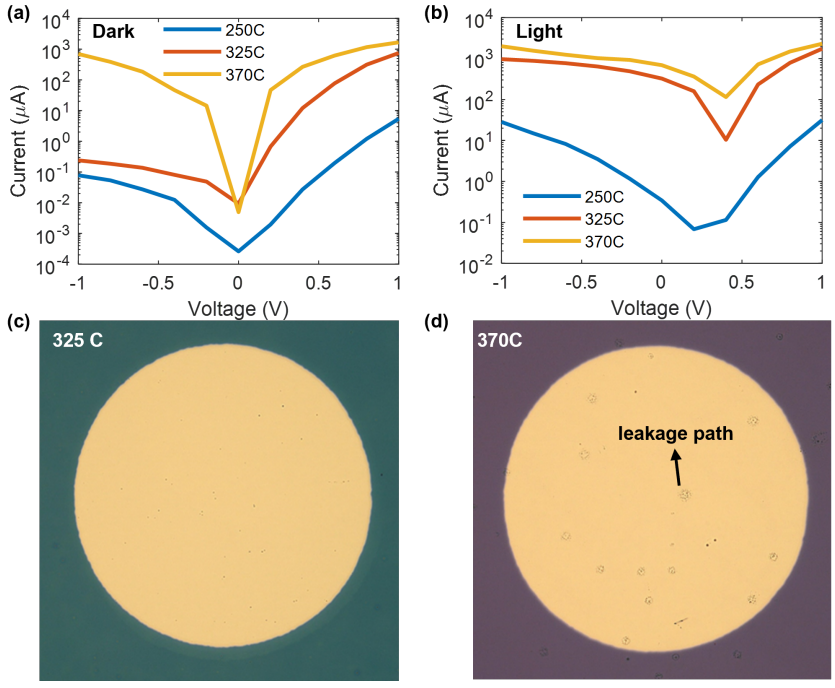

Figure 3.6: The influence of annealing temperature on the performance of QDPDs. (a) and (b) I-V curves under dark and light conditions respectively, annealed in air for 30 min at different temperatures. (c) and (d) microscope images of QDPDs annealing at 325 °C and 370 °C.

3.2.2 Optimization of QDPD stack for 2.1 µm

All PbS QDs were synthesized [3] by reacting lead oleate with a substituted thiourea, where different QD sizes were obtained by using differently substituted thioureas in agreement with the literature [197]. The absorption spectrum of QDs in n-octane is shown in Figure 3.7 The resulting PbS QDs have a surface terminated by lead oleate. More details on the synthesis of these QDs can be found in Appendix A.

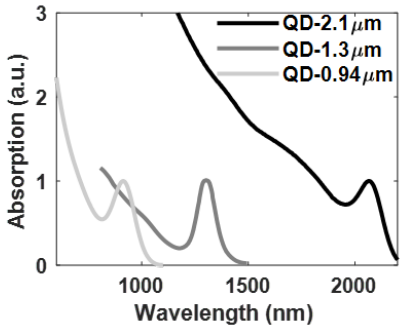

Figure 3.7: Absorption spectra for three types of QD inks (dispersed in n-octane) used in QPDDs.

As shown in Figure 3.8 (a), we constructed QDPD stacks consisting of a 100 nm thick ITO transparent bottom electrode, a 30 nm thick sol-gel ZnO film functioning as an electron transport and hole blocking layer, a multilayer QD stack, and an Au top electrode. Within the QD film, the photosensitive layer consisted of QDs with a band-gap transition at 2.1 μm (see Figure 3.7). In the first design (Structure A in Figure 3.8 (a)), this film—formed by spin coating—was exposed to a methanol solution containing 10 mg/mL TBAI for 30 s. This process removes as-synthesized surface ligands, thereby turning the QD film n-type and enhancing the electron mobility. In contrast to the solution-phase ligand exchange method employed in Chapter 2, we opt for solid-phase ligand exchange for the absorption layer here, motivated by its straightforward fabrication process and reproducibility. As the hole transport and electron blocking layer, we employed a film of PbS QDs featuring a 0.94 μm band-gap transition. This film was similarly exposed to a 0.01 vol% EDT in methanol solution, which leads to p-type doping [5, 198], and a gold contact was evaporated on top.

However, as shown in Figure 3.8 (b) (red line), this stack showed little rectification and a dark current density of nearly 10 mA/cm^2 at -2 V reverse bias, which is more than two orders higher than QDPDs using PbS QDs with a 1.3 μm bandgap

[3] PbS QDs were synthesized by Ezat Kheradmand from PCN group.

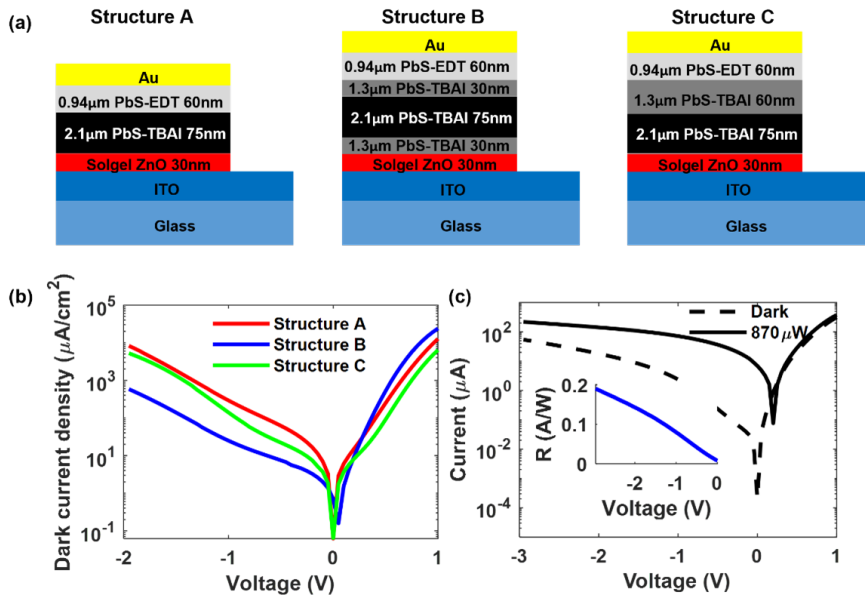

Figure 3.8: Structure and Characterization of QDPD. (a) Vertical QDPD structures with surface illumination. (b) Influence of the interface layer on dark current density. (c) Dark current and photocurrent of Structure B QDPD, with an area of 1.77 mm^2. The photocurrent was measured with a 2.1 µm laser Gaussian beam illuminated from the bottom glass side, with a peak power density of 220 mW/cm^2. Inset: responsivity of QDPD vs. bias voltage.

transition as photosensitive layers (see Figure 3.9). In an attempt to reduce the dark current, we explored two additional QDPD stacks: one in which the film of 2.1 μm PbS QDs was sandwiched between layers of 1.3 μm PbS QDs, which we also treated using TBAI, and a second where the 1.3 μm PbS QDs were only included between the 2.1 and 0.94 μm PbS QD films (see Structure B and C in Figure 3.8 (a)). Interestingly, Structure B showed strongly enhanced rectification and a 10-fold reduction of the dark current compared to the initial stack, while Structure C only featured a minor reduction of the dark current. This difference indicates that the primary source of dark current is the leakage of charge carriers between the 2.1 μm PbS QDs and the ZnO contact, possibly assisted through trap states at the ZnO surface [55], for which the 1.3 μm PbS QD film provides an additional barrier.

The optimized QDPD with Structure B was characterized using a 2.1 μm laser with a power of 870 μW and a peak power density of 220 mW/cm^2, employing a similar setup as that used in Figure 2.2. Under a -3 V bias, the QDPD shows a dark current of 50.3 µA (dark current density of 2.8 mA/cm² for a device area of 1.77 mm2) and a responsivity of 0.19 A/W (EQE of 11.2%), as illustrated in Figure 3.8 (c). This relatively low EQE probably reflects the limited absorption of the vertically incident

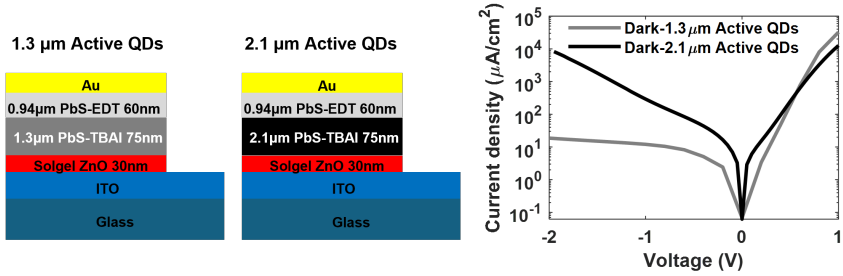

Figure 3.9: Structure and dark I-V curves of QDPD with 1.3 μm and 2.1 μm PbS active layers.

light in the thin layer of 2.1 μm PbS QDs, and the relatively low transmittance of ITO at 2.1 μm [2]. The 1.3 μm PbS-TBAI layer between the 2.1 μm PbS-TBAI and PbS-EDT layers should be n-doped [5], posing challenges for hole transport and potentially leading to an increase in the series resistance of the QDPD. However, the I-V characteristics at forward bias did not show degradation compared to Structure A (Figure 3.8 (b)). Possibly, this layer is turned p-type during the subsequent EDT ligand exchange process for the 0.94 μm PbS QD layer on top. EDT, known for its high reactivity compared to TBAI [199], can soak the 1.3 μm PbS-TBAI layer underneath, resulting in a change of doping to p-type. To validate this hypothesis, QDPDs with Structure B were fabricated, but the ligand exchange of the top 1.3 μm PbS QDs was altered to EDT instead of TBAI. QDPDs with either TBAI or EDT ligand exchange on the 1.3 μm QDs exhibited nearly identical dark and light I-V characteristics (see Figure 3.10), thus confirming our above assumption. The spectral response of the QDPD with structure B was measured by sweeping the laser wavelength, showing photo response extending up to 2.2 µm (Figure 3.11), consistent with the absorption spectrum of the QDs.

3.3 Integration of QDPDs on waveguides

Figure 3.12(a)-(e) depicts the process flow used to integrate the QDPD on waveguides. The integration process of 2.1 μm QDPD on waveguides is developed based on the 1.3 μm WG-QDPD on SiN, as shown in Section 2.4. The optimized process shows improved stability and yield. The main optimization is to replace ALD ZnO with ITO and sol-gel ZnO.

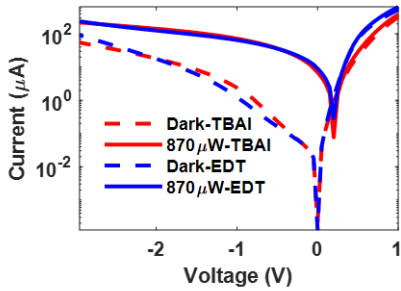

Figure 3.10: Dark current and photocurrent of QDPD with an area of 1.77 mm^2. The photocurrent was measured with a 2.1 µm laser with a Gaussian beam illuminating the sample from the bottom glass side, with a peak power density of 220 mW/cm^2. Red: ZnO / 1.3 µm-PbS-TBAI / 2.1 µm-PbS-TBAI / 1.3 µm-PbS-TBAI / 0.94 µm-PbS-EDT. Blue: ZnO / 1.3 µm-PbS-TBAI / 2.1 µm-PbS-TBAI / 1.3 µm-PbS-EDT / 0.94 µm-PbS-EDT.

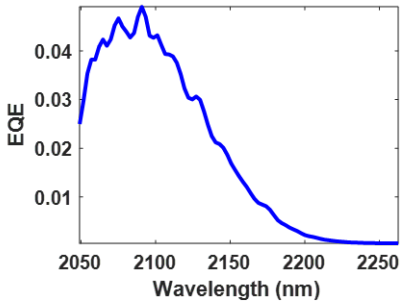

Figure 3.11: Spectral response of the QDPD with structure B, measured at a bias of -1 V and a peak power density of 220 mW/cm^2.

Passive waveguides

The waveguides were patterned with EBL and dry etching. We used standard SOI substrates with 220 nm Si on top of 2 μm buried oxide in this work. A 400 nm layer of ARP6200.13 e-beam resist was used as a mask, exposed by EBL (Voyager Raith 50 kV) with a dose of 160 μC/cm^2 and developed in n-amyl acetate for 60 s. The resist pattern was transferred to Si by reactive ion etching (ICP-RIE, Oxford Instruments) using SF_6 and CHF_3 chemistry. A 70 nm shallow etch in Si was used to define the optical structures. To alleviate the power saturation problem of WG-QDPDs, as observed in previous demonstrations in Chapter 2, we defined 30 µm wide waveguides. As before, this adjustment serves to lower the optical power density in the QD film.

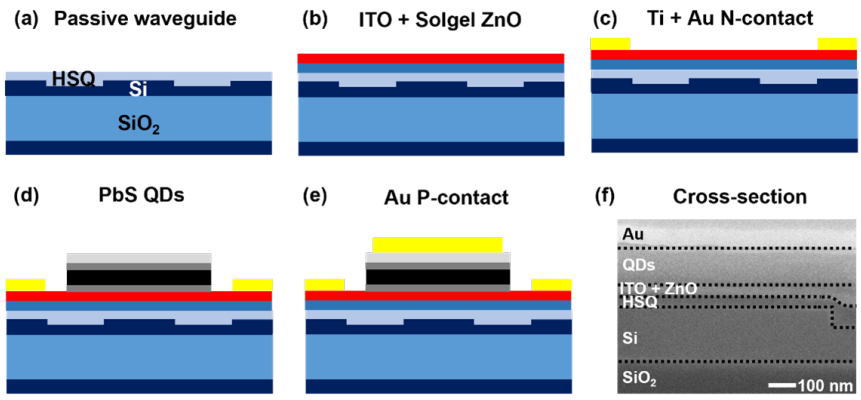

Figure 3.12: Integration steps to fabricate WG-QDPD. (a) Si rib waveguide patterning and planarization. (b) ITO sputtering and patterning with wet etching, followed by ZnO deposition with sol-gel method and patterning with wet etching. (c) N-contact metal patterning with liftoff. (d) QD film patterning with PMMA resist and liftoff. (e) P-contact metal patterning with PMMA resist and liftoff. (f) Cross-section of fabricated WG-QDPD.

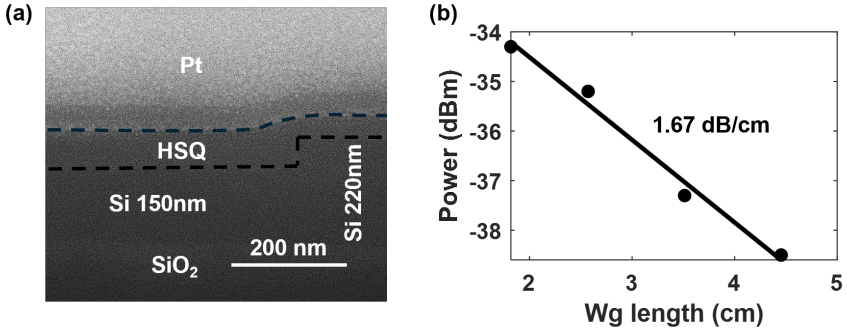

Figure 3.13: HSQ as a low loss cladding layer for planarization. (a) Cross-section. (b) Transmitted power of spiral waveguides with varying lengths, with a waveguide width of 1.6 μm.

We used HSQ as a transparent top cladding layer for planarization of the waveguides. Diluted HSQ (HSQ : MIBK = 1:4) was spun with a speed of 4000 rpm and an acceleration of 1000 rpm/s, followed by annealing at 400 °C for 2 hours in a nitrogen atmosphere, achieving a cladding thickness of approximately 45 nm on the waveguides. The step at the waveguide edge decreased from 70 nm to around 35 nm, with a smooth slope, as shown in Figure 3.13(a). In addition, HSQ exhibited negligible absorption. The propagation loss, measured using spiral waveguides with a width of 1.6 μm, is 1.67 dB/cm at 2.1 μm, as depicted in Figure 3.13(b).

ITO patterning

The QDPD stack was then integrated on top of the planarized waveguides, starting with sputtering of an 18 nm thick ITO layer as the bottom electrode. ITO demonstrates acceptable optical absorption at 2.1 μm. Adding an 18 nm ITO layer on top of the planarized waveguides increased the waveguide loss to around 0.02 dB/μm, as depicted in Figure 3.19(b). The layer thickness was reduced compared to the dummy BI-QDPD structure (100 nm) to minimize optical losses in the ITO and maximize light absorption in the PbS QD film. To further mitigate optical loss, the ITO layer was confined to the designated area for photodetection using HCl-based wet etching. Specifically, the ITO film was patterned using photolithography (AZ5214 E in positive mode, standard recipe) and wet etching (37% HCl:H_2O=1:5, 15s). Here, we avoided the use of adhesion promoter Ti prime for a cleaner electrical interface. After ITO patterning, the sample was cleaned with acetone and IPA, followed by O_2 plasma (PVA TePla 600) for 1 min.

ZnO patterning

A 30 nm layer of ZnO was formed on top of the ITO layer via spin-coating a precursor solution and annealing at 325 °C for 30 minutes in ambient air, consistent with our process for the BI-QDPDs. Subsequently, the ZnO film was patterned using photolithography (AZ5214 E in positive mode, following the standard recipe) and wet etching (37% HCl:H_2O = 1:1000, 5s). Once again, we avoided the use of the adhesion promoter Ti prime for a cleaner electrical interface. Sol-gel ZnO exhibits favorable optical transparency around 2.1 μm, as depicted in Figure 3.19(b).

Complete coverage of ITO with ZnO is crucial to prevent direct contact between ITO and the subsequently deposited QD film, as this could lead to a significant leakage current.We initially tested the integration process using 1300 nm QDPDs integrated on SiN waveguides. In our initial fabrication attempt, the ZnO layer did not fully cover the ITO, resulting in direct contact between ITO and the QD film, as depicted in Figure 3.14(b). This contact led to a significant leakage current. The dark current of the WG-QDPD with the ITO/QD leakage path, illustrated in Figure 3.14(a), measures 25.4 nA at a -1 V bias, approximately 70 times greater than that of the WG-QDPD without a leakage path (0.36 nA). This difference becomes even more pronounced with increased bias (157 nA vs. 0.48 nA @ -2V). The absence of ZnO results in hole injection from the n-contact electrode into the QDPD, causing the QDPD to function as a photoconductor.

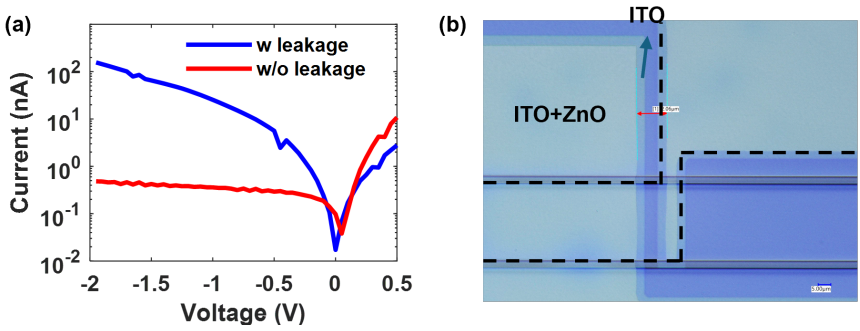

Figure 3.14: Leakage current from ITO/QD contact. (a) Dark current of 1300 nm WG-QDPDs with and without ITO/QD leakage path. (b) Image of WG-QDPD design that will lead to an ITO/QD leakage path. The dashed line indicates the area where QDs and Au will be integrated in the following steps.

n-contact patterning

The N-contact was patterned using photolithography and the liftoff method. The desired pattern was generated using AZ5214 E photoresist (standard recipe for image reversal), followed by metal evaporation with a composition of 20 nm Ti and 100 nm Au. The sacrificial photoresist and the metal layer on top were removed by immersing the sample in acetone for 1 hour.

QD patterning

The same QD stacks with Structure B, as we used in the BI-QDPD, were deposited layer by layer and lifted off simultaneously to achieve the desired pattern. The resist patterning and liftoff method employed are consistent with those outlined in Section 2.4.5.

P-contact patterning

The p-contact pads were formed by depositing 80 nm of Au on top of the QD stack through thermal evaporation and lift-off, following the procedure outlined in Section 2.4.6.

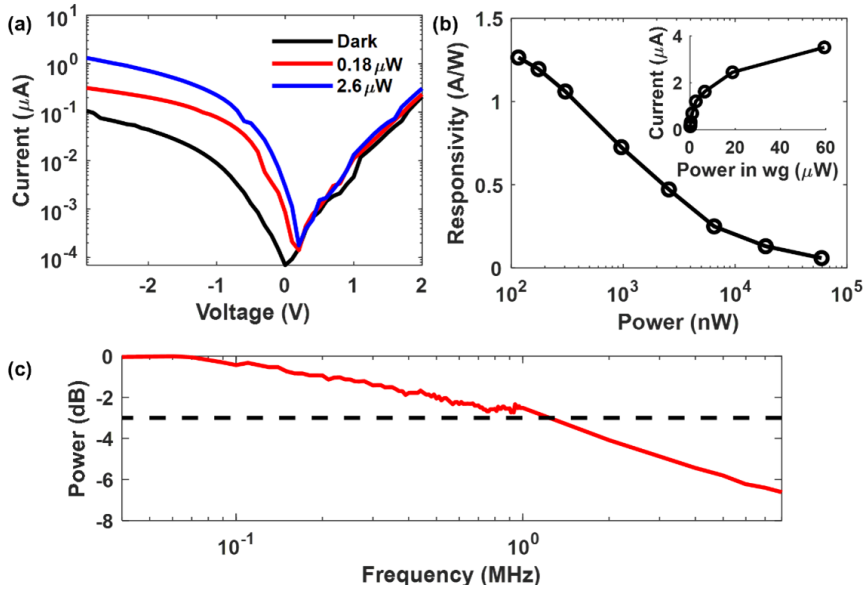

Figure 3.15: Response of WG-QDPDs. (a) I-V curves of WG-QDPDs under dark condition and illumination at 2.1 µm. (b) Responsivity vs. optical power at -3 V bias voltage. Inset: photo-current vs. optical power. (c) Bandwidth of the integrated WG-QDPD.

3.4 Characterization of WG-QDPDs

We characterized the DC performance of the WG-QDPDs using a 2.1 μm laser (Cr^{2+}:ZnS laser, IPG Photonics), employing grating couplers for convenient light coupling into and out of the waveguide, and a source measure unit (Keithley 2400). The optical power in the waveguide was calibrated by measuring the coupling efficiency of the grating coupler for a reference waveguide without QDPDs. The WG-QDPD showed a dark current of 106 nA at -3 V, as illustrated in Figure 3.15 (a). Considering a WG-QDPD width of 30 μm and a length of 200 μm, the dark current density (1.8 mA/cm^2) is in line with the measurements obtained on the BI-QDPDs (2.8 mA/cm^2), indicating that the integration process does not introduce spurious leakage paths. The responsivity reaches 1.3 A/W (EQE of 74.8%) at an optical power of 116 nW, as shown in Figure 3.15 (b). The significantly higher EQE compared to BI-QDPDs is attributed to increased absorption during propagation within the waveguides. For WG-QDPDs, the Si and QD stack constitute the hybrid waveguide designed for the propagation of the fundamental TE mode. Light is absorbed via the evanescent tail of the optical mode during its propagation, as depicted in Figure 3.16. In contrast to surface-illuminated QDPDs, which require a thick QD absorption layer for efficient light absorption, the extended absorption

path of guided light in WG-QDPDs ensures efficient absorption even with a thin layer of QDs. The combination of low dark current and high responsivity leads to a low estimated noise equivalent power (NEP=$\sqrt{2I_{\text{dark}}q}/R$, where q is the elementary charge, and R is the responsivity) of 0.15 pW/$\sqrt{\text{Hz}}$, indicating that WG-QDPDs are well-suited for weak signal detection. The photocurrent exhibits nonlinear growth with optical power, a phenomenon attributed to QDPD saturation due to high series resistance, as observed in prior studies [194].

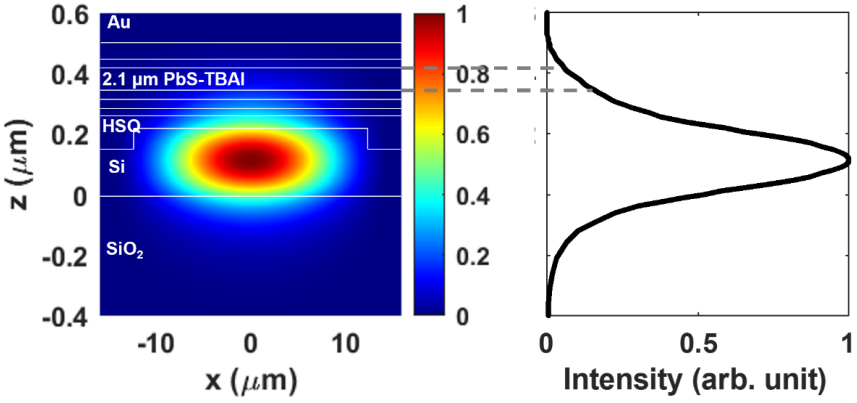

Figure 3.16: Intensity profile of the fundamental TE mode in the WG-QDPD. The cross-section at position x=0 is shown in the right figure. Light is absorbed through the evanescent tail of the optical mode extended into the 2.1 μm QD film.

For AC measurements, the setup, as illustrated in Figure 3.17, involved a 1.55 μm laser (Santec 510) that was modulated by a Mach-Zehnder Electro-optical Modulator (EOM). The EOM was adjusted to its linear operation point, where the applied radio frequency signals (SMT03, Rohde & Schwarz) were converted to optical intensity modulation. The modulated optical signals were amplified by an Erbium-doped Fiber Amplifier (EDFA) and then coupled to the WG-QDPD through edge coupling. Polarization Controllers (PCs) were employed before the EOM and our chip to achieve the desired polarization. A DC bias was applied to the WG-QDPD using a source measure unit (Keithley 2400). The photodetector signal was collected by an electrical spectrum analyzer (ESA, FSP, Rohde & Schwarz). Both the DC bias and ESA were connected to the WG-QDPD with a bias tee. The speed of our WG-QDPD was not characterized using a 2.1 μm laser due to the lack of a high-speed optical modulator operating at this wavelength in our lab. However, since absorption only occurs in the 2.1 μm PbS QD layer for both 1.55 μm and 2.1 μm wavelengths, the bandwidth is expected to be similar at both wavelengths.

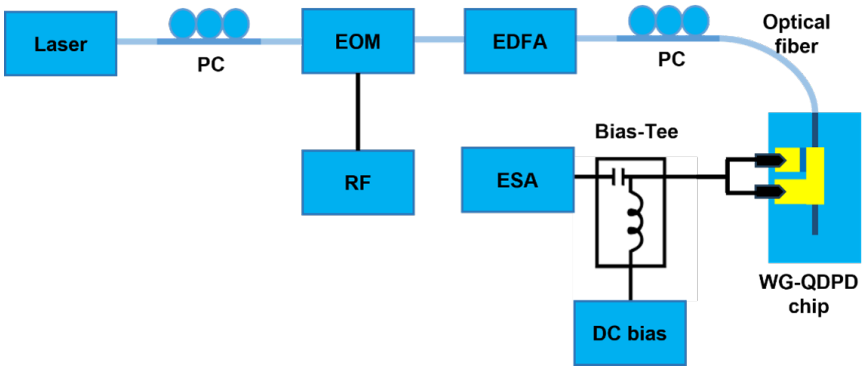

Figure 3.17: Setup schematics used for bandwidth measurement. PC: polarization controller, EOM: electro-optical modulator, EDFA: Erbium-doped fiber amplifier, RF: radio-frequency source, ESA: electrical spectrum analyzer.

The fabricated WG-QDPD exhibits a bandwidth of 1.1 MHz, as shown in Figure 3.15 (c). Under large reverse bias of -3V, the thin QD absorption layer can be considered completely depleted [200]. Therefore, the response time (τ_{res}) of the photodetector is determined by the drift progress (τ_{drift}) and the resistance-capacitance constant (τ_{RC}) of the electrical circuit $\tau_{res} = \sqrt{\tau_{drift}^2 + (2.2\tau_{RC})^2}$. [201] The drift time τ_{drift} is governed by the carrier mobility (μ) and the voltage drop (V) across the depleted film thickness (d), with $\tau_{drift} = d^2/(\mu V)$. The other term, $\tau_{RC} = RC$, where R represents the series resistance and C denotes the capacitance. For a fully depleted QDPD, we estimate the series resistance R using the access resistance (ITO sheet resistance and contact resistance between n-contact and ZnO), measured to be approximately 100 Ω for our WG-QDPDs. The capacitance C is estimated to be around 4.1 pF ($C = (\epsilon_0 \epsilon_r A)/d$, where ϵ_0 represents the vacuum permittivity, $\epsilon_r = 15.5$ denotes the dielectric constant of the PbS-QD film [200], A = 6000 μm^2 is the area of QDPD and d = 195 nm is the thickness of the PbS QD film). The estimated τ_{RC} is 0.41 ns, corresponding to a BW of 388 MHz using the relationship: BW = 0.35/τ_{res} [201]. Considering a measured BW of 1.1 MHz, the speed of our WG-QDPD is likely drift-limited. Furthermore, we measured the BW of WG-QDPDs with areas of 6000 μm^2 and 600 μm^2 and both exhibited similar bandwidths (Figure 3.18). Also this area-insensitive BW does not match the scenario where τ_{RC} dominates the speed of QDPDs [57, 200], considering a consistent series resistance and area-related capacitance. This drift-limit speed can be further supported by examining τ_{drift}. The carrier mobility of the 2.1 μm PbS-TBAI absorption layer, extracted via field effect transistor (FET) measurements [200], is $(0.94 \pm 0.6) \times 10^{-4}$ cm^{2}V^{-1}s^{-1} for electrons and $(1.41 \pm 0.35) \times 10^{-4}$ cm^{2}V^{-1}s^{-1} for holes. Considering a thickness of 75 nm for

the absorption layer and a voltage drop of 3 V, the estimated τ_{drift} is around 0.2 µs, corresponding to a bandwidth of 1.75 MHz. The carrier transition time in the 1.3 μm PbS-TBAI and 0.94 μm PbS-EDT layers is disregarded due to the significantly faster carrier mobilities exceeding 1×10^{-3} $cm^2V^{-1}s^{-1}$ in both layers [200]. Although the bandwidth of our demonstrated WG-QDPDs may not be as high as that of III-V photodiodes, it meets the requirements of many sensing applications. Further improvement on the speed of the WG-QDPD relies on improved ligand exchange strategies to boost the mobility of the 2.1 μm PbS QD layer. Reducing the thickness of the QD film can also decrease τ_{drift}. This strategy was recently adopted to achieve QDPDs with a response time of 4 ns [200].

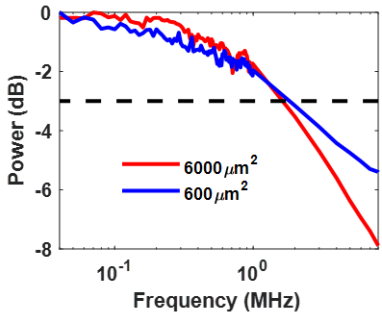

Figure 3.18: Bandwidth of WG-QDPDs with different areas. WG-QDPDs, with a dimension of 30 μm × 200 μm and 3 μm × 200 μm, were measured under a reverse bias of -5 V.

On the same chip, we incorporated WG-QDPDs with varying lengths, as shown in Figure 3.19(a). We conducted transmission measurements on the waveguides after patterning each material. These measurements allowed us to ascertain the optical loss induced by each material, as shown in Figure 3.19(b). The ITO layer introduced an optical loss of around 0.02 dB/μm, resulting from strong free carrier absorption in the infrared [202]. The addition of the ZnO layer did not introduce measurable extra absorption. The entire QDPD stack raised the optical loss to 0.08 dB/μm, indicating the absorption is dominated by the QD film. This strong absorption competes with the absorption from the ITO bottom electrode, ensuring high responsivity of our WG-QDPDs. The dark current of these WG-QDPDs is proportional to the area, with a slope of 1.8 mA/cm^2, as shown in Figure 3.19(c). The responsivity of WG-QDPDs, measured at -3 V bias and 400 nW optical power, shows a saturation behavior with respect to PD length, as shown in Figure 3.19(d). The saturation behavior aligns with the prediction from optical loss measurements, as indicated by the blue dashed line in Figure 3.19(d).

We also investigated WG-QDPDs with different shapes as shown in Figure 3.20(a). As we mentioned before, the waveguide width is extended to 30 μm to alleviate the

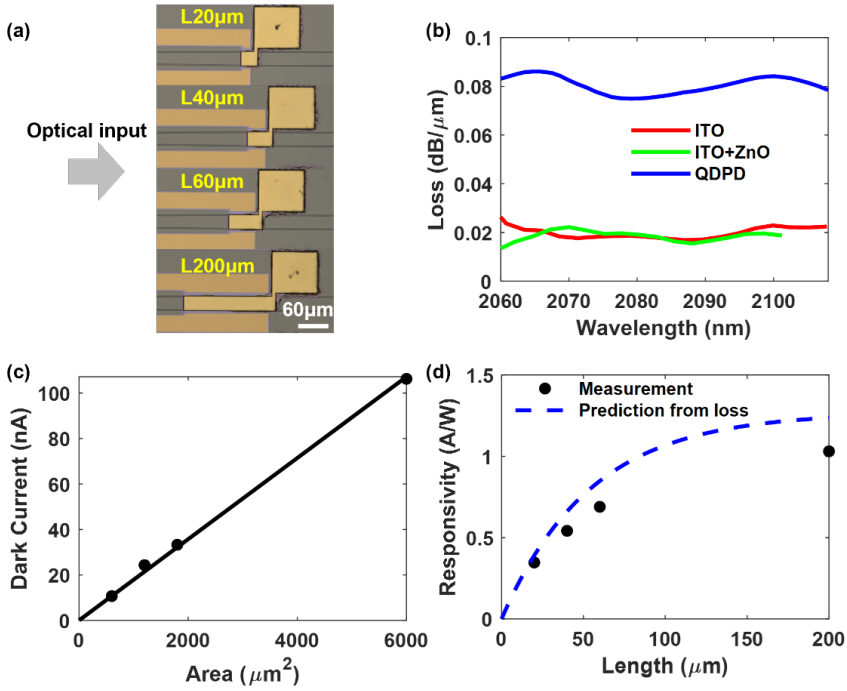

Figure 3.19: Performance of WG-QDPDs with different lengths. (a) Top view of WG-QDPDs. (b) Optical absorption resulting from materials integrated onto waveguides. Measurements were obtained through optical transmission, with varying lengths for each material. (c) Darck current of devices with different area. (d) Responsivity of WG-QDPDs with different lengths. The predicted relationship between responsivity and length is presented by a dashed blue line, derived from optical loss measurements shown in (b)

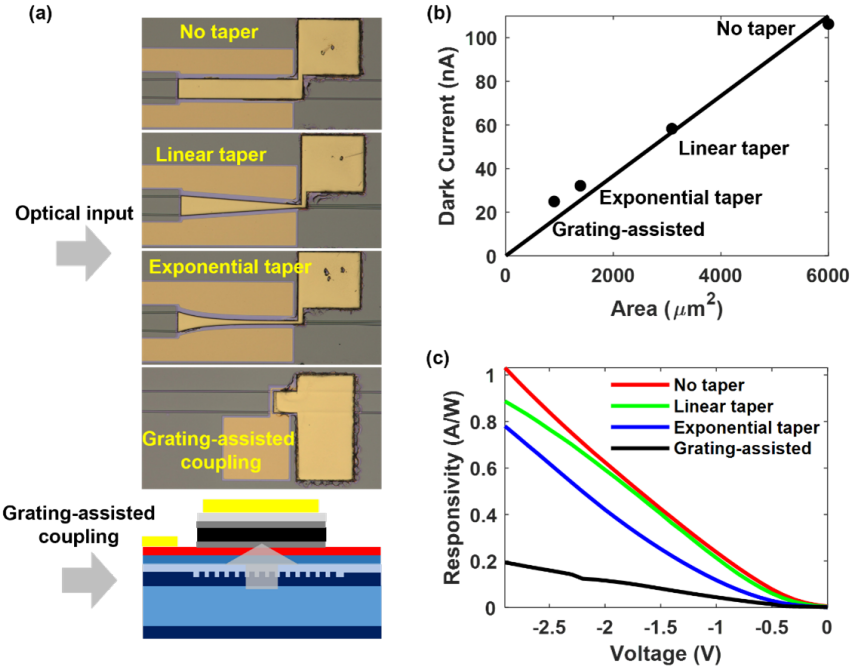

Figure 3.20: Performance of WG-QDPDs with different shapes. (a) Top view of WG-QDPDs. Light is coupled into waveguides from the left side. (b) Dark current of different WG-QDPDs. (c) Responsivity of different WG-QDPDs.

optical power saturation, ensuring an efficient responsivity. However, this strategy also increases dark current due to the larger WG-QDPD area. Consequently, the NEP exhibits a trade-off between responsivity and dark current. Notably, heavy optical power saturation predominantly occurs in the initial section of the WG-QDPD. As light propagates within the waveguides, the optical power decreases exponentially. This insight allows us to narrow down the waveguide width at the far end without introducing significant power saturation. In our design, we implemented waveguide narrowing from 30 μm to 0.9 μm using both linear and exponential tapers, while keeping a consistent length of 200 μm. For the exponential taper, the width decreases at a rate of 0.023 μm^{-1} (0.1 dB/μm), similar to the optical absorption measurement in Figure 3.20(b). The QDPD follows the same shape as these tapered waveguides. The intensity profiles of both tapered WG-QDPDs are shown in Figure 3.21. The light remains stronger at the input side for both taper shapes, indicating the QD absorption-induced optical intensity drop is still stronger than the taper-induced light concentration. The rapid decrease in waveguide width in the exponential tapered WG-QDPD leads to multimode interference in the waveguide but should not cause a significant change in photoresponse.

The linear taper reduces the WG-QDPD area to approximately 1/2, and the exponential taper further decreases the area to around 1/3. Consequently, the decrease in area reduces the dark current to 1/2 and 1/3, respectively, as shown in Figure 3.20(b). As expected, the responsivity of the tapered devices does not degrade significantly, as shown in Figure 3.20(c). This results in a champion NEP of 0.13 pW/$\sqrt{\text{Hz}}$ for the exponentially tapered WG-QDPD, representing a 30% improvement compared to the NEP of the uniform WG-QDPD (0.18 pW/$\sqrt{\text{Hz}}$). Notably, there is an underestimation of the NEP here. The measurements were conducted at a relatively high optical power of 400 nW, which, combined with the nonlinear response to optical power, results in an underestimated responsivity.

In addition, we fabricated a grating-assisted QDPD, where light injected from the left side was scattered vertically and absorbed by the QDPD, as shown in Figure 3.20(a). This configuration yielded the lowest dark current due to the smallest QDPD size of 30 μm by 30 μm. However, the responsivity was significantly lower compared to the evanescent coupling scheme, as shown in Figure 3.20(c). The degradation in responsivity is attributed to a combined effect of upwards coupling efficiency, incomplete optical absorption in the thin QDs layer, and possibly stronger power saturation.

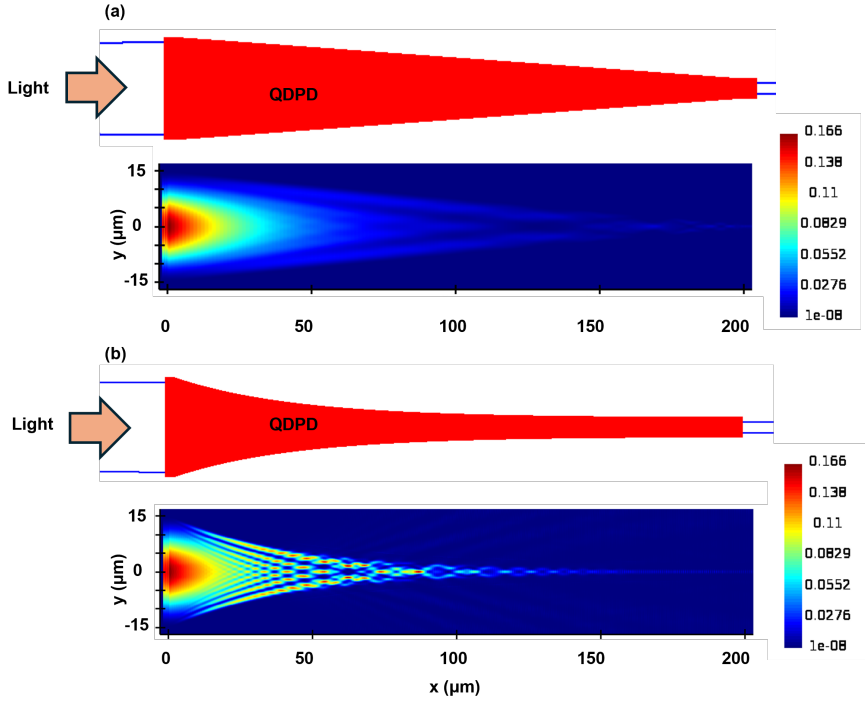

Figure 3.21: Simulated light propagation (E^2) in tapered WG-QDPD. (a) Linear taper. (b) Exponential taper. Both tapers have a starting width of 30 µm and a ending width of 0.9 µm. Exponential taper follows a decreasing rate of 0.023 μm^{-1}.

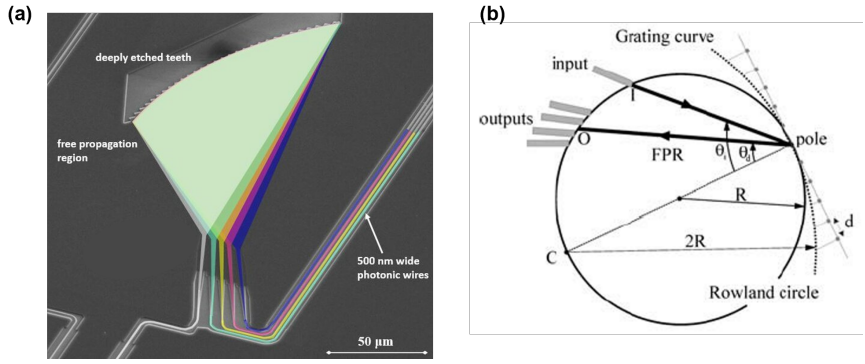

Figure 3.22: Principle of the PCG. (a) Schematic, reproduced from [12]. (b) Operational diagram, reproduced from [13].

3.5 Demonstration of a 2.1 µm spectrometer

To demonstrate the capabilities of our proposed WG-QDPD integration approach, we combined a WG-QDPD array with an eight-channel PCG to form a compact spectrometer.

3.5.1 Basic operation of the PCG

A concave grating, is a type of diffraction grating where the grooves are curved inwards, forming a concave surface. Unlike traditional plane or blazed gratings, which have flat surfaces, concave gratings use a curved surface to disperse light. This curvature allows the grating to focus light of different wavelengths to different focal points, similar to how a concave lens focuses light, as shown in Figure 3.22(a).

The most widely used configuration of the concave grating is based on the Rowland mounting, for reduced aberration during the imaging, as shown in Figure 3.22(b). In this configuration, The input and output waveguides are arranged along a circular path with a radius R, known as the Rowland circle. Conversely, the grating facets are positioned along a separate circular path with a radius of 2R, referred to as the grating circle. These two circles intersect at the center of the grating, termed the pole.

The light from the input aperture on the Rowland circle will be imaged to the output aperture on the same circle when the reflections from all facets are synchronized in phase (grating equation):

$$d \cdot n_{eff}(\sin\theta_{in} + \sin\theta_d) = m\lambda \tag{3.1}$$

where n_{eff} is the effective refractive index of the slab waveguide in the free propagation region, and m is the diffraction order. θ_{in} and θ_d are the angles of input and diffracted beam, respectively, as shown in Figure 3.22(b).

From the grating equation 3.1, the FSR of the PCG λ_{FSR} can be approximately expressed as:

$$\begin{aligned} \lambda_{FSR} &= \frac{\lambda}{m}\frac{n_{eff}}{n_g} \\ &= \frac{\lambda^2}{n_g d(\sin\theta_{in} + \sin\theta_d)} \end{aligned} \tag{3.2}$$

where n_g is the group refractive index of the slab waveguide.

Differentiating the grating equation yields the grating angular dispersion:

$$\begin{aligned} \frac{\mathrm{d}\theta_d}{\mathrm{d}\lambda} &= \frac{1}{\cos\theta_d}\frac{m}{d}\frac{n_g}{n_{eff}^2} \\ &= \frac{\lambda}{\lambda_{FSR} n_{neff} d\cos\theta_d} \end{aligned} \tag{3.3}$$

3.5.2 Integrated spectrometer

The WG-QDPD array was integrated with an eight-channel PCG, as illustrated in Figure 3.23(a). The PCG, designed using IPKISS [159], features a central wavelength of 2.1 μm and a wavelength range of approximately 70 nm. Fabrication was conducted on the same 220 nm SOI chip as the previously mentioned components. To streamline the fabrication process, we utilized 70 nm shallow-etched Distributed Bragg Reflector (DBR) as retroreflectors [203]. Finite-difference Time-domain (FDTD) simulations revealed that these DBR mirrors, with a period of 437 nm, exhibit reflection centered at 2.1 μm ($>$ 90% reflection) and a 3 dB bandwidth of 200 nm, meeting the requirements for our demonstration.

The transmission spectrum of the PCG was measured prior to QDPD integration using a tunable laser around 2.1 μm, and normalized to eliminate the spectral response of the grating couplers used for light coupling into and out of the PCG. The fabricated PCG covers a wavelength range from 2063 nm to 2135 nm, with a cross-talk better than -20 dB and insertion loss less than 3 dB, as depicted in Figure 3.23(b), consistent with design metrics.

For the WG-QDPDs, we utilized a width of 30 μm and a length of 200 μm to achieve an efficient photo response. After integrating the WG-QDPD array, the photo-response of each channel was measured at -1 V bias by sweeping the wavelength of the input laser. The response of the QDPD array aligns with the spectrum of the grating coupler (gray line in Figure 3.23(c)), as measured from a reference

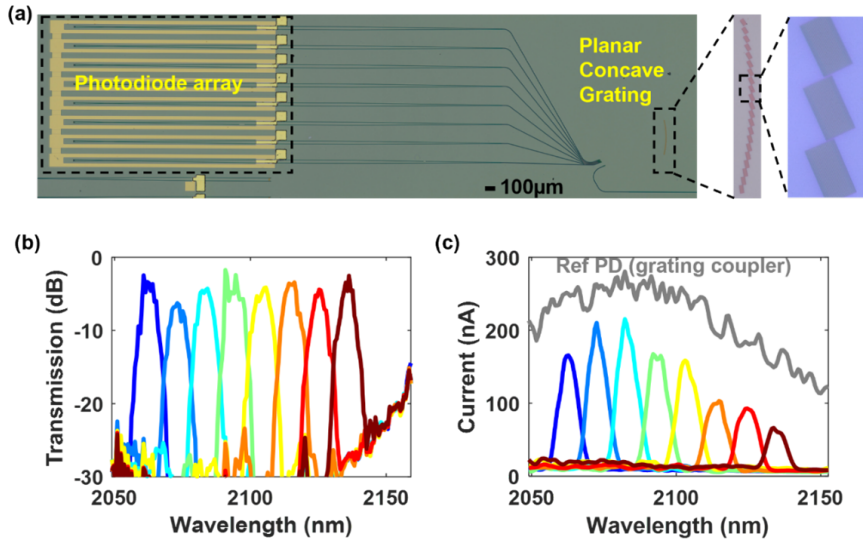

Figure 3.23: Compact spectrometer based on a WG-QDPD array and a planar concave grating. (a) Top view of the spectrometer. Light is injected from the grating coupler on the right side. (b) Transmission spectrum of the planar concave grating. (c) Response of WG-QDPDs from eight channels and a reference waveguide (gray line).

WG-QDPD. This consistent spectral shape indicates uniform responses of the WG-QDPDs, thereby suggesting its potential for scalable integration. The array of WG-QDPDs was measured directly without requiring further calibration. This type of spectrometer is interesting for sensing applications, such as glucose concentration monitoring.

3.6 Discussion

Compared with previously reported plasmonic HgTe QD photoconductors integrated on silicon waveguides [140], our integration approach achieves a similar level of dark current (106 nA), demonstrating more than one-order improvement in responsivity (1.3 A/W) and two-order improvement in bandwidth (1.1 MHz). When compared to alternative approaches for extending photodetection capabilities on the SOI platform, our proposed WG-QDPDs are competitive in terms of dark current and responsivity. Notably, these results are on par with the best-performing bonded III-V photodetectors reported in the literature (responsivity 0.4-1.4 A/W around 2.3 μm, dark current 10 nA-2.5 μA) [179–182], outperforming monolithically grown GeSn (responsivity $<$0.52 A/W, dark current $>$1 mA) [186–189]. Another class

of heterogeneous materials, 2D materials like graphene [204] or black phosphorus [205, 206], also possess the potential to operate beyond the telecommunication wavelength. However, they face challenges in achieving high responsivity (0.07-0.3 A/W at wavelength of 2-3 μm) [184, 185, 207] and scalable integration. It is acknowledged that, despite advancements, the bandwidth of our WG-QDPD still lags behind compared to the GHz bandwidth demonstrated by other approaches. Furthermore, additional efforts are necessary to mitigate the nonlinear response of our WG-QDPD.

The performance of the WG-QDPD could be further improved by optimizing the device structure. Previous reports on QDPDs at 2.1 μm have demonstrated an impressively low dark current density of 10^{-5} A/cm^2 and high responsivity [2]. Implementing such advancements could reduce the dark current of integrated photodetectors to sub-nanoampere levels, which is particularly advantageous for the detection of weak signals in sensing applications.

Also exploring alternative materials for long-wavelength WG-QDPDs, such as HgTe [3, 61, 208] and Ag_2Se [192, 193], is compelling to extend the photodetection capabilities within silicon photonics into the mid-infrared range, aligning with heightened interest in sensing applications. Ag_2Se QDs, which rely on intra-band absorption, are thereby the more attractive material because of the greatly reduced toxicity. However, efforts are still needed to improve the responsivity and reduce the dark current for these materials.

3.7 Conclusion

In this work, we have demonstrated the integration of PbS QDPDs onto silicon waveguides, extending the photodetection capabilities beyond the traditional telecommunication range in silicon photonics. The achieved results at room temperature, including a low dark current of 106 nA, a high responsivity of 1.3 A/W at 2.1 μm, and a bandwidth of 1.1 MHz, highlight the effectiveness of our approach. The scalability of our integration method is exemplified through the presentation of an 8-channel compact spectrometer integrated with a WG-QDPD array. This integrated system offers a promising solution for on-chip spectroscopy around 2.1 μm. We believe that QDPD technology holds significant promise for cost-effective photodetection in the near and mid-infrared ranges in silicon photonics, especially for diverse sensing applications. Future work should focus on improving the QDPD characteristics, including detectivity, bandwidth, and linearity, and extending the sensing wavelength range.

4

Spectrometer based on multi-color cascaded WG-QDPDs

4.1 Introduction 83
4.2 Principle 85
4.3 Spectrometer design 89
4.3.1 Choice of dispersive optics 89
4.3.2 Optimization of lengths of cascaded QDPDs 94
4.4 Fabrication 96
4.5 Characterization of QDPDs 100
4.6 Characterization of spectrometer 104
4.7 Discussion 106
4.8 Conclusion 107

4.1 Introduction

One of the standout features of QDs is that their absorption peak can be tuned easily. By adjusting the size or composition of QDs, the whole spectral range from the visible to the mid-infrared can be covered. This feature has been used for realizing low-cost focal plane arrays for imagers. [77, 208–211]. In another example, Tang

et al. presented a dual-band imager that utilizes two sizes of HgTe QDs arranged in a cascaded vertical n-p-n type photodiode stack. This configuration enables to switch the spectral response between the short-wave and the mid-wave infrared range [212]. Furthermore, the widely tunable absorption characteristics of QDs have found applications in computational spectroscopy. Bao et al, for instance, placed 195 different types of QDs, each with distinct absorption spectra, atop a CCD camera, achieving a micro-spectrometer covering a spectral range of 300 nm in the visible range [176]. This innovative approach was soon extended into the infrared region, leveraging either commercial infrared CMOS imagers [213] or QD-based photodetector arrays [214].

The tunable features of QDs also hold promise when integrated into more complex optical systems. In Chapter 2 and 3, QD photodetectors based on PbS QDs with different sizes have been introduced into silicon photonics. This approach enables the construction of versatile optical components on a single chip, leveraging mature CMOS technology. The combination of waveguide-coupled QDPDs with AWG or PCG allowed to successfully demonstrate compact spectrometers operating around 1.3 μm and 2.1 μm, respectively. While complex dispersive components such as AWGs and PCGs are commonly used in silicon photonics for realizing on-chip spectrometers [203, 215–217], a fundamental trade-off exists between the operational spectral range and spectral resolution [218]. Achieving better spectral resolution within a similar footprint requires larger optical dispersion, typically implying a larger diffraction order and, consequently, a smaller FSR and a more narrow spectral bandwidth. This traditional trade-off persists since a single photodetector is used in each channel, making optical signals from adjacent diffraction orders indistinguishable. Placing different types of photodetectors on each channel in cascade, each with a distinct response to different diffraction orders, would separate signals from more than one FSR, thereby eliminating the aforementioned trade-off. Hence the question whether the widely tunable spectral response of QDPDs can be leveraged for this purpose.

In this work, we propose and demonstrate the integration of the tunable features of QDs with dispersive PICs, pushing the spectral bandwidth beyond a single FSR. In our demonstration, we integrate two distinct types of QDs with their respective excitonic absorption peaks overlapping with two adjacent diffraction orders of the PCG. The QDs are integrated as waveguide-coupled photodiodes, and in cascade, on the output channels of the PCG, with each exhibiting a unique spectral response. By carefully designing the response of the QDPDs, we demonstrate a spectral bandwidth of approximately 180 nm using an eight-channel PCG with an intrinsic FSR of 90 nm, breaking the FSR limit of the spectrometer. By leveraging the versatility of QDs in terms of wavelength tunability and ease-of-processing, this work highlights the potential of these materials for integrated photonics, and creates

a path towards on-chip broadband spectrometers through straightforward adaptions to enhance resolution and spectral sensitivity.

4.2 Principle

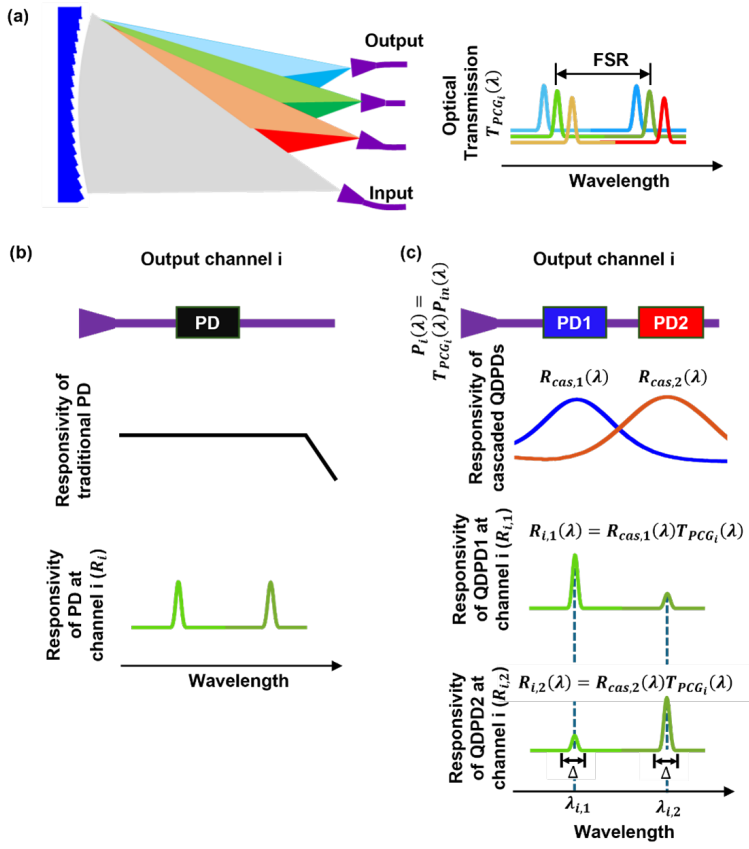

Figure 4.1: Principle of breaking the FSR limit. (a) Planar concave grating and optical transmission at different channels. (b) Traditional photodetection solution for a spectrometer. Signals from different diffraction orders are mixed, so working range is limited to one FSR. (c) Cascaded QDPDs for photodetection. Different QDPDs have different responses to different diffraction orders, extra information is achieved to separate signals beyond one FSR.

Figure 4.1 illustrates the principle of decoupling signals from different diffraction orders pursued in this study. In an optical dispersive component, such as a PCG, light with different wavelengths is deflected at distinct angles and collected by

separate channels, as shown in Figure 4.1(a). However, each channel captures light from different diffraction orders, separated by the FSR. In conventional dispersive spectrometers, a single photodetector is placed on each channel, converting optical power into an electrical signal for readout, as shown in Figure 4.1(b). The presence of a single photodetector on each channel implies that optical signals from different diffraction orders simply add up, obviously limiting the operational spectral bandwidth to one FSR.

Contrastingly, as outlined in Figure 4.1(c), incorporating multiple photodetectors with distinct wavelength response on each channel can result in different responsivities for various diffraction orders. Such an innovative approach provides additional information, enabling signals from different diffraction orders to be separated. More specifically, considering an input signal with a power spectral density of $P_{\text{in}}(\lambda)$, the power density measured by the PCG is discretized into $P_{\text{in}}(\lambda_{i,k})$, where $\lambda_{i,k}$ is the peak transmission wavelength of channel i within diffraction order k. For two diffraction orders and two cascaded QDPDs on channel i, the power density within each order is linked to the photocurrents of these QDPDs by a 2×2 matrix $\mathbf{M}_i = [m_{i,jk}]$:

$$\begin{pmatrix} I_{i,1} \\ I_{i,2} \end{pmatrix} = \begin{pmatrix} m_{i,11} & m_{i,12} \\ m_{i,21} & m_{i,22} \end{pmatrix} \begin{pmatrix} P_{\text{in}}(\lambda_{i,1}) \\ P_{\text{in}}(\lambda_{i,2}) \end{pmatrix} \tag{4.1}$$

Here, $I_{i,j}$ is the photocurrent measured by QDPD of type j on channel i. An unknown input spectrum, confined within the range of the targeted two FSRs, can then be reconstructed by measuring $I_{i,j}$ and inverting the linear relation Equation 4.1.

Let's break it down step by step to understand how to reach this relationship. As shown in Figure 4.2, assuming the input optical spectrum is $P_{\text{in}}(\lambda)$, the light coupled into each channel i of the PCG is $P_i(\lambda) = P_{\text{in}}(\lambda) T_{\text{PCG}_i}(\lambda)$, for a PCG with a transmission spectrum of $T_{\text{PCG}_i}(\lambda)$. Subsequently, this light couples to QDPD 1, where it undergoes partial absorption, generating a photocurrent of $I_{i,1}$. The residual light exits QDPD 1 with a spectrum of $P_{\text{aD1}_i}(\lambda)$. This light then couples once again, this time to QDPD 2, producing a photocurrent of $I_{i,2}$.

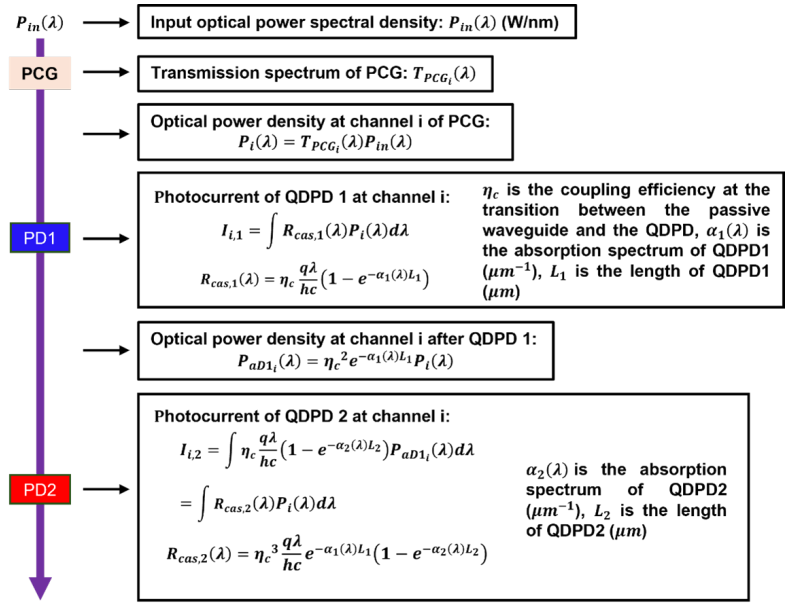

Figure 4.2: Operating principle of the spectrometer based on two-color cascaded QDPDs.

The relationship between $I_{i,j}$ and $P_{\text{in}}(\lambda_{i,k})$ is governed by Equation 4.2:

$$
\begin{aligned}
I_{i,1} &= \int \eta_c \frac{q\lambda}{hc}(1 - e^{-\alpha_1(\lambda)L_1})T_{\text{PCG}_i}(\lambda)P_{\text{in}}(\lambda)\,d\lambda \\
&= \int R_{\text{cas},1}(\lambda)T_{\text{PCG}_i}(\lambda)P_{\text{in}}(\lambda)\,d\lambda \\
&= \int R_{i,1}(\lambda)P_{\text{in}}(\lambda)\,d\lambda \\
&= \int_{\lambda_{i,1}-\Delta/2}^{\lambda_{i,1}+\Delta/2} R_{i,1}(\lambda)P_{\text{in}}(\lambda)\,d\lambda + \int_{\lambda_{i,2}-\Delta/2}^{\lambda_{i,2}+\Delta/2} R_{i,1}(\lambda)P_{\text{in}}(\lambda)\,d\lambda \\
&\approx P_{\text{in}}(\lambda_{i,1}) \int_{\lambda_{i,1}-\Delta/2}^{\lambda_{i,1}+\Delta/2} R_{i,1}(\lambda)\,d\lambda + P_{\text{in}}(\lambda_{i,2}) \int_{\lambda_{i,2}-\Delta/2}^{\lambda_{i,2}+\Delta/2} R_{i,1}(\lambda)\,d\lambda \\
&= m_{i,11}P_{\text{in}}(\lambda_{i,1}) + m_{i,12}P_{\text{in}}(\lambda_{i,2})
\end{aligned}
\tag{4.2a}
$$

$$
\begin{aligned}
I_{i,2} &= \int \eta_c^3 e^{-\alpha_1(\lambda)L_1}(1-e^{-\alpha_2(\lambda)L_2})T_{\text{PCG}_i}(\lambda)P_{\text{in}}(\lambda)\,d\lambda \\
&= \int R_{\text{cas},2}(\lambda)T_{\text{PCG}_i}(\lambda)P_{\text{in}}(\lambda)\,d\lambda \\
&= \int R_{i,2}(\lambda)P_{\text{in}}(\lambda)\,d\lambda \\
&= \int_{\lambda_{i,1}-\Delta/2}^{\lambda_{i,1}+\Delta/2} R_{i,2}(\lambda)P_{\text{in}}(\lambda)\,d\lambda + \int_{\lambda_{i,2}-\Delta/2}^{\lambda_{i,2}+\Delta/2} R_{i,2}(\lambda)P_{\text{in}}(\lambda)\,d\lambda \\
&\approx P_{\text{in}}(\lambda_{i,1})\int_{\lambda_{i,1}-\Delta/2}^{\lambda_{i,1}+\Delta/2} R_{i,2}(\lambda)\,d\lambda + P_{\text{in}}(\lambda_{i,2})\int_{\lambda_{i,2}-\Delta/2}^{\lambda_{i,2}+\Delta/2} R_{i,2}(\lambda)\,d\lambda \\
&= m_{i,21}P_{\text{in}}(\lambda_{i,1}) + m_{i,22}P_{\text{in}}(\lambda_{i,2})
\end{aligned}
\tag{4.2b}
$$

Here, we assume that $P_{\text{in}}(\lambda)$ does not change significantly around the transmission peak wavelength $\lambda_{i,k}$ of diffraction order k at channel i, within the range of the peak width Δ (Figure 4.1(c)). Simply, the relationship between the measured current and the input power spectral density is linked by the matrix $\mathbf{M}_i = [m_{i,jk}]$, as shown in Equation 4.1. The matrix element can be expressed as:

$$
m_{i,jk} = \int_{\lambda_{i,k}-\Delta/2}^{\lambda_{i,k}+\Delta/2} R_{i,j}(\lambda)\,d\lambda \tag{4.3a}
$$

$$
R_{i,j}(\lambda) = R_{\text{cas},j}(\lambda)\,T_{\text{PCG}_i}(\lambda) \tag{4.3b}
$$

$$
R_{cas,j}(\lambda) = \begin{cases} \eta_c \frac{q\lambda}{hc}(1-e^{-\alpha_1(\lambda)L_1}), & \text{if } j=1 \\ \eta_c^3 \frac{q\lambda}{hc} e^{-\alpha_1(\lambda)L_1}(1-e^{-\alpha_2(\lambda)L_2}), & \text{if } j=2 \end{cases} \tag{4.3c}
$$

Here, η_c is the coupling efficiency at the transition between the passive waveguide and the QDPD. q is the elementary charge, h is Planck's constant, c is the speed of light, $\alpha_j(\lambda)$ is the absorption coefficient of QDPD j, and L_j is the length of QDPD j. $R_{\text{cas},j}(\lambda)$ is the responsivity of cascaded QDPD j. Note that the responsivity of QDPD 2 as expressed in Equation 4.3c accounts for loss incurred by QDPD 1. $R_{i,j}(\lambda)$ is the channel responsivity combining the responsivity of cascaded QDPD j and the transmission of the PCG $T_{\text{PCG}_i}(\lambda)$. In practice, $R_{i,j}(\lambda)$ can be measured by sweeping a monochromatic light source and recording the photocurrent of each QDPD.

4.3 Spectrometer design

In practical scenarios, measurement noise is inevitable and can be amplified during the linear inversion if the matrix M_i is ill-conditioned. For a linear inversion problem, $\mathbf{Mx} = \mathbf{b}$. If the measurement has noise $\delta\mathbf{b}$, the solution becomes $\mathbf{x} + \delta\mathbf{x}$, where the relative deviation of the solution follows the relationship:

$$\frac{\|\delta\mathbf{x}\|}{\|\mathbf{x}\|} \leq \kappa(\mathbf{M})\frac{\|\delta\mathbf{b}\|}{\|\mathbf{b}\|} \tag{4.4}$$

where $\kappa(\mathbf{M}) = \|\mathbf{M}^{-1}\|\|\mathbf{M}\|$ is the condition number of matrix $\mathbf{M}$. A well-conditioned matrix has a small condition number.

Hence, a crucial aspect of the spectrometer design is ensuring a sufficiently small overall condition number κ:

$$\kappa = \frac{1}{n}\sum_i \kappa(\mathbf{M_i}) \tag{4.5a}$$

$$\kappa(\mathbf{M_i}) = \|\mathbf{M_i^{-1}}\|\|\mathbf{M_i}\| \tag{4.5b}$$

Here, $\|\cdot\|$ denotes the matrix norm, with the l_2 norm employed in this work.

Small condition numbers can be achieved by increasing the difference in response of the cascaded QDPDs to different diffraction orders, a step that promotes dissimilarity between the column vectors in the matrix. In our matrix optimization strategy, we tailored the FSR of the PCG to match the FWHM of the excitonic absorption peak of QDs films, and we adjusted the size of the QDs to align their respective excitonic peaks with the central wavelengths of the two targeted orders of the PCG. Our designed PCG has a FSR of 90 nm, with central wavelengths of the two target orders positioned at 1250 nm and 1340 nm. The synthesized QDs exhibit absorption peaks slightly red-shifted to 1280 nm and 1355 nm, as illustrated in Figure 4.3. As a next step, a more precise adaptation of this exciton absorption to the central wavelengths of the diffraction order can be explored to further reduce the condition number.

4.3.1 Choice of dispersive optics

The AWG and PCG are both commonly used dispersive optical components in integrated photonics, and have been used in our previous demonstration of the 1.3 μm spectrometer (Section 2.6) and 2.1 μm spectrometer (Section 3.5), respectively. For this demonstration, we opted for a PCG due to its reduced sensitivity to fabrication variations in our cleanroom, particularly for designs requiring a large FSR.

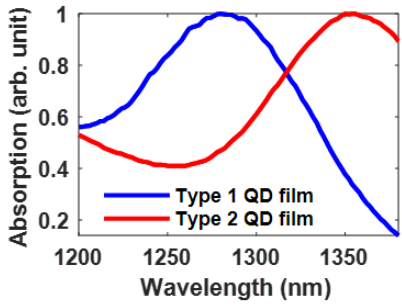

Figure 4.3: Normalized absorption spectrum of both types of QD.

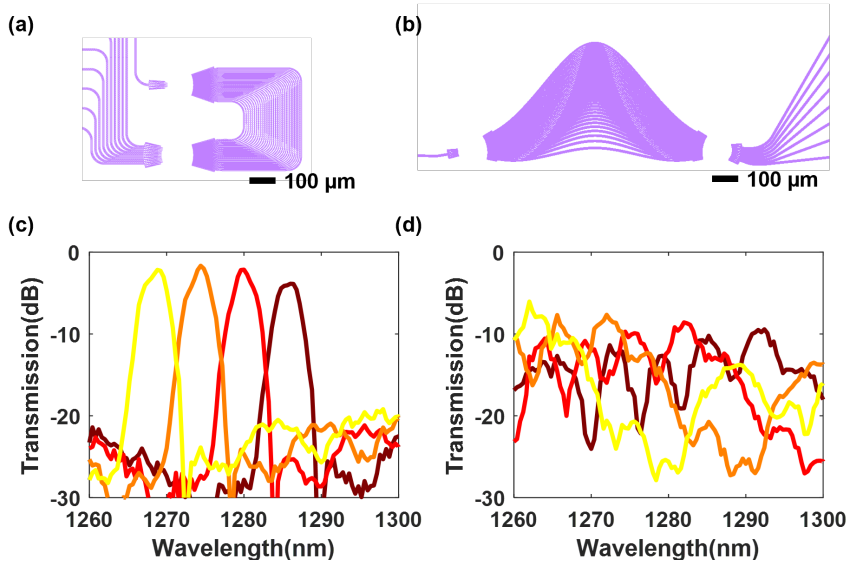

Figure 4.4: AWG with different FSR. (a) Waveguide array in Manhattan shape for FSR of 60 nm. (b) Waveguide array with a free-form curved shape for FSR of 90 nm. (c) and (d) Transmission spectra of AWG with FSR of 60 nm (a) and 90 nm (b), respectively.

AWG

First an AWG was explored as the dispersive component as its design is supported by a well-developed package in IPKISS. However, the preferred large FSR makes the fabrication of a high-quality AWG challenging in our cleanroom. As indicated in Equation 2.5, a large FSR requires a smaller length difference between adjacent waveguides. To meet this requirement, we transitioned from rectangular Manhattan-shaped waveguides, suitable for smaller FSRs (Figure 4.4(a)), to free-form curves

(Figure 4.4(b)) in the array to prevent overlap between waveguides.

Unfortunately, this change resulted in a severe degradation of the performance, particularly evident in high crosstalk for the AWG with a 90 nm FSR, as shown in Figure 4.4(c) and (d). This degradation is attributed to increased phase errors in the waveguide array. Several factors in our cleanroom fabrication process contribute to this sensitivity, including stitching in the waveguide array due to its size exceeding one write field of our EBL system (500 μm $\times$ 500 μm), and non-uniform patterning density exacerbated by the proximity effect in the EBL. The proximity effect, causing unintended exposure or dose variations due to the scattering of secondary electrons, particularly affects feature size. It is noteworthy that we used positive resist for patterning, which results in narrower waveguides in denser areas.

To improve the proximity effect-induced fabrication variation, we conducted Proximity Effect Correction (PEC) on the design using Beamfox. Despite the improved performance of the AWG, as depicted in Figure 4.5(a), the crosstalk remains worse than -10 dB. This limited enhancement is likely attributed to the imperfect correction of the proximity effect. As illustrated in Figure 4.5(b), for the pattern with a lower base dose, the resist is incompletely developed in regions with denser patterns, indicating overcorrection of the proximity effect. While increasing the base dose can achieve cleaner development, as seen in Figure 4.5(c), it may introduce variations in waveguide width, as mentioned earlier. We believe that optimizing the PEC process can further enhance the performance of the AWG.

PCG

The PCG seems to be a more favorable option for in-house demonstration as it is less sensitive to fabrication variations. Regarding the grating facet type, there are different options. A DBR, as we used in Section 3.5, was initially preferred due to its ease of fabrication and low insertion loss. However, a DBR often exhibits limited bandwidth, particularly for materials with low refractive index contrast (e.g., n = 1.93 for SiN vs. n = 1.38 for HSQ @ 1.3 μm), as illustrated in Figure 4.6. Alternatively, etched facet offers a broadband reflector but typically demonstrates lower reflectivity, especially for this low refractive index contrast. The fabricated PCG with an etched facet as the grating element demonstrated a high insertion loss of -20 dB, as depicted in Figure 4.7.

To improve the insertion loss, we applied a metal coating to the facets to enhance reflectivity. The fabrication process for the PCG with metal reflectors involved two separate patterning steps. In the first step, we defined all optical structures, excluding the grating facets, on a 300 nm SiN layer atop 3 μm buried oxide substrates, using EBL and RIE dry etching. Then, in a second patterning step, we

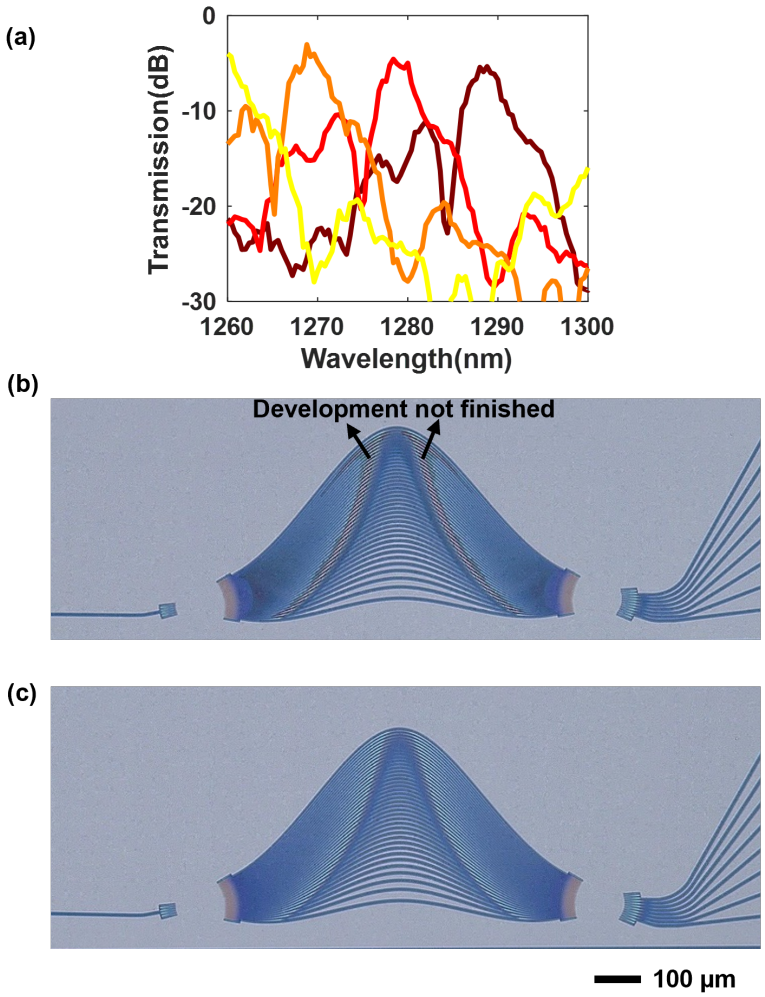

Figure 4.5: AWG fabricated using EBL with proximity effect correction. (a) The transmission spectrum of the 90 nm FSR AWG. (b) and (c) indicate the imperfect correction of the proximity effect. Patterning in (c) used a higher base exposure dose compared to (b).

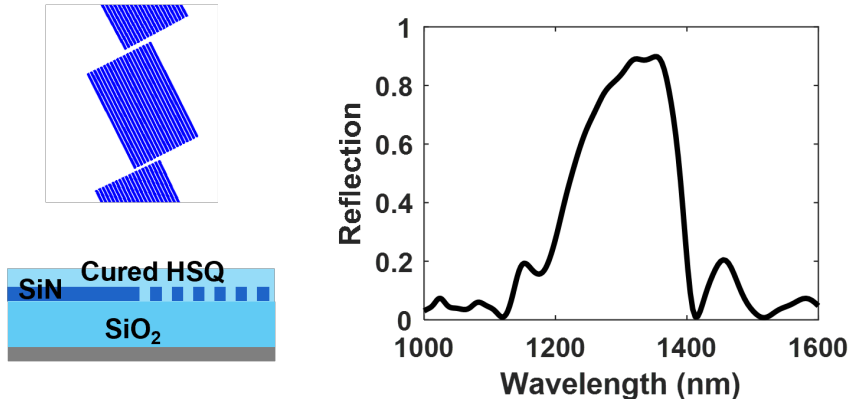

Figure 4.6: DBR as the grating facet for the PCG. The reflection spectrum is simulated using a 300 nm thick slab of SiN waveguide, featuring a 50/50 duty cycle DBR with a period of 430 nm.

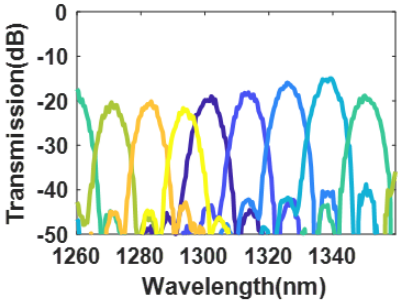

Figure 4.7: Transmission spectrum of the PCG with etched facet as the grating element.

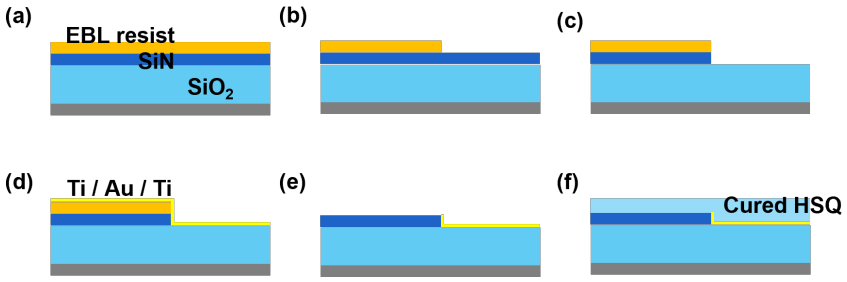

Figure 4.8: Fabrication steps for the metal-coated grating facet. (a) The sample is coated with EBL resist. (b) EBL is employed to define the position of the facets. (c) RIE is used to etch the SiN, exposing the facets. (d) Metal is evaporated onto the sample at a 45-degree angle with rotation for better coverage on the vertical facets. (e) Any remaining metal on the chip is removed through lift-off using resist remover. (f) HSQ is spun on top to serve as the top cladding.

specifically etched the grating facets using the same process (Figure 4.8(a)-(c)). A metal coating consisting of 5 nm Ti / 100 nm Au / 5 nm Ti was then evaporated onto the facets. During evaporation, the sample was positioned at a 45° angle to the evaporation source and rotated to ensure better coating on the vertical etched facet. The thin layers of Ti on both sides served to enhance adhesion between Au and SiN or the subsequent top cladding layer. Any remaining metal on the chip was removed through lift-off using resist remover. In this step, the thickness of the EBL resist before metal evaporation was around 400 nm to ensure the success of the liftoff process. Finally, the chip was planarized with a 370 nm flowable oxide HSQ as a top cladding, providing a smooth interface for subsequent integration. This cladding also reduced optical power density in the QDPD integrated on top, mitigating power saturation and improving the linear response range.

Figure 4.9(a) depicts the layout of the PCG, highlighting the metal coating on the etched grating trench (indicated by the yellow region). A tilted SEM image of the facet confirms the successful coating, as illustrated in Figure 4.9(b). Remarkably, the metal coating significantly reduced the insertion loss from -20 dB to less than -3 dB. Moreover, the crosstalk is better than -20 dB, meeting the requirements for our demonstration. This PCG configuration was used in our following demonstration.

4.3.2 Optimization of lengths of cascaded QDPDs

Since the QDPDs will be placed in series, a second design aspect involves the length of both QDPDs, which is a determining factor in matrix $\mathbf{M}_i$ (see Equation 4.3) and thus affects the condition number. For this optimization, we need $\alpha_j(\lambda)$

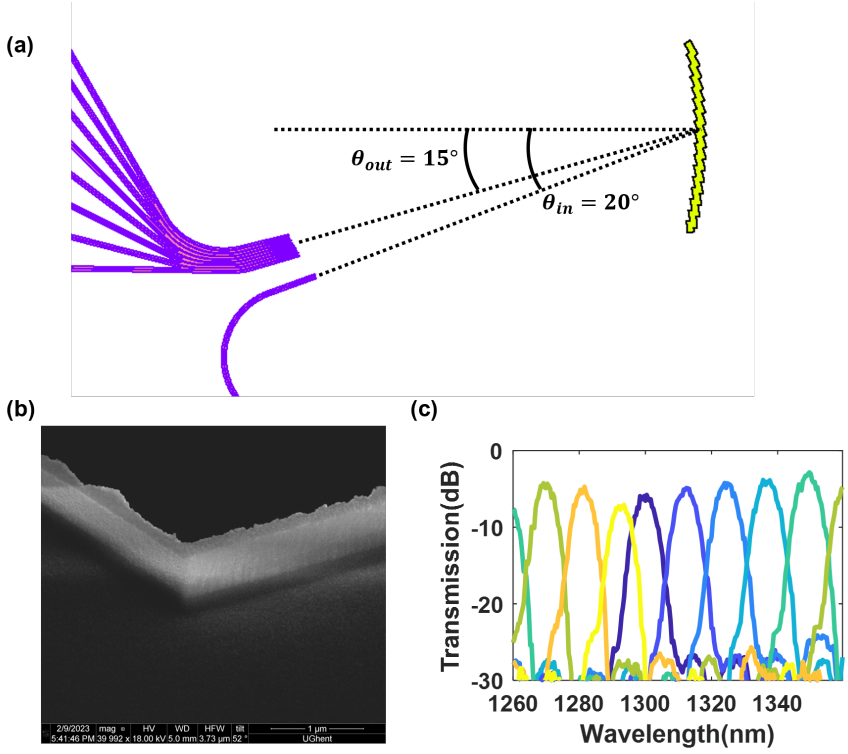

Figure 4.9: The PCG with metal-coated facets. (a) The layout of the PCG. The etched grating (yellow region) will be coated with metal. (b) The SEM image of the tilted metal-coated facet. (c) Transmission spectrum of the PCG.

and $T_{\mathrm{PCG}_i}(\lambda)$ to calculate the matrix elements.

The absorption coefficient spectrum $\alpha_j(\lambda)$ was measured using waveguide-coupled QDPDs with varying lengths. We conducted transmission measurements on the two types of QDPD with lengths of 50, 100, 200 and 300 μm, at a wavelength of 1275 nm, as shown in Figure 4.10(a). The type 1 QDPD exhibits absorption-induced losses of 0.025 dB/μm, as depicted in Figure 4.10(b) with a linear fit. Similarly, Type 2 QDPD displays a comparable loss of 0.02 dB/μm, as shown in Figure 4.10(c). Measuring the absorption spectrum of QDPDs across the entire target wavelength range of 1200 nm to 1400 nm directly is challenging and typically requires a broadband tunable laser or a high-power broadband light source. In this study, we employed a monochromator to measure the absorption spectrum shape of the QD films under normal incidence, which, combined with the absorption values of the QDPDs measured at 1275 nm, enabled the calculation of the absorption spectra for both types of QDPDs within the full target wavelength range, as shown in Figure 4.10(d). For QDPD 1, we obtained an absorption coefficient of 5.8 mm^{-1} (0.0252 dB/μm) at the peak wavelength of 1280 nm, while QDPD 2 had an absorption coefficient of 10.3 mm^{-1} (0.0447 dB/μm) at the peak wavelength of 1355 nm. The stronger absorption in QDPD 2 aligns with expectations, and is attributed to a thicker QD layer utilized in its construction. These two spectra are employed as $\alpha_j(\lambda)$ in the simulation.

The PCG was designed and simulated with IPKISS [159]. Figure 4.11 shows the simulated transmission spectrum for each channel of the 8-channel PCG ($T_{\mathrm{PCG}_i}(\lambda)$). The FSR is designed to match the number of channels multiplied by the channel spacing, resulting in the cascading of two adjacent diffraction orders without a spectral gap in between. Channels away from the center experience more loss as light is distributed almost equally to two adjacent diffraction orders.

Subsequently, Figure 4.12(a) maps κ as a function of the lengths L_1 and L_2 of the first and second detector, using Equations 4.2 and 4.5. The combination of L_1=50 μm and L_2=200 μm yields a small κ of 9.6, which was used for our demonstration. The channel responsivity $R_{i,j}(\lambda)$ at these lengths is shown in Figure 4.12(b) and (c). As expected, this optimized design results in distinct responses of the two QDPDs to the two successive diffraction orders. QDPD 1 exhibits a stronger response to order 1, while QDPD 2 shows a more pronounced response to order 2.

4.4 Fabrication

The PCG with metal grating facets was fabricated as shown in Section 4.3.1. Next, the QDPD stacks were integrated, starting from the planarized waveguide, as

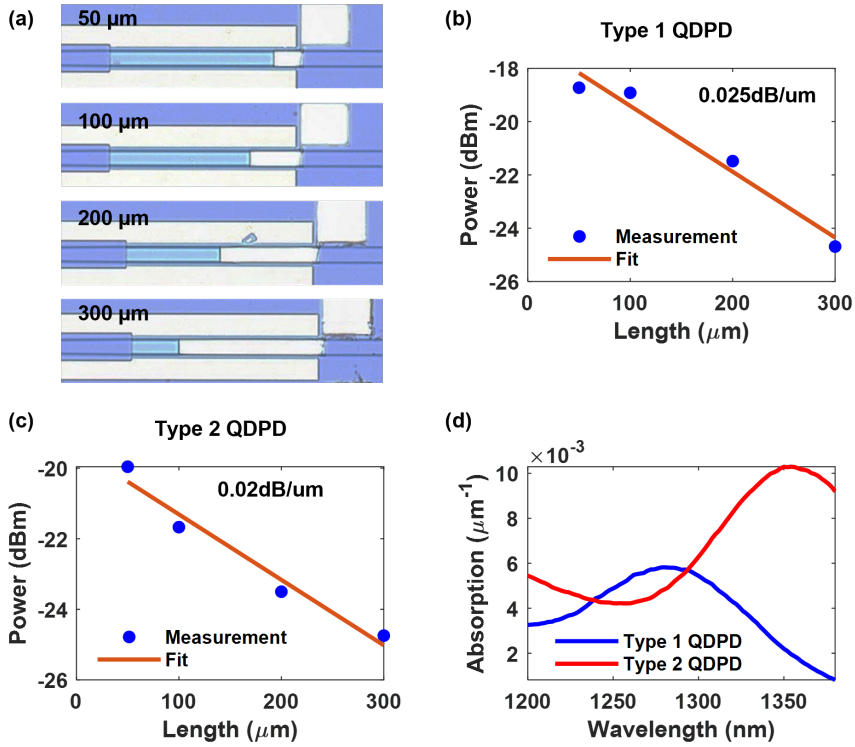

Figure 4.10: Measurement of absorption spectra for both types of QDPD. (a) The microscope image of QDPDs with different lengths for absorption loss measurement. (b) Transmission of type 1 QDPD with variable lengths measured at the wavelength of 1275 nm. (c) Transmission of type 2 QDPD with variable lengths measured at the wavelength of 1275 nm. (d) Absorption spectra of both types of QDPD.

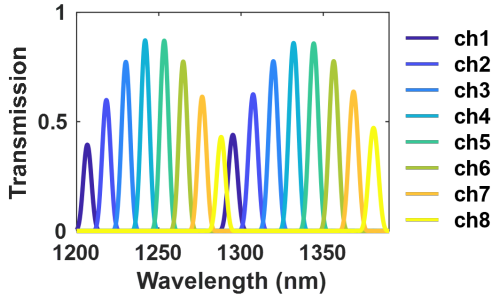

Figure 4.11: Simulated transmission spectrum of the 8-channel PCG.

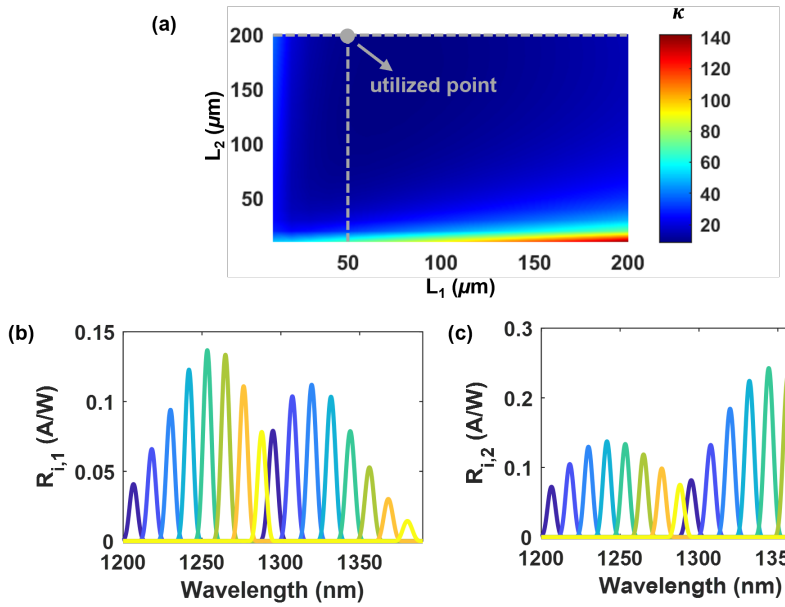

Figure 4.12: Optimization of the length of cascaded QDPDs. (a) Condition number mapped for different combinations of the QDPD lengths. (b) and (c) Responsivity of QDPD 1 & 2 for the 8 different channels i, with a length combination of $L_1 = 50\mu m$ and $L_2 = 200\mu m$.

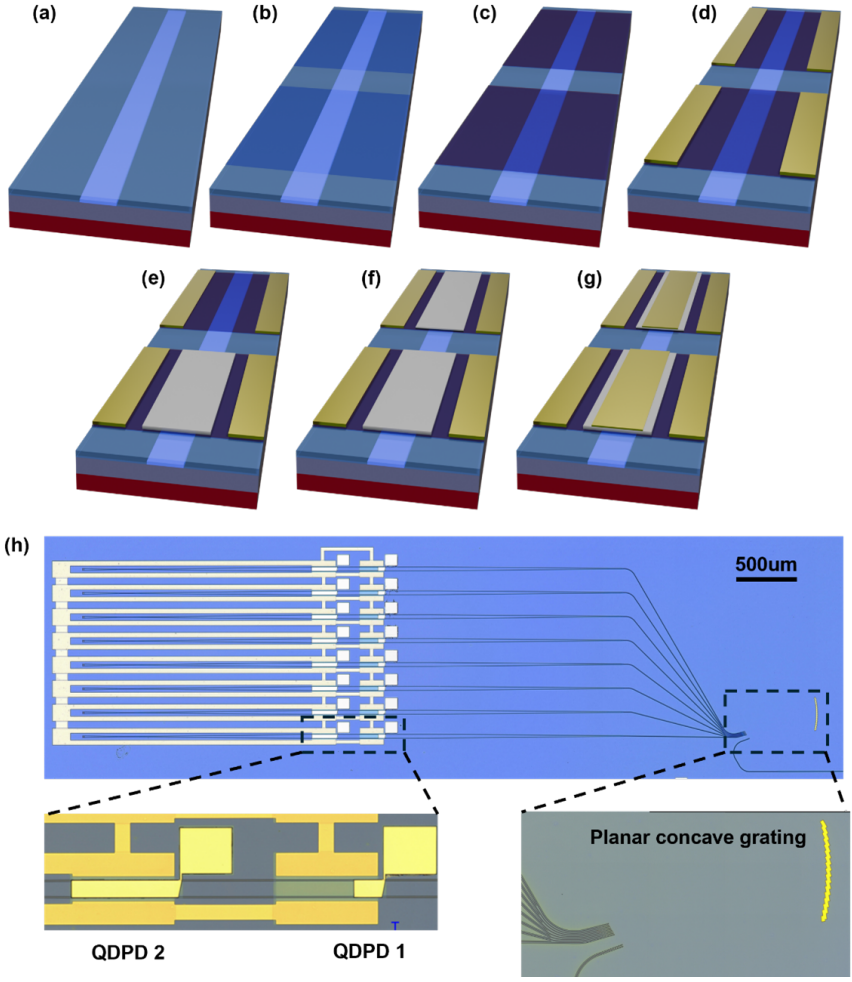

Figure 4.13: Integration steps to fabricate cascaded QDPDs. (a) Optical passive structures fabrication and planarization. (b) ITO sputtering and patterning with wet etching. (c) ZnO deposition with solgel method and patterning with wet etching. (d) N-contact evaporation and pattering with liftoff. (e) QDPD 1 deposition and patterning with liftoff. (f) QDPD 2 deposition and patterning with liftoff. (g) P-contact evaporation and patterning with liftoff. (h) Top view of the fabricated spectrometer.

depicted in Figure 4.13(a). The integration followed the process flow developed in Section 3.3.

First, a 20 nm thick ITO layer was sputtered as the bottom electrode, followed by HCl-based wet etching to confine the ITO to the target QDPD regions as shown in Figure 4.13(b). Subsequently, a 50 nm ZnO layer was deposited using sol-gel chemistry and patterned with a dilute HCl solution, as shown in Figure 4.13(c). We then defined 20 nm Ti / 100 nm Au n-contact pads on the side using a lift-off technique, as shown in Figure 4.13(d).

On top of the ZnO layer, we sequentially deposited and patterned the QD stacks for QDPD 1 and QDPD 2 using the lift-off method, as shown in Figure 4.13(e) and (f). For QDPD 1, PbS QDs with a band-gap transition at 1250 nm were used for the absorption layer. This layer was treated with TBAI in a methanol solution to replace the as-synthesized long surface ligands. On top, PbS QDs with a 940 nm band-gap transition were spin-coated and treated with EDT in a methanol solution. Both QD layers, with a thickness of 60 nm each, were lifted off simultaneously to achieve the desired pattern. QDPD 2 was processed similarly to QDPD 1, but with QDs having a 1355 nm transition bandgap for the absorption layer, which was increased in thickness to 90 nm to enhance absorption.

Finally, a 100 nm Au layer was deposited on both types of QD stacks to form the p-contact pads. The completed spectrometer, shown in Figure 4.13(h), features eight channels, each equipped with two cascaded QDPDs. All n-contacts were interconnected forming a common ground, to simplify measurements.

4.5 Characterization of QDPDs

Both types of QDPDs were characterized using a 1275 nm laser, with the optical power coupled into the waveguide using a grating coupler. The coupling efficiency of the grating was measured using a reference waveguide without QDPDs. Both types of QDPDs were characterized under dark and light conditions. The 200 µm-long QDPDs exhibited a clear diode behavior. QDPD 1, with an absorption peak at 1280 nm, displayed a dark current of 5 nA at -1 V bias, as shown in Figure 4.14(a). This QDPD showed a linear response, with a responsivity of 0.41 A/W at low optical power, as shown in Figure 4.14(b). The saturation (10% deviation from the linear response) observed above 40 μW optical power level was likely influenced by the series resistance within the WG-QDPDs. The carrier extraction in QDPD 2, with a 1355 nm absorption peak, was less efficient, as illustrated in Figure 4.14(c). Lowering the reverse bias to -2V improved carrier extraction, resulting in a linear responsivity of 0.4 A/W and saturation power around 25 μW, with a

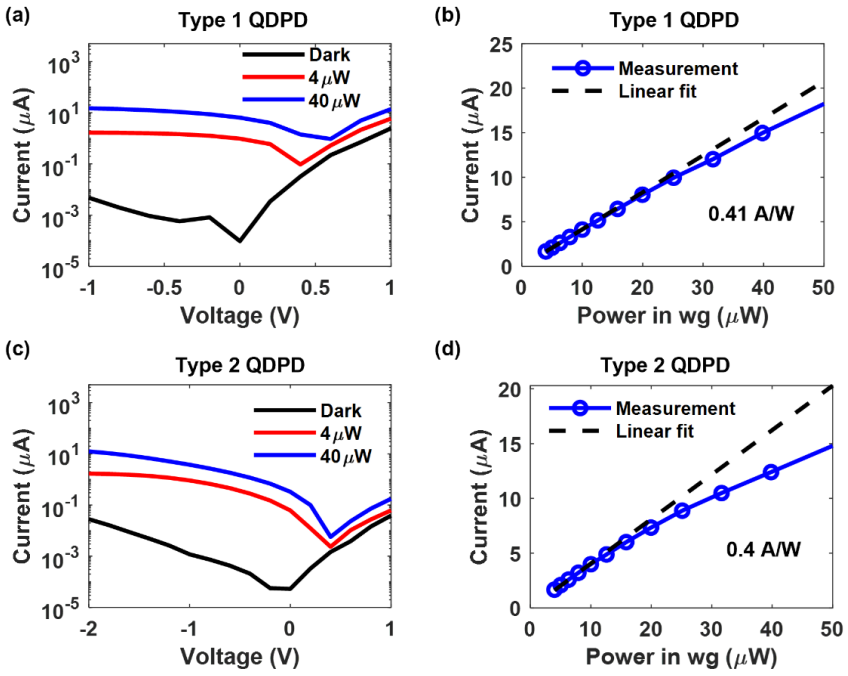

Figure 4.14: Response of the two types of integrated QDPDs. (a) and (c) I-V curves under dark condition and illumination at 1275 nm for QDPD 1 and QDPD 2 respectively. (b) Photo-current vs. optical power of QDPD 1 at a bias of -1 V. (d) Photo-current vs. optical power of QDPD 2 at a bias of -2 V.

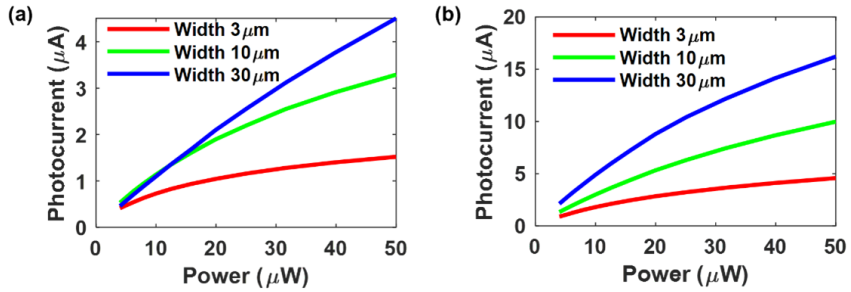

Figure 4.15: Photoresponse of QDPDs with different widths. (a) Photoresponse of type 1 QDPDs with a length of 50 μm, measured at a bias of -1 V. (b) Photoresponse of type 2 QDPDs with a length of 200 μm, measured at a bias of -2 V.

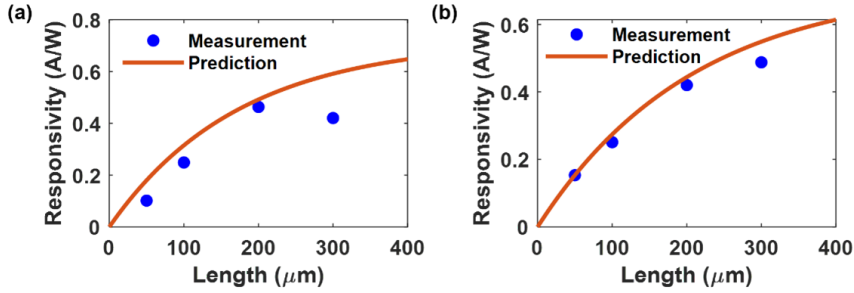

Figure 4.16: Responsivity vs. QDPD length at an optical power of 4 μW. (a) Responsivity of type 1 QDPDs, measured at a bias of -1 V. (b) Responsivity of type 2 QDPDs, measured at a bias of -2 V.

dark current of approximately 28 nA. The easier carrier extraction for QDPD 1 with larger bandgap QDs possibly originates from better-aligned conduction and valence band edges at the heterostructure interfaces. For both types of QDPDs, the responsivity was limited by incomplete light absorption and coupling loss at the waveguide-QDPD boundary. To avoid errors due to a saturation-induced nonlinear response, all subsequent characterization of the spectrometer was performed at a power level below 10 μW within the waveguides.

To mitigate power saturation in the waveguide-coupled QDPDs, the waveguides were widened to 30 μm, a strategy demonstrated to be effective in alleviating saturation [194], as illustrated in Figure 4.15.

QDPDs with different lengths were also fabricated on the same chip. The responsivity increased with length, as shown in Figure 4.16. The red lines represent the predicted responsivity using the equation $R = \eta_c \frac{q\lambda}{hc}(1 - e^{-\alpha_j L})$. Here, α_j denotes

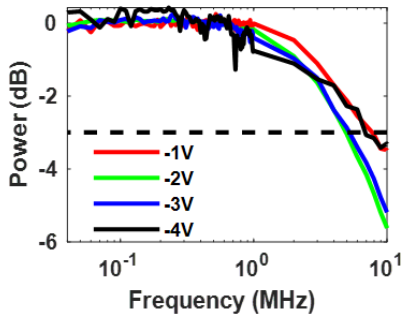

Figure 4.17: Bandwidth of the WG-QDPD.

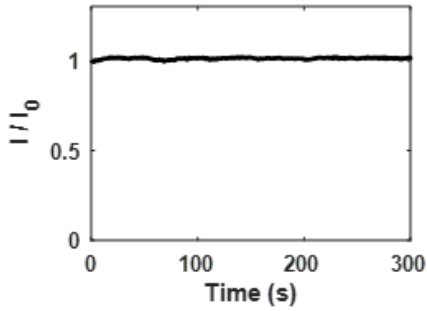

Figure 4.18: Time stability of the WG-QDPD.

the absorption-induced loss for both types of QDPDs, with $\alpha_1 = 0.0058\mu m^{-1}$ and $\alpha_2 = 0.0048\mu m^{-1}$ measured in Figure 4.10(d). A coupling efficiency (η_c) of 70% is applied in the calculations.

The bandwidth of the WG-QDPD, with a length of 200 μm, was measured to be approximately 6 MHz at a wavelength of 1275 nm, as shown in Figure 4.17, corresponding to a response time of 58 ns. Increasing the voltage bias from 1 V to 4 V resulted in minimal change in bandwidth, suggesting that the speed of the WG-QDPD is RC-limited. The speed is slower than expected, as discussed in Chapter 2, likely due to increased series resistance.

Moreover, the WG-QDPD demonstrates good short-term stability, as shown in Figure 4.18, with no significant decrease in photocurrent observed over the 300 s measurement period. Further investigation is required to assess its long-term and temperature stability.

4.6 Characterization of spectrometer

The input waveguide of the spectrometer was cleaved to eliminate the bandwidth limitation imposed by the grating coupler. The wavelength-dependent channel responsivity $R_{i,j}(\lambda)$ of each QDPD was measured with a tunable laser, as shown in Figure 4.19. However, the response from two targeted diffraction orders could not be fully measured due to limitations in the tuning range of the available laser (1260 nm to 1360 nm). We therefore extrapolated the response to the full wavelength

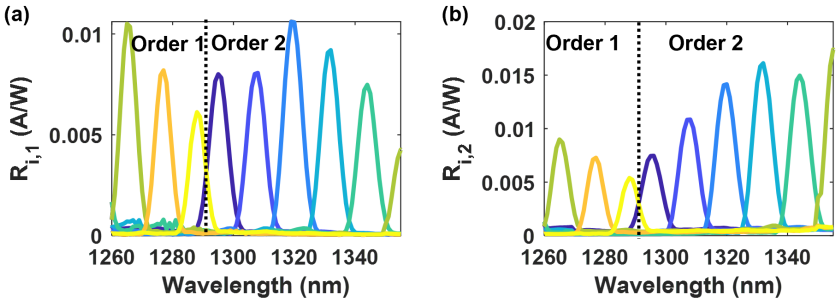

Figure 4.19: Measured channel spectral responsivity of QDPDs on eight channels of the PCG. (a) QDPD 1. (b) QDPD 2.

range targeted using the absorption spectra of both QDPDs (Figure 4.10(d)). Based on Equation 4.3, the responsivity of cascaded QDPD j ($R_{cas,j}(\lambda)$) was computed, as shown in Figure 4.20. The measured spectral responsivity, spanning from 1260 nm to 1360 nm, covers one FSR range. To obtain the missing spectral responsivity from 1200 nm to 1260 nm and from 1360 nm to 1380 nm, the following calculations

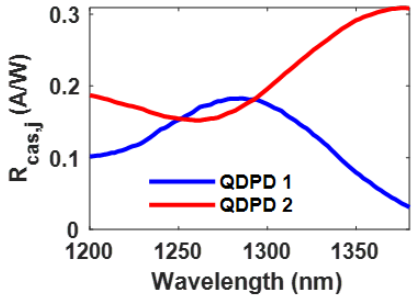

Figure 4.20: Spectral responsivity of cascaded QDPD j.

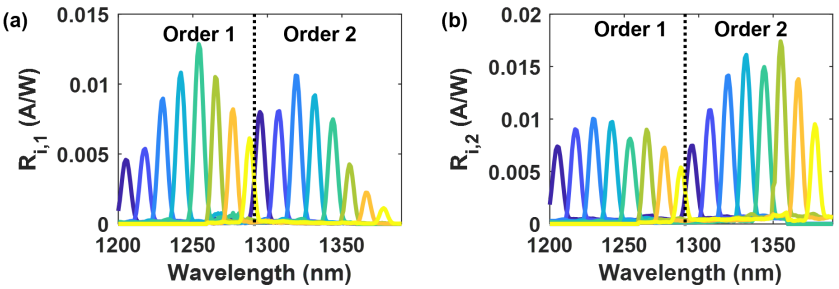

Figure 4.21: Resotred channel spectral responsivity of cascaded QDPDs covering two target diffraction orders. (a) QDPD 1. (b) QDPDs 2.

were performed:

$$R_{i,j}(\lambda) = \begin{cases} R_{i,j}(\lambda + FSR)\frac{R_{cas,j}(\lambda)}{R_{cas,j}(\lambda+FSR)}, & \text{for } 1200 \text{ nm} < \lambda < 1260 \text{ nm} \\ R_{i,j}(\lambda - FSR)\frac{R_{cas,j}(\lambda)}{R_{cas,j}(\lambda-FSR)}, & \text{for } 1360 \text{ nm} < \lambda < 1380 \text{ nm} \end{cases} \tag{4.6}$$

Here, $R_{i,j}(\lambda)$ represents the missing channel spectral responsivity at channel i, QDPD j, while $R_{i,j}(\lambda \pm FSR)$ denotes the measured channel spectral responsivity at the adjacent diffraction order. The assumption was made that the optical transmission spectrum of the PCG has equal amplitude at the two adjacent diffraction orders. The restored channel spectral responsivity, spanning two FSRs, is shown in Figure 4.21, showcasing shapes similar to simulations (Figure 4.12). Note that the measured channel responsivity was approximately 10 times lower than the simulated values, a difference most likely related to the additional optical losses from the PCG and the coupling loss from the optical fiber to the waveguide.

Leveraging the measured channel responsivities $R_{i,j}(\lambda)$, the matrix M_i was calculated as described above. The performance of the two-color QDPD spectrometer was demonstrated by measuring the ASE spectra from an O-band semiconductor amplifier, and benchmarked with respect to the spectrum measured with a YOKOGAWA spectrometer. Figure 4.22(a) and (b) provide the photocurrents measured by both QDPDs for all eight channels for two different ASE spectra, which we obtained using two different current settings of the amplifier. Using the 16 measured photocurrents and the transmission matrices $\mathbf{M}_i$, the input spectra as displayed in Figure 4.22(c) were then reconstructed. As can be seen, the discrete spectrum obtained in this way matches the profile of the input spectrum as measured using a commercial benchtop spectrometer. Notably, both test spectra covered two FSRs of the PCG. Hence, measuring such a spectrum is impossible using a conventional on-chip spectrometer. Note that the spectral reconstruction led to relatively large deviations at channel 2 (wavelength of 1217 nm and 1307 nm) and channel 3

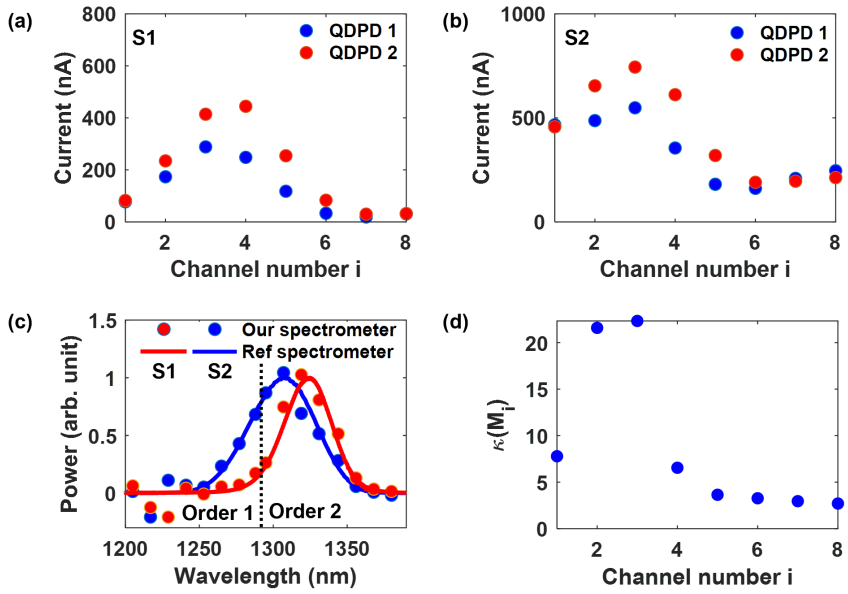

Figure 4.22: Spectrum reconstruction. (a) and (b) Measured photocurrent from both types of QDPDs at all 8 channels with different input spectra S1 and S2, respectively. (c) Reconstructed spectrum of spectrum S1 and S2 and their reference spectrum measured from a commercial spectrometer. (d) Condition number of the reconstruction matrix for each channel.

(wavelength of 1229 nm and 1319 nm). This outcome is consistent with the larger condition numbers $\kappa(M_i)$ of these channels, as shown in Figure 4.22(d), indicating higher sensitivity to measurement noise.

4.7 Discussion

In this work, we successfully extended the spectral bandwidth of a PCG beyond a single FSR, by leveraging the tunable spectral response and ease-of-processing of colloidal QDPDs. Our demonstrated spectrometer utilizes two different QDPDs, and covers a bandwidth of around 180 nm with a resolution of 12 nm. Compared with traditional integrated dispersive spectrometers that use fixed spectral-response germanium photodetectors, our approach replaces these with tunable spectral-response cascaded QDPDs, breaking the inherent bandwidth-resolution limit.

Integrated computational spectrometers have seen rapid development in recent years. The flexibility to design diverse optical filters [219–223] or scattering [224, 225]

systems, facilitates the creation of a large number of channels with uncorrelated chaotic transmission. With computational reconstruction, these schemes have demonstrated excellent performance, achieving resolutions of < 10 pm over a broad bandwidth of > 200 nm [219], comparable to benchtop spectrometers. However, these demonstrated spectrometers are almost exclusively passive, lacking integrated photodetectors due to the cost or complexity of such integration, especially for the more robust, temperature-stable SiN platform where monolithic integration of photodetectors are currently absent. Combining our proposed cascaded QDPDs with other computational spectroscopy methods could greatly improve the capabilities of these on-chip computational spectrometers. Our cascaded QDPD approach not only provides a cost-effective photodetection solution for the spectrometer chip but also introduces an additional degree of freedom to customize the spectral response of the sampling channels, thereby enhancing the spectral range and robustness of computational spectrometers.

Due to the absence of sweeping components, our spectrometer offers fast one-shot acquisition capability. By sacrificing response speed, such as by introducing a tunable ring filter at the input of the PCG, with the ring FSR matching the channel spacing of the PCG, we can enhance the resolution to pm level [218] without significantly changing the footprint. Additionally, the reconstruction accuracy of our spectrometer can be improved by fine-tuning the absorption spectra of the two types of QDs used. Also, the length of the QDPDs can be further improved. Now it was kept constant for each type of quantum dot, but it could be finetuned for each channel separately without complicating the fabrication process, thereby improving the robustness of the reconstruction process. Moreover, the proposed concept can be extended to incorporate more diffraction orders by introducing additional cascaded QDPDs, thereby expanding the working range. The successful cascading of more QDPDs depends on controlling the coupling loss between the passive waveguide and the QDPDs, which can be addressed through the implementation of taper structures that allow for an adiabatic transition at the interface.

4.8 Conclusion

In this chapter, we have demonstrated a new integrated spectrometer scheme using a PCG and cascaded QDPDs on a SiN platform. Leveraging the wavelength response disparity of two consecutive QDPDs, we successfully decoupled two diffraction orders of the PCG. Our implementation achieved a broad spectral bandwidth of approximately 180 nm on an eight-channel PCG with a 90 nm FSR, achieving a resolution of 12 nm. The tunable wavelength response of the proposed cascaded QDPDs opens avenues for their integration with various optical configurations,

promising enhanced resolution, broader bandwidth, and increased robustness for on-chip computational spectroscopy applications.

5

Fourier transform spectrometer using QDPD array nano-samplers

5.1 Introduction 109
5.2 Principle 110
5.3 Design 115
5.3.1 Sampling waveguide 116
5.3.2 Multi-mode interferometer beam splitter 119
5.3.3 Thermal phase shifter 121
5.4 Fabrication 126
5.5 Characterization 131
5.6 Discussion 134
5.7 Conclusion 135

5.1 Introduction

Fourier transform spectrometers (FTSs) are renowned for their wide bandwidth, high resolution, and superior signal-to-noise ratio in infrared spectroscopy. In traditional FTS systems, light is divided by a beam splitter into two paths, reflecting off a stationary mirror and a moving mirror [226]. As the moving mirror changes

position, the optical path length difference between the two beams varies. When the beams are recombined at the beam splitter, they interfere with each other, producing an interferogram that is recorded by a detector. By analyzing how the intensity of the combined beams varies with the mirror's position and applying a Fourier transform on the interferogram, the spectral information of the light source is retrieved. Integrated FTSs, on the other hand, commonly employ static architectures, utilizing either tunable phase shifters to sweep the optical path delay between two arms of a Mach–Zehnder interferometer (MZI) [227, 228] or an array of MZIs with increasing path differences [229–231].

One such variant, the stationary-wave integrated FTS (SWIFTS), operates by directly sampling the stationary wave generated within a waveguide. Nanosamplers positioned above the waveguide probe the evanescent field of the formed interferogram, offering a means to develop high-resolution spectrometers with compact and robust designs. However, sampling the stationary wave presents a challenge. It requires a nano-detector array with subwavelength-sized elements, a task difficult with existing semiconductor detectors. Most demonstrations to date have utilized nano-scale scatter centers on top of the waveguide to scatter the light upwards, which is then collected by an optical imaging system [232–235]. Superconducting nanowire single-photon detectors (SNSPDs) offer a potential nano-detector solution for SWIFTS [229], but the cryogenic working conditions add complexity to the system. Recent advancements have showcased that the limited carrier diffusion lengths in QD layers [236] offer potential for QD-based photodetectors as nano-scale probes for integrated FTS [141]. However, existing demonstrations integrate only a single QDPD on the waveguide, necessitating a moving mirror to shift the stationary wave. In this chapter, we explore the feasibility of employing a QDPD array as nano-samplers for SWIFTS. The spectrometer is designed on a SiN platform, aiming to sample the interferogram formed by counter-propagated light in a waveguide.

5.2 Principle

The fundamental operation of QDPDs as nano-probes is depicted in Figure 5.1(a). Due to the small diffusion length within the QD film (tens of nm), only carriers photo-generated in the proximity of the p-contact contribute to the photocurrent, while those outside this region undergo non-radiative recombination. Interestingly, although this characteristic is typically considered a limitation for QDPDs as it restricts the thickness of the QD film for absorption, consequently limiting achievable EQE, it makes QDPDs an ideal choice for nano-detection. The detection region of QDPDs is simply defined by the p-contact metal, facilitating practical

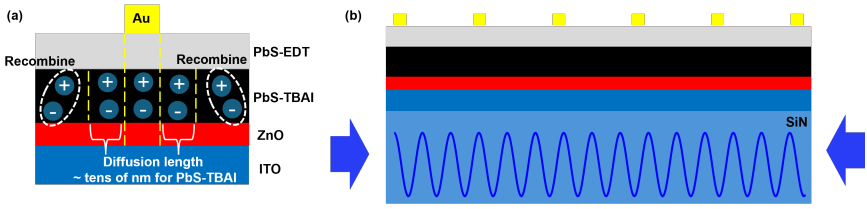

Figure 5.1: QDPDs as nano-samplers for SWIFTS. (a) Fundamentals of QDPDs as nano-probes. Due to the short diffusion length within the QD layer, only carriers photo-generated in the vicinity of the p-contact contribute to the photocurrent, while carriers outside this region recombine non-radiatively. (b) Schematic of the QDPD array as nano-samplers for SWIFTS. By defining a p-contact array on top of the QDs, the QDPD array effectively serves as an array of nano-samplers for SWIFTS. These nano-samplers efficiently capture the stationary wave pattern within the SiN waveguide via evanescent absorption.

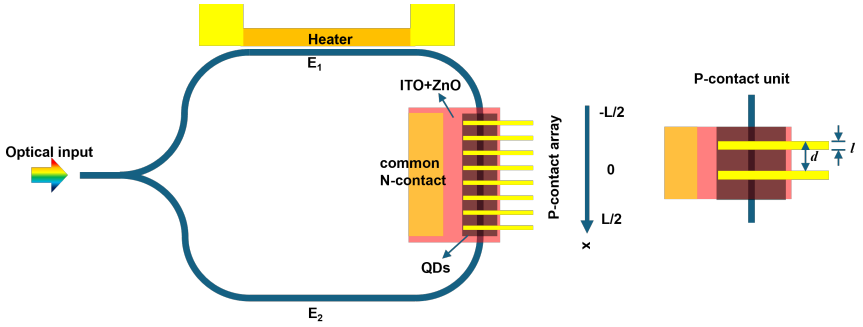

Figure 5.2: The architecture of our proposed SWIFTS system based on QDPD nano-samplers. On top of the waveguide, the QDPD array is integrated to sample the formed stationary wave. The p-contacts within the array feature a length l and are spaced apart by a pitch d. A thermal phase shifter is positioned on top of one arm to facilitate optical path tuning.

fabrication.

Exploiting this principle, we propose to realize an array of nano-samplers for SWIFTS by creating a nano-sized p-contact array atop the QD film. These nano-samplers can then capture the stationary wave pattern within the waveguide through evanescent absorption, as illustrated in Figure 5.1(b). Variations in the input optical spectra produce distinct stationary-wave shapes, which can be discerned through Fourier transform analysis.

The architecture of our SWIFTS is shown in Figure 5.2. The input light is split into two paths, which counter-propagate within the target waveguide. The QDPD array is integrated on top of the target waveguide, sampling the formed stationary wave.

This waveguide will be referred to as the "sampling waveguide" for clarity. To increase the length of the sampling region (improve the spectral resolution) and ease the fanout of the QDPD array for measurement, we space out the nano-QDPDs with a pitch d, each QDPD with a p-contact length l. To ensure sampling of the entire stationary wave, a thermal phase shifter is integrated on top of one arm. This heater can adjust the position of the stationary wave by tuning its optical path through varying the heating power.

The photocurrent of each nano QDPD can be expressed as:

$$I = q \iiint G(x,y,z)dxdydz \tag{5.1a}$$

$$G(x,y,z) = \frac{P_{abs}(x,y,z)}{hv} = \frac{2\pi n\kappa\epsilon_0}{h}\left|E(x,y,z)\right|^2 \tag{5.1b}$$

where $G(x,y,z)$ is the generation rate of photocarriers, q is the elementary charge, $P_{abs}(x,y,z)$ is the optical power absorbed per unit volume, hv is the energy of the photon, n and κ correspond to the real and imaginary part of the refractive index, respectively, and $E(x,y,z)$ denotes the electrical field of the light. x represents the propagation axis of the waveguide, as depicted in Figure 5.2. If there is no waveguide mode mixing, $G(x,y,z) = G(x)G(y,z)$, and $G(y,z)$ is the same for all nano QDPDs. Therefore, we only consider $G(x)$ in the following analysis.

Let's consider a monochromatic input light with an angular frequency ω. Light injected into the sampling waveguide has an electrical field of E_1 (upper path) and E_2 (lower path), respectively:

$$E_1(x) = E_0 e^{-\alpha(\frac{L}{2}+x)} e^{j\left[\beta(\frac{L}{2}+x)-\omega t+\phi_1\right]} \tag{5.2a}$$

$$E_2(x) = E_0 e^{-\alpha(\frac{L}{2}-x)} e^{j\left[\beta(\frac{L}{2}-x)-\omega t+\phi_2\right]} \tag{5.2b}$$

where α is the propagation loss of the sampling waveguide, L is the length of the sampling waveguide, E_0 is the amplitude of the electrical field of light injected into the sampling waveguide, $\beta = 2\pi n_{eff}/\lambda$ is the effective propagation constant of the optical mode, and ϕ_1 and ϕ_2 denote the phases of the counter-propagated light. $G(x)$ is proportional to $|E(x)|^2$, and it can be expressed as:

$$\begin{aligned} G(x) &\propto [E_1(x)+E_2(x)][E_1(x)+E_2(x)]^* \\ &= E_0^2\left[e^{-\alpha(L+2x)} + e^{-\alpha(L-2x)} + 2e^{-\alpha L}\cos(2\beta x+\phi_1-\phi_2)\right] \\ &= E_0^2 e^{-\alpha L}\left[e^{-2\alpha x} + e^{2\alpha x} + 2\cos\left(\frac{4\pi n_{eff}}{\lambda}x+\Delta\phi\right)\right] \\ &= E_0^2 e^{-\alpha L}\left[2\cosh(-2\alpha x) + 2\cos\left(\frac{4\pi n_{eff}}{\lambda}x+\Delta\phi\right)\right] \end{aligned} \tag{5.3}$$

where $\Delta\phi = \phi_1 - \phi_2$ represents the phase difference between the counter-propagated lights, which equals 0 without phase tuning.

For a nano-QDPD, with length l at position x, the photocurrent is:

$$\begin{aligned} I(x) &= qG(x)l \iint G(y,z)dydz \\ &= I_0 \alpha l e^{-\alpha L}\left[2\cosh\left(-2\alpha x\right) + 2\cos\left(\frac{4\pi n_{eff}}{\lambda}x + \Delta\phi\right)\right] \end{aligned} \tag{5.4a}$$

$$I_0 = \frac{qn\epsilon_0\lambda E_0^2}{h}\iint |E(y,z)|^2\, dydz \tag{5.4b}$$

Here, we consider $G(x)$ as a constant over the short length l. $\cosh(x) = \frac{e^{-x}+e^{x}}{2}$ is the hyperbolic cosine function. The propagation loss α induced by the QDs introduces a slowly varying component of $\cosh\left(-2\alpha x\right)$ as shown in Figure 5.3(a), which does not significantly affect the spectral shape obtained with the Fourier transform shown in Figure 5.3(b). However, α does influence the signal intensity. The intensity of the interferogram is proportional to $e^{-\alpha L}$ as indicated in Equation 5.2 and Figure 5.3(a). The intensity of the collected current signal from QDPDs is proportional to $\alpha l e^{-\alpha L}$, with a factor of αl related to the absorption. For a sampling waveguide length L of 100 μm, the collected signal reaches its maximum value around $\alpha = 500$ dB/cm (115 cm^{-1}), as shown in Figure 5.3(c). The design of sampling waveguide loss should be confined to the range of 100 cm^{-1} to 1160 cm^{-1} to ensure less than a 50% signal intensity drop.

For the nano-detector array, separated by a pitch d, the current of each QDPD is:

$$I_m = I(md), \quad m = -\frac{L}{2d}, \ldots, -1, 0, 1, \ldots, \frac{L}{2d} \tag{5.5}$$

With the thermal phase shifter, we can shift the interferogram pattern along the waveguide direction x. This operation is equivalent to shifting the nano-detector array in the opposite direction. To stitch together the entire stationary wave pattern, we need to shift the interferogram pattern, step by step with interval Δx, over a distance d. This requires the phase change induced by the heater to be:

$$\Delta\phi > \frac{4\pi n_{eff} d}{\lambda} \tag{5.6}$$

In our SWIFTS architecture, we sample the stationary wave within a range L, employing a sampling window with a width l. The interferogram is truncated by the limited sampling waveguide length L, which introduces a sinc-shaped broadening in the spectrum:

$$s_{trunc}(x) = s(x) \cdot rect\left(\frac{x}{L}\right) \tag{5.7a}$$

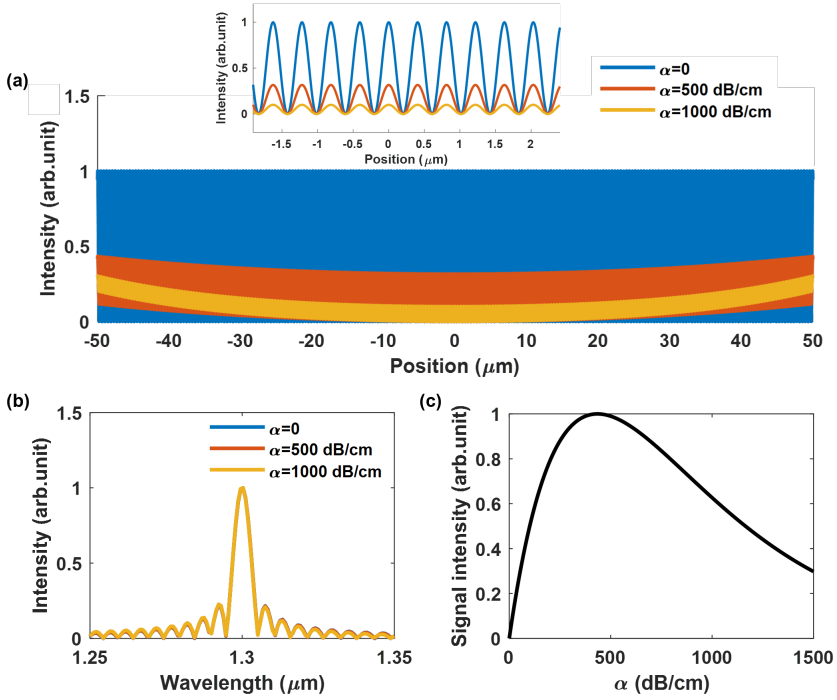

Figure 5.3: Influence of propagation loss α of the sampling waveguide on SWIFTS performance. (a) Interferogram formed with different propagation loss, using a 1.3 μm monochromatic light as input. The inset shows a zoomed-in view of the interferogram. (b) Normalized Fourier transform of the interferogram under different propagation loss. (c) Intensity of collected signal from QDPD vs. propagation loss.

$$S_{trunc}(\omega) = S(\omega) * L\text{sinc}\left(\frac{\omega L}{2}\right) \tag{5.7b}$$

where $s(x)$ is the stationary wave pattern, $s_{trunc}(x)$ denotes the stationary wave truncated by the sampling waveguide. $rect\left(\frac{x}{L}\right)$ is the rectangular function, which equals 1 when $-L/2 < x < L/2$ and 0 elsewhere. The symbol $*$ denotes the convolution operation. $S_{trunc}(\omega)$ and $S(\omega)$ are the corresponding Fourier transforms. Here, $\omega = \frac{4\pi n_{eff}}{\lambda}$, and $\text{sinc}(x) = \sin(x)/x$.

According to the Rayleigh criterion, two monochromatic sources are considered to be just resolvable when the central maximum of the spectral pattern of one source coincides with the first minimum of the spectral pattern of the other. This leads to the resolution of the spectrometer, denoted as $\Delta\lambda$:

$$\Delta\lambda = \frac{\lambda^2}{2n_g L} \tag{5.8}$$

As depicted in Figure 5.4(a), for monochromatic input light, increasing the sampling waveguide length results in a narrower spectrum, consistent with the predictions derived from Equation 5.2.

Sampling the stationary wave with nano-QDPDs is equivalent to convolving the stationary wave with a rectangular window of length l. Consequently, this convolution introduces a sinc-shaped window in the frequency domain:

$$s_{ave}(x) = s(x) * rect\left(\frac{x}{l}\right) \tag{5.9a}$$

$$S_{ave}(\omega) = S(\omega) \cdot l \cdot sinc\left(\frac{\omega l}{2}\right) \tag{5.9b}$$

where $s_{ave}(x)$ denotes the stationary wave sampled by the nano-QDPD and $S_{ave}(\omega)$ is the corresponding Fourier transform. The sinc-shape acts as a low-pass filter in the frequency domain, averaging out high-frequency patterns and thereby establishing a lower boundary for the optical bandwidth for a given l:

$$\lambda_{min} = 2n_{eff}l \tag{5.10}$$

The simulation results in Figure 5.4(b) clearly illustrate this effect. When using a short pulse (broadband) as the input signal, reducing the QDPD length l results in an increased signal intensity at lower wavelengths.

If the input spectrum is broadband, with a shape of $S(\lambda)$, the interferogram is not a simple sine shape but an integration over all spectral components:

$$I(x) = \int I_0 \alpha l e^{-\alpha L}\left[2\cosh\left(-2\alpha x\right) + 2\cos\left(\frac{4\pi n_{eff}}{\lambda}x + \Delta\phi\right)\right] d\lambda \tag{5.11}$$

The bandgap of the QDs sets the upper limit of our spectrometer. For longer wavelengths below the QD bandgap, the photodetector will not respond. As long as the spectral components of the input light are above λ_{min} and below the bandgap of the QDs, we can record the interferogram pattern and retrieve the source spectrum via Fourier transform.

5.3 Design

We aim to demonstrate our SWIFTS on the SiN platform, enabling wavelength sensing capabilities up to 1.4 μm, which is constrained by the absorption characteristics of our well-established WG-QDPD described in Chapter 4. SiN is favored over SOI owing to its lower refractive index, resulting in larger effective wavelength within the wavegude and hence a slower variation of the stationary wave pattern. This allows for larger p-contact sizes, alleviating fabrication challenges.

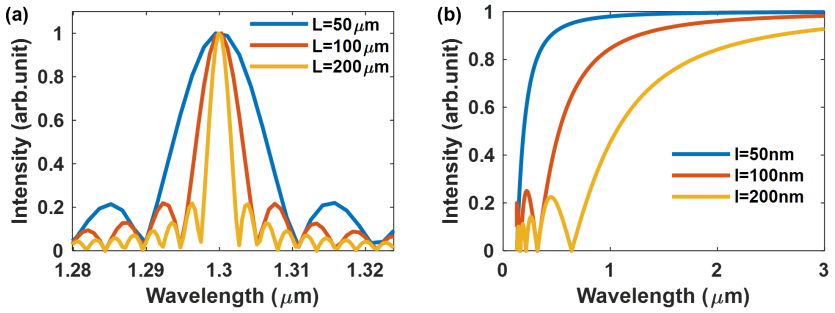

Figure 5.4: The impact of the sampling waveguide length and QDPD size on SWIFTS performance. (a) The simulated Fourier spectrum of SWIFTS with varying sampling waveguide lengths. Monochromatic light of 1.3 μm wavelength serves as the input. (b) The simulated Fourier spectrum of SWIFTS with different QDPD lengths. A short (broadband) optical pulse serves as the input signal.

5.3.1 Sampling waveguide

Selection of waveguide mode

Due to the larger refractive index of the PbS QD layer (n=2.55 for PbS-TBAI and n=2.25 for PbS-EDT) compared to SiN, the TE mode extends into the QD layer in the hybrid waveguide, as illustrated in Figure 5.5(a). However, in the detector region where the p-contact metal is deposited on top of the QDs, the TE mode is pushed downward, as depicted in Figure 5.5(b) and (g). The refractive index and propagation loss of both modes are presented in Figure 5.6(a) and (b). The region without p-contact exhibits significantly stronger absorption loss compared to the QDPD region with p-contact on top (8369 dB/cm vs. 583 dB/cm) due to the stronger electrical field in the QD layer, which is undesirable. In the sampling waveguide, the absorption in the region with p-contact contributes to the signal, while the other part introduces optical loss.

For the same waveguide structure, the TM mode exhibits similar mode profiles for both regions in the sampling waveguide, as illustrated in Figure 5.5(e), (f), and (h). The absorption loss of the region without p-contact is lower than that with p-contact (Figure 5.6(d)) due to the stronger electrical field in the QDs, which is desirable as more light will contribute to the signal. Therefore, we will utilize the TM mode for our demonstration and subsequent design efforts.

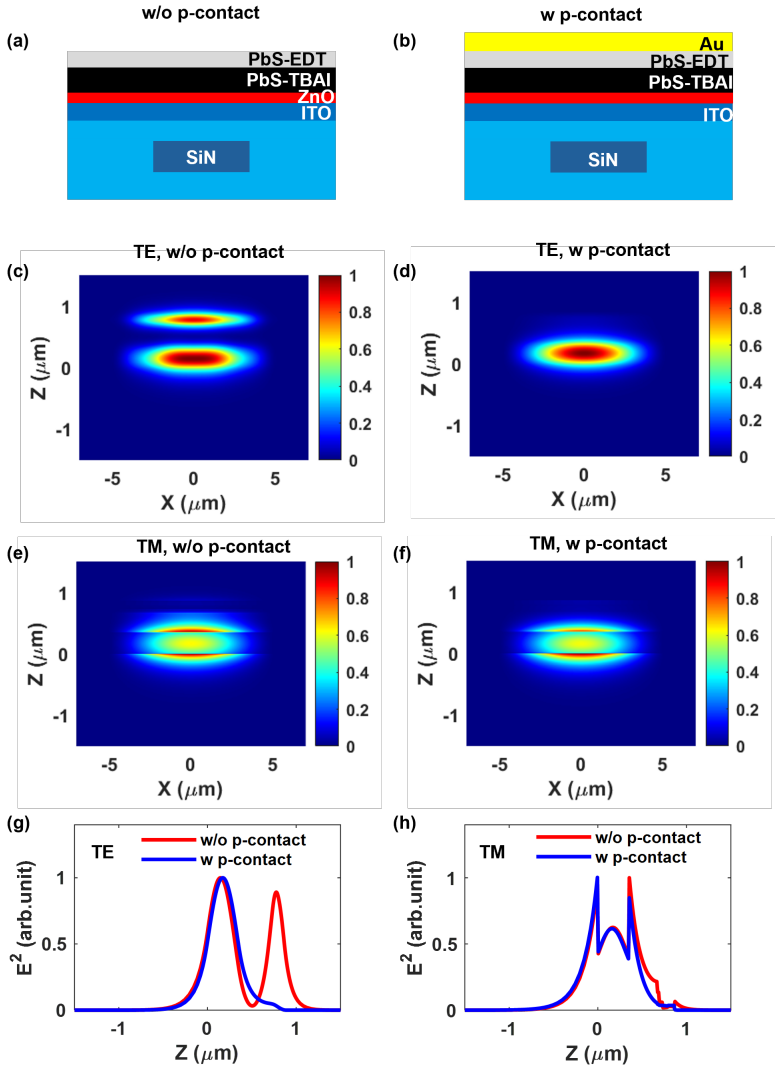

Figure 5.5: TE and TM modes in the sampling waveguide region. (a) and (b) depict the structure of two types of hybrid waveguides, one without and the other with a p-contact, respectively. The dimensions of each layer are as follows: SiN 350 nm × 10 μm, HSQ 320 nm, ITO 20 nm, ZnO 40 nm, PbS-TBAI 60 nm, PbS-EDT 75 nm, Au 50 nm. The simulations are conducted at a wavelength of 1.3 μm. (c) and (d) illustrate the mode profiles of the fundamental TE mode in the region without and with p-contact metal, respectively. (e) and (f) display the mode profiles of the fundamental TM mode in the region without and with p-contact metal, respectively. (g) and (h) depict the cross-section in the middle of the waveguides for TE modes and TM modes, respectively.

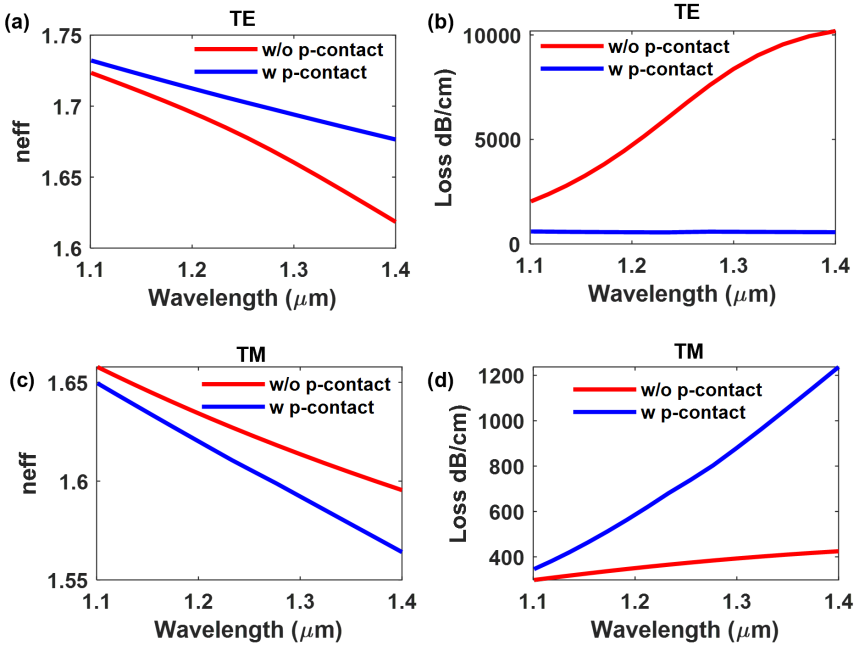

Figure 5.6: Effective refractive index and propagation loss of optical modes in the sampling waveguide region. (a) and (b) Fundamental TE modes. (c) and (d) Fundamental TM modes. The simulation is conducted under the same conditions as in Figure 5.5.

QD taper to reduce reflection

The discontinuity at the boundary between the sampling waveguide and the passive waveguide typically introduces reflection, affecting the interferogram within the sampling waveguide. To mitigate this reflection, we incorporate a taper in the QD layer, as illustrated in Figure 5.7(a). The SiN waveguide is designed with a width of 10 μm to minimize power saturation effects. The QD film is tapered from 100 nm to 16 μm. Simulation results obtained using Lumerical FDTD demonstrate that increasing the taper length to 15 μm reduces the reflection from the sampling waveguide to the passive waveguide to just 0.2%.

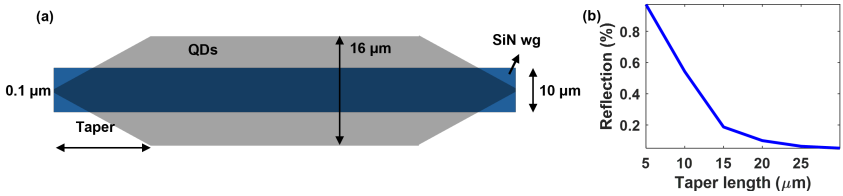

Figure 5.7: Tapering QD layer to reduce the reflection in the sampling waveguide. (a) The taper structure. (b) The reflection of fundamental TM mode from sampling waveguide (with QDs) to passive waveguide (without QDs), with varying taper lengths.

Sampling waveguide simulation

The stationary wave in the sampling waveguide is simulated using the 2D FDTD solver in Lumerical, based on the structure depicted in Figure 5.8(a), with counter-propagated light. We utilize 100 p-contacts with a length l of 100 nm and a pitch d of 1 μm. Figure 5.8(b) illustrates the averaged electric field intensity in the PbS-TBAI absorption layer using 1.3 μm monochromatic light. The slight bowl shape of the profile arises from the absorption loss-induced cosh function, as indicated in Equation 5.2. A zoom-in of the stationary wave is provided in Figure 5.8(c), revealing a sin-shaped pattern. Conducting the Fourier transform allows us to obtain the period of this stationary wave. Light with different wavelengths exhibits varying periods, as demonstrated in Figure 5.8(d). This structure, together with the 15 μm long QD tapers at both sides described above, constitutes the sampling waveguide in our SWIFTS design.

5.3.2 Multi-mode interferometer beam splitter

The input light should be uniformly split into two paths, generating two counter-propagated beams within the sampling waveguide. We employ a MMI as the power

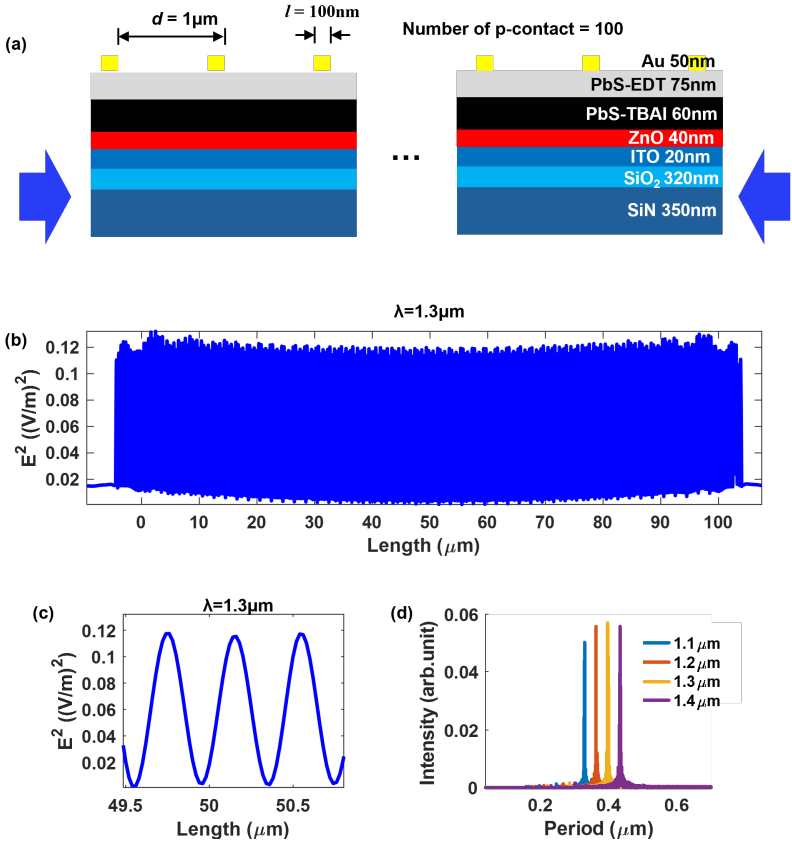

Figure 5.8: Simulation results of the sampling waveguide with counter-propagated input light. (a) The optical structure utilized for simulation, conducted using the 2D FDTD solver in Lumerical. (b) The simulated electrical field intensity in the PbS-TBAI absorption layer, at the wavelength of 1.3 μm. (c) A zoomed-in view of the stationary wave in (b). (d) The Fourier transform of the stationary wave employing monochromatic light at various wavelengths. Different wavelengths are associated with distinct periods.

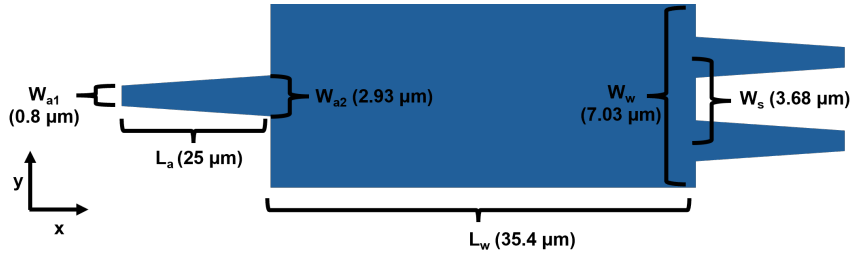

Figure 5.9: Structure of a Multi-Mode Interferometer (MMI). L_w: the length of the multi-mode waveguide section. W_w: The width of the multi-mode section. L_a: aperture length. W_{a1}: the width of the narrow side of the apertures. W_{a2}: the width of the expanded side of the apertures. W_s: the central distance between two output apertures. The optimized parameters for our application are denoted in the brackets.

splitter due to its higher tolerance to dimension changes in the fabrication process. A common 1×2 MMI structure is illustrated in Figure 5.9. For a symmetric input (input aperture in the middle of the y-axis of the MMI), only the even modes can be excited. In this case, the self-imaging length can be approximated as [237]:

$$L_{si} = \frac{n_w W_w^2}{\lambda} \tag{5.12}$$

Here, n_w and W_w represent the refractive index and width of the multi-mode waveguide core, respectively. The 2-port power splitting occurs at the position $L_{si}/2$. This expression enables us to estimate the length of the MMI for a given MMI width. We fine-tune the MMI parameters using the EME solver in Lumerical, employing its built-in particle swarm optimization. The optimized parameters of the MMI are denoted in brackets in Figure 5.9.

The electrical field distribution of the optimized MMI is depicted in Figure 5.10(a), showing the power is equally split into the two output ports. The transmission of each port is displayed in Figure 5.10(b). Over a 300 nm optical bandwidth (from 1.1 μm to 1.4 μm), the transmission decreases slightly from 0.48 to 0.402, with a drop of 7.9%. This bandwidth is sufficient for our SWIFTS demonstration.

5.3.3 Thermal phase shifter

As discussed in Section 5.2, to sample the entire stationary wave, it's necessary to shift the interference pattern by adjusting the phase delay in one arm. We employ a thermal phase shifter for this purpose due to its ease of fabrication. Given a QDPD array pitch d of 1 μm, a phase change as substantial as 6π (as described in Equation 5.2) is required for a wavelength of 1.1 μm. The induced phase shift ($\Delta\phi$) by the

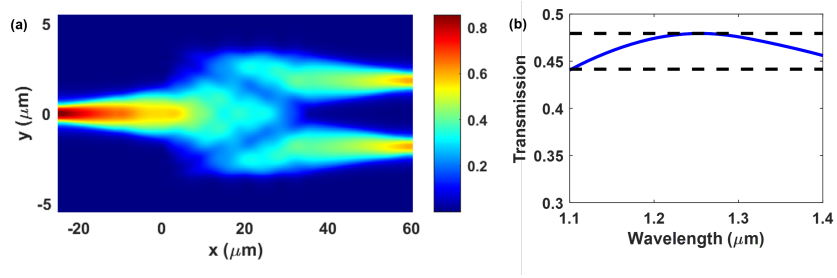

Figure 5.10: Simulation results of designed MMI. (a) Wavelength response. (b) Electrical field distribution.

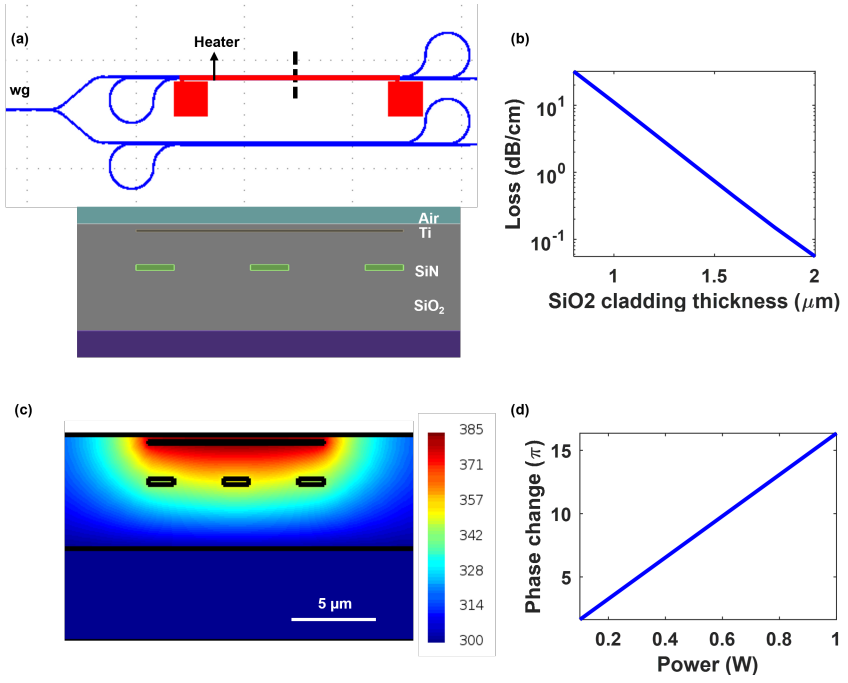

Figure 5.11: Design and simulation of the thermal phase shifter. (a) The structure of the thermal phase shifter. Triple-path waveguides are employed to obtain a larger achievable phase shift. The top view and cross-section of the structure are presented in the upper and lower parts of the figure, respectively. (b) The simulated optical loss with increased top cladding thickness. (c) The simulated thermal map using a 2D model. The length of the phase shifter is set to 3 mm, and an applied electrical power of 1 W is considered. The top cladding thickness is set to 2 μm. (d) The simulated thermal phase shift with increased electrical power.

thermal phase shifter can be computed using the formula:

$$\Delta\phi = \left(\frac{dn_{eff}}{dT}\right)\Delta T\frac{2\pi}{\lambda}L_{heater} \tag{5.13}$$

where $\frac{dn_{eff}}{dT}$ is the thermo-optic coefficient, ΔT is the temperature change induced by the applied electrical power, and L_{heater} is the heater length.

To accommodate such a substantial phase change without risking damage to the heater, we extend the length of the heated waveguide to mitigate the potential degradation induced by overheating. To achieve this, we employ triple-path waveguides beneath the heater, effectively tripling the length of the heated waveguide, as illustrated in Figure 5.11(a).

To minimize metal-induced optical loss, a top cladding layer is used as an optical spacer. The loss decreases exponentially with increasing top cladding thickness, as depicted in Figure 5.11(b). A thickness of 2 μm is chosen to reduce the heater-induced loss to below 0.1 dB/cm.

Utilizing the HEAT solver in Lumerical, we simulate the thermal-induced temperature change. The resulting temperature map of a 3 mm long heater under 1 W electrical power is illustrated in Figure 5.11(c). Leveraging the thermo-optic coefficients of $2.5 \times 10^{-5}K^{-1}$ for SiN and $9.6 \times 10^{-6}K^{-1}$ for SiO_2 [238], we can simulate the phase change at varying electrical power using the mode solver in Lumerical. As depicted in Figure 5.11(d), a phase shift as large as 16 π can be achieved at an electrical power of 1 W.

SWIFTS layout

Our design is shown in Figure 5.12. SWIFTS, as the core component, is positioned in the middle of the chip. The nano-QDPD array, consisting of 100 individual QDPDs separated by a pitch of 1 μm, is connected to the contact pads on the upper and lower sides of the chip. These contact pads are designed with a pitch of 200 μm, aligning with the Printed Circuit Board (PCB) design for wire bonding. To mitigate resistance of connection wires, we employ a 5-stage planar fan-out, progressively increasing the wire width from 100 nm (p-contact width) to 20 μm.

Moreover, we included a number of reference structures, including MZIs with the same heater design as the one used in the actual device, to support the calibration procedure. These calibration structures allow us to quantify the relationship between the optical delay change and heating power, which can then be used to stitch the interferogram in our proposed SWIFTS. Additionally, the input waveguide of the SWIFTS and the reference can be cleaved for butt coupling, accommodating a larger optical bandwidth.

Furthermore, our chip incorporates discrete QDPDs with varying p-contact lengths, ranging from 50 nm to 1 μm. These QDPDs serve to measure the effective QDPD length corresponding to each p-contact length, as discussed in Section 5.5.

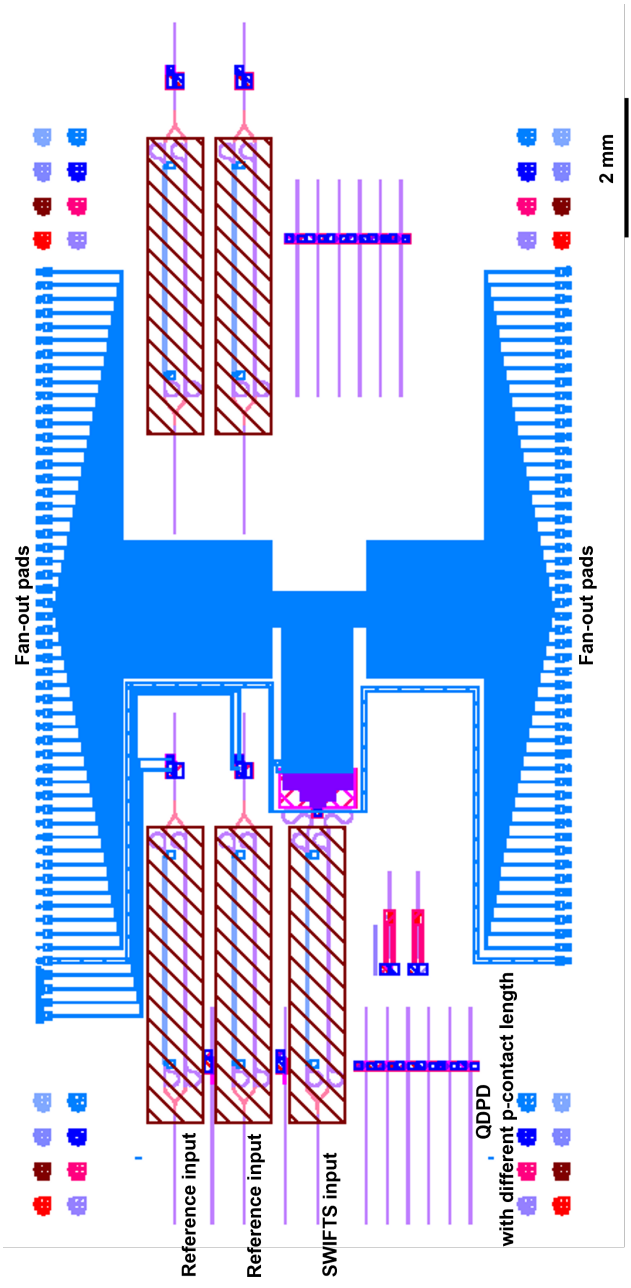

Figure 5.12: Layout of the designed SWIFTS chip.

5.4 Fabrication

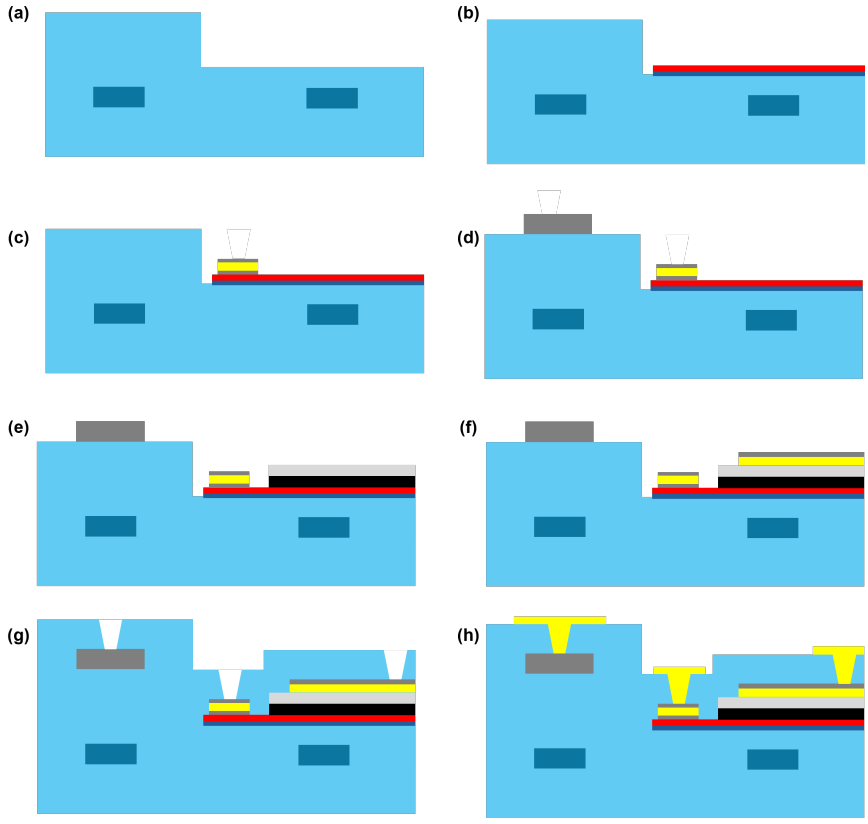

Figure 5.13: Integration steps to fabricate the SWIFTS. (a) Preparation of the passive waveguides. (b) ITO and ZnO patterning. (c) n-contact patterning. (d) Ti heater patterning. (e) QDs patterning. (f) p-contact patterning. (g) PECVD SiO_2 deposition and contact opening. (h) Connection metal patterning.

The fabrication started from a silicon wafer, initially coated with 3.7 μm SiO_2. Subsequently, SiN with a thickness of 350 nm was deposited using PECVD, followed by patterning using EBL and RIE dry etching (refer to Section 2.4.1 for process details). For the top cladding, both flowable oxide (HSQ) and PECVD SiO_2 were employed. HSQ can planarize the surface for the following steps as we mentioned in previous chapters.

Initially, HSQ was utilized for the entire 2 μm thick top cladding that we designed to minimize optical absorption from the thermal phase shifter. However, it proved challenging to achieve the desired 2 μm thickness with HSQ.

For better planarization, we divided the 2 μm HSQ into four layers, each spin-coated and annealed at 400 °C in N_2 for 2 hours, resulting in a thickness of 500 nm per layer. Unfortunately, slight cracks were observed in the film during the third layer, which worsened after the fourth layer deposition, as depicted in Figure 5.14(a). These cracks, likely induced by stress during the HSQ annealing process, could introduce optical scattering and more critically, disrupt the electrical connection of the metal deposited on top.

To attain a crack-free top cladding, we used the combination of HSQ and PECVD SiO_2: two layers of HSQ, each layer with a thickness of 400 nm, were utilized for planarization, supplemented by a 1.2 μm SiO_2 layer deposited via PECVD at 270 °C to achieve the desired cladding thickness, as shown in Figure 5.14(b).

The region designated for the placement of the QDPDs requires a top cladding thickness of 320 nm to facilitate evanescent absorption. To achieve this, the top cladding was patterned with photolithography and RIE dry etching. Photoresist (Ti35 E) with a thickness of 4 μm was patterned in positive mode, utilizing an exposure dose of 500 mJ/cm^2 (5 mW/cm^2, 100s, MA6), followed by development in AZ400:H_2O = 1:3 for 90s. RIE with CF_4, SF_6, H_2 chemistry was then employed to thin down the thickness of the top cladding to 320 nm, as depicted in Figure 5.13(a). A 20s O_2 plasma treatment was conducted to at the beginning of the etching to eliminate any potential photoresist residue. The etch rates of PECVD SiO_2, HSQ, and Ti35 photoresist are 35.2 nm/min, 52.2 nm/min, and 40 nm/min, respectively.

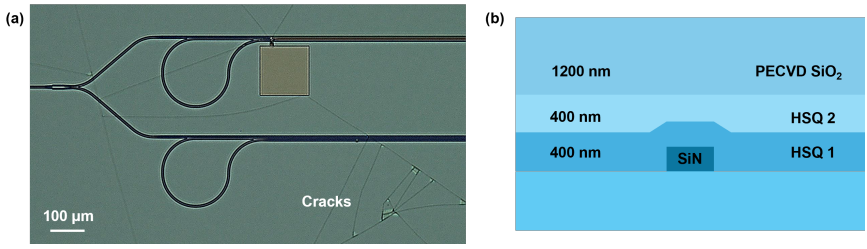

Figure 5.14: Top cladding deposition. (a) A 2 µm thick HSQ layer was utilized as the top cladding. This was achieved through four rounds of spin-coating and annealing, with each cycle forming a 500 nm thick layer. (b) An 800 nm thick HSQ layer and a 1.2 µm PECVD SiO_2 layer were employed as the top cladding. For improved planarization, two layers of HSQ, each 400 nm thick, were utilized.

Afterwards, a 20 nm ITO layer was sputtered onto the sample and patterned using photolithography and HCl-based wet etching. Following this, a 40 nm ZnO layer was deposited via sol-gel chemistry and patterned using a dilute HCl solution, as illustrated in Figure 5.13(b). Subsequently, 20 nm Ti / 100 nm Au / 5 nm n-contact

pads were placed on the side using the lift-off technique, as shown in Figure 5.13(c). Further details on this process can be found in Section 3.3.

Next, a 300 nm Ti layer was deposited on top of one arm using photolithography and the lift-off method, forming the phase shifter, as depicted in Figure 5.13(d). A sacrificial layer of 1.8 μm photoresist (AZ5214) was patterned using the image reversal mode (12 s exposure, 120 °C image reversal bake for 3 min, 50 s flood exposure at 5 mW/cm^2). After development in AZ400K:H_2O = 1:3 for 28 s and a 10 s O_2 plasma treatment with RIE for surface cleaning, 300 nm Ti was deposited using E-gun evaporation. Subsequently, the sample was immersed in acetone for 1 hour to complete the Ti patterning process, as shown in Figure 5.13(e).

On top of the ZnO layer, the QD stacks were placed using the lift-off method. PbS QDs with a band-gap transition of 1355 nm were spin-coated and treated with TBAI in a methanol solution, serving as the absorption layer with a thickness of 60 nm. On top of this, PbS QDs with a 940 nm band-gap transition were spin-coated and treated with EDT in methanol, serving as the HTL with a thickness of 75 nm. The resist patterning and lift-off methods used were consistent with those outlined in Section 2.4.5. Subsequently, 100 nm Au was placed on the QD stacks as the p-contact using another lift-off process, as shown in Figure 5.13(f).

This step is one of the most critical due to the targeted small p-contact size of 100 nm. Previously, we used PMMA with an adapted baking temperature of 60 °C for the p-contact lift-off process. However, this approach did not work for patterning the nano p-contacts.

As depicted in Figure 5.15(a), PMMA baked at 60 °C failed to achieve a clean lift-off in the region with small patterns, likely due to less undercut at the resist sidewall, making it difficult to remove the metal during the resist dissolution process. Conversely, for the standard 150 °C baking, the lift-off was clean, as shown in Figure 5.15(a). The detailed process is as follows: 220 nm PMMA was spin-coated onto the sample, then baked at 150 °C for 3 minutes on the hotplate. A thin layer of conductive polymer (Electra 92, All resist) was spun on top at a speed of 3000 rpm and baked at 90 °C for 2 minutes to dissipate e-beam charges on insulating substrates. The structures were exposed under EBL (Raith, 50kV), with the aid of proximity effect correction at a base dose of 300 μC/cm^2. The resist was developed in AR600-55 for 90 seconds, with a short sonication at the end of the process. A 45 nm Au / 5 nm Ti layer was deposited using E-gun evaporation. The sample was then immersed in acetone for 1 hour, with a short sonication at the beginning of the lift-off process. Nano metal wires with a width down to 20 nm can be achieved with this recipe, as shown in Figure 5.15(b).

To ensure these nanowires are of high quality without breaks, we fabricated 5

nanowires, each with a width of 100 nm and a length of 400 μm, and connected them with two pads on both sides, as shown in Figure 5.15(c). All these nanowires exhibited similar I-V behaviors (Figure 5.15(c)), with a resistance of around 12.6 kΩ.

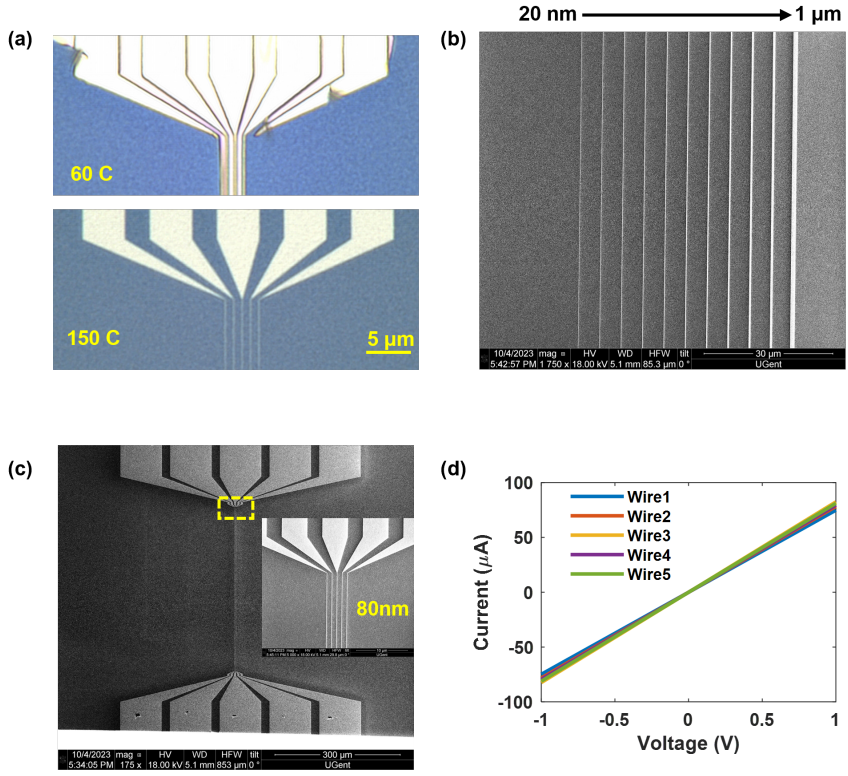

Figure 5.15: Nano p-contact patterning. (a) Liftoff with PMMA baked at different temperatures. (b) Nano p-contact from 20 nm to 1μm. (c) The structure used to test the quality of the nano metal lines with 100 nm width. (d) I-V curves of nano metal lines in (c).

The patterning of the p-contact array was successful as well, as demonstrated in Figure 5.16. The initial fanout of the p-contact array was conducted in three stages of expansion, gradually widening the wire width from 0.1 μm to 3 μm and increasing the pitch between the wires from 1 μm to 10 μm.

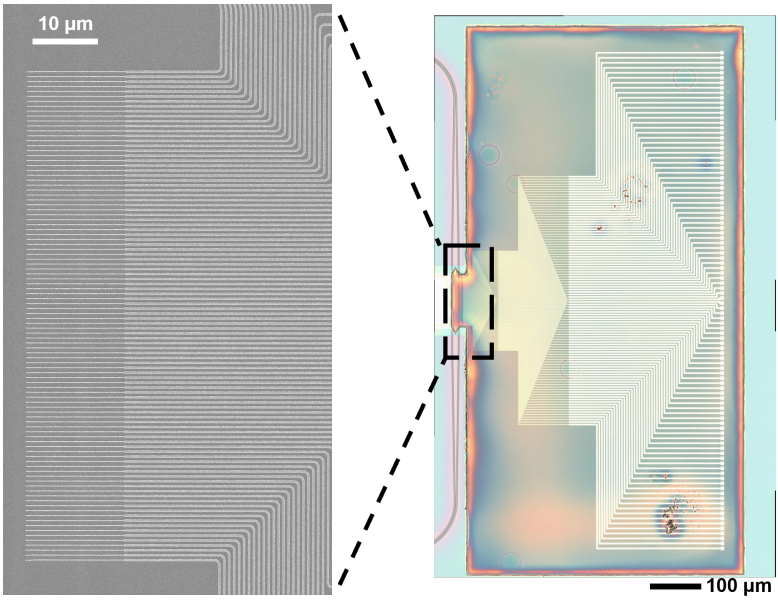

Figure 5.16: Image of the fabricated P-contact array.

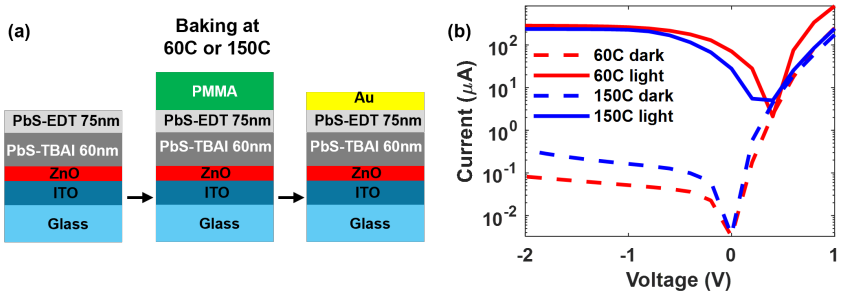

Figure 5.17: Influence of baking temperature on the performance of QDPDs. (a) Structures used for test. (b) The dark and light responses of the QDPDs. The optical power is 1.13 mW and the optical peak power density is around 1 W/cm^2.

We also checked the impact of increased baking temperature on the performance of the QDPD. Two sets of dummy QDPDs were fabricated on glass/ITO substrates, as depicted in Figure 5.17(a). After QD film deposition, they were covered with PMMA and baked either at 60 °C or 150 °C. Following this, the resist was removed with acetone, and Au was evaporated on top. As illustrated in Figure 5.17(b), the QDPD baked at 150 °C exhibited a dark current of 163 nA at -1 V, which was three

times larger than that of the sample baked at 60 °C (52 nA). However, the optical response did not vary significantly under reverse bias. The observed degradation in QDPD performance under the standard baking temperature of 150 °C is acceptable.

Following the integration of QDPDs, a 500 nm SiO_2 layer was deposited atop the sample at 60 °C via PECVD for encapsulation. The SiO_2 cover protects QDPDs from exposure to O_2 and water which are unavoidable during the final metalization process. Metal contacts were subsequently opened using photolithography and RIE dry etching, as illustrated in Figure 5.13(g). Ti35 photoresist, with a thickness of 3.5 μm and patterned in positive mode, served as the etching mask.

Finally, a layer of 20 nm Ti / 400 nm Au was deposited and patterned to provide access to the contacts, as depicted in Figure 5.13(h). For this final pattern, 1.6 μm AZ5214 photoresist patterned in image reversal mode was utilized. The application of Ti prime between the substrate and the photoresist was essential to prevent the photoresist pattern from peeling.

5.5 Characterization

The thermal phase shifters, with varying heater lengths, were characterized on an MZI structure, as depicted in Figure 5.18(a). Characterization was performed using a 1.3 μm laser and a Keithley 2400. The heater length ranged from 1 mm to 4 mm, corresponding to heated waveguide lengths of 3 mm to 12 mm, respectively.

As shown in Figure 5.18(b), as the heater length increased, more bias was required to achieve the same current level due to the increased resistance. However, longer heaters could sustain larger electrical power before thermal damage, thereby offering a greater phase tuning capability. At lower electrical power levels, the current exhibited almost linear behavior with voltage, exhibiting a resistor-like behavior. However, surpassing a certain threshold of electrical power caused the heater's resistance to change, indicating proximity to the limit before thermal damage occurred. For the 1 mm long heater, the maximum power achievable before thermal damage was approximately 1 W. For longer heaters, the damage threshold extended to higher power levels, which were not obtained within the driving voltage range.

The transmission exhibited periodic changes with increased electrical power, as depicted in Figure 5.18(c). Each period indicates a 2π phase change. For an electrical power of 1 W, a phase change of approximately 16π was achieved, consistent with the simulations. The phase tuning behavior of 1 mm and 4 mm long heaters showed no significant difference within the measured electrical power range. However, longer heaters were capable of achieving larger phase shifts

before reaching the thermal damage threshold, potentially reducing the number of nano-QDPDs requiring measurement.

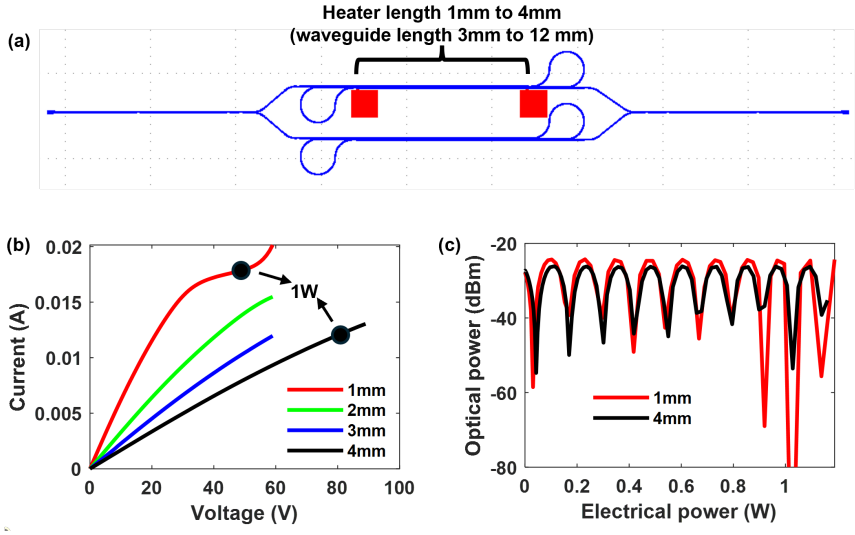

Figure 5.18: Performance of thermal phase shifters. (a) MZI structure used for thermal phase shift measurement. (b) I-V curves of heaters with different lengths. (c) Transmission spectra of MZI (heater length 1 mm and 4 mm) with varying electrical power.

Moreover, we fabricated QDPDs with varying p-contact lengths, ranging from 50 nm to 1 μm, as depicted in Figure 5.19(a). In these structures, the QD film maintained a consistent length of 100 μm, with the p-contacts positioned in the middle of the QD layers. Consequently, the input light encounters the same optical decay from QD absorption and reaches a similar carrier generation rate G_0 at the middle of the QD film, where each nano-QDPD is located. Therefore, the photocurrent generated by each QDPD can be expressed as $I = qG_0l$, where l stands for the p-contact length.

As depicted in Figure 5.19(b), with an increase in p-contact length, the photoresponse exhibits a corresponding increase. Figure 5.19(c) presents the averaged photocurrent from -3.5 V to -4.5 V. As expected, the photocurrent demonstrates a linear increase with p-contact length. Notably, the linear fit reveals that the intercept at the y-axis is not zero when the p-contact length approaches zero. This observation suggests that photocarriers generated in the vicinity of the p-contact can be collected and contribute to the photocurrent. The effective length of this vicinity region can be determined from the intercept at the x-axis, and is found to be 31 nm. This implies that for a 100 nm p-contact length, as utilized for sampling the

interferogram, the effective length extends to 131 nm. Such a small effective length of the vicinity region underscores the essence of employing QDPDs as nanoprobes.

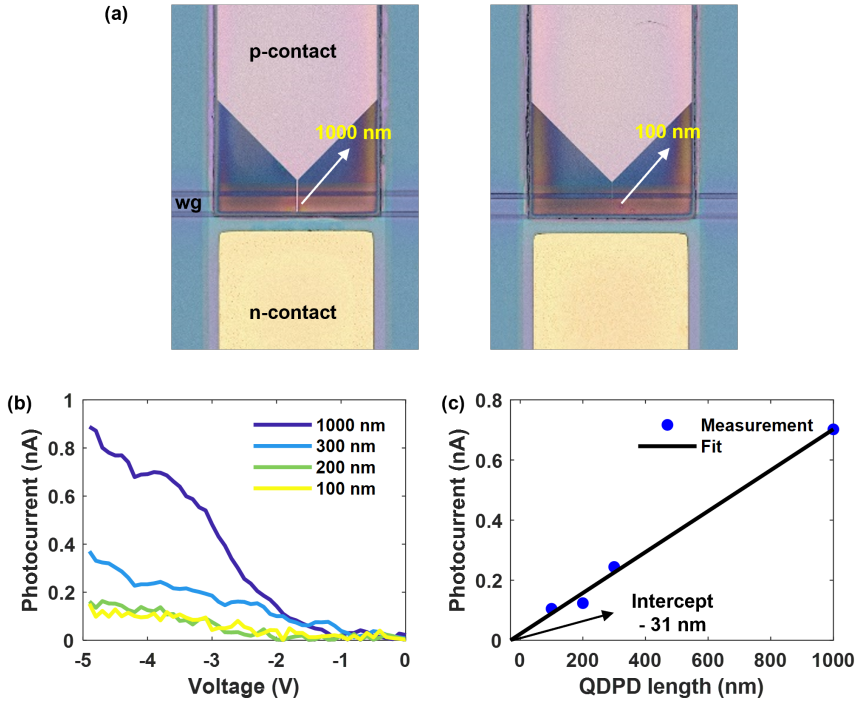

Figure 5.19: Photoresponse of nano QDPDs with different p-contact lengths. (a) Mircoscope image of fabricated nano QDPDs. (b) I-V curves of QDPDs with different p-contact lengths under 1.3 μm illumination. (c) The averaged photocurrent (from -3.5 V to -4.5 V) with different p-contact lengths.

It appears that each individual component of our SWIFTS system operates effectively. However, at the time of writing, we didn't achieve a functional SWIFTS system. The patterning of the final connection wires (Figure 5.13(h)) encountered difficulties due to the unsuccessful peeling of the metal on the resist, as illustrated in Figure 5.20. This issue was particularly pronounced in regions with denser patterns, leading to the shorting of all nano-QDPDs as a whole. Nevertheless, this obstacle is not unsolvable and does not preclude the realization of our SWIFTS system. Employing a thicker photoresist for liftoff should offer a straightforward solution to this problem.

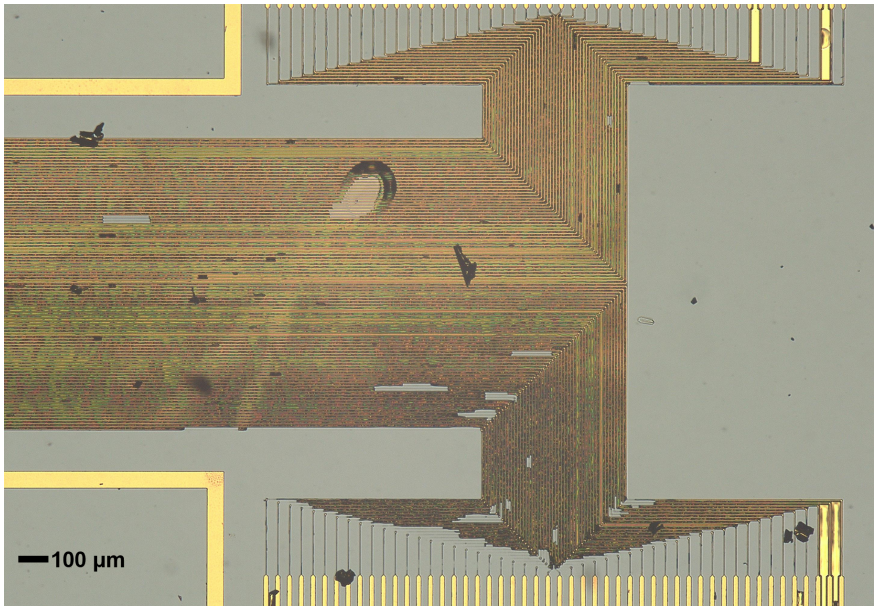

Figure 5.20: Failed connection metal wire patterning.

5.6 Discussion

Based on the preliminary experimental results, we determined that for a 100 nm p-contact size in our SWIFTS system, the effective size of the QDPD is approximately 131 nm. This establishes the lower limit on the optical bandwidth of our system to around 890 nm, assuming a refractive index (n_{eff}) of 1.7, as per Equation 5.2. The upper limit is constrained by the absorption spectrum of our QDs, estimated to be 1.4 μm. QDs with smaller bandgaps are particularly appealing, as they can extend the SWIFTS operation to longer wavelengths, possibly even into the mid-infrared range, thereby broadening the scope of spectroscopic applications. Moreover, shifting to longer wavelengths would relax the requirement on the p-contact size due to the increased stationary wave period in the waveguide. This relaxation opens up the possibility of using the SOI platform, where thermal tuning is more efficient due to the significantly larger thermo-optic coefficient of silicon ($1.5 \times 10^{-4} K^{-1}$) [239].

The spectral resolution of the designed SWIFTS system is estimated to be 5 nm, as calculated by Equation 5.2, limited by the length of the sampling waveguide. To enhance the spectral resolution, one can increase the sampling waveguide length by incorporating more QDPDs or by increasing the pitch of the QDPD array.

5.7 Conclusion

In this chapter, we proposed the utilization of a QDPD array as nano-samplers for SWIFTS. Our spectrometer design is based on a 350 nm SiN waveguide, incorporating a 100-channel QDPD array as the nano-samplers. These QDPDs feature a compact length of 100 nm to locally probe power density in the waveguide and a pitch of 1 μm to facilitate fan-out. A thermal phase shifter with triple-path waveguides underneath proved to supply sufficient phase change to move the interferogram for stiching. A process flow was developed in our cleanroom to fabricate such SWIFTS.

Our investigation revealed that the effective length of the nano QDPD closely aligns with the top p-contact size, thereby validating the feasibility of employing QDPDs as nano-probers. Although the experimental demonstration of the SWIFTS system is still pending, all individual components have exhibited promising performance. Thus far, no significant hurdles have been encountered that would impede our demonstration efforts.

6

Integrated electrically driven QD light sources

6.1 Introduction 137
6.2 Challenges related to QD-based lasing 138
6.3 Integration on waveguide 142
6.3.1 Fabrication 142
6.3.2 Characterization 149
6.4 Optimization of the HTL 153
6.4.1 NPB doped with HAT-CN 154
6.4.2 NPB doped with MoO_3 155
6.4.3 BF-DPB doped with F6-TCNNQ 155
6.5 Discussion 157
6.6 Conclusion 159

6.1 Introduction

Integrating light sources into silicon photonics has been a significant challenge due to the inherent properties of silicon. Silicon is an indirect bandgap semiconductor, which means it is inefficient at emitting light. Traditionally, III-V semiconductors

boasting direct bandgaps, such as GaAs and InP, have been introduced into silicon photonics as light sources. Various methods, including flip-chip mounting, transfer printing, wafer bonding, and monolithic epitaxial growth, have been explored for this hybrid integration. However, these approaches often prove costly for mass fabrication or pose significant challenges in integration, as mentioned in Section 1.3.1.

QDs offer a promising solution to overcome this hurdle. QDs can be deposited onto silicon substrates using simple and cost-effective solution-based techniques, facilitating seamless integration with existing silicon photonics fabrication processes. Notably, CdSe QD-based lasers have been successfully demonstrated on SiN platforms as visible light sources under optical pumping [136, 137, 240]. Despite this progress, the realization of electrically driven QD-based lasers remains challenging. Klimov's group has made significant strides in this area, progressing from the first demonstration of DC-driven gain [111] to recent breakthroughs in electrically driven ASE [114]. On the integration side, Elsinger et al. have showcased the integration of QLEDs on SiN waveguides [139].

In this chapter, we investigate the integration of an electrically driven QD-based light source on SiN waveguides through process flow and material optimization. The optimization builds on the structure proposed by Elsinger et al, using ALD ZnO as the low-loss ETL and thick organic semiconductors as the HTL. We start by analyzing the challenges in achieving net optical gain under electrical pumping. We argue that the high resistance of the thick HTL, employed to mitigate the optical loss from the p-contact metal, leads to a hole-injection problem. Our efforts focus on optimizing the HTL for improved hole transport and employing pulsed electrical pumping to mitigate heating damage. While We observe optical emission from a higher state, further optimization is required to achieve optical gain.

6.2 Challenges related to QD-based lasing

Despite significant advancements in QLEDs, which are approaching commercial viability, transitioning them to quantum dot-based laser diodes remains challenging. To achieve lasing, the gain provided by the QDs must surpass the cavity loss during a round trip. Typically, QLEDs employ a p-i-n structure, with a thin quantum dot film sandwiched between thin electron transport and hole transport layers (ETL and HTL), each tens of nanometers thick. The combination of zinc oxide (ZnO) as the ETL and organic semiconductors as the HTL represents the state-of-the-art material choice for QLEDs. However, this structure suffers from significant optical loss due to the proximity of the optically lossy top and bottom contacts to the guided optical mode.

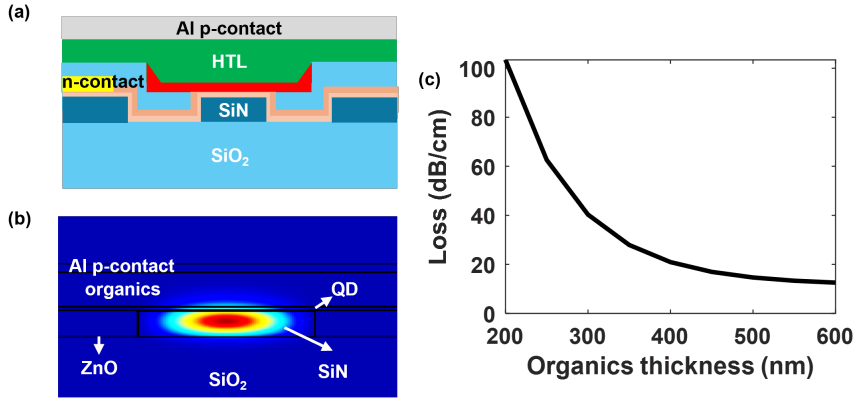

Figure 6.1: Simulation results for waveguide-coupled QLED. (a) Cross-sectional schematic of the hybrid waveguide with the integrated QLED on top. (b) Mode profile showing the fundamental TE mode of this hybrid waveguide. (c) Simulated optical loss with versus thickness of the organics. An ALD ZnO thickness of 10 nm, SiN height of 300 nm and width of 3 μm were used in the simulation.

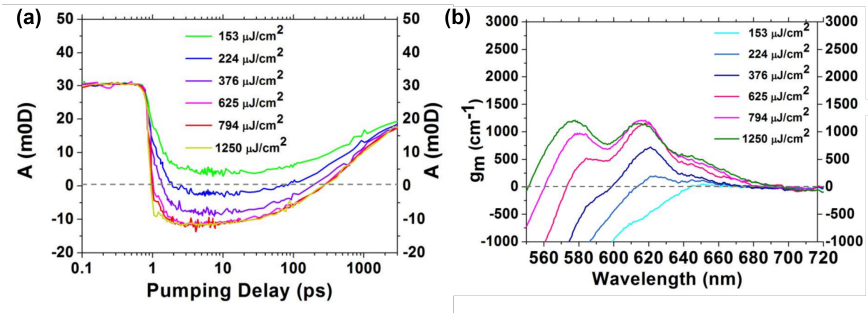

Figure 6.2: Transient absorption characterization of QDs. (a) Time-resolved absorption dynamics at a probe wavelength of 630 nm with excitation at 520 nm. (b) Material gain measured 2.5 ps after excitation. [14]

In our investigation, we utilized the low-loss platform initially developed by Lukas Elsinger for integration [139]. CdSe/CdS core/shell QDs, with an excitonic emission peak around 640 nm, were employed as emitters. These QDs exhibit a gain lifetime of approximately 270 ps and a biexciton lifetime of around 500 ps [14], as shown in Figure 6.2 (a). The material gain reaches up to 1000 cm^{-1} near the first excitonic peak [14], as shown in Figure 6.2 (b).

As depicted in Figure 6.1(a), a SiN waveguide with a height of 300 nm and a width of 3 μm forms the lossless waveguide core. ALD ZnO, with a thickness of 10 nm, served as the low-loss semiconductor for electron injection into the QDs emission layer. A 30 nm thick quantum dot layer atop the waveguide provided gain. Organic semiconductors and an aluminum p-contact injected holes vertically into the QDs. SiN, with its higher refractive index compared to other materials (SiN 1.95, ALD ZnO 1.89+0.0007i, QDs 1.75, organics 1.78), effectively confined light in the SiN core, as illustrated in Figure 6.1(b). Although the intrinsic material gain (g_i) of the utilized QDs could reach as high as 1000 cm^{-1} [14], the modal gain of the fundamental TE mode was around 20 cm^{-1} (87 dB/cm) due to the low confinement factor (Γ) of 3.6% in the QD film ($g_{modal} = \eta\Gamma g_i$, where the QD packaging fraction η was assumed to be 0.5). This low modal gain necessitated optimization of the optical loss to achieve light amplification. TM modes are not used due to the large optical loss they experience from the p-contact metal.

The primary optical loss in this structure stemmed from the top p-contact metal. Decreasing the thickness of the HTL exponentially increased optical loss due to the evanescent tail of the mode, as demonstrated in Figure 6.1(c). To minimize metal absorption, a thick HTL was preferred. For the HTL, tris(4-carbazoyl-9-ylphenyl)amine (TCTA) (sublimed grade, Ossila) and N,N'-Di(1-naphthyl)-N,N'-diphenyl-(1,1'-biphenyl)-4,4'-diamine (NPB) (sublimed grade, Ossila) were employed for better energy alignment with the band edge of the QDs. 1,4,5,8,9,11-Hexaazatriphenylenehexacarbonitrile (HAT-CN) (sublimed grade, Ossila) was used for better hole injection from the aluminum electrode to the NPB HTL [241]. These organic semiconductors also exhibited good optical transparency. Depositing TCTA and NPB on SiN waveguides introduces no obvious optical loss. However, these pristine organic HTLs have low conductivity. We measured the conductivity of NPB using the TLM, with pairs of 3 cm-long interdigitated electrodes with gap distances ranging from 20 μm to 50 μm, as depicted in Figure 6.3(a). The measured resistivity of NPB was approximately $9 \times 10^4 \Omega \cdot m$ at -5 V, indicating that QLEDs with a thick HTL would struggle to achieve high current density. QLEDs with NPB thicknesses of 500 nm and 50 nm, as shown in Figure 6.3(c), exhibited significant differences in their measured I-V curves, as illustrated in Figure 6.3(d). This difference increased at higher voltages, attributed to the current being dominated by space-charge-limited conduction ($J = \frac{9}{8}\epsilon_0\epsilon_r\mu\frac{V^2}{L^3}$, where J represents current

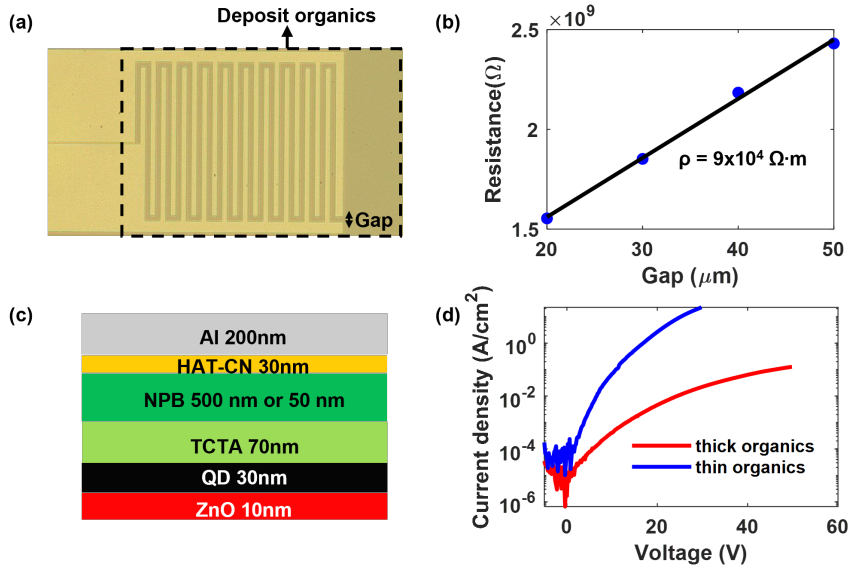

Figure 6.3: Resistivity of NPB and its influence on QLEDs. (a) TLM structure used to measure the resistivity of NPB. NPB was evaporated to a thickness of 100 nm on pairs of gold electrodes with varying gaps. Interdigitated electrodes, 3 cm in length, were employed to facilitate measurable current. (b) Measured resistance corresponding to different electrode gaps under a bias of 5 V. (c) and (d) Structure and I-V curves of QLEDs with NPB thicknesses of 50 nm and 500 nm, respectively.

density, ϵ_0 is the vacuum permittivity, ϵ_r is the relative permittivity, μ is the mobility of the hole, V is the applied voltage, and L is the thickness of the organics), and increased hole mobility at higher electrical field [242, 243]. This prompted us to seek a more conductive HTL (higher mobility or larger doping) to improve hole transport performance in the scenario of thicker layers.

It was reported that a (HAT-CN/NPB)$_n$ alternating structure exhibits significantly improved hole mobility ($5.3 \times 10^{-1} cm^2 V^{-1} s^{-1}$) compared to pure NPB ($2.2 \times 10^{-4} cm^2 V^{-1} s^{-1}$) [244]. Consequently, we tried to use this alternating stack as the HTL for the QLED to enhance hole transport. The HAT-CN layer exhibits relatively higher optical loss compared to NPB and TCTA. Deposition of a 100 nm thick layer of HAT-CN on SiN waveguides with a dimension of 300 nm $\times$ 1 μm resulted in an increase in propagation loss to approximately 40 dB/cm. By fitting to a simulation model, we estimated the complex refractive index to be 1.8+0.0005i. To mitigate optical loss, TCTA and NPB, characterized by low optical absorption, can be interposed between the QDs and the (HAT-CN/NPB)$_n$ stack, as illustrated in Figure 6.4(a). For a total HTL thickness of 400 nm, a dimension chosen to mitigate p-contact absorption, increasing the proportion of low-loss HTL results in reduced

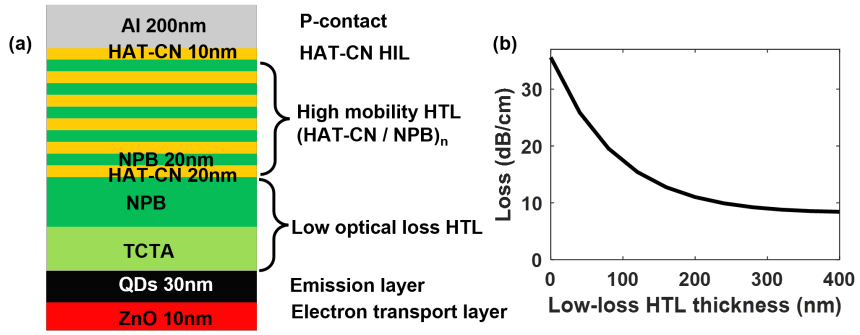

Figure 6.4: Optimization of the QLED structure for integration on SiN waveguide. (a) The QLED structure with 10 nm ALD ZNO, 30 nm QD layer, low-loss HTL consisting of TCTA and NPB, high-mobility HTL consisting of (HAT-CN 20 nm / NPB 20 nm)$_n$ alternating stacks, 10 nm HAT-CN HIL and 200 nm Al top electrode. (b) Simulated optical loss induced by the HTL and p-contact metal at varying thicknesses of the low-loss HTL. The total thickness of the HTL was fixed at 400 nm. Other materials were assumed to be transparent in this simulation.

optical loss due to decreased absorption from the high-mobility HTL layers, as demonstrated in Figure 6.4(b). We selected a combination of 200 nm low-loss HTL (100 nm TCTA + 100 nm NPB) and 200 nm high-mobility HTL ((HAT-CN 20 nm / NPB 20 nm)$\times$5) as the final HTL configuration for our QLED. This selection is expected to introduce an additional loss of approximately 15 dB/cm. Taking into account the loss from ALD ZnO, the total loss is estimated to be 27 dB/cm.

6.3 Integration on waveguide

6.3.1 Fabrication

The fabrication steps used to integrate the QLED stack on top of waveguides are shown in Figure 6.5.

Waveguide paterning

First, a 300 nm SiN layer was deposited on a Si substrate with 1 μm thermal oxide. The SiN was patterned using EBL and RIE dry etching (see Section 2.4.1 for details), as shown in Figure 6.5(a).

The initial step involved depositing a 300 nm layer of SiN on a silicon substrate with

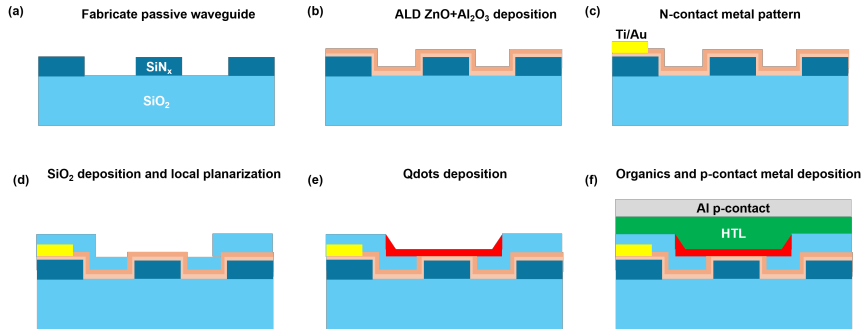

Figure 6.5: Processing steps to integrate QLED stack on SiN waveguides. (a) SiN waveguide patterning, defined with EBL and dry etching. (b) ZnO was deposited using ALD as the ETL, while Al_2O_3 was applied as a protective layer. These layers were patterned through photolithography and wet etching techniques to confine the active region, effectively reducing optical loss. (c) N-contact metal patterning with photolithography and liftoff. (d) SiO_2 deposition with PECVD and local planarization using EBL and dry etching. (e) QD film patterning with EBL and liftoff. (f) Organic semiconductor and Al metal electrode patterning using evaporation through a shadow mask.

a 1 μm thermal oxide. Subsequently, the SiN was patterned using EBL followed by RIE dry etching (for detailed procedures, refer to Section 2.4.1), as illustrated in Figure 6.5(a).

ALD ZnO patterning

Subsequently, 10 nm ZnO and 10 nm Al_2O_3 were deposited on the waveguide conformally using the ALD method (See Section 2.4.2 for deposition details), as shown in Figure 6.5(b). The ALD film was annealed at 400 °C using rapid thermal annealing for 1 min to decrease the optical loss and enhance the electrical conductivity. The annealing temperature significantly influenced the waveguide loss, decreasing from 21 dB/cm before annealing to 5 dB/cm after annealing at the optimized temperature of 400 °C, as depicted in Figure 6.6(a). This improvement is likely attributed to the passivation of intra-band defects [245]. Additionally, annealing at this temperature led to a slight enhancement in the conductivity of the ZnO film, as demonstrated in Figure 6.6(b).

To further reduce optical loss, the ALD ZnO was confined to the active region through photolithography and HCl-based wet etching (refer to Section 2.4.4 for processing details).

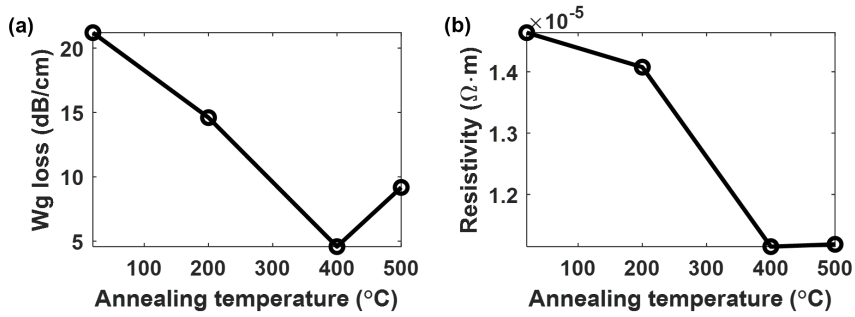

Figure 6.6: Optimization of annealing temperature for ALD ZnO. (a) The propagation loss of waveguides (300 nm × 3 μm) coated with 10 nm ALD ZnO and a 10 nm Al_2O_3 protection layer, rapidly annealed at various temperatures. Optical loss was measured at a wavelength of 640 nm. (b) The resistivity of the ZnO film at different annealing temperatures. Both the optical loss and resistivity were measured using varying length methods.

n-contact patterning

Following that, we deposited 20 nm of Ti / 100 nm of Au / 5 nm of Ti as n-contacts, which were patterned using lift-off methods with photoresist serving as the sacrificial layer (refer to Section 2.4.3 for detailed procedures). The bottom Ti layer was utilized to achieve low contact resistance with ZnO, while the top thin layer of Ti was employed to enhance adhesion to the subsequent SiO_2 cover.

SiO_2 deposition and local planarization

The waveguide needed to be planarized to mitigate the step in height, which could otherwise impede the deposition of QDs.To achieve this, we deposited a 300 nm layer of SiO_2 using PECVD at 150 °C, matching the thickness of SiN, to fill the trench surrounding the waveguide (Figure 6.7(a)). Then EBL was used to precisely expose the extra SiO_2 region on top of the waveguide. Subsequently, ELB was employed to precisely expose the extra SiO_2 region atop the waveguide. Following this, RIE was utilized to remove the SiO_2. To ensure precise control over the etching process, an interference-based in-line etching monitor was employed to ensure that the SiO_2 etching precisely terminated at the Al_2O_3 surface, as depicted in Figure 6.7(c). Finally, O_2 plasma ashing was employed to eliminate any remaining e-beam resist.

This step is the most critical in the fabrication process, and significant effort was devoted to achieve a stable outcome. Several challenges were encountered. Initially, the thin layers of ZnO and Al_2O_3 were prone to damage following planarization.

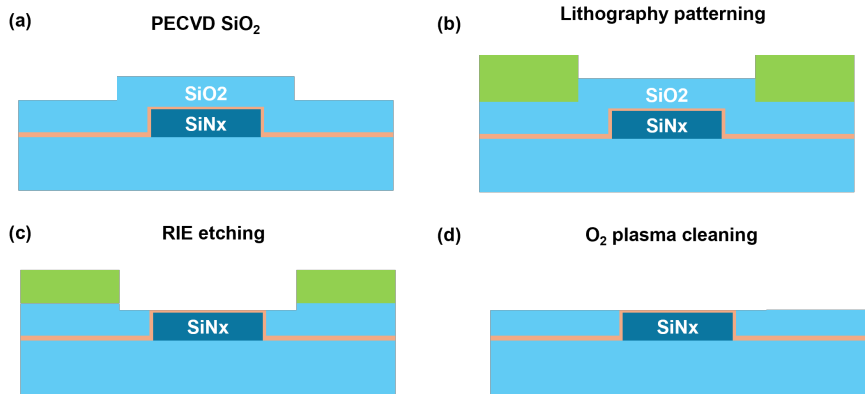

Figure 6.7: Process steps of local planarization. (a) Deposition of 300 nm SiO_2 using PECVD. (b) Patterning of e-beam resist using EBL. We took precise control of the overlap alignment and size dimension. The region with additional surface morphology was exposed, while other parts were protected by the resist after development. (c) RIE dry teaching to remove the excess SiO_2. (d) Removal of the resist with O_2 plasma.

This damage was inconsistent and varied between batches, as illustrated in Figure 6.8(a)-(c) from different planarization tests. One potential source of the damage was the ion bombardment from the RIE process during SiO_2 etching. To address this issue, we reduced the radio-frequency (RF) power used to generate the plasma, thereby decreasing the self-bias of the RIE during etching from 380 V to 200 V. Following this adjustment, the planarization process became more stable, resulting in consistent surface quality after etching, as shown in Figure 6.8(d).

Precise control of the position and dimensions of the etching mask is critical. When the etching width is narrower than the required size of SiO_2 to be planarized, unetched SiO_2 lumps may remain on both sides of the waveguide, as depicted in Figure 6.9(a). This surface morphology can adversely affect the spin-coating of QDs and potentially lead to the formation of pinholes in the fabricated devices.

Another potential issue is misalignment during the process, resulting in a SiO_2 lump on one side and an over-etched valley on the other side, as shown in Figure 6.9(b). The SiO_2 deposited via PECVD exhibits strong stress and relatively weak adhesion to the sidewall of the waveguide. As a result, the SiO_2 on the sidewall becomes isolated due to overetching and tends to peel off, particularly after wet etching of Al_2O_3 for electrical contact with QDs, as depicted in Figure 6.9(c).

Figure 6.9(d) illustrates a scenario of local planarization with poor alignment and size control, where unetched SiO_2 lumps, over-etched valleys, and peeling of SiO_2 from the sidewall are clearly observed.

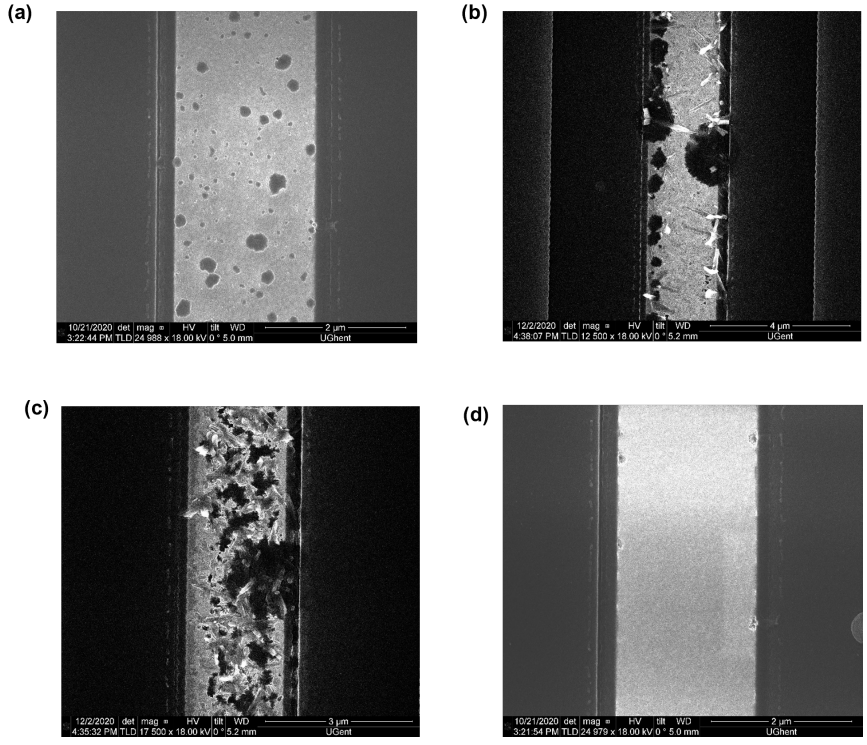

Figure 6.8: SEM images of waveguides after planarization. (a)-(c) SiO_2 etch back using RIE with a self-bias of 380 V. The ZnO and Al_2O_3 layers were susceptible to damage due to the intense ion bombardment. (d) SiO_2 etching with RIE employing a reduced self-bias of 200 V. This resulted in significantly reduced damage to the ZnO and Al_2O_3 layers, and the process exhibited greater stability.

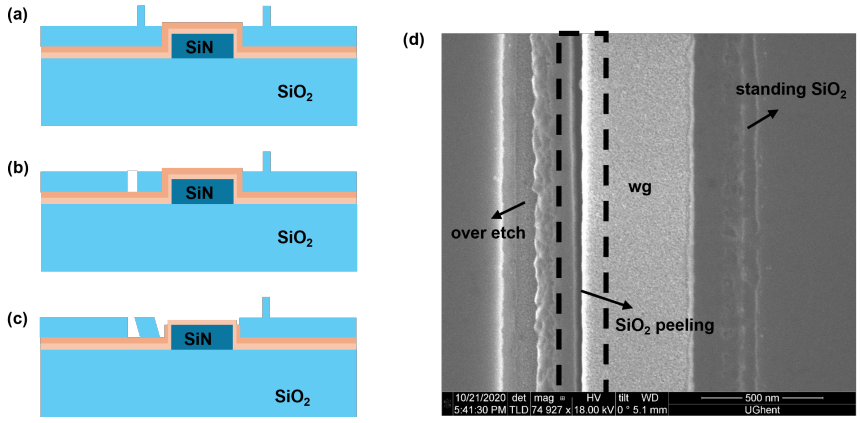

Figure 6.9: Influence of alignment and dimensional accuracy on local planarization. (a) The width of the etched-back area is smaller than the actual SiO_2 width, resulting in unetched SiO_2 lumps on both sides of the waveguide. This phenomenon affects subsequent QD spin-coating processes and introduces pinholes in the devices. (b) The overlap alignment is shifted compared to the target region. On one side, unetched SiO_2 lumps are present, while on the other side, over-etching of SiO_2 leads to a valley formation. (c) The consequence of the over-etched valley is illustrated. Weak adhesion on the SiO_2 deposited on the sidewall of the waveguide, coupled with strong stress in the deposited SiO_2, causes the SiO_2 to peel off, especially after wet etching of Al_2O_3 to expose the ZnO. (d) SEM image of a planarized waveguide with overetching on the left side and a lump on the right side. Peeling of the SiO_2 on the sidewall is evident.

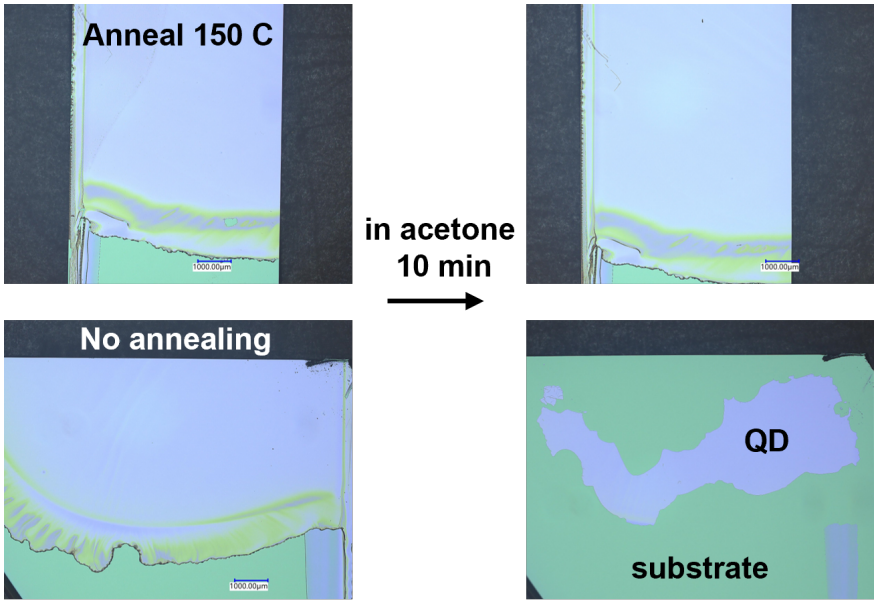

Figure 6.10: The influence of QD annealing is significant. Without annealing, the QD film on the substrate tends to peel off when immersed in acetone during the liftoff process. However, with annealing, the QD film becomes more physically robust, thereby preventing peeling.

QD film patterning

PMMA and liftoff were used for QD film patterning. ARP 672.08 e-beam resist was patterned following the process outlined in Figure 2.4.5. Subsequently, the Al_2O_3 protection layer was removed for electrical contact of ZnO with QDs.

CdSe/CdS core/shell QDs dispersed in n-octane were then spin-coated on top, resulting in a film thickness of approximately 30 nm. To enhance the physical robustness of the QD film and aid in the evaporation of residual solvent, the QD film was annealed in N_2 at 150 °C for 5 minutes. This annealing process is crucial as it prevents the risk of peeling during the subsequent liftoff process in acetone, as illustrated in Figure 6.10.

To assess the impact of annealing on lasing behavior, hybrid waveguides embedding a 50 nm QD film annealed at different temperatures between two SiN films were fabricated. The fabrication process followed the methodology developed by Xie [246] and Zhu [14]. Initially, a 125 nm SiN layer was deposited using PECVD with low frequency to minimize optical loss. The QDs were then spin-coated on top and annealed at various temperatures under N_2 atmosphere for 5 minutes. Subsequently, another layer of 125 nm SiN was deposited on top at 120 °C, employing mixed

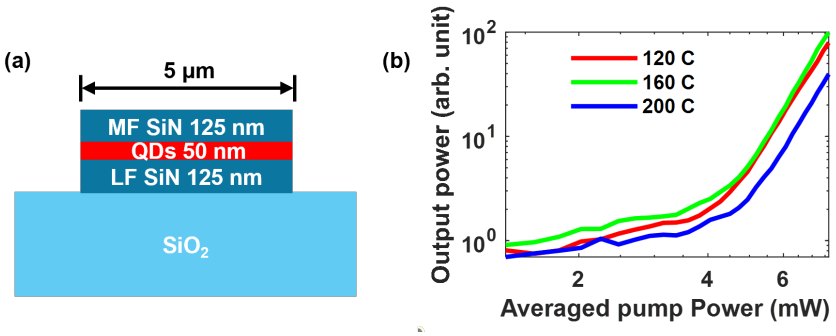

Figure 6.11: Influce of annealing temperature on the performance of ASE under optical pump. (a) Hybrid waveguide with QDs as gain material embedded in SiN. (b) L-L curves of waveguides with QDs annealed at different temperatures under N_2 atmosphere.

frequency mode to reduce stress and form the hybrid waveguides. This hybrid film was patterned into wavegudie shapes using photolithography and RIE dry etching. These waveguides, with lengths around 1500 μm, were pumped using nanosecond pulses with a repetition rate of 938 Hz. The L-L curves (Output power vs. pump power) exhibited similar behavior for annealing temperatures of 120 °C and 160 °C, indicating that annealing does not significantly influence the lasing performance of QDs when annealed at 150 °C for improved physical stability during liftoff. However, a higher annealing temperature of 200 °C slightly increased the ASE threshold, likely due to the increased defect density and faster non-radiative rate at such high temperatures.

Organics and p-contact metal evaporation

The material stack mentioned in Section 6.2, 100 nm TCTA, 100 nm NPB, (HAT-CN 20 nm / NPB 20 nm) $\times 5$, 10 nm HAT-CN, 200 nm Al, were deposited in sequence by thermal evaporation in a deposition chamber (Trovato) in the glovebox [1]. Patterning was achieved using shadow masks positioned in front of the samples during evaporation to prevent overlap with n-contacts.

6.3.2 Characterization

To mitigate overheating, electrical pulses were utilized instead of a DC drive for the sample. The setup is depicted in Figure 6.12. Electrical pulses, featuring a

[1] Deposition of the organic layers and p-contact metal was performed by Frederik Van Acker, associated with the Liquid Crystals and Photonics (LCP) research group of Ghent University.

duration of 2 μs and a period of 0.2 ms, were generated using a function generator (AFG3102, Tektronix). These pulses were then amplified using a high-voltage amplifier (WMA-320, Falco system). The amplified electrical pulse was connected to the device under test via a pair of electrical probes. A 100 Ω load resistor was incorporated in series with the device to convert the current to voltage, which was subsequently measured using an oscilloscope (MSO6021A, Keysight) with high input impedance (1MΩ). The electrical amplifier can boost the electrical pulse to a maximum of 150 V. The emitted light from the device was collected from the cleaved facet using a micro-lensed fiber and then measured using a spectrometer cooled at -80 °C (SR303i, Andor).

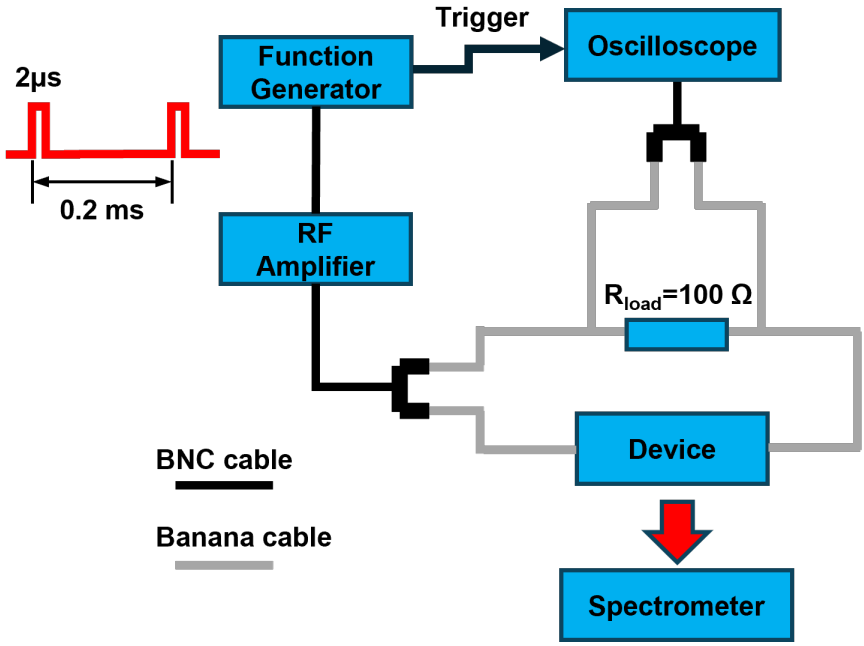

Figure 6.12: The setup for electrical pulse pumping. The device was connected electrically with probes. The emission was collected from the cleaved facet using a micro-lensed fiber.

Figure 6.13(a) shows the current measured with the oscilloscope from the load resistor at different driving voltages. Notably, transient responses occur at the onset and end of the electrical pulse, attributed to the charging and discharging of the capacitor. The actual current driving the QLED can be read from the stable region noted with the black frame.

To understand this, we can analyze the equivalent circuit of the device, depicted in Figure 6.13(b). As illustrated in Figure 6.13(c), the emission region (Region 1) atop the SiN waveguide core can be represented as a diode in series with resistance

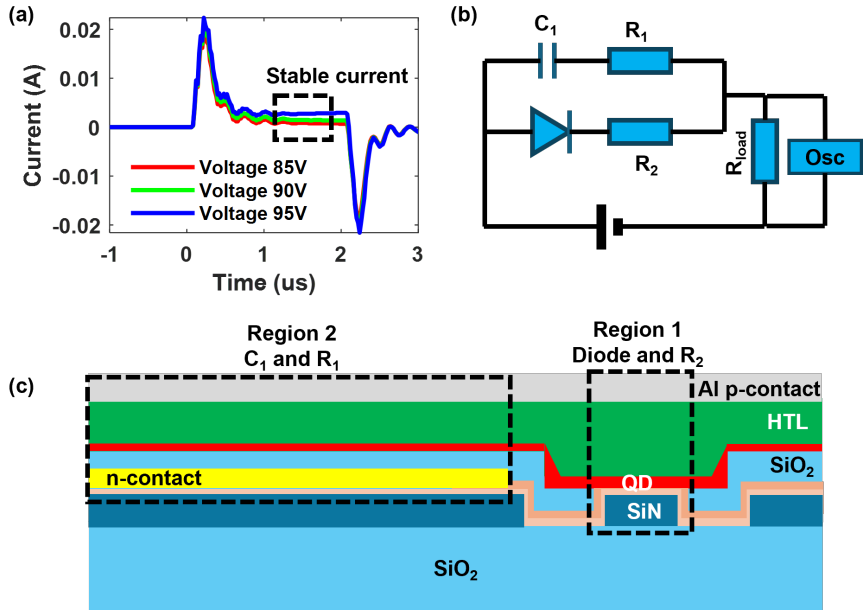

Figure 6.13: Measurement of current driving the QLED under pulsed electrical pumping. (a) The measured current for an active area of 9000 μm^2 at various driving voltages. The measured current exhibits transient behavior at the onset and end of the electrical pulse. The actual current driving the QLED can be determined from the stable region, as indicated by the black frame. (b) and (c) The equivalent circuit of the device and its origin. The emission region, with a narrow area of 9000 μm^2, can be equated to a diode and series resistance R_2. The n-contact, separated from the p-contact by SiO_2 and other layers, constitutes a capacitor C_1 and resistor R_1, in parallel with the diode and R_2. Notably, this area surpasses the emission region in size, exceeding 45000 μm^2, signifying that R_1 is considerably smaller than R_2. A load resistor is positioned in series with these components to convert current into voltage for measurement using the oscilloscope (OSC).

R_2. On the other hand, the n-contact, situated on the side and separated from the p-contact atop by SiO_2 and other layers (Region 2), forms a capacitor C_1 and resistor R_1, which are parallel to the diode and R_2. These components are connected in series with a load resistor. Notably, the area of Region 2 significantly exceeds that of Region 1 ($> 45000\ \mu m^2$ vs. $9000\ \mu m^2$), implying $R_1 << R_2$. At the beginning of the electrical pulse, current predominantly traverses the upper path (capacitor path) due to the substantially lower resistance of R_1 in comparison to R_2. As the capacitor charges, it impedes current flow until reaching equilibrium. Subsequently, current predominantly flows through the lower path (diode path) upon attaining stability, as observed within the delineated region in Figure 6.13(a). Analogously, at the end of the electrical pulse, the capacitor discharging is observed.

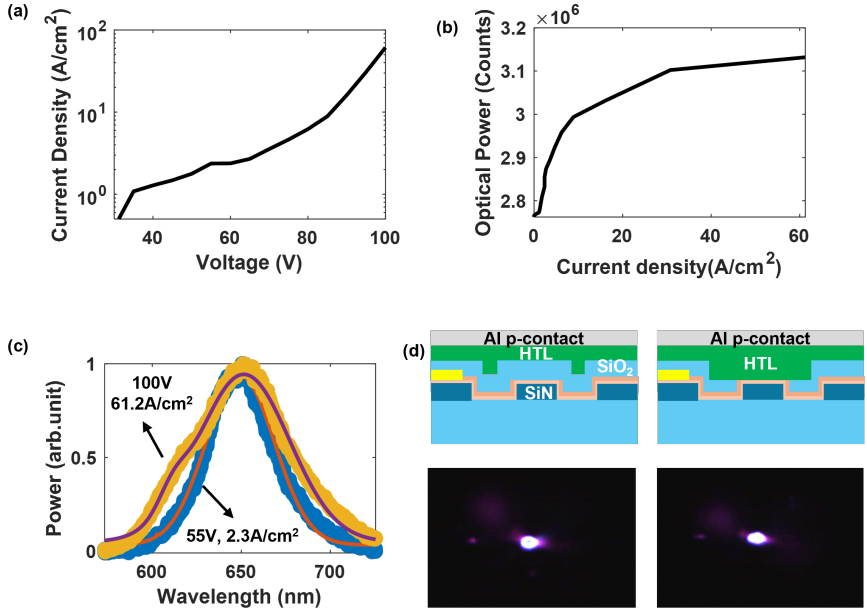

Figure 6.14: Characterization of the waveguide coupled QLED. (a) Current density at different driving voltage. (b) Output power from the cleaved facet at different current densities. (c) The emission spectra at different current densities. (d) Optical transmission measurement on two types of structures. 640 nm laser was injected into the waveguide from the cleaved facet, and the output power from the grating coupler shows a similar level.

The relationship between current density and driving voltage is shown in Figure 6.14(a). At a driving voltage of 100 V, we achieved a current density of 61.2 A/cm^2. While the emission increases with current density, ASE behavior is unfortunately absent, as evidenced in Figure 6.14(b). The increase of output power slows down with higher current density, indicating a decline in EQE. This roll-off is typical in QLEDs and is commonly attributed to Joule heating [247] and increased non-radiative Auger recombination [96] due to imbalanced electron and hole injection.

At higher current densities, additional emission at shorter wavelengths is observed, as shown in Figure 6.14(c), indicating that the ground state is nearly filled, and carriers are beginning to recombine from higher energy states. This emission is not from the organics, since for structures without QDs emission layer, we didn't see measurable emission. To understand the absence of ASE at this high pump level, we assessed the loss from organics and p-contact metal using a pair of structures fabricated on the same chip, as depicted in Figure 6.14(d). The left structure, with a waveguide covered by a 300 nm SiO_2 top cladding, is minimally influenced by the organics and p-contact metal, while the right structure, lacking the SiO_2 top cladding, is more susceptible to absorption from organics and p-contact. We injected a 640 nm laser from the cleaved facet and monitored the transmission power through these two waveguides, each 2 mm in length. The transmission is very similar, with a difference of less than 2 dB, corroborated by the similar emission brightness from the grating coupler (6.14(d) bottom line). This indicates that the optical loss is less than 10 dB/cm, aligning with simulation expectations.

Hence, we attribute the absence of ASE to low optical gain. Achieving a net gain necessitates higher current density. However, further increases in driving voltage and current density resulted in device damage, even under pulsed electrical pumping. Therefore, additional material optimization is required to achieve higher current density and larger optical gain.

6.4 Optimization of the HTL

Achieving an optically low-loss and highly conductive HTL is crucial for attaining net gain in our current platforms. One established strategy for enhancing the HTL conductivity is doping, accomplished by co-evaporating the pristine organic semiconductor with a dopant material. The basic mechanism of p-doping is believed to be the electron transfer from HOMO (termed as valance band maximum in inorganic semiconductor) of the organics semiconductor to the dopant, thereby increasing the hole concentration [248]. However, doping may introduce additional energy states, potentially leading to strong undesired parasitic absorption. Therefore, optimizing the HTL requires careful consideration of both electrical conductivity

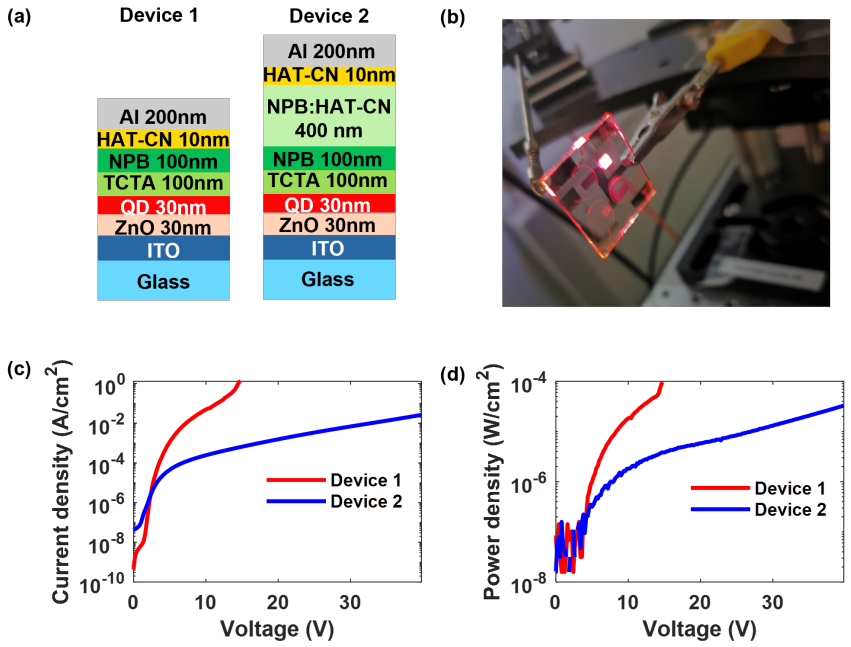

Figure 6.15: The influence of thick NPB:HAT-CN HTL on the performance of QLEDs. (a) QLED structures, device 2 has an extra layer of 400 nm thick NPB doped with HAT-CN. The emission pixel has a dimension of 2 mm × 3 mm, defined by the overlap of the bottom ITO electrode and the top p-contact. (b) Characterization of the QLED. Bright emission from the QLED can be distinctly observed. (c) Current density vs. driving voltage. (d) Output optical power density vs. driving voltage.

and optical absorption characteristics.

6.4.1 NPB doped with HAT-CN

The $(\text{NPB/HAT-CN})_n$ stack was integrated into the waveguide-coupled QLED due to its reported high mobility. To assess its conductivity, we fabricated two types of dummy QLED devices on glass ITO substrates, as illustrated in Figure 6.15(a). Device 1 utilized 100 nm TCTA / 100 nm NPB as the HTL, with a structure of ITO/ 30 nm sol-gel ZnO / 30 nm QDs / 100 nm TCTA / 100 nm NPB / 10 nm HAT-CN / 200 nm Al. Device 2 incorporated an additional layer of NPB doped with HAT-CN, with a structure of ITO/ 30 nm sol-gel ZnO / 30 nm QDs / 100 nm TCTA / 100 nm NPB / 400 nm NPB:HAT-CN / 10 nm HAT-CN / 200 nm Al [2]. Instead of using the

[2]Deposition of the organic layers and p-contact metal was performed by Bernhard Siegmund and Xueshi Jiang, associated with the Organic Opto-Electronics (OOE) research group of Hasselt University.

sequential deposition of (NPB/HAT-CN))$_n$ stack, we used co-evaporation of both materials (NPB:HAT-CN) at the same rate to ease the fabrication. The fabricated QLEDs have a large pixel of around 2 mm $\times$ 3 mm, defined by the overlap of the bottom ITO electrode and top p-contact.

QLEDs were characterized under DC conditions. The emission was collected with a large-area photodiode from the glass side. As shown in Figure 6.15(b), clear red emission from the QDs can be observed. The current density and optical power density of Device 1 exhibit a more rapid increase compared to Device 2, as shown in Figure 6.15(c) and (d) respectively, indicating that the conductivity of NPB:HAT-CN is not sufficiently high compared to pristine NPB and TCTA. This suggests the (NPB/HAT-CN))$_n$ stack used in our waveguide-coupled QLED might also not be conductive enough. Further optimization of the material deposition is needed to achieve the reported improvement in the electrical performance.

6.4.2 NPB doped with MoO_3

Metal oxides such as MoO_3 have been widely studied for the p-doping of organic semiconductors [249, 250]. We conducted measurements of electrical conductivity and optical loss by depositing a 100 nm doped layer on pairs of interdigitated electrodes and SiN waveguides [3], as depicted in Figure 6.16. Indeed, NPB doped with MoO_3 exhibited improved electrical conductivity, as outlined in Table 6.1. Specifically, NPB doped with 15 wt% MoO_3 demonstrates a 3.8-fold reduction in resistivity to $2.4 \times 10^4 \Omega \cdot m$. Further increasing the doping concentration to 33 wt% results in a further decrease in resistivity to $1.9 \times 10^3 \Omega \cdot m$.

However, this doping process significantly increased the optical loss, with an imaginary refractive index reaching as high as 0.021 for a 33 wt% MoO_3 doping concentration. If utilized as an HTL with a thickness of 400 nm, the optical loss would exceed 2000 dB/cm. Such high optical absorption levels are unacceptable for our lasing applications.

6.4.3 BF-DPB doped with F6-TCNNQ

Organic dopants have been widely utilized for p-doping organic semiconductors. In our study, we aimed to dope the pristine HTL N4,N4'-Bis(9,9-dimethyl-9H-fluoren-2-yl)-N4,N4'-diphenylbiphenyl-4,4'-diamine (BF-DPB) due to its high glass transition temperature of 160°C, making it more resistant to heat damage [251]. We

[3] Deposition of the organic layers and p-contact metal was performed by Frederik Van Acker, associated with the Liquid Crystals and Photonics (LCP) research group of Ghent University.

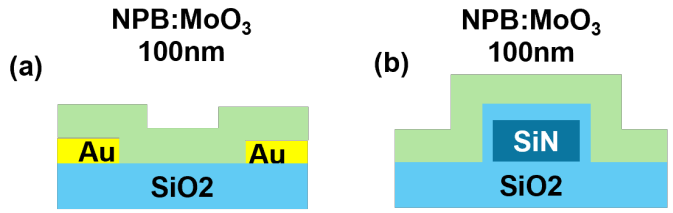

Figure 6.16: Structures to measure the conductivity and optical absorption of NPB doped with MoO_3. (a) A pair of Au electrodes with varying gaps from 10 μm to 50 μm was designed, configured into interdigitated shapes with a length of 3 cm, as illustrated in Figure 6.3(a). (b) Spiral SiN waveguides with dimensions of 300 nm × 1 μm and lengths ranging from 0.9 cm to 1.5 cm were fabricated. To mitigate optical absorption and facilitate measurable transmission power, a 180 nm PECVD SiO_2 layer was deposited on top in the case of NPB with 33wt% MoO_3 doping. 100 nm NPB doped with MoO_3 was coated on these samples.

Material	Resistivity (Ω·m)	Complex refractive index
NPB	9×10^4	1.77
NPB : 15wt% MoO_3	2.4×10^4	-
NPB : 33wt% MoO_3	1.9×10^3	1.81 + 0.021i

Table 6.1: Resistivity and complex refractive index of NPB doped with MoO_3. The resistivity was measured using the TLM method. The real refractive index was measured from ellipsometry. The imaginary refractive index was obtained by measuring the waveguide loss and fitting it into a simulation model. Materials with a thickness of 100 nm were deposited on these characterization samples. The missing value for 15% MoO_3 doping is due to the absence of SiO_2 between the SiN core and the deposited organics in this case. The high absorption results in no measurable transmitted optical power.

co-evaporated (1,3,4,5,7,8-Hexafluoronaphthalene-2,6-diylidene)bis(malononitrile) (F6-TCNNQ) with BF-DPB at a ratio of 4 wt% for p-doping.

Two types of QLED samples were fabricated: one with (Device 3) and one without (Device 4) a 200 nm thick BF-DPB:F6-TCNNQ doped layer, as illustrated in Figure 6.17(a). Interestingly, both QLEDs exhibited similar I-V behavior under high driving conditions, as depicted in Figure 6.17(b), suggesting that the 200 nm thick doped layer introduced little resistance to hole injection into the QD emission layer. This observation was further confirmed by conductivity measurements (Device 5 in Figure 6.17(a)), indicating a resistivity of $2.9 \times 10^2 \Omega \cdot m$, which is approximately one order of magnitude better than NPB doped with MoO_3 and more than 300 times better than pristine NPB. The relatively rapid increase in current at low voltage for Device 3 can be attributed to possible shunt paths resulting from the thin organics thickness. Moreover, the output optical power of Device 4 was three times

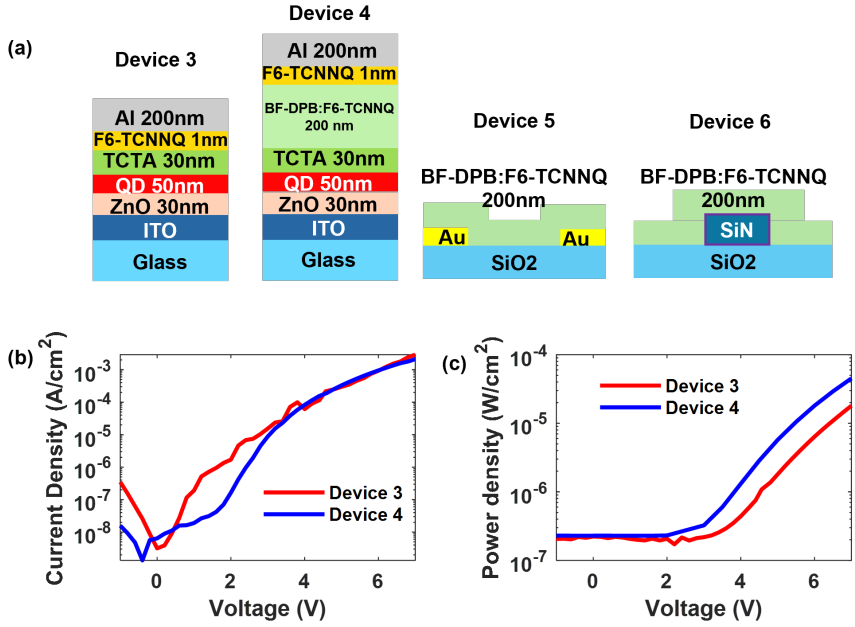

Figure 6.17: The performance of BF-DPB doped with F6-TCNNQ. (a) Device 3 and 4 represent QLED samples with or without a 200 nm layer of BF-DPB:F6-TCNNQ, respectively. Device 5 was employed for conductivity measurement, while Device 6 facilitated absorption measurement. (b) Current density vs. driving voltage. (c) Output optical power density vs. driving voltage.

better than that of Device 3, as shown in Figure 6.17(c), possibly due to improved outcoupling efficiency and reduced shunt current.

We assessed the optical absorption of this doped HTL by depositing it (200 nm thick) on top of the SiN waveguide, as shown in Figure 6.17(a). The measured optical loss was around 1520 dB/cm, corresponding to a complex refractive index of $1.8 + 0.0097i$ when fitted to the simulation model. Although the absorption of BF-DPB:F6-TCNNQ was two times lower than NPB:MoO_3, it was still too high to achieve net gain for lasing.

6.5 Discussion

To achieve net gain with electrical pumping in our current integration platform, we face the challenge of balancing the trade-off between hole injection and optical loss. Increasing the thickness of the HTL to separate the optical mode from the p-

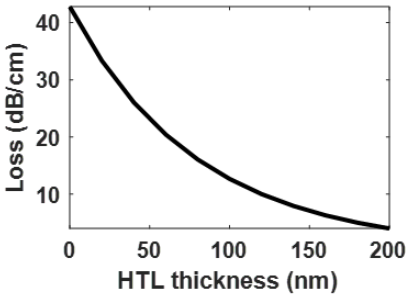

Figure 6.18: ITO induced optical loss for waveguide-coupled LED with different HTL thickness.

contact metal can help reduce optical absorption. However, the low conductivity of commonly used pristine HTL materials poses a challenge in achieving high current density for stimulated emission. Doping the HTL can enhance its conductivity, but this may also introduce parasitic absorption, exacerbating optical losses.

There are several potential approaches to pursuing lasing:

1. Exploration of low-Loss, conductive HTL materials. Candidates can be identified from OLED development, where recent advancements have demonstrated ultrathick HTL OLEDs using hole transport materials with higher mobility. For instance, organic–inorganic perovskite methylammonium lead chloride ($MAPbCl_3$) exhibits high hole mobility (1 $cm^2V^{-1}s^{-1}$) and is transparent to visible light, enabling OLEDs with 1 μm thick HTLs without requiring high voltages [252]. Similarly, 4,4'-(cyclohexane-1,1-diyl)bis(N,N-di-p-tolylaniline) (TAPC) with reasonable hole mobility (3.3×10^{-3} $cm^2V^{-1}s^{-1}$) has demonstrated highly efficient and stable OLEDs with thicknesses exceeding 1 μm and low operating voltages [253]. HAT-CN exhibits very high electron mobility ($0.1 - 1$ $cm^2V^{-1}s^{-1}$) and its deep LUMO aligns well with the HOMO of HTL materials, making it a promising hole transport material. OLEDs with a 1000-nm-thick HAT-CN transport layer functioned properly without a significant decrease in current density [252, 254].

2. Utilization of transparent top electrodes. Another strategy to mitigate optical losses from the top p-contact is to employ a transparent electrode. Covering a SiN waveguide (300 nm $\times$ 3 μm) with a 20 nm ITO layer introduces a propagation loss of only 49 dB/cm (complex refractive index of 2.21 + 0.003i). Consequently, using a 20 nm ITO layer as a p-contact on top of our waveguide-coupled QLEDs would introduce an additional loss of only 13 dB/cm, even with a 100 nm thick HTL layer (see Figure 6.18). The performance of QLEDs with sputtered ITO electrodes deserves further investigation.

3. Optimizzation of the QD layer. Using QDs with suppressed Auger non-radiative recombination is considered one of the most important factors in QLD development. The threshold current density (j_{th}) required to achieve population inversion can be estimated using the equation:

$$j_{th} = \frac{e}{\sigma_e \sqrt{\tau_X \tau_{XX}}} \tag{6.1}$$

where e represents the elementary charge, σ_e is the electrical cross-section, τ_X is the single-exciton lifetime and τ_{XX} is the bi-exciton lifetime. Optimized strategies, such as using a compositionally graded shell, can increase τ_{XX} to ns. Recent advancements have demonstrated ASE with electrical pumping using QDs with enhanced lifetimes [114].

Unbalanced carrier injection into the emission layer, with electrons injected much faster than holes, can lead to QD charging. While this is beneficial for achieving population inversion at lower pump levels, it reduces the maximum achievable optical gain. QDs with higher achievable gain are preferred, as they provide more margin to compensate for optical losses. Recently demonstrated bulk nanocrystals are promising candidates due to their high material gain of around 50000 cm^{-1}, along with reduced Auger recombination and low lasing thresholds [240].

6.6 Conclusion

In this chapter, we investigated the feasibility of integrating CdSe/CdS QDs on SiN waveguides as electrically driven gain material. We identified the insufficient hole injection into the emission layer as the bottleneck for achieving electrically driven gain, mainly due to the thick HTL used to reduce optical loss from the top p-contact metal. To address this issue, we introduced an alternating (NPB/HAT-CN)$_n$ stack into the HTL, leveraging its reported superior hole transport capability and low optical loss. Additionally, we optimized the process flow to integrate the QLED stack on waveguides, combined with an electrical pulse pump featuring a duration of 2 μs and a period of 0.2 ms, resulting in a high current density of 61.2 A/cm^2 at a driving voltage of 100 V and emission from the high state.

To achieve ASE or lasing, improved hole injection is crucial. We explored doping pristine organic semiconductors to enhance conductivity. BF-DPB doped with F6-TCNNQ yielded a significantly more conductive HTL, with a resistivity of $2.9 \times 10^2 \Omega \cdot m$, over 300 times lower than pristine NPB HTL. The insertion of a 200 nm doped HTL layer did not notably affect the performance of QLEDs. However, the doping introduced excessive parasitic absorption, hindering the attainment of net optical gain for lasing. We believe a conductive and low-loss HTL is essential

to achieve waveguide-coupled laser diodes.

7

Conclusion and outlook

7.1 Conclusion 161
7.2 Outlook 163

7.1 Conclusion

In this thesis, we have developed heterogeneous integration processes to bring colloidal quantum dots (QDs) into the field of integrated photonics, serving as photodetectors and electrically driven light sources. Furthermore, we have demonstrated both traditional and two new types of miniaturized spectrometers using QD-based photodetectors as key building blocks.

Unlike the widely studied heterogeneous integration of III-V expixial stacks, where functional stacks are grown in high quality and integration primarily focuses on patterning these stacks using a subtraction process, integrating QDs offers us significant flexibility to add materials heterogeneously layer by layer. However, this also presents challenges in developing a functional process flow. We need to find materials with high optical and electrical quality for each layer and ensure that the integration process itself does not significantly degrade their quality.

First, we developed an integration process to integrate a QD-based photodiode

(QDPD) design on SiN waveguides. We found the main limitation waveguide-coupled QDPDs (WG-QDPDs) face is detector saturation induced by the high optical power density of the guided light. Using the cladding thickness and waveguide width as design parameters, we mitigated this issue, and we demonstrated WG-QDPDs with a responsivity of 0.69 A/W at 1275 nm that exhibit a linear photoresponse for input powers up to 400 nW. Moreover, we successfully demonstrated the integration of a QDPD array with an eight-channel arrayed waveguide grating demultiplexer, effectively functioning as a compact infrared spectrometer. This integration of multiple QDPDs represents a significant step towards the scalable integration of QDPDs in complex photonic integrated circuits, with promising applications in a wide range of fields.

Subsequently, we conducted optimization efforts on both the QDPD material stack and the integration process. This led to the successful integration of QDPDs onto silicon waveguides using larger-size PbS quantum dots, thus extending the photodetection capabilities beyond the traditional telecommunication range in silicon photonics. The achieved results at room temperature, including a low dark current of 106 nA, a high responsivity of 1.3 A/W at 2.1 μm, and a bandwidth of 1.1 MHz. Both the QDPD stack and the integration process were optimized to achieve this level of performance. The scalability of our integration method was exemplified through the presentation of an 8-channel compact spectrometer integrated with a WG-QDPD array. This integrated system offers a promising solution for on-chip spectroscopy around 2.1 μm.

Moreover, we explored the combination of the tunable spectral response of QDPDs with dispersive PICs, demonstrating a spectrometer with a working spectral range beyond one free spectral range (FSR). Leveraging the wavelength response disparity within two cascaded QDPDs, we successfully decoupled two diffraction orders of the planar concave grating (PCG). Our implementation achieved a broad operational range of approximately 180 nm on an eight-channel PCG with a 90 nm FSR, achieving a resolution of 12 nm. The tunable wavelength response of the proposed cascaded QDPDs opens avenues for their integration in various optical configurations, promising enhanced resolution, broader bandwidth, and increased robustness for on-chip computational spectroscopy applications.

In addition, we proposed the utilization of a QDPD array as nano-samplers for a Stationary-Wave Integrated Fourier Transform Spectrometer (SWIFTS). Our spectrometer design was based on a 350 nm SiN waveguide, incorporating a 100-channel QDPD array as the nano-samplers. These QDPDs featured a compact length of 100 nm allowing to locally probe the power density in the waveguide. Our experimental results revealed that the effective length of the nano QDPD closely aligns with the top p-contact size, thereby validating the feasibility of

employing QDPDs as nano-probers. Although the experimental demonstration of the SWIFTS system is still pending, all individual components have exhibited promising performance. We believe the demonstration of our SWIFTS is around the corner.

We also investigated the feasibility of integrating CdSe/CdS QDs on SiN waveguides as electrically driven gain material. We identified the problematic hole injection into the emission layer as the bottleneck for achieving electrically driven gain, mainly due to the thick HTL used to reduce optical loss from the top p-contact metal. To address this issue, we introduced an alternating $(\text{NPB/HAT-CN})_n$ stack into the HTL, leveraging its reported superior hole transport capability and low optical loss. Additionally, we optimized the process flow to integrate the QLED stack on waveguides, combined with an electrical pulse pump featuring a duration of 2 μs and a period of 0.2 ms, resulting in a high current density of 61.2 A/cm^2 at a driving voltage of 100 V and emission from the high state. To achieve ASE or lasing, improved hole injection is crucial. We explored doping pristine organic semiconductors to enhance conductivity. However, the doping introduced excessive parasitic absorption, hindering the attainment of net optical gain for lasing. We believe a conductive and low-loss HTL is essential to achieve waveguide-coupled laser diodes.

7.2 Outlook

For waveguide-coupled QDPDs, there are several directions to explore:

- Optimizing the QDPD material stack to withstand higher optical power saturation thresholds. This will make WG-QDPDs operate efficiently within a smaller footprint and avoid the need of using a thick top cladding, a long absorption length and a wide waveguide width.
- Integrating QDs with extended wavelength absorption capabilities into silicon photonics to broaden its sensing range. Potential candidates include larger PbS QDs, HgTe, and Ag_2Se QDs. This expansion would extend the photodetection capabilities of silicon photonics into the mid-infrared range, aligning with the growing interest in sensing applications.
- Integrating WG-QDPDs on flexible photonic integrated circuits. QDs offer superior mechanical flexibility compared to conventional rigid semiconductors [255]. Exploring the integration of QDPDs onto flexible photonic platforms holds promise for wearable sensing applications.

- Integrating a QDPD array as nano-samplers for SWIFTS. Demonstrating SWIFTS using QDPD array nano-samplers, as pursued in Chapter 5, has the potential to yield a compact on-chip spectrometer with large bandwidth and high resolution.

For QD-based light sources, potential strategies to push towards electrically-driven laser diodes or amplifiers include:

- Exploration of low-loss and conductive hole transport materials. Investigating thick hole transport materials with high conductivity and low parasitic absorption can reduce optical loss from top metal while maintaining a high current density. Materials such as perovskite methylammonium lead chloride ($MAPbCl_3$) [252], TAPC [253], and HAT-CN [252, 254] show promise in this regard.
- Utilization of low-loss top electrodes. Thin layers of transparent electrodes like ZnO or ITO can replace traditional lossy metals, maintaining low optical loss even with a thin hole transport layer.
- Improvement of gain materials. Colloidal nanocrystals, which exhibit suppressed Auger recombination for easier population inversion and offer a larger achievable gain to compensate for optical loss, can facilitate the development of electrically-driven gain. Promising candidates for this purpose include nano-platelets [256] and bulk-like nanocrystals [240].

Given the potential for scalable integration of QDs as both light sources and photodetectors, the prospect of developing a complete spectroscopy chip is highly promising. QDs of varying sizes can be employed to create a broadband light source, while long spiral waveguides can serve as the sensing unit. Integrated spectrometers with QDPDs, as demonstrated in this thesis, can be effectively utilized for signal detection. The low cost of QDs, along with their ease of integration, positions them as competitive candidates for such systems. This integration could lead to compact, cost-effective, and high-performance spectroscopy chips suitable for a wide range of applications, including environmental monitoring, medical diagnostics, and industrial process control.

A

Material synthesis and deposition

A.1 Synthesis of 950 nm PbS CQDs

Lead oleate and N-(3,5-bis(trifluoromethylphenyl))-N'-phenylthiourea were synthesized according to Hendricks et al. [197]. In a three-neck flask, 7.00 mmol lead oleate (5.38 g, 1.50 eq.) was dissolved in 25 mL anhydrous n-octane at 90 °C under a nitrogen atmosphere. In a vial, 4.67 mmol of N-(3,5-bis(trifluoromethylphenyl))-N'-phenylthiourea (1,70 g, 1 eq.) and 2 mL of 1-methoxy-2-(2-methoxyethoxy)ethaan were mixed and heated to 90 °C as well. The thiourea solution was then quickly injected into the lead oleate solution via a syringe and the flask was cooled down to room temperature by immersion into a water batch after one minute. The resulting dispersion was purified four times with the aid of n-octane and acetone under ambient conditions and stored in anhydrous n-octane for further use. The synthesis yielded about 1.5 grams of PbS QDs with a first exciton peak at 950 nm.

A.2 Synthesis of 1300 nm PbS CQDs

In a three-neck flask, 2 mmol lead oleate (1.54 g, 1.33 eq.) was dissolved in 20 mL n-dodecane at 120 °C under a nitrogen atmosphere, and flushed for 30 min. Next, 1.5 mmol of N-(p-(trifluoro-methyl)phenyl)-N'-dodecylthiourea (0.5828 g, 1 eq.)

was mixed with 1 mL of 1-methoxy-2-(2-methoxyethoxy)ethaan or diglyme under a nitrogen atmosphere, preheated at 120 °C and quickly injected into the lead oleate solution at 120 °C. The reaction mixture was cooled down to room temperature by immersing the flask in a water bath after 80 sec. The resulting dispersion was then purified at least four times with the aid of octane/acetone and finally passed through a 0.45 μm pore size syringe filter before re-dispersion in anhydrous n-octane and adjusting the desired concentration.

A.3 Synthesis of 2100 nm PbS CQDs

In a three-neck flask, 1.2 mmol lead oleate (0.9241 g) was dissolved in 20 mL n-dodecane at 150 °C under a nitrogen atmosphere. Separately, N-n-hexyl-N'-dodecylthiourea (1 mmol, 0.3286 g) was mixed with 1 mL of diglyme (Diethylene Glycol Dimethyl Ether) in a vial and heated to 150 °C. The pre-heated thiourea solution was then injected swiftly into the lead oleate solution via a syringe and the reaction was allowed to run for 20 minutes at 150 °C. Subsequently, the flask was cooled down to ambient temperature by immersion into a water bath. The final dispersion underwent four purification cycles inside a nitrogen-filled glovebox, using a solvent mixture of 4:1 toluene to hexane, with methyl acetate as the non-solvent. The purified PbS QDs were dispersed in anhydrous n-octane to achieve the desired concentration.

A.4 Preparation of sol-gel ZnO presursor

Zinc acetate dihydrate (0.132 g) and ethanolamine (37 μL) were dissolved in 2-methoxyethanol (2 mL) inside a N2 glovebox. The precursor solution is filtered with a 0.2 μm pore size syringe filter and stored in ambient conditions for further use.

References

[1] F Pelayo García de Arquer, Dmitri V Talapin, Victor I Klimov, Yasuhiko Arakawa, Manfred Bayer, and Edward H Sargent. *Semiconductor quantum dots: Technological progress and future challenges*. Science, 373(6555):eaaz8541, 2021.

[2] Chen Dong, Shuyi Liu, Nilesh Barange, Jaewoong Lee, Tyler Pardue, Xueping Yi, Shichen Yin, and Franky So. *Long-wavelength lead sulfide quantum dots sensing up to 2600 nm for short-wavelength infrared photodetectors*. ACS applied materials & interfaces, 11(47):44451–44457, 2019.

[3] Emmanuel Lhuillier, Sean Keuleyan, and Philippe Guyot-Sionnest. *Optical properties of HgTe colloidal quantum dots*. Nanotechnology, 23(17):175705, 2012.

[4] Jason P Clifford, Gerasimos Konstantatos, Keith W Johnston, Sjoerd Hoogland, Larissa Levina, and Edward H Sargent. *Fast, sensitive and spectrally tuneable colloidal-quantum-dot photodetectors*. Nature nanotechnology, 4(1):40–44, 2009.

[5] Chia-Hao M Chuang, Patrick R Brown, Vladimir Bulović, and Moungi G Bawendi. *Improved performance and stability in quantum dot solar cells through band alignment engineering*. Nature materials, 13(8):796–801, 2014.

[6] Jaehoon Kim, Jeongkyun Roh, Myoungjin Park, and Changhee Lee. *Recent Advances and Challenges of Colloidal Quantum Dot Light-Emitting Diodes for Display Applications*. Advanced Materials, page 2212220, 2023.

[7] A Moscoso-Mártir, F Merget, J Mueller, J Hauck, S Romero-García, B Shen, F Lelarge, R Brenot, A Garreau, E Mentovich, et al. *Hybrid silicon photonics flip-chip laser integration with vertical self-alignment*. In Conference on Lasers and Electro-Optics/Pacific Rim, page s2069. Optica Publishing Group, 2017.

[8] Yuting Shi, Zhechao Wang, Joris Van Campenhout, Marianna Pantouvaki, Weiming Guo, Bernardette Kunert, and Dries Van Thourhout. *Optical pumped InGaAs/GaAs nano-ridge laser epitaxially grown on a standard 300-mm Si wafer*. Optica, 4(12):1468–1473, 2017.

[9] Jing Zhang, Grigorij Muliuk, Joan Juvert, Sulakshna Kumari, Jeroen Goyvaerts, Bahawal Haq, Camiel Op de Beeck, Bart Kuyken, Geert Morthier, Dries Van Thourhout, et al. *III-V-on-Si photonic integrated circuits realized using micro-transfer-printing*. APL photonics, 4(11), 2019.

[10] Di Liang, Gunther Roelkens, Roel Baets, and John E Bowers. *Hybrid integrated platforms for silicon photonics*. Materials, 3(3):1782–1802, 2010.

[11] Shibnath Pathak. *Silicon nano-photonics based arrayed waveguide gratings*. PhD thesis, Ghent University, 2014.

[12] Eva Ryckeboer, Xiaomin Nie, Ananth Z Subramanian, Daan Martens, Peter Bienstman, Stephane Clemmen, Simone Severi, Roelof Jansen, Gunther Roelkens, and Roel Baets. *CMOS-compatible silicon nitride spectrometers for lab-on-a-chip spectral sensing*. In Silicon Photonics and Photonic Integrated Circuits V, volume 9891, pages 274–282. SPIE, 2016.

[13] Joost Brouckaert. *Integration of photodetectors on silicon photonic integrated circuits (PICs) for spectroscopic applications*. PhD thesis, 2010.

[14] Yunpeng Zhu. *Colloidal quantum dots as the active material for silicon nitride photonics*. PhD thesis, Ghent University, 2018.

[15] Emmanuel Lhuillier, Jonathan S Steckel, Clément Livache, and Peter Reiss. *Chemistry Nobel Prize Celebrates Colloidal Quantum Dots: Highly-Engineered, Spectrally Pure Light*. Photoniques, (122):18–20, 2023.

[16] R Rossetti and L Brus. *Electron-hole recombination emission as a probe of surface chemistry in aqueous cadmium sulfide colloids*. The Journal of Physical Chemistry, 86(23):4470–4472, 1982.

[17] R Rossetti, S Nakahara, and Louis E Brus. *Quantum size effects in the redox potentials, resonance Raman spectra, and electronic spectra of CdS crystallites in aqueous solution*. The Journal of Chemical Physics, 79(2):1086–1088, 1983.

[18] Louis E Brus. *Electron–electron and electron-hole interactions in small semiconductor crystallites: The size dependence of the lowest excited electronic state*. The Journal of chemical physics, 80(9):4403–4409, 1984.

[19] CBea Murray, David J Norris, and Moungi G Bawendi. *Synthesis and characterization of nearly monodisperse CdE (E= sulfur, selenium, tellurium) semiconductor nanocrystallites*. Journal of the American Chemical Society, 115(19):8706–8715, 1993.

[20] Dadi Tian, Haiguang Ma, Guangguang Huang, Min Gao, Fensha Cai, Yan Fang, Chenguang Li, Xiaohong Jiang, Aqiang Wang, Shujie Wang, et al. *A Review on Quantum Dot Light-Emitting Diodes: From Materials to Applications*. Advanced Optical Materials, 11(2):2201965, 2023.

[21] Namyoung Ahn, Clément Livache, Valerio Pinchetti, and Victor I Klimov. *Colloidal Semiconductor Nanocrystal Lasers and Laser Diodes*. Chemical Reviews, 123(13):8251–8296, 2023.

[22] Cherie R Kagan, Lee C Bassett, Christopher B Murray, and Sarah M Thompson. *Colloidal quantum dots as platforms for quantum information science*. Chemical reviews, 121(5):3186–3233, 2020.

[23] Graham H Carey, Ahmed L Abdelhady, Zhijun Ning, Susanna M Thon, Osman M Bakr, and Edward H Sargent. *Colloidal quantum dot solar cells*. Chemical reviews, 115(23):12732–12763, 2015.

[24] Haobo Wu and Zhijun Ning. *Tutorial: Lead sulfide colloidal quantum dot infrared photodetector*. Journal of Applied Physics, 133(4), 2023.

[25] Haiwei Chen, Juan He, and Shin-Tson Wu. *Recent advances on quantum-dot-enhanced liquid-crystal displays*. IEEE Journal of Selected Topics in Quantum Electronics, 23(5):1–11, 2017.

[26] Zhaojun Liu, Chun-Ho Lin, Byung-Ryool Hyun, Chin-Wei Sher, Zhijian Lv, Bingqing Luo, Fulong Jiang, Tom Wu, Chih-Hsiang Ho, Hao-Chung Kuo, et al. *Micro-light-emitting diodes with quantum dots in display technology*. Light: Science & Applications, 9(1):83, 2020.

[27] Jiwoong Yang, Moon Kee Choi, U Jeong Yang, Seo Young Kim, Young Seong Kim, Jeong Hyun Kim, Dae-Hyeong Kim, and Taeghwan Hyeon. *Toward full-color electroluminescent quantum dot displays*. Nano Letters, 21(1):26–33, 2020.

[28] Vladimir Pejović, Epimitheas Georgitzikis, Jiwon Lee, Itai Lieberman, David Cheyns, Paul Heremans, and Paweł E Malinowski. *Infrared colloidal quantum dot image sensors*. IEEE Transactions on Electron Devices, 69(6):2840–2850, 2021.

[29] Roel Baets, Ananth Z Subramanian, Stéphane Clemmen, Bart Kuyken, Peter Bienstman, Nicolas Le Thomas, Günther Roelkens, Dries Van Thourhout, Philippe Helin, and Simone Severi. *Silicon photonics: Silicon nitride versus silicon-on-insulator*. In Optical Fiber Communication Conference, pages Th3J–1. Optica Publishing Group, 2016.

[30] Joel Jean, Justin Xiao, Robert Nick, Nicole Moody, Michel Nasilowski, Moungi Bawendi, and Vladimir Bulović. *Synthesis cost dictates the commercial viability of lead sulfide and perovskite quantum dot photovoltaics*. Energy & Environmental Science, 11(9):2295–2305, 2018.

[31] *https://news.stanford.edu/pr/2015/pr-chips-laser-lift-032415.html*. Accessed 2 February 2024.

[32] Qian Zhao, Rui Han, Ashley R Marshall, Shuo Wang, Brian M Wieliczka, Jian Ni, Jianjun Zhang, Jianyu Yuan, Joseph M Luther, Abhijit Hazarika, et al. *Colloidal Quantum Dot Solar Cells: Progressive Deposition Techniques and Future Prospects on Large-Area Fabrication*. Advanced Materials, 34(17):2107888, 2022.

[33] Illan J Kramer, James C Minor, Gabriel Moreno-Bautista, Lisa Rollny, Pongsakorn Kanjanaboos, Damir Kopilovic, Susanna M Thon, Graham H Carey, Kang Wei Chou, David Zhitomirsky, et al. *Efficient spray-coated colloidal quantum dot solar cells*. Advanced materials, 27(1):116–121, 2015.

[34] Min-Jae Choi, YongJoo Kim, Hunhee Lim, Erkki Alarousu, Aniruddha Adhikari, Basamat S Shaheen, Yong Ho Kim, Omar F Mohammed, Edward H Sargent, Jin Young Kim, et al. *Tuning Solute-Redistribution Dynamics for Scalable Fabrication of Colloidal Quantum-Dot Optoelectronics*. Advanced Materials, 31(32):1805886, 2019.

[35] Yang Liu, Fushan Li, Zhongwei Xu, Congxiu Zheng, Tailiang Guo, Xiangwei Xie, Lei Qian, Dong Fu, and Xiaolin Yan. *Efficient all-solution processed quantum dot light emitting diodes based on inkjet printing technique*. ACS applied materials & interfaces, 9(30):25506–25512, 2017.

[36] Peihua Yang, Long Zhang, Dong Jin Kang, Robert Strahl, and Tobias Kraus. *High-resolution inkjet printing of quantum dot light-emitting microdiode arrays*. Advanced Optical Materials, 8(1):1901429, 2020.

[37] Chaoyu Xiang, Longjia Wu, Zizhe Lu, Menglin Li, Yanwei Wen, Yixing Yang, Wenyong Liu, Ting Zhang, Weiran Cao, Sai-Wing Tsang, et al. *High efficiency and stability of ink-jet printed quantum dot light emitting diodes*. Nature communications, 11(1):1646, 2020.

[38] Frédéric Doumenc, Jean-Baptiste Salmon, and Béatrice Guerrier. *Modeling flow coating of colloidal dispersions in the evaporative regime: Prediction of deposit thickness*. Langmuir, 32(51):13657–13668, 2016.

[39] Havid Aqoma and Sung-Yeon Jang. *Solid-state-ligand-exchange free quantum dot ink-based solar cells with an efficiency of 10.9%*. Energy & Environmental Science, 11(6):1603–1609, 2018.

[40] Gabriele Rainò, Nuri Yazdani, Simon C Boehme, Manuel Kober-Czerny, Chenglian Zhu, Franziska Krieg, Marta D Rossell, Rolf Erni, Vanessa Wood, Ivan Infante, et al. *Ultra-narrow room-temperature emission from single CsPbBr3 perovskite quantum dots*. Nature communications, 13(1):2587, 2022.

[41] Iek-Heng Chu, Marina Radulaski, Nenad Vukmirovic, Hai-Ping Cheng, and Lin-Wang Wang. *Charge transport in a quantum dot supercrystal*. The Journal of Physical Chemistry C, 115(43):21409–21415, 2011.

[42] Lilei Hu and Andreas Mandelis. *Advanced characterization methods of carrier transport in quantum dot photovoltaic solar cells*. Journal of Applied Physics, 129(9), 2021.

[43] Dmitri V Talapin, Jong-Soo Lee, Maksym V Kovalenko, and Elena V Shevchenko. *Prospects of colloidal nanocrystals for electronic and optoelectronic applications*. Chemical reviews, 110(1):389–458, 2010.

[44] Patrick R Brown, Donghun Kim, Richard R Lunt, Ni Zhao, Moungi G Bawendi, Jeffrey C Grossman, and Vladimir Bulovic. *Energy level modification in lead sulfide quantum dot thin films through ligand exchange*. ACS nano, 8(6):5863–5872, 2014.

[45] Neil C Greenham, Xiaogang Peng, and A Paul Alivisatos. *Charge separation and transport in conjugated-polymer/semiconductor-nanocrystal composites studied by photoluminescence quenching and photoconductivity*. Physical review B, 54(24):17628, 1996.

[46] Philippe Guyot-Sionnest and Congjun Wang. *Fast voltammetric and electrochromic response of semiconductor nanocrystal thin films*. The Journal of Physical Chemistry B, 107(30):7355–7359, 2003.

[47] Dong Yu, Congjun Wang, and Philippe Guyot-Sionnest. *n-Type conducting CdSe nanocrystal solids*. Science, 300(5623):1277–1280, 2003.

[48] MV Jarosz, VJ Porter, BR Fisher, MA Kastner, and MG Bawendi. *Photoconductivity studies of treated CdSe quantum dot films exhibiting increased exciton ionization efficiency*. Physical Review B, 70(19):195327, 2004.

[49] Gerasimos Konstantatos, Ian Howard, Armin Fischer, Sjoerd Hoogland, Jason Clifford, Ethan Klem, Larissa Levina, and Edward H Sargent. *Ultrasensitive solution-cast quantum dot photodetectors*. Nature, 442(7099):180–183, 2006.

[50] SA McDonald, PW Cyr, L Levina, and EH Sargent. *Photoconductivity from PbS-nanocrystal/ semiconducting polymer composites for solution-processible, quantum-size tunable infrared photodetectors*. Applied physics letters, 85(11):2089–2091, 2004.

[51] Steven A McDonald, Gerasimos Konstantatos, Shiguo Zhang, Paul W Cyr, Ethan JD Klem, Larissa Levina, and Edward H Sargent. *Solution-processed PbS quantum dot infrared photodetectors and photovoltaics*. Nature materials, 4(2):138–142, 2005.

[52] Gerasimos Konstantatos, Michela Badioli, Louis Gaudreau, Johann Osmond, Maria Bernechea, F Pelayo Garcia De Arquer, Fabio Gatti, and Frank HL Koppens. *Hybrid graphene–quantum dot phototransistors with ultrahigh gain*. Nature nanotechnology, 7(6):363–368, 2012.

[53] Zhenhua Sun, Zhike Liu, Jinhua Li, Guo-an Tai, Shu-Ping Lau, and Feng Yan. *Infrared photodetectors based on CVD-grown graphene and PbS quantum dots with ultrahigh responsivity*. Advanced materials, 24(43):5878–5883, 2012.

[54] Jason P Clifford, Keith W Johnston, Larissa Levina, and Edward H Sargent. *Schottky barriers to colloidal quantum dot films*. Applied Physics Letters, 91(25), 2007.

[55] Shuaicheng Lu, Peilin Liu, Junrui Yang, Shijie Liu, Yang Yang, Long Chen, Jing Liu, Yuxuan Liu, Bo Wang, Xinzheng Lan, et al. *High-Performance Colloidal Quantum Dot Photodiodes via Suppressing Interface Defects*. ACS Applied Materials & Interfaces, 15(9):12061–12069, 2023.

[56] Darshan H Parmar, Joao M. Pina, Tong Zhu, Maral Vafaie, Ozan Atan, Margherita Biondi, Amin M Najjariyan, Sjoerd Hoogland, and Edward H Sargent. *Controlled Crystal Plane Orientations in the ZnO Transport Layer Enable High-Responsivity, Low-Dark-Current Infrared Photodetectors*. Advanced Materials, 34(17):2200321, 2022.

[57] Maral Vafaie, James Z Fan, Amin Morteza Najarian, Olivier Ouellette, Laxmi Kishore Sagar, Koen Bertens, Bin Sun, F Pelayo García de Arquer, and Edward H Sargent. *Colloidal quantum dot photodetectors with 10-ns response time and 80% quantum efficiency at 1,550 nm*. Matter, 4(3):1042–1053, 2021.

[58] Jesse R Manders, Tzung-Han Lai, Yanbin An, Weikai Xu, Jaewoong Lee, Do Young Kim, Gijs Bosman, and Franky So. *Low-noise multispectral photodetectors made from all solution-processed inorganic semiconductors*. Advanced Functional Materials, 24(45):7205–7210, 2014.

[59] Jing Liu, Peilin Liu, Dengyang Chen, Tailong Shi, Xixi Qu, Long Chen, Tong Wu, Jiangping Ke, Kao Xiong, Mingyu Li, et al. *A near-infrared colloidal quantum dot imager with monolithically integrated readout circuitry*. Nature Electronics, 5(7):443–451, 2022.

[60] Rafal Sliz, Marc Lejay, James Z Fan, Min-Jae Choi, Sachin Kinge, Sjoerd Hoogland, Tapio Fabritius, F Pelayo Garcia de Arquer, and Edward H Sargent. *Stable colloidal quantum dot inks enable inkjet-printed high-sensitivity infrared photodetectors*. ACS nano, 13(10):11988–11995, 2019.

[61] Sean Keuleyan, Emmanuel Lhuillier, Vuk Brajuskovic, and Philippe Guyot-Sionnest. *Mid-infrared HgTe colloidal quantum dot photodetectors*. Nature Photonics, 5(8):489–493, 2011.

[62] Sean E Keuleyan, Philippe Guyot-Sionnest, Christophe Delerue, and Guy Allan. *Mercury telluride colloidal quantum dots: Electronic structure, size-dependent spectra, and photocurrent detection up to 12 μm*. ACS nano, 8(8):8676–8682, 2014.

[63] Min-Jae Choi, Laxmi Kishore Sagar, Bin Sun, Margherita Biondi, Seungjin Lee, Amin Morteza Najjariyan, Larissa Levina, F Pelayo Garcia de Arquer, and Edward H Sargent. *Ligand exchange at a covalent surface enables balanced stoichiometry in III–V colloidal quantum dots*. Nano letters, 21(14):6057–6063, 2021.

[64] Bin Sun, Amin Morteza Najarian, Laxmi Kishore Sagar, Margherita Biondi, Min-Jae Choi, Xiyan Li, Larissa Levina, Se-Woong Baek, Chao Zheng, Seungjin Lee, et al. *Fast Near-Infrared Photodetection Using III-V Colloidal Quantum Dots*. Advanced Materials, 34(33):2203039, 2022.

[65] Jari Leemans, Vladimir Pejović, Epimitheas Georgitzikis, Matthias Minjauw, Abu Bakar Siddik, Yu-Hao Deng, Yinghuan Kuang, Gunther Roelkens, Christophe Detavernier, Itai Lieberman, et al. *Colloidal III–V Quantum Dot Photodiodes for Short-Wave Infrared Photodetection*. Advanced Science, 9(17):2200844, 2022.

[66] Jianying Ouyang, Neil Graddage, Jianping Lu, Yufang Zhong, Ta-Ya Chu, Yanguang Zhang, Xiaohua Wu, Oltion Kodra, Zhao Li, Ye Tao, et al. *Ag2Te colloidal quantum dots for near-infrared-II photodetectors*. ACS Applied Nano Materials, 4(12):13587–13601, 2021.

[67] Yongjie Wang, Lucheng Peng, Julien Schreier, Yu Bi, Andres Black, Aditya Malla, Stijn Goossens, and Gerasimos Konstantatos. *Silver telluride colloidal quantum dot infrared photodetectors and image sensors*. Nature Photonics, pages 1–7, 2024.

[68] Rinku Saran and Richard J Curry. *Lead sulphide nanocrystal photodetector technologies*. Nature Photonics, 10(2):81–92, 2016.

[69] Clément Livache, Bertille Martinez, Nicolas Goubet, Julien Ramade, and Emmanuel Lhuillier. *Road map for nanocrystal based infrared photodetectors*. Frontiers in Chemistry, 6:575, 2018.

[70] Qun Hao, Haifei Ma, Xida Xing, Xin Tang, Zhipeng Wei, Xue Zhao, and Menglu Chen. *Mercury Chalcogenide Colloidal Quantum Dots for Infrared Photodetectors*. Materials, 16(23):7321, 2023.

[71] *https://en.wikipedia.org/wiki/Readout_integrated_circuit*.

[72] Tobias Rauch, Michaela Böberl, Sandro F Tedde, Jens Fürst, Maksym V Kovalenko, Günter Hesser, Uli Lemmer, Wolfgang Heiss, and Oliver Hayden. *Near-infrared imaging with quantum-dot-sensitized organic photodiodes*. nature photonics, 3(6):332–336, 2009.

[73] Vladimir Pejović, Jiwon Lee, Epimitheas Georgitzikis, Yunlong Li, Joo Hyoung Kim, Itai Lieberman, Paweł E Malinowski, Paul Heremans, and David Cheyns. *Thin-film photodetector optimization for high-performance short-wavelength infrared imaging*. IEEE Electron Device Letters, 42(8):1196–1199, 2021.

[74] Mark Allen, Alexander Bessonov, and Tapani Ryhänen. *66-4: Invited paper: Graphene enhanced QD image sensor technology*. In SID Symposium Digest of Technical Papers, volume 52, pages 987–990. Wiley Online Library, 2021.

[75] Lionel Barrow, Nikolai Bock, Aurelien Bouvier, Dario Clocchiatti, Jian Feng, Naveen Kolli, Andras Pattantyus, Vitanshu Sharma, Tzi-Hsiung Shu, and Emanuele Mandelli. *A QuantumFilm based quadVGA 1.5 μm pixel image sensor with over 40% QE at 940 nm for actively illuminated applications*. IISW Dig. Tech. Pap, pages 378–381, 2017.

[76] Christopher Gregory, Allan Hilton, Katherine Violette, and Ethan JD Klem. *Colloidal Quantum Dot Photodetectors for Large Format NIR, SWIR, and ESWIR Imaging Arrays*. In SID Symposium Digest of Technical Papers, volume 52, pages 982–986. Wiley Online Library, 2021.

[77] Ya Wang, Huicheng Hu, Mohan Yuan, Hang Xia, Xingchen Zhang, Jing Liu, Ji Yang, Shaoqiu Xu, Zhaorong Shi, Jungang He, et al. *Colloidal PbS Quantum Dot Photodiode Imager with Suppressed Dark Current*. ACS Applied Materials & Interfaces, 15(50):58573–58582, 2023.

[78] Jiwon Lee, Epimitheas Georgitzikis, Yunlong Li, Ziduo Lin, Jihoon Park, Itai Lieberman, David Cheyns, Murali Jayapala, Andy Lambrechts, Steven Thijs, et al. *Imaging in short-wave infrared with 1.82 μm pixel pitch quantum dot image sensor*. In 2020 IEEE International Electron Devices Meeting (IEDM), pages 16–5. IEEE, 2020.

[79] Zach M Beiley, Robin Cheung, Erin F Hanelt, Emanuele Mandelli, Jet Meitzner, Jae Park, Andras Pattantyus-Abraham, and Edward H Sargent. *Device design for global shutter operation in a 1.1-um pixel image sensor and its application to near-infrared sensing*. In Physics and Simulation of Optoelectronic Devices XXV, volume 10098, pages 287–291. SPIE, 2017.

[80] S Manda, R Matsumoto, S Saito, S Maruyama, H Minari, T Hirano, T Takachi, N Fujii, Y Yamamoto, Y Zaizen, et al. *High-definition visible-SWIR InGaAs image sensor using Cu-Cu bonding of III-V to silicon wafer*. In 2019 IEEE International Electron Devices Meeting (IEDM), pages 16–7. IEEE, 2019.

[81] SWIR.

[82] Christopher Buurma, Richard E Pimpinella, Anthony J Ciani, Jered S Feldman, Christoph H Grein, and Philippe Guyot-Sionnest. *MWIR imaging with low cost colloidal quantum dot films*. In Optical Sensing, Imaging, and Photon Counting: Nanostructured Devices and Applications 2016, volume 9933, page 993303. SPIE, 2016.

[83] Shuo Zhang, Cheng Bi, Tianling Qin, Yanfei Liu, Jie Cao, Jiaqi Song, Yongjun Huo, Menglu Chen, Qun Hao, and Xin Tang. *Wafer-scale fabrication of CMOS-compatible trapping-mode infrared imagers with colloidal quantum dots*. ACS Photonics, 10(3):673–682, 2023.

[84] Peter Palomaki. *Quantum Dots+ OLED= Your Next TV: Formerly rival technologies will come together in new Samsung displays*. IEEE Spectrum, 59(1):52–53, 2022.

[85] Lishuang Wang, Jie Lin, Ying Lv, Bingsuo Zou, Jialong Zhao, and Xingyuan Liu. *Red, green, and blue microcavity quantum dot light-emitting devices with narrow line widths*. ACS Applied Nano Materials, 3(6):5301–5310, 2020.

[86] Yunzhou Deng, Feng Peng, Yao Lu, Xitong Zhu, Wangxiao Jin, Jing Qiu, Jiawei Dong, Yanlei Hao, Dawei Di, Yuan Gao, et al. *Solution-processed green and blue quantum-dot light-emitting diodes with eliminated charge leakage*. Nature Photonics, 16(7):505–511, 2022.

[87] Ji Eun Yeom, Dong Hyun Shin, Raju Lampande, Young Hun Jung, Nagarjuna Naik Mude, Jung Hwan Park, and Jang Hyuk Kwon. *Good charge balanced inverted red InP/ZnSe/ZnS-quantum dot light-emitting diode with new high mobility and deep HOMO level hole transport layer*. ACS Energy Letters, 5(12):3868–3875, 2020.

[88] Christian Ippen, Benjamin Newmeyer, Don Zehnder, Daekyoung Kim, Diego Barrera, Charlie Hotz, and Ruiqing Ma. *Progress in High-Efficiency Heavy-Metal-Free QD-LED Development*. In SID Symposium Digest of Technical Papers, volume 51, pages 858–861. Wiley Online Library, 2020.

[89] Taehyung Kim, Kwang-Hee Kim, Sungwoo Kim, Seon-Myeong Choi, Hyosook Jang, Hong-Kyu Seo, Heejae Lee, Dae-Young Chung, and Eunjoo Jang. *Efficient and stable blue quantum dot light-emitting diode*. Nature, 586(7829):385–389, 2020.

[90] Yibin Jiang, Le Jiang, Fion Sze Yan Yeung, Ping Xu, Shuming Chen, Hoi-Sing Kwok, and Guijun Li. *All-inorganic quantum-dot light-emitting diodes with reduced exciton quenching by a MgO decorated inorganic hole transport layer*. ACS applied materials & interfaces, 11(12):11119–11124, 2019.

[91] Fan Cao, Qianqian Wu, Yizhen Sui, Sheng Wang, Yongjiang Dou, Weihong Hua, Lingmei Kong, Lin Wang, Jianhua Zhang, Tian Jiang, et al. *All-Inorganic Quantum Dot Light-Emitting Diodes with Suppressed Luminance Quenching Enabled by Chloride Passivated Tungsten Phosphate Hole Transport Layers*. Small, 17(19):2100030, 2021.

[92] Yu Liu, Congbiao Jiang, Chen Song, Juanhong Wang, Lan Mu, Zhiwei He, Zhenji Zhong, Yangke Cun, Chaohuang Mai, Jian Wang, et al. *Highly efficient all-solution processed inverted quantum dots based light emitting diodes*. ACS nano, 12(2):1564–1570, 2018.

[93] My Duyen Ho, Daekyoung Kim, Namhun Kim, Sung Min Cho, and Heeyeop Chae. *Polymer and small molecule mixture for organic hole transport layers in quantum dot light-emitting diodes*. ACS Applied Materials & Interfaces, 5(23):12369–12374, 2013.

[94] Pengyu Tang, Liming Xie, Xueying Xiong, Changting Wei, Wenchao Zhao, Ming Chen, Jinyong Zhuang, Wenming Su, and Zheng Cui. *Realizing 22.3% EQE and 7-fold lifetime enhancement in QLEDs via blending polymer TFB*

and cross-linkable small molecules for a solvent-resistant hole transport layer. ACS applied materials & interfaces, 12(11):13087–13095, 2020.

[95] Yunfeng Fang, Penglong Bai, Jiayi Li, Binbin Xiao, Yiqing Wang, and Yanping Wang. *Highly efficient red quantum dot light-emitting diodes by balancing charge injection and transport*. ACS Applied Materials & Interfaces, 14(18):21263–21269, 2022.

[96] Xingliang Dai, Zhenxing Zhang, Yizheng Jin, Yuan Niu, Hujia Cao, Xiaoyong Liang, Liwei Chen, Jianpu Wang, and Xiaogang Peng. *Solution-processed, high-performance light-emitting diodes based on quantum dots*. Nature, 515(7525):96–99, 2014.

[97] Jaehoon Lim, Young-Shin Park, Kaifeng Wu, Hyeong Jin Yun, and Victor I Klimov. *Droop-free colloidal quantum dot light-emitting diodes*. Nano letters, 18(10):6645–6653, 2018.

[98] Xiyan Li, Yong-Biao Zhao, Fengjia Fan, Larissa Levina, Min Liu, Rafael Quintero-Bermudez, Xiwen Gong, Li Na Quan, James Fan, Zhenyu Yang, et al. *Bright colloidal quantum dot light-emitting diodes enabled by efficient chlorination*. Nature Photonics, 12(3):159–164, 2018.

[99] Eunjoo Jang and Hyosook Jang. *Quantum Dot Light-Emitting Diodes*. Chemical Reviews, 123(8):4663–4692, 2023.

[100] Victor I Klimov, Alexander A Mikhailovsky, DW McBranch, Catherine A Leatherdale, and Moungi G Bawendi. *Quantization of multiparticle Auger rates in semiconductor quantum dots*. Science, 287(5455):1011–1013, 2000.

[101] VI Klimov, AA Mikhailovsky, Su Xu, A Malko, JA Hollingsworth, a CA Leatherdale, H-J Eisler, and MG Bawendi. *Optical gain and stimulated emission in nanocrystal quantum dots*. science, 290(5490):314–317, 2000.

[102] Young-Shin Park, Wan Ki Bae, Thomas Baker, Jaehoon Lim, and Victor I Klimov. *Effect of Auger recombination on lasing in heterostructured quantum dots with engineered core/shell interfaces*. Nano Letters, 15(11):7319–7328, 2015.

[103] Victor I Klimov, Sergei A Ivanov, Jagjit Nanda, Marc Achermann, Ilya Bezel, John A McGuire, and Andrei Piryatinski. *Single-exciton optical gain in semiconductor nanocrystals*. Nature, 447(7143):441–446, 2007.

[104] Christos Grivas, Chunyong Li, Peristera Andreakou, Pengfei Wang, Ming Ding, Gilberto Brambilla, Liberato Manna, and Pavlos Lagoudakis. *Single-mode tunable laser emission in the single-exciton regime from colloidal nanocrystals*. Nature communications, 4(1):2376, 2013.

[105] Kaifeng Wu, Young-Shin Park, Jaehoon Lim, and Victor I Klimov. *Towards zero-threshold optical gain using charged semiconductor quantum dots*. Nature Nanotechnology, 12(12):1140–1147, 2017.

[106] Oleg V Kozlov, Young-Shin Park, Jeongkyun Roh, Igor Fedin, Tom Nakotte, and Victor I Klimov. *Sub–single-exciton lasing using charged quantum dots coupled to a distributed feedback cavity*. Science, 365(6454):672–675, 2019.

[107] Fengjia Fan, Oleksandr Voznyy, Randy P Sabatini, Kristopher T Bicanic, Michael M Adachi, James R McBride, Kemar R Reid, Young-Shin Park, Xiyan Li, Ankit Jain, et al. *Continuous-wave lasing in colloidal quantum dot solids enabled by facet-selective epitaxy*. Nature, 544(7648):75–79, 2017.

[108] George E Cragg and Alexander L Efros. *Suppression of Auger processes in confined structures*. Nano letters, 10(1):313–317, 2010.

[109] Wan Ki Bae, Lazaro A Padilha, Young-Shin Park, Hunter McDaniel, Istvan Robel, Jeffrey M Pietryga, and Victor I Klimov. *Controlled alloying of the core–shell interface in CdSe/CdS quantum dots for suppression of Auger recombination*. ACS nano, 7(4):3411–3419, 2013.

[110] Young-Shin Park, Jaehoon Lim, Nikolay S Makarov, and Victor I Klimov. *Effect of interfacial alloying versus "volume scaling" on Auger recombination in compositionally graded semiconductor quantum dots*. Nano letters, 17(9):5607–5613, 2017.

[111] Jaehoon Lim, Young-Shin Park, and Victor I Klimov. *Optical gain in colloidal quantum dots achieved with direct-current electrical pumping*. Nature Materials, 17(1):42–49, 2018.

[112] Jaehoon Lim, Young-Shin Park, and Victor I Klimov. *Optical gain in colloidal quantum dots achieved with direct-current electrical pumping*. Nature Materials, 17(1):42–49, 2018.

[113] Heeyoung Jung, Young-Shin Park, Namyoung Ahn, Jaehoon Lim, Igor Fedin, Clément Livache, and Victor I Klimov. *Two-band optical gain and ultrabright electroluminescence from colloidal quantum dots at 1000 A cm-2*. Nature Communications, 13(1):3734, 2022.

[114] Namyoung Ahn, Clément Livache, Valerio Pinchetti, Heeyoung Jung, Ho Jin, Donghyo Hahm, Young-Shin Park, and Victor I Klimov. *Electrically driven amplified spontaneous emission from colloidal quantum dots*. Nature, 617(7959):79–85, 2023.

[115] Namyoung Ahn, Young-Shin Park, Clément Livache, Jun Du, Kivanc Gungor, Jaehoon Kim, and Victor I Klimov. *Optically Excited Lasing in a Cavity-Based, High-Current-Density Quantum Dot Electroluminescent Device*. Advanced Materials, 35(9):2206613, 2023.

[116] Heeyoung Jung, Namyoung Ahn, and Victor I Klimov. *Prospects and challenges of colloidal quantum dot laser diodes*. Nature Photonics, 15(9):643–655, 2021.

[117] Young-Shin Park, Jeongkyun Roh, Benjamin T Diroll, Richard D Schaller, and Victor I Klimov. *Colloidal quantum dot lasers*. Nature Reviews Materials, 6(5):382–401, 2021.

[118] Kiyoshi Asakawa, Yoshimasa Sugimoto, and Shigeru Nakamura. *Silicon photonics for telecom and data-com applications*. Opto-Electronic Advances, 3(10):200011–1, 2020.

[119] Xiaohan Shen, Ben Chen, Yu Zhu, and Weiming Shi. *Silicon photonic integrated circuits and its application in data center*. In Seventh Symposium on Novel Photoelectronic Detection Technology and Applications, volume 11763, pages 2110–2123. SPIE, 2021.

[120] Ananth Z Subramanian, Eva Ryckeboer, Ashim Dhakal, Frédéric Peyskens, Aditya Malik, Bart Kuyken, Haolan Zhao, Shibnath Pathak, Alfonso Ruocco, Andreas De Groote, et al. *Silicon and silicon nitride photonic circuits for spectroscopic sensing on-a-chip*. Photonics Research, 3(5):B47–B59, 2015.

[121] Farshid Ashtiani, Alexander J Geers, and Firooz Aflatouni. *An on-chip photonic deep neural network for image classification*. Nature, 606(7914):501–506, 2022.

[122] Sudip Shekhar, Wim Bogaerts, Lukas Chrostowski, John E Bowers, Michael Hochberg, Richard Soref, and Bhavin J Shastri. *Roadmapping the next generation of silicon photonics*. Nature Communications, 15(1):751, 2024.

[123] David WU Chan, Xiong Wu, Zunyue Zhang, Chao Lu, Alan Pak Tao Lau, and Hon Ki Tsang. *C-band 67 GHz silicon photonic microring modulator for dispersion-uncompensated 100 Gbaud PAM-4*. Optics Letters, 47(11):2935–2938, 2022.

[124] Changhao Han, Zhao Zheng, Haowen Shu, Ming Jin, Jun Qin, Ruixuan Chen, Yuansheng Tao, Bitao Shen, Bowen Bai, Fenghe Yang, et al. *Slow-light silicon modulator with 110-GHz bandwidth*. Science Advances, 9(42):eadi5339, 2023.

[125] S Lischke, A Peczek, JS Morgan, K Sun, D Steckler, Y Yamamoto, F Korndörfer, C Mai, S Marschmeyer, M Fraschke, et al. *Ultra-fast germanium photodiode with 3-dB bandwidth of 265 GHz*. Nature Photonics, 15(12):925–931, 2021.

[126] Gunther Roelkens, Utsav Dave, Alban Gassenq, Nannicha Hattasan, Chen Hu, Bart Kuyken, Francois Leo, Aditya Malik, Muhammad Muneeb, Eva Ryckeboer, et al. *Silicon-based heterogeneous photonic integrated circuits for the mid-infrared*. Optical Materials Express, 3(9):1523–1536, 2013.

[127] Nouman Zia, Heidi Tuorila, Jukka Viheriälä, Samu-Pekka Ojanen, Eero Koivusalo, Joonas Hilska, and Mircea Guina. *Hybrid silicon photonics DBR laser based on flip-chip integration of GaSb amplifiers and μm-scale SOI waveguides*. Optics Express, 30(14):24995–25005, 2022.

[128] Aleksandrs Marinins, Sebastian Hänsch, Huseyin Sar, François Chancerel, Negin Golshani, Hsiao-Lun Wang, Artemisia Tsiara, David Coenen, Peter Verheyen, Giovanni Capuz, et al. *Wafer-Scale Hybrid Integration of InP DFB Lasers on Si Photonics by Flip-Chip Bonding With sub-300 nm Alignment Precision*. IEEE Journal of Selected Topics in Quantum Electronics, 29(3: Photon. Elec. Co-Inte. and Adv. Trans. Print.):1–11, 2022.

[129] Gunther Roelkens, Jing Zhang, Laurens Bogaert, Emadreza Soltanian, Maximilien Billet, Ali Uzun, Biwei Pan, Yang Liu, Evangelia Delli, Dongbo Wang, et al. *Present and future of micro-transfer printing for heterogeneous photonic integrated circuits*. APL Photonics, 9(1), 2024.

[130] Javad Rahimi, Joris Van Kerrebrouck, Bahawal Haq, Johan Bauwelinck, Gunther Roelkens, and Geert Morthier. *Demonstration of a high-efficiency short-cavity iii-v-on-si c-band dfb laser diode*. IEEE Journal of Selected Topics in Quantum Electronics, 28(3: Hybrid Integration for Silicon Photonics):1–6, 2021.

[131] Javad Rahimi Vaskasi, Nishant Singh, Joris Van Kerrebrouck, Johan Bauwelinck, Gunther Roelkens, and Geert Morthier. *High wall-plug efficiency and narrow linewidth III-V-on-silicon C-band DFB laser diodes*. Optics Express, 30(15):27983–27992, 2022.

[132] Jae-Seong Park, Mingchu Tang, Siming Chen, and Huiyun Liu. *Heteroepitaxial growth of iii-v semiconductors on silicon*. Crystals, 10(12):1163, 2020.

[133] Wen-Qi Wei, An He, Bo Yang, Zi-Hao Wang, Jing-Zhi Huang, Dong Han, Ming Ming, Xuhan Guo, Yikai Su, Jian-Jun Zhang, et al. *Monolithic inte-*

gration of embedded III-V lasers on SOI. Light: Science & Applications, 12(1):84, 2023.

[134] Chen Shang, Kaiyin Feng, Eamonn T Hughes, Andrew Clark, Mukul Debnath, Rosalyn Koscica, Gerald Leake, Joshua Herman, David Harame, Peter Ludewig, et al. *Electrically pumped quantum-dot lasers grown on 300 mm patterned Si photonic wafers*. Light: Science & Applications, 11(1):299, 2022.

[135] Bernardette Kunert, Weiming Guo, Yves Mols, Bin Tian, Zhechao Wang, Yuting Shi, Dries Van Thourhout, Marianna Pantouvaki, Joris Van Campenhout, Robert Langer, et al. *III/V nano ridge structures for optical applications on patterned 300 mm silicon substrate*. Applied Physics Letters, 109(9), 2016.

[136] Weiqiang Xie, Thilo Stöferle, Gabriele Raino, Tangi Aubert, Suzanne Bisschop, Yunpeng Zhu, Rainer F Mahrt, Pieter Geiregat, Edouard Brainis, Zeger Hens, et al. *On-Chip Integrated Quantum-Dot–Silicon-Nitride Microdisk Lasers*. Advanced Materials, 29(16):1604866, 2017.

[137] Yunpeng Zhu, Weiqiang Xie, Suzanne Bisschop, Tangi Aubert, Edouard Brainis, Pieter Geiregat, Zeger Hens, and Dries Van Thourhout. *On-chip single-mode distributed feedback colloidal quantum dot laser under nanosecond pumping*. ACS photonics, 4(10):2446–2452, 2017.

[138] Alexander Eich, Tobias C Spiekermann, Helge Gehring, Lisa Sommer, Julian R Bankwitz, Philip PJ Schrinner, Johann A Preuß, Steffen Michaelis de Vasconcellos, Rudolf Bratschitsch, Wolfram HP Pernice, et al. *Single-photon emission from individual nanophotonic-integrated colloidal quantum dots*. ACS Photonics, 9(2):551–558, 2022.

[139] Lukas Elsinger, Robin Petit, Frederik Van Acker, Natalia K Zawacka, Ivo Tanghe, Kristiaan Neyts, Christophe Detavernier, Pieter Geiregat, Zeger Hens, and Dries Van Thourhout. *Waveguide-coupled colloidal quantum dot light emitting diodes and detectors on a silicon nitride platform*. Laser & Photonics Reviews, 15(7):2000230, 2021.

[140] Bingqing Zhu, Mengyu Chen, Qiang Zhu, Guodong Zhou, Nema M Abdelazim, Wen Zhou, Stephen V Kershaw, Andrey L Rogach, Ni Zhao, and Hon Ki Tsang. *Integrated plasmonic infrared photodetector based on colloidal HgTe quantum dots*. Advanced Materials Technologies, 4(10):1900354, 2019.

[141] Matthias J Grotevent, Sergii Yakunin, Dominik Bachmann, Carolina Romero, Javier R Vázquez de Aldana, Matteo Madi, Michel Calame, Maksym V

Kovalenko, and Ivan Shorubalko. *Integrated photodetectors for compact Fourier-transform waveguide spectrometers*. Nature Photonics, 17(1):59–64, 2023.

[142] Nicola A Tyler, Daivid Fowler, Stephane Malhouitre, Stephanie Garcia, Philippe Grosse, Wilfried Rabaud, and Bertrand Szelag. *SiN integrated optical phased arrays for two-dimensional beam steering at a single near-infrared wavelength*. Optics express, 27(4):5851–5858, 2019.

[143] Moshe Zadka, You-Chia Chang, Aseema Mohanty, Christopher T Phare, Samantha P Roberts, and Michal Lipson. *On-chip platform for a phased array with minimal beam divergence and wide field-of-view*. Optics express, 26(3):2528–2534, 2018.

[144] Christopher V Poulton, Matthew J Byrd, Manan Raval, Zhan Su, Nanxi Li, Erman Timurdogan, Douglas Coolbaugh, Diedrik Vermeulen, and Michael R Watts. *Large-scale silicon nitride nanophotonic phased arrays at infrared and visible wavelengths*. Optics letters, 42(1):21–24, 2017.

[145] Frédéric Peyskens, Pieter Wuytens, Ali Raza, Pol Van Dorpe, and Roel Baets. *Waveguide excitation and collection of surface-enhanced Raman scattering from a single plasmonic antenna*. Nanophotonics, 7(7):1299–1306, 2018.

[146] Giuseppe Antonacci, Jeroen Goyvaerts, Haolan Zhao, Bettina Baumgartner, Bernhard Lendl, and Roel Baets. *Ultra-sensitive refractive index gas sensor with functionalized silicon nitride photonic circuits*. APL photonics, 5(8), 2020.

[147] Caterina Taballione, Tom AW Wolterink, Jasleen Lugani, Andreas Eckstein, Bryn A Bell, Robert Grootjans, Ilka Visscher, Jelmer J Renema, Dimitri Geskus, Chris GH Roeloffzen, et al. *8× 8 programmable quantum photonic processor based on silicon nitride waveguides*. In Laser Science, pages JTu3A–58. Optica Publishing Group, 2018.

[148] Alexander Senichev, Samuel Peana, Zachariah O Martin, Omer Yesilyurt, Demid Sychev, Alexei S Lagutchev, Alexandra Boltasseva, and Vladimir M Shalaev. *Silicon nitride waveguides with intrinsic single-photon emitters for integrated Quantum photonics*. ACS Photonics, 9(10):3357–3365, 2022.

[149] Galan Moody, Volker J Sorger, Daniel J Blumenthal, Paul W Juodawlkis, William Loh, Cheryl Sorace-Agaskar, Alex E Jones, Krishna C Balram, Jonathan CF Matthews, Anthony Laing, et al. *2022 roadmap on integrated quantum photonics*. Journal of Physics: Photonics, 4(1):012501, 2022.

[150] Piotr J Cegielski, Anna Lena Giesecke, Stefanie Neutzner, Caroline Porschatis, Marina Gandini, Daniel Schall, Carlo AR Perini, Jens Bolten, Stephan Suckow, Satender Kataria, et al. *Monolithically integrated perovskite semiconductor lasers on silicon photonic chips by scalable top-down fabrication*. Nano letters, 18(11):6915–6923, 2018.

[151] Weiqiang Xie, Raquel Gomes, Tangi Aubert, Suzanne Bisschop, Yunpeng Zhu, Zeger Hens, Edouard Brainis, and Dries Van Thourhout. *Nanoscale and single-dot patterning of colloidal quantum dots*. Nano letters, 15(11):7481–7487, 2015.

[152] Yueyang Chen, Albert Ryou, Max R Friedfeld, Taylor Fryett, James Whitehead, Brandi M Cossairt, and Arka Majumdar. *Deterministic positioning of colloidal quantum dots on silicon nitride nanobeam cavities*. Nano letters, 18(10):6404–6410, 2018.

[153] Qianhuan Yu, Junyi Gao, Nan Ye, Boheng Chen, Keye Sun, Linli Xie, Kartik Srinivasan, Michael Zervas, Gabriele Navickaite, Michael Geiselmann, et al. *Heterogeneous photodiodes on silicon nitride waveguides with 20 GHz bandwidth*. In 2020 Optical Fiber Communications Conference and Exhibition (OFC), pages 1–3. IEEE, 2020.

[154] Jeroen Goyvaerts, Sulakshna Kumari, Sarah Uvin, Jing Zhang, Roel Baets, Agnieszka Gocalinska, Emanuele Pelucchi, Brian Corbett, and Günther Roelkens. *Transfer-print integration of GaAs pin photodiodes onto silicon nitride photonic integrated circuits*. In 2020 IEEE Photonics Conference (IPC), pages 1–2. IEEE, 2020.

[155] Byung Ku Jung, Ho Kun Woo, Chanho Shin, Taesung Park, Ning Li, Kyu Joon Lee, Woosik Kim, Jung Ho Bae, Jae-Pyoung Ahn, Tse Nga Ng, et al. *Suppressing the dark current in quantum dot infrared photodetectors by controlling carrier statistics*. Advanced Optical Materials, 10(2):2101611, 2022.

[156] Niall Killilea, Mingjian Wu, Mykhailo Sytnyk, Amir Abbas Yousefi Amin, Oleksandr Mashkov, Erdmann Spiecker, and Wolfgang Heiss. *Pushing PbS/Metal-Halide-Perovskite Core/Epitaxial-Ligand-Shell Nanocrystal Photodetectors beyond 3 μm Wavelength*. Advanced Functional Materials, 29(14):1807964, 2019.

[157] Urvashi Bothra, Miguel Albaladejo-Siguan, Yana Vaynzof, and Dinesh Kabra. *Impact of Ligands on the Performance of PbS Quantum Dot Visible–Near-Infrared Photodetectors*. Advanced Optical Materials, 11(1):2201897, 2023.

[158] Ahmad R Kirmani, Graham H Carey, Maged Abdelsamie, Buyi Yan, Dongkyu Cha, Lisa R Rollny, Xiaoyu Cui, Edward H Sargent, and Aram Amassian. *Effect of solvent environment on colloidal-quantum-dot solar-cell manufacturability and performance*. Advanced Materials, 26(27):4717–4723, 2014.

[159] Wim Bogaerts, Yanlu Li, Shibnath Pathak, Alfonso Ruocco, Martin Fiers, Antonio Ribeiro, Emmanuel Lambert, and Pieter Dumon. *Integrated design for integrated photonics: from the physical to the circuit level and back*. In Integrated Optics: Physics and Simulations, volume 8781, page 878102. Spie, 2013.

[160] Molly Piels, Jared F Bauters, Michael L Davenport, Martijn JR Heck, and John E Bowers. *Low-loss silicon nitride AWG demultiplexer heterogeneously integrated with hybrid III–V/silicon photodetectors*. Journal of lightwave technology, 32(4):817–823, 2014.

[161] Daan Martens, Ananth Z Subramanian, Shibnath Pathak, Michael Vanslembrouck, Peter Bienstman, Wim Bogaerts, and Roel G Baets. *Compact silicon nitride arrayed waveguide gratings for very near-infrared wavelengths*. IEEE Photonics Technology Letters, 27(2):137–140, 2014.

[162] Shibnath Pathak, Michael Vanslembrouck, Pieter Dumon, Dries Van Thourhout, and Wim Bogaerts. *Optimized silicon AWG with flattened spectral response using an MMI aperture*. Journal of Lightwave Technology, 31(1):87–93, 2013.

[163] Lhoucine Ben Mohammadi, Thomas Klotzbuecher, Susanne Sigloch, Knut Welzel, Michael Goeddel, Thomas R Pieber, and Lukas Schaupp. *In vivo evaluation of a chip based near infrared sensor for continuous glucose monitoring*. BIOSENSORS & BIOELECTRONICS, 53:99–104, 2014.

[164] Eva Ryckeboer, Ronny Bockstaele, Michal Vanslembrouck, and Roel Baets. *Glucose sensing by waveguide-based absorption spectroscopy on a silicon chip*. Biomedical optics express, 5(5):1636–1648, 2014.

[165] Andrea Trita, Eli Voet, Jan Vermeiren, Danae Delbeke, Pieter Dumon, Shibnath Pathak, and Dries Van Thourhout. *Simultaneous interrogation of multiple fiber Bragg grating sensors using an arrayed waveguide grating filter fabricated in SOI platform*. IEEE Photonics Journal, 7(6):1–11, 2015.

[166] Dennis Maes, Sam Lemey, Gunther Roelkens, Mohammed Zaknoune, Vanessa Avramovic, Etienne Okada, Pascal Szriftgiser, Emilien Peytavit, Guillaume Ducournau, and Bart Kuyken. *High-speed uni-traveling-carrier photodiodes on silicon nitride*. APL Photonics, 8(1), 2023.

[167] S Lischke, D Knoll, C Mai, A Hesse, G Georgieva, A Peczek, A Kroh, M Lisker, D Schmidt, M Fraschke, et al. *Silicon nitride waveguide coupled 67+ GHz Ge photodiode for non-SOI PIC and ePIC platforms*. In 2019 IEEE International Electron Devices Meeting (IEDM), pages 33–2. IEEE, 2019.

[168] Wesley D Sacher, Jared C Mikkelsen, Ying Huang, Jason CC Mak, Zheng Yong, Xianshu Luo, Yu Li, Patrick Dumais, Jia Jiang, Dominic Goodwill, et al. *Monolithically integrated multilayer silicon nitride-on-silicon waveguide platforms for 3-D photonic circuits and devices*. Proceedings of the IEEE, 106(12):2232–2245, 2018.

[169] Juan Francisco Gonzalez Marin, Dmitrii Unuchek, Kenji Watanabe, Takashi Taniguchi, and Andras Kis. *MoS2 photodetectors integrated with photonic circuits*. npj 2D Materials and Applications, 3(1):14, 2019.

[170] Rivka Gherabli, SRKC Indukuri, Roy Zektzer, Christian Frydendahl, and Uriel Levy. *MoSe2/WS2 heterojunction photodiode integrated with a silicon nitride waveguide for near infrared light detection with high responsivity*. Light: Science & Applications, 12(1):60, 2023.

[171] Yannick Salamin, Ping Ma, Benedikt Baeuerle, Alexandros Emboras, Yuriy Fedoryshyn, Wolfgang Heni, Bojun Cheng, Arne Josten, and Juerg Leuthold. *100 GHz plasmonic photodetector*. ACS photonics, 5(8):3291–3297, 2018.

[172] Geun Ho Ahn, Alexander D White, Hyungjin Kim, Naoki Higashitarumizu, Felix M Mayor, Jason F Herrmann, Wentao Jiang, Kevin KS Multani, Amir H Safavi-Naeini, Ali Javey, et al. *Platform-agnostic waveguide integration of high-speed photodetectors with evaporated tellurium thin films*. Optica, 10(3):349–355, 2023.

[173] Faiz Rahman, Daniel J Carbaugh, Jason T Wright, Parthiban Rajan, Sneha G Pandya, and Savas Kaya. *A review of polymethyl methacrylate (PMMA) as a versatile lithographic resist–With emphasis on UV exposure*. Microelectronic Engineering, 224:111238, 2020.

[174] Daniel J Carbaugh, Jason T Wright, Rajan Parthiban, and Faiz Rahman. *Photolithography with polymethyl methacrylate (PMMA)*. Semiconductor Science and Technology, 31(2):025010, 2015.

[175] Tsung-Yang Liow, Kah-Wee Ang, Qing Fang, Jun-Feng Song, Yong-Zhong Xiong, Ming-Bin Yu, Guo-Qiang Lo, and Dim-Lee Kwong. *Silicon modulators and germanium photodetectors on SOI: monolithic integration, compatibility, and performance optimization*. IEEE Journal of Selected Topics in Quantum Electronics, 16(1):307–315, 2009.

[176] Jie Bao and Moungi G Bawendi. *A colloidal quantum dot spectrometer*. Nature, 523(7558):67–70, 2015.

[177] Ruijun Wang, Anton Vasiliev, Muhammad Muneeb, Aditya Malik, Stephan Sprengel, Gerhard Boehm, Markus-Christian Amann, Ieva Šimonytė, Augustinas Vizbaras, Kristijonas Vizbaras, et al. *III–V-on-silicon photonic integrated circuits for spectroscopic sensing in the 2–4 μm wavelength range*. Sensors, 17(8):1788, 2017.

[178] Ting Hu, Bowei Dong, Xianshu Luo, Tsung-Yang Liow, Junfeng Song, Chengkuo Lee, and Guo-Qiang Lo. *Silicon photonic platforms for mid-infrared applications*. Photonics Research, 5(5):417–430, 2017.

[179] Eva Ryckeboer, Alban Gassenq, Muhammad Muneeb, Nannicha Hattasan, Shibnath Pathak, Laurent Cerutti, Jean-Baptiste Rodriguez, E Tournié, Wim Bogaerts, Roel Baets, et al. *Silicon-on-insulator spectrometers with integrated GaInAsSb photodiodes for wide-band spectroscopy from 1510 to 2300 nm*. Optics express, 21(5):6101–6108, 2013.

[180] Nannicha Hattasan, Alban Gassenq, Laurent Cerutti, Jean-Baptiste Rodriguez, Eric Tournié, and Gunther Roelkens. *Heterogeneous integration of GaInAsSb pin photodiodes on a silicon-on-insulator waveguide circuit*. IEEE Photonics Technology Letters, 23(23):1760–1762, 2011.

[181] Alban Gassenq, Nannicha Hattasan, Laurent Cerutti, Jean Batiste Rodriguez, Eric Tournié, and Gunther Roelkens. *Study of evanescently-coupled and grating-assisted GaInAsSb photodiodes integrated on a silicon photonic chip*. Optics Express, 20(11):11665–11672, 2012.

[182] Ruijun Wang, Stephan Sprengel, Muhammad Muneeb, Gerhard Boehm, Roel Baets, Markus-Christian Amann, and Gunther Roelkens. *2 μm wavelength range InP-based type-II quantum well photodiodes heterogeneously integrated on silicon photonic integrated circuits*. Optics express, 23(20):26834–26841, 2015.

[183] Mingsheng Long, Peng Wang, Hehai Fang, and Weida Hu. *Progress, challenges, and opportunities for 2D material based photodetectors*. Advanced Functional Materials, 29(19):1803807, 2019.

[184] Xiaomu Wang, Zhenzhou Cheng, Ke Xu, Hon Ki Tsang, and Jian-Bin Xu. *High-responsivity graphene/silicon-heterostructure waveguide photodetectors*. Nature Photonics, 7(11):888–891, 2013.

[185] Jingshu Guo, Jiang Li, Chaoyue Liu, Yanlong Yin, Wenhui Wang, Zhenhua Ni, Zhilei Fu, Hui Yu, Yang Xu, Yaocheng Shi, et al. *High-performance*

silicon- graphene hybrid plasmonic waveguide photodetectors beyond 1.55 μm. Light: Science & Applications, 9(1):29, 2020.

[186] Yu-Hsiang Peng, HH Cheng, Vladimir I Mashanov, and Guo-En Chang. *GeSn pin waveguide photodetectors on silicon substrates*. Applied Physics Letters, 105(23), 2014.

[187] Cheng-Hsun Tsai, Kuan-Chih Lin, Chin-Yuan Cheng, Kuo-Chih Lee, HH Cheng, and Guo-En Chang. *GeSn lateral pin waveguide photodetectors for mid-infrared integrated photonics*. Optics letters, 46(4):864–867, 2021.

[188] Soumava Ghosh, Radhika Bansal, Greg Sun, Richard A Soref, Hung-Hsiang Cheng, and Guo-En Chang. *Design and optimization of GeSn waveguide photodetectors for 2-μm band silicon photonics*. Sensors, 22(11):3978, 2022.

[189] Cheng-Hsun Liu, Radhika Bansal, Chen-Wei Wu, Yue-Tong Jheng, and Guo-En Chang. *GeSn waveguide photodetectors with vertical p–i–n heterostructure for integrated photonics in the 2 μm wavelength band*. Advanced Photonics Research, 3(7):2100330, 2022.

[190] Jiang Wu, Qi Jiang, Siming Chen, Mingchu Tang, Yuriy I Mazur, Yurii Maidaniuk, Mourad Benamara, Mykhaylo P Semtsiv, W Ted Masselink, Kimberly A Sablon, et al. *Monolithically integrated InAs/GaAs quantum dot mid-infrared photodetectors on silicon substrates*. Acs Photonics, 3(5):749–753, 2016.

[191] Ji Yang, Huicheng Hu, Yifei Lv, Mohan Yuan, Binbin Wang, Ziyang He, Shiwu Chen, Ya Wang, Zhixiang Hu, Mengxuan Yu, et al. *Ligand-engineered HgTe colloidal quantum dot solids for infrared photodetectors*. Nano Letters, 22(8):3465–3472, 2022.

[192] Shihab B Hafiz, Michael R Scimeca, Peter Zhao, Ingrid J Paredes, Ayaskanta Sahu, and Dong-Kyun Ko. *Silver selenide colloidal quantum dots for mid-wavelength infrared photodetection*. ACS Applied Nano Materials, 2(3):1631–1636, 2019.

[193] Shihab Bin Hafiz, Mohammad M Al Mahfuz, Sunghwan Lee, and Dong-Kyun Ko. *Midwavelength infrared p–n heterojunction diodes based on intraband colloidal quantum dots*. ACS Applied Materials & Interfaces, 13(41):49043–49049, 2021.

[194] Chao Pang, Yu-Hao Deng, Ezat Kheradmand, Nithin Poonkottil, Robin Petit, Lukas Elsinger, Christophe Detavernier, Pieter Geiregat, Zeger Hens, and Dries Van Thourhout. *Integrated PbS Colloidal Quantum Dot Photodiodes on Silicon Nitride Waveguides*. ACS photonics, 10(12):4215–4224, 2023.

[195] A Mang, K Reimann, et al. *Band gaps, crystal-field splitting, spin-orbit coupling, and exciton binding energies in ZnO under hydrostatic pressure*. Solid state communications, 94(4):251–254, 1995.

[196] Tommi Tynell and Maarit Karppinen. *Atomic layer deposition of ZnO: a review*. Semiconductor Science and Technology, 29(4):043001, 2014.

[197] Mark P Hendricks, Michael P Campos, Gregory T Cleveland, Ilan Jen-La Plante, and Jonathan S Owen. *A tunable library of substituted thiourea precursors to metal sulfide nanocrystals*. Science, 348(6240):1226–1230, 2015.

[198] Slawomir Braun, William R Salaneck, and Mats Fahlman. *Energy-level alignment at organic/metal and organic/organic interfaces*. Advanced materials, 21(14-15):1450–1472, 2009.

[199] Margherita Biondi, Min-Jae Choi, Olivier Ouellette, Se-Woong Baek, Petar Todorović, Bin Sun, Seungjin Lee, Mingyang Wei, Peicheng Li, Ahmad R Kirmani, et al. *A chemically orthogonal hole transport layer for efficient colloidal quantum dot solar cells*. Advanced Materials, 32(17):1906199, 2020.

[200] Yu-Hao Deng, Chao Pang, Ezat Kheradmand, Jari Leemans, Jing Bai, Matthias Minjauw, Jiayi Liu, Korneel Molkens, Jeroen Beeckman, Christophe Detavernier, et al. *Short-Wave Infrared Colloidal QDs Photodetector with Nanosecond Response Times Enabled by Ultrathin Absorber Layers*. Advanced Materials, page 2402002, 2024.

[201] Qiwei Xu, Lingju Meng, Kaustubh Sinha, Farsad I Chowdhury, Jun Hu, and Xihua Wang. *Ultrafast colloidal quantum dot infrared photodiode*. ACS Photonics, 7(5):1297–1303, 2020.

[202] Ignacio Del Villar, Carlos R Zamarreño, Miguel Hernaez, Francisco J Arregui, and Ignacio R Matias. *Lossy mode resonance generation with indium-tin-oxide-coated optical fibers for sensing applications*. Journal of Lightwave Technology, 28(1):111–117, 2010.

[203] Joost Brouckaert, Wim Bogaerts, Shankar Selvaraja, Pieter Dumon, Roel Baets, and Dries Van Thourhout. *Planar concave grating demultiplexer with high reflective Bragg reflector facets*. IEEE Photonics technology letters, 20(4):309–311, 2008.

[204] Stefan M Koepfli, Michael Baumann, Yesim Koyaz, Robin Gadola, Arif Güngör, Killian Keller, Yannik Horst, Shadi Nashashibi, Raphael Schwanninger, Michael Doderer, et al. *Metamaterial graphene photodetector with bandwidth exceeding 500 gigahertz*. Science, 380(6650):1169–1174, 2023.

[205] Nathan Youngblood, Che Chen, Steven J Koester, and Mo Li. *Waveguide-integrated black phosphorus photodetector with high responsivity and low dark current*. Nature photonics, 9(4):247–252, 2015.

[206] Chaoyue Liu, Jingshu Guo, Laiwen Yu, Jiang Li, Ming Zhang, Huan Li, Yaocheng Shi, and Daoxin Dai. *Silicon/2D-material photodetectors: from near-infrared to mid-infrared*. Light: Science & Applications, 10(1):123, 2021.

[207] Yanlong Yin, Rui Cao, Jingshu Guo, Chaoyue Liu, Jiang Li, Xianglian Feng, Huide Wang, Wei Du, Akeel Qadir, Han Zhang, et al. *High-speed and high-responsivity hybrid silicon/black-phosphorus waveguide photodetectors at 2 μm*. Laser & Photonics Reviews, 13(6):1900032, 2019.

[208] Matthew M Ackerman, Xin Tang, and Philippe Guyot-Sionnest. *Fast and sensitive colloidal quantum dot mid-wave infrared photodetectors*. ACS nano, 12(7):7264–7271, 2018.

[209] Jiwon Lee, Epimitheas Georgitzikis, Yannick Hermans, Nikolas Papadopoulos, Naresh Chandrasekaran, Minhyun Jin, Abu Bakar Siddik, Florian De Roose, Griet Uytterhoeven, Joo Hyoung Kim, et al. *Thin-film image sensors with a pinned photodiode structure*. Nature Electronics, 6(8):590–598, 2023.

[210] Jonathan S Steckel, Andras G Pattantyus-Abraham, Emmanuel Josse, Eric Mazaleyrat, and Krysten Rochereau. *66-1: High resolution quantum dot global shutter imagers*. In SID Symposium Digest of Technical Papers, volume 52, pages 975–977. Wiley Online Library, 2021.

[211] Abhijit Chatterjee, Janani Balakrishnan, Naresh Babu Pendyala, and KSR Koteswara Rao. *Room temperature operated HgCdTe colloidal quantum dot infrared focal plane array using shockwave dispersion technique*. Applied Surface Science Advances, 1:100024, 2020.

[212] Xin Tang, Matthew M Ackerman, Menglu Chen, and Philippe Guyot-Sionnest. *Dual-band infrared imaging using stacked colloidal quantum dot photodiodes*. Nature photonics, 13(4):277–282, 2019.

[213] Huiyu Li, Liheng Bian, Kai Gu, Hao Fu, Gaoling Yang, Haizheng Zhong, and Jun Zhang. *A near-infrared miniature quantum dot spectrometer*. Advanced Optical Materials, 9(15):2100376, 2021.

[214] Andrea De Iacovo, Carlo Venettacci, Carlo Giansante, and Lorenzo Colace. *Narrowband colloidal quantum dot photodetectors for wavelength measurement applications*. Nanoscale, 12(18):10044–10050, 2020.

[215] Joost Brouckaert, Wim Bogaerts, Pieter Dumon, Shankar Kumar Selvaraja, Gunther Roelkens, Dries Van Thourhout, and Roel Baets. *Planar concave grating demultiplexer with distributed Bragg reflection facets*. In 2007 4th IEEE International Conference on Group IV Photonics, pages 1–3. IEEE, 2007.

[216] Shibnath Pathak, Dries Van Thourhout, and Wim Bogaerts. *Design trade-offs for silicon-on-insulator-based AWGs for (de) multiplexer applications*. Optics letters, 38(16):2961–2964, 2013.

[217] Wim Bogaerts, Shankar Kumar Selvaraja, Pieter Dumon, Joost Brouckaert, Katrien De Vos, Dries Van Thourhout, and Roel Baets. *Silicon-on-insulator spectral filters fabricated with CMOS technology*. IEEE journal of selected topics in quantum electronics, 16(1):33–44, 2010.

[218] Bernardo BC Kyotoku, Long Chen, and Michal Lipson. *Sub-nm resolution cavity enhanced micro-spectrometer*. Optics express, 18(1):102–107, 2010.

[219] Chunhui Yao, Kangning Xu, Wanlu Zhang, Minjia Chen, Qixiang Cheng, and Richard Penty. *Integrated reconstructive spectrometer with programmable photonic circuits*. Nature Communications, 14(1):6376, 2023.

[220] Ang Li and Yeshaiahu Fainman. *On-chip spectrometers using stratified waveguide filters*. Nature communications, 12(1):2704, 2021.

[221] Chunhui Yao, Minjia Chen, Ting Yan, Liang Ming, Qixiang Cheng, and Richard Penty. *Broadband picometer-scale resolution on-chip spectrometer with reconfigurable photonics*. Light: Science & Applications, 12(1):156, 2023.

[222] Chunlei Sun, Zequn Chen, Yuting Ye, Kunhao Lei, Hui Ma, Maoliang Wei, Renjie Tang, Jianghong Wu, Hongtao Lin, and Lan Li. *Scalable on-chip microdisk resonator spectrometer*. Laser & Photonics Reviews, 17(5):2200792, 2023.

[223] Hongnan Xu, Yue Qin, Gaolei Hu, and Hon Ki Tsang. *Breaking the resolution-bandwidth limit of chip-scale spectrometry by harnessing a dispersion-engineered photonic molecule*. Light: Science & Applications, 12(1):64, 2023.

[224] Brandon Redding, Seng Fatt Liew, Raktim Sarma, and Hui Cao. *Compact spectrometer based on a disordered photonic chip*. Nature Photonics, 7(9):746–751, 2013.

[225] Brandon Redding, Seng Fatt Liew, Yaron Bromberg, Raktim Sarma, and Hui Cao. *Evanescently coupled multimode spiral spectrometer*. Optica, 3(9):956–962, 2016.

[226] Lichao Zhang, Jiamin Chen, Chaowei Ma, Wangzhe Li, Zhimei Qi, and Ning Xue. *Research progress on on-chip Fourier transform spectrometer*. Laser & Photonics Reviews, 15(9):2100016, 2021.

[227] Mario CMM Souza, Andrew Grieco, Newton C Frateschi, and Yeshaiahu Fainman. *Fourier transform spectrometer on silicon with thermo-optic non-linearity and dispersion correction*. Nature communications, 9(1):665, 2018.

[228] Ang Li and Yeshaiahu Fainman. *Integrated silicon Fourier transform spectrometer with broad bandwidth and ultra-high resolution*. Laser & Photonics Reviews, 15(4):2000358, 2021.

[229] Aitor V Velasco, Pavel Cheben, Przemek J Bock, André Delâge, Jens H Schmid, Jean Lapointe, Siegfried Janz, María L Calvo, Dan-Xia Xu, Mirosław Florjańczyk, et al. *High-resolution Fourier-transform spectrometer chip with microphotonic silicon spiral waveguides*. Optics letters, 38(5):706–708, 2013.

[230] Liangjun Lu, Hongyi Zhang, Xin Li, Jianping Chen, and Linjie Zhou. *Low temperature sensitivity on-chip Fourier-transform spectrometer based on dual-layer Si 3 N 4 spiral waveguides*. Photonics Research, 11(4):591–599, 2023.

[231] Thi Thuy Duong Dinh, David González-Andrade, Miguel Montesinos-Ballester, Lucas Deniel, Bertrand Szelag, Xavier Le Roux, Eric Cassan, Delphine Marris-Morini, Laurent Vivien, Pavel Cheben, et al. *Silicon photonic on-chip spatial heterodyne Fourier transform spectrometer exploiting the Jacquinot's advantage*. Optics Letters, 46(6):1341–1344, 2021.

[232] Etienne Le Coarer, Sylvain Blaize, Pierre Benech, Ilan Stefanon, Alain Morand, Gilles Lérondel, Grégory Leblond, Pierre Kern, Jean Marc Fedeli, and Pascal Royer. *Wavelength-scale stationary-wave integrated Fourier-transform spectrometry*. Nature Photonics, 1(8):473–478, 2007.

[233] David Pohl, Marc Reig Escalé, Mohammad Madi, Fabian Kaufmann, Peter Brotzer, Anton Sergeyev, Benedikt Guldimann, Philippe Giaccari, Edoardo Alberti, Urs Meier, et al. *An integrated broadband spectrometer on thin-film lithium niobate*. Nature Photonics, 14(1):24–29, 2020.

[234] Mohammad Madi, Frederik Ceyssens, Ivan Shorubalko, Hans Peter Herzig, Benedikt Guldimann, and Philippe Giaccari. *Lippmann waveguide spectrometer with enhanced throughput and bandwidth for space and commercial applications*. Optics express, 26(3):2682–2707, 2018.

[235] Xiaomin Nie, Eva Ryckeboer, Gunther Roelkens, and Roel Baets. *CMOS-compatible broadband co-propagative stationary Fourier transform spectrometer integrated on a silicon nitride photonics platform*. Optics express, 25(8):A409–A418, 2017.

[236] Audrey Chu, Charlie Gréboval, Yoann Prado, Hicham Majjad, Christophe Delerue, Jean-Francois Dayen, Grégory Vincent, and Emmanuel Lhuillier. *Infrared photoconduction at the diffusion length limit in HgTe nanocrystal arrays*. Nature Communications, 12(1):1794, 2021.

[237] Lucas B Soldano and Erik CM Pennings. *Optical multi-mode interference devices based on self-imaging: principles and applications*. Journal of lightwave technology, 13(4):615–627, 1995.

[238] Ali W Elshaari, Iman Esmaeil Zadeh, Klaus D Jöns, and Val Zwiller. *Thermo-optic characterization of silicon nitride resonators for cryogenic photonic circuits*. IEEE Photonics Journal, 8(3):1–9, 2016.

[239] Adil Masood, Marianna Pantouvaki, Guy Lepage, Peter Verheyen, Joris Van Campenhout, Philippe Absil, Dries Van Thourhout, and Wim Bogaerts. *Comparison of heater architectures for thermal control of silicon photonic circuits*. In 10th International Conference on Group IV Photonics, pages 83–84. IEEE, 2013.

[240] Ivo Tanghe, Margarita Samoli, Isabella Wagner, Servet Ataberk Cayan, Ali Hossain Khan, Kai Chen, Justin Hodgkiss, Iwan Moreels, Dries Van Thourhout, Zeger Hens, et al. *Optical gain and lasing from bulk cadmium sulfide nanocrystals through bandgap renormalization*. Nature Nanotechnology, 18(12):1423–1429, 2023.

[241] Soon Mi Park, Yoon Hak Kim, Yeonjin Yi, Hyoung-Yun Oh, and Jeong Won Kim. *Insertion of an organic interlayer for hole current enhancement in inverted organic light emitting devices*. Applied Physics Letters, 97(6), 2010.

[242] Ta-Ya Chu and Ok-Keun Song. *Hole mobility of N, N'-bis (naphthalen-1-yl)-N, N'-bis (phenyl) benzidine investigated by using space-charge-limited currents*. Applied physics letters, 90(20), 2007.

[243] Benjamin S Mashford, Matthew Stevenson, Zoran Popovic, Charles Hamilton, Zhaoqun Zhou, Craig Breen, Jonathan Steckel, Vladimir Bulovic, Moungi Bawendi, Seth Coe-Sullivan, et al. *High-efficiency quantum-dot light-emitting devices with enhanced charge injection*. Nature photonics, 7(5):407–412, 2013.

[244] Woo Sik Jeon, Jung Soo Park, Ling Li, Dae Chul Lim, Young Hoon Son, Min Chul Suh, and Jang Hyuk Kwon. *High current conduction with high mobility by non-radiative charge recombination interfaces in organic semiconductor devices*. Organic electronics, 13(6):939–944, 2012.

[245] Ji-Li Tian, Hua-Yu Zhang, Gui-Gen Wang, Xin-Zhong Wang, Rui Sun, Lei Jin, and Jie-Cai Han. *Influence of film thickness and annealing temperature on the structural and optical properties of ZnO thin films on Si (1 0 0) substrates grown by atomic layer deposition*. Superlattices and Microstructures, 83:719–729, 2015.

[246] Weiqiang Xie. *Development of passive and active integrated silicon nitride photonics*. PhD thesis, Ghent University, 2016.

[247] Yizhe Sun, Qiang Su, Heng Zhang, Fei Wang, Shengdong Zhang, and Shuming Chen. *Investigation on thermally induced efficiency roll-off: toward efficient and ultrabright quantum-dot light-emitting diodes*. ACS nano, 13(10):11433–11442, 2019.

[248] Alberto D Scaccabarozzi, Aniruddha Basu, Filip Aniés, Jian Liu, Osnat Zapata-Arteaga, Ross Warren, Yuliar Firdaus, Mohamad Insan Nugraha, Yuanbao Lin, Mariano Campoy-Quiles, et al. *Doping approaches for organic semiconductors*. Chemical Reviews, 122(4):4420–4492, 2021.

[249] Dong-Seok Leem, Hyung-Dol Park, Jae-Wook Kang, Jae-Hyun Lee, Ji Whan Kim, and Jang-Joo Kim. *Low driving voltage and high stability organic light-emitting diodes with rhenium oxide-doped hole transporting layer*. Applied Physics Letters, 91(1), 2007.

[250] Baolin Tian, Dayan Ban, and Hany Aziz. *Enhanced bulk conductivity and bipolar transport in mixtures of MoOx and organic hole transport materials*. Thin Solid Films, 536:202–205, 2013.

[251] Caroline Murawski, Cornelius Fuchs, Simone Hofmann, Karl Leo, and Malte C Gather. *Alternative p-doped hole transport material for low operating voltage and high efficiency organic light-emitting diodes*. Applied Physics Letters, 105(11), 2014.

[252] Toshinori Matsushima, Fatima Bencheikh, Takeshi Komino, Matthew R Leyden, Atula SD Sandanayaka, Chuanjiang Qin, and Chihaya Adachi. *High performance from extraordinarily thick organic light-emitting diodes*. Nature, 572(7770):502–506, 2019.

[253] Guanhao Liu, Zhiyi Li, Xiaoxiao Hu, Yuanyuan Qin, Chun-Sing Lee, Dongqi Chen, Lingxue Wang, Jianjun Liu, Pengfei Wang, Yong-Jin Pu, et al. *Efficient and stable one-micrometre-thick organic light-emitting diodes*. Nature Photonics, 16(12):876–883, 2022.

[254] Kenta Yamaguchi, Yu Esaki, Toshinori Matsushima, and Chihaya Adachi. *A 1, 4, 5, 8, 9, 11-hexaazatriphenylenehexacarbonitrile (HAT-CN) transport layer with high electron mobility for thick organic light-emitting diodes*. AIP Advances, 10(5), 2020.

[255] Xin Tang, Matthew M Ackerman, Guohua Shen, and Philippe Guyot-Sionnest. *Towards infrared electronic eyes: flexible colloidal quantum dot photovoltaic detectors enhanced by resonant cavity*. Small, 15(12):1804920, 2019.

[256] Burak Guzelturk, Matthew Pelton, Murat Olutas, and Hilmi Volkan Demir. *Giant modal gain coefficients in colloidal II–VI nanoplatelets*. Nano letters, 19(1):277–282, 2018.